UNIVERSITY OF SOUTHAMPTON

Faculty of Engineering and the Environment

Institute of Sound and Vibration Research, Dynamics Group

Models of vehicle/track/ground interaction in the time domain

by

Jou-Yi Shih

Thesis submitted for the degree of Doctor of Philosophy

April 2017

UNIVERSITY OF SOUTHAMPTON

ABSTRACT

FACULTY OF ENGINEERING AND THE ENVIRONMENT

Institute of Sound and Vibration Research, Dynamics Group

Thesis submitted for the degree of Doctor of Philosophy

MODELS OF VEHICLE/TRACK/GROUND INTERACTION IN THE TIME DOMAIN

Jou-Yi Shih

Due to the demands of increasing population and environmental concerns, the high-speed train has become an important means of transportation in many countries. However, severe vibration induced by high-speed trains can occur when train speeds approach the speed of waves in the ground and track deflections can then become large. Consequently, the track and ground may no longer behave linearly. The aim of this work is to develop a three-dimensional model of vehicle/track/ground interaction in the time domain that can include the consideration of soil nonlinearity.

A three-dimensional time-domain model of a coupled vehicle, track and ground has been developed in the finite element (FE) software ABAQUS. A new analysis approach has been adopted for modelling the moving vehicle without the need for a user-defined subroutine. The results from a track on a hemispherical ground model surrounded by infinite elements show good agreement with the results from a wavenumber finite element / boundary element method at lower speeds. However, significant differences are found for load speeds close to the critical speed for a homogeneous ground. This has been shown to be due to a relatively long transient in the numerical simulation that requires a considerable distance to achieve convergence to steady-state results. As a result, a very long model is required to derive the steady-state results. However, this becomes expensive because of the model geometry.

Moreover, the results from the hemispherical model contain incorrect whole-body displacements due to the use of the infinite elements that make the ground model become unconstrained. Therefore, a cuboid model with a fixed boundary at the bottom is used for the further simulations to prevent these incorrect phenomena. Two different cuboid models, with or without the infinite elements at the sides, are compared. Finally, a wider cuboid model with fixed boundaries is used with appropriate Rayleigh damping which shows the best results and efficiency. A very long model, around 150~300 m, is required when the load speed is equal to the critical speed for a homogeneous soft ground. However, a shorter model is sufficient to obtain the steady-state results for a layered half-space.

For a load moving close to the critical speed on a layered half-space, the track oscillates with a certain dominant frequency. An investigation is presented into the dependence of the oscillating frequency on the ground properties, taking account of the dispersive surface waves. Three different methods are used to investigate this oscillating frequency for a layered half-space ground and a parametric study is carried out. The oscillating frequency is found to vary with the speed of the moving load and tends to decrease when the load speed increases. It mainly depends on the shear wave speed of the upper soil layer and the depth of this layer. A formula is introduced to estimate this oscillating frequency in a layered half-space.

Finally, soil nonlinearity is introduced in the FE model through a user-defined subroutine. The nonlinearity is specified in terms of the shear modulus reduction as a function of octahedral shear strain, based on data obtained from laboratory tests on soil samples. The model is applied to the soft soil site at Ledsgård in Sweden, from which extensive measurements are available from the late 1990s. It is shown that the use of a linear model based on the small-strain soil parameters leads to an underestimation of the track displacements when the train speed approaches the critical speed, whereas the nonlinear model gives improved agreement with the measurements. However, the results are quite sensitive to the choice of nonlinear model. In addition, an equivalent linear model is considered in which the equivalent soil modulus is derived from the laboratory curve of shear modulus reduction using an ‘effective’ shear strain. It is shown that the predictions are improved by using a value of 20% of the maximum strain as the effective strain rather than the value of 65% commonly used in earthquake studies.

Table of Contents

Table of Contents i
List of Tables vii
List of Figures ix
List of Symbols xxiii
List of abbreviations xxvii
Acknowledgements xxix
Chapter 1: Introduction 1
1.1 Background 1
1.2 Aims of the current work and overview of thesis 3
1.3 Original contributions of thesis 4
Chapter 2: Literature review 5
2.1 Critical speed 5
2.2 Resonance phenomenon of layered half-space 7
2.3 Ground models 7
2.3.1 Elementary (non-transmitting) boundaries 8
2.3.2 Locally absorbing (imperfect transmitting) boundaries 9
2.4 Train-induced ground-borne vibration 11
2.4.1 Analytical models 11
2.4.2 Numerical models 15
2.5 Railpad nonlinearity 17
2.6 Ballast nonlinearity 18
2.6.1 Experiments 18
2.6.2 Modelling of ballast by continuous approach 21
2.6.3 Discrete element method (DEM) 23
2.7 Soil and subgrade nonlinearity 24
2.7.1 Experiments 24
2.7.2 Equivalent linear model 28
2.7.3 Cyclic nonlinear model 30
2.7.4 Advanced constitutive model 32

2.8 Summary of literature review and overview of thesis 33

Chapter 3: Modelling of the moving vehicle coupled with the track 35

3.1 Introduction 35
3.2 Simulation procedure 35
3.2.1 Contact model 35
3.2.2 User-defined subroutine 38
3.3 Simply supported beam with moving sprung mass 40
3.4 Use of solid elements to represent simply supported beam subjected to a moving sprung mass 44
3.4.1 Element types 44
3.4.2 Simply supported beam 45
3.4.3 Moving sprung mass 47
3.5 Summary 49

Chapter 4: Ballasted track model 51

4.1 Introduction 51
4.2 Analysis of one and two-layer track with stationary harmonic load 51
4.2.1 Static analysis 53
4.2.2 Single–layer support analysis 55
4.2.3 Two–layer support analysis 58
4.3 Analysis of single-layer track with a moving point load 60
4.3.1 Static analysis of Winkler foundation 62
4.3.2 Moving load applied on Winkler foundation 63
4.4 Analysis of two-layer ballast track with moving dynamic loads 72
4.4.1 Numerical results from moving vehicle simulation 76
4.5 Three-dimensional ballasted track model using ABAQUS 80
4.5.1 Three-dimensional ballasted track model with continuous sleepers 81
4.5.2 Three-dimensional ballasted track model with discrete sleepers 83
4.5.3 Numerical results 84
4.6 Summary 88

Chapter 5: Three-dimensional ground/track model based on hemispherical mesh 91

5.1 Introduction......91
5.2 Infinite elements......91
5.3 Modelling the ground using finite/infinite elements in ABAQUS......92
5.4 Additional displacement due to the unconstrained model......94
5.5 Static analysis of half-space ground model......97
5.6 Investigation of mesh required for half-space ground/track model with a moving load......99
5.7 Investigation of model size for homogeneous half-space ground model with a moving load......103
5.8 Assessment of critical speed for homogeneous half-space ground......109
5.9 Analysis of layered half-space ground model with a moving load......111
5.10 Summary......113

Chapter 6: Three-dimensional ground/track model based on cuboid mesh...115

6.1 Introduction......115
6.2 Modelling of track and ground by using cuboid mesh......115
6.3 Cuboid model for homogeneous half-space with a moving load......118
 6.3.1 Boundary effect for the fixed cuboid model......118
 6.3.2 Influence of the Rayleigh damping parameters......125
 6.3.3 Investigation of the required length......130
6.4 Cuboid model for layered half-space with a moving load......134
6.5 Response of track/ground model to a harmonic load......137
6.6 Influence of discrete sleepers......140
6.7 Summary......144

Chapter 7: Analysis of resonance effect for a track on a layered ground......145

7.1 Introduction......145
7.2 Parameters used in the study......146
7.3 Investigation of the critical speed......147
7.4 Investigation of the resonance frequency for layered half-space......149
 7.4.1 Responses to a stationary harmonic load......149
 7.4.2 Responses from moving point load......150
 7.4.3 Dispersion curves......154

7.4.4 Discussion 157

7.5 Summary 161

Chapter 8: Soil nonlinearity 163

8.1 Introduction 163
8.2 Soil nonlinear model 164

8.2.1 Traxial test modelling 167

8.3 Numerical model for Ledsgård site in Sweden 169
8.4 Results for nonlinear models 172

8.4.1 Parameters for nonlinear models 172

8.4.2 Track displacements from nonlinear models 173

8.4.3 Assessment of octahedral shear strain 176

8.4.4 Assessment of critical speed 180

8.5 Equivalent linear model 182

8.5.1 Procedure 182

8.5.2 Investigation of the value R_r for the equivalent linear model based on nonlinear results 183

8.6 Moving vehicle analysis 187

8.6.1 Data analysis 189

8.6.2 Validation of model including vehicle 192

8.7 Summary 193

Chapter 9: Conclusions and Recommendations for future work 195

9.1 Conclusions 195

9.1.1 Development of vehicle/track/ground interaction model that can account for soil nonlinearity 195

9.1.2 Numerical modelling guidelines for vehicle/track/ground interaction model in the time domain 196

9.1.3 Critical speed and resonance frequency of different grounds 197

9.1.4 Better understanding the influence of soil nonlinearity 197

9.2 Recommendations for future work 198

9.2.1 Investigation of the nonlinear shear modulus degradation curve 198

9.2.2 Long-term behaviour for ballast and soil ... 199

9.2.3 Investigation of the railpad properties ... 199

9.2.4 Investigation of the soil damping ... 199

9.2.5 Further investigation of the factor of effective strain for equivalent linear analysis 199

9.2.6 Further investigation of the need to consider soil nonlinearity ... 200

9.2.7 Mesh strategies ... 200

Appendices ... 201

Appendix A. Track modelling ... 203

A.1 Analytical model of ballasted track with harmonic load ... 203

A.2 Analytical model of moving load applied on a single-layer track system ... 205

Appendix B. Wavenumber FE/BE method for track/ground interaction with a moving load ... 209

Appendix C. Shear modulus reduction curve ... 210

List of References ... 211

List of Tables

Table 2-1 Record speeds of high-speed trains 7

Table 3-1 Simulation CPU cost comparison between two schemes for a typical desktop computer. Times given in seconds...44

Table 3-2 Element description 45

Table 4-1 Single-layer support track parameters 54

Table 4-2 Displacement of the beam at the midpoint 55

Table 4-3 Two-layer support track parameters 58

Table 4-4 One-layer support track parameters...61

Table 4-5 Percentage differences between rail midpoint deflection from FE model compared with analytical solution..62

Table 4-6 Vehicle properties...73

Table 4-7 Two-layer support properties for continuous and discrete sleeper models (models represent two rails) 76

Table 4-8. 3D continuous ballasted track properties..83

Table 4-9. 3D discrete sleeper ballast track properties 84

Table 4-10. Cut-on frequencies from different track models...88

Table 5-1 Half-space Ground model properties...93

Table 5-2 Starting point for different model sizes (radius *r*) and different load speeds 95

Table 5-3 Six different mesh types 101

Table 5-4 Layered half-space ground model properties 111

Table 6-1 List of Rayleigh damping parameters...125

Table 6-2. Calculation times and model sizes required for various models in ABAQUS 130

Table 6-3. Ballast track properties for discrete sleepers 141

Table 6-4 Maximum and minimum stress for railpad from different railpad element (track model) 142

Table 6-5 Maximum and minimum stress for railpad from different railpad element (track/ground model) 143

Table 6-6 Maximum and minimum stress in ballast layer at load speed 40 m/s 143

Table 6-7 Maximum and minimum stress in ballast layer at load speed 80 m/s 143

Table 7-1 Parameters used to define the ground 147

Table 7-2 Track properties (for two rails) 147

Table 7-3 The resonance frequencies found in seven cases 149

Table 7-4 Comparison of resonance frequency based on three different equations with the results from stationary harmonic load 161

Table 7-5 Difference between the results based on Eqs (7-1) to (7-3) and the results for a stationary harmonic load 161

Table 7-6 Difference between the results based on Eqs (7-1) to (7-3) and the results at V_{cr} from the spectrum of quasi-static response 161

Table 8-1. Embankment and ground properties 171

Table 8-2 Embankment and ground Rayleigh damping coefficients 171

Table 8-3. Details of X2000 high speed train used in field tests (Costa et al., 2010) 172

Table 8-4. Comparison of calculation times for train speed of 56.7 m/s in the southbound direction 187

List of Figures

Figure 1-1 Ballast track (a) lateral viewl (b) longitudinal view (Selig and Waters, 1994)............2

Figure 1-2 Three-dimensional vehicle-track-ground model 3

Figure 2-1 Equivalent viscoelastic artificial boundary 9

Figure 2-2 Viscous dashpot boundary 9

Figure 2-3 Track models with discrete track components (adapted from Knothe and Grassie, 1993) 12

Figure 2-4 Spherical ground model (Kouroussis, Verlinden, et al., 2011) 16

Figure 2-5 Elongated spherical ground model (Connolly et al., 2013)..17

Figure 2-6 Cuboid ground model (Hall, 2003) 17

Figure 2-7 Triaxial cells used for testing ballast material; (a) Triaxial cell used by Suiker, et al., 2005; (b) Triaxial cell used by (Buddhima, et al., 2011)................................19

Figure 2-8 The railway test facility at University of Nottingham (Aursudkij et al., 2009) 20

Figure 2-9 Southampton Railway Testing Facility at University of Southampton (Abadi et al., 2016)..20

Figure 2-10 Geopavement and railway accelerated fatigue testing facility at Heriot-Watt University (Kennedy, et al., 2012) 20

Figure 2-11 Nonlinear elastic strain behaviour during one cycle of compressive load application (Varandas, 2013); (a) elastoplastic; (b) nonlinear elastic 21

Figure 2-12 Drained torsional shear test on Toyoura sand; (a) stress-strain behaviour; (b) shear moduli and damping ratio (Iwasaki, et al., 1978) 25

Figure 2-13 Reduction curve of shear modulus versus shear strain (a) Stress-strain curve with variation of shear modulus; (b) modulus reduction curve (Kramer, 1996) 26

Figure 2-14 Tri-axial cyclic test strain for dense sand with different confining pressures; (a)Variation of shear modulus ratio and shear strain (b) Variation of damping ratio and shear strain (Kokusho, 1980)..27

Figure 2-15 Relationship between cyclic strength and content of fines in soils (Ishihara et al., 1978) 27

Figure 2-16 Results for fine-grained soils of different plasticity; (a) modulus reduction curve; (b) damping ratio (Vucetic et al., 1991)... 27

Figure 2-17 Results from Ottawa sand; (a) variation of shear modulus with frequency; (b) variation of damping ratio with frequency (Lin et al., 1996) 28

Figure 2-18 Influence of the shear strain amplitude on cyclic load; (a) shear modulus; (b) damping ratio (Seed et al., 1970) 28

Figure 2-19 Backbone curve of shear modulus versus shear strain.. 31

Figure 2-20 Extended Masing rules; (a) variation of shear stress with time; (b) resulting stress-strain behaviour (Kramer, 1996) 31

Figure 3-1. ABAQUS contact model; (a) Node-to-Surface contact discretization; (b) Surface-to-Surface contact discretization... 36

Figure 3-2. Non-uniform distributed load in each element during analysis 39

Figure 3-3. Nodal displacement for *i* element 39

Figure 3-4. Moving oscillator with a simply support beam.. 41

Figure 3-5. Vertical displacement of the beam at its midpoint for a moving load and a moving sprung mass 42

Figure 3-6. Vertical displacement of the sprung mass.. 43

Figure 3-7. Comparison of midpoint and vehicle displacement between two schemes 43

Figure 3-8. Four different meshes for a simply supported beam using solid elements 46

Figure 3-9. Effect of mesh density with three types of element; (a) mesh 1, *n*=2; (b) mesh 2, *n*=4; (c) mesh 3, *n*=6; (d) mesh 4, *n*=8 47

Figure 3-10. Vertical displacement by using fully integrated C3D8 element; (a) midpoint displacement; (b) sprung-mass displacement... 48

Figure 3-11. Vertical displacement by using reduced-integration C3D8R element; (a) midpoint displacement; (b) sprung-mass displacement... 48

Figure 3-12. Vertical displacement by using incompatible mode C3D8I element; (a) midpoint displacement; (b) sprung-mass displacement... 49

Figure 3-13. Vertical displacement by using higher-order fully integrated C3D20 element; (a) midpoint displacement; (b) sprung-mass displacement 49

Figure 4-1. Typical ballasted track system 51

Figure 4-2. Track model with single-layer support..52

Figure 4-3. Track model with two-layer support 52

Figure 4-4. Track model in ABAQUS with constraint function 53

Figure 4-5. 10 m long track model with single-layer support modelled in ABAQUS 54

Figure 4-6. Comparison of rail deflection from ABAQUS with analytical results......................55

Figure 4-7. Point receptance magnitude of single-layer track model for $\eta = 0.1$ (10 m model) 56

Figure 4-8. Point receptance magnitude of single-layer track model for $\eta = 0.2$ (10 m model) 57

Figure 4-9. Point receptance magnitude of single-layer track model for $\eta = 0.5$ (10 m model) 57

Figure 4-10. Point receptance magnitude of single-layer track model for $\eta = 0.1$ (30 m model)57

Figure 4-11. 10 m long track model with two-layer support modelled in ABAQUS 59

Figure 4-12. Point receptance magnitude of two-layer support track model 59

Figure 4-13. Three-dimensional single-layer support track model by using ABAQUS 60

Figure 4-14. Static deflection of the solid beam model with different element size *dx* (E_s=100 MPa) 62

Figure 4-15. Static deflection of the solid beam model with different element size *dx* (E_s=20 MPa) 63

Figure 4-16. Displacement of the rail on Winkler foundation with different load speeds, E_s=100 MPa, $\xi = 0.1$ (a) 50 m/s; (b) 250 m/s; (c) 500 m/s; (d) 700 m/s; (e) 800 m/s; (f) 900 m/s..65

Figure 4-17. Displacement of the rail on Winkler foundation with different load speeds; E_s=20 MPa, $\xi = 0.1$; (a) 50 m/s; (b) 100 m/s; (c) 200 m/s; (d) 400 m/s; (e) 500 m/s; (f) 600 m/s..66

Figure 4-18. Displacement of the rail on Winkler foundation with different load speeds; E_s=20MPa, $\xi = 0.045$ (a) 50 m/s; (b) 100 m/s; (c) 200 m/s; (d) 400 m/s; (e) 500 m/s; (f) 600 m/s 67

Figure 4-19. Maximum displacement at different positions along the track during the simulation with E_s=100 MPa, for different load speeds; (a) *V*=50 m/s; (b) *V*=250 m/s; (c) *V*=500 m/s; (d) *V*=700 m/s; (e) *V*=800 m/s; (f) *V*=900 m/s 68

Figure 4-20. Maximum displacement at different positions along the track during the simulation with E_s=20 MPa, $\xi = 0.1$, for different load speeds. (a) V=50 m/s; (b) V=250 m/s; (c) V=500 m/s; (d) V=700 m/s; (e) V=800 m/s; (f) V=900 m/s.... 69

Figure 4-21. Maximum displacement at different positions along the track during the simulation with E_s=20 MPa, $\xi = 0.045$, for different load speeds. (a) V=50 m/s; (b) V=250 m/s; (c) V=500 m/s; (d) V=700 m/s; (e) V=800 m/s; (f) V=900 m/s.... 70

Figure 4-22. Distance requirements of the moving load problem: length of transient zone required for convergence to steady-state solution and length of waveform in the rail; (a) E_s=100 MPa, $\xi = 0.1$; (b) E_s=20 MPa, $\xi = 0.045$; (c) E_s=20 MPa, $\xi = 0.1$; (d) comparison of lengths of transient zone three different track models............ 72

Figure 4-23. 10 degree of freedom vehicle model.. 73

Figure 4-24. Rail roughness used for load speed 19 m/s; (a) roughness in spatial domain; (b) roughness spectrum.. 74

Figure 4-25. Rail roughness used for load speed 56.67 m/s; (a) roughness in spatial domain; (b) roughness spectrum.. 74

Figure 4-26. Comparison with moving frame results in the time domain at load speed 19 m/s (Euler-Bernoulli beam) (a) quasi-static loads; (b) dynamic loads.................. 77

Figure 4-27. Comparison with moving frame results in the time domain at load speed 56 m/s (Euler-Bernoulli beam) (a) quasi-static loads; (b) dynamic loads.................. 77

Figure 4-28. Comparison with moving frame results in the time domain at load speed 19 m/s (Timoshenko beam) (a) quasi-static loads; (b) dynamic loads........................ 77

Figure 4-29. Comparison with moving frame results in the time domain at load speed 56 m/s (Timoshenko beam) (a) quasi-static loads; (b) dynamic loads........................ 78

Figure 4-30. Comparison with moving frame results after FFT at load speed at 19 m/s (a) Quasi-static loads; (b) dynamic loads... 79

Figure 4-31. Comparison with moving frame results after FFT at load speed 56 m/s (a) Quasi-static loads; (b) dynamic loads.. 79

Figure 4-32. Rail deflection at position of applied axle load for load speed 19 m/s 79

Figure 4-33. Ratio between the results from Timoshenko and Euler-Bernoulli beam models for moving axle loads plotted against deflection wavelength............................... 80

Figure 4-34 Three-dimensional continuous ballasted track model... 81

Figure 4-35 Three-dimensional discrete support ballasted track model using solid element for railpad 82

Figure 4-36. Point receptance from 3D continuous sleeper ballast track compared with analytical results 85

Figure 4-37. Comparison between continuous and discrete sleeper track model with different correction factors for the ballast stiffness 86

Figure 4-38. Comparison between results for discrete sleepers with orthotropic and isotropic elements for the railpad against the continuous sleeper model (c=0.3) 87

Figure 4-39. Comparison between results for orthotropic and isotropic railpad elements 87

Figure 5-1 Half-space ground model 92

Figure 5-2 Schematic view of model geometry 93

Figure 5-3 Relationship between Rayleigh damping parameters and loss factor 94

Figure 5-4 The maximum displacements at each position along the rail due to moving load; (a) V=10 m/s; (b) V=25 m/s; (c) V=40 m/s; (d) V=50 m/s; (e) V=57 m/s; (f) V=60 m/s; (g) V=70 m/s; (h) V=80 m/s 96

Figure 5-5 Incorrect displacment occuring due to the motion of the moving load (exaggerated)97

Figure 5-6 A uniform load applied to a half-space ground model 98

Figure 5-7 Surface deflection of the half-space ground model due to a uniform pressure over 1 m radius 99

Figure 5-8 Ground displacement for a constant load of 1 N moving at different load speeds; (a) *V*=10 m/s; (b) *V*=57 m/s. Results obtained using semi-analytical model, (Sheng, 1999) 101

Figure 5-9 Six different mesh types for radius 10m; (a) Mesh1; (b) Mesh2; (c) Mesh3; (d) Mesh4; (e) Mesh5; (f) Mesh6 102

Figure 5-10 Mid-point maximum rail displacement for moving load of amplitude 1 N on homogeneous half-space at different speeds 103

Figure 5-11 Displacement of the rail at the centre of the model plotted against load position for different load speeds; (a) *V*=25m/s; (b) *V*=40m/s; (c) *V*=50m/s; (d) *V*=57m/s; (e) *V*=70m/s; (f) *V*=80m/s 105

Figure 5-12 Displacement of the ground at the centre of the model plotted against load position at different depths; (a) *V*=25m/s; (b) *V*=40m/s; (c) *V*=50m/s; (d) *V*=57m/s; (e) *V*=70m/s; (f) *V*=80m/s 106

Figure 5-13 Displacement of the homogeneous half-space for two different load speeds; (a) load speed 25 m/s; (b) load speed 80m/s 107

Figure 5-14 Displacements of the ground at *x*=0 plotted against the transverse direction *z*, when the load is at different positions *x*; (a) *V*=10m/s; (b) *V*=25m/s; (c) *V*=50m/s; (d) *V*=57m/s; (e) *V*=70m/s; (f) *V*=80m/s 108

Figure 5-15 Maximum deflection for a moving load of amplitude 1 N for the homogeneous half-space ground 109

Figure 5-16 Evolution of the deformation under a moving load when load speed is 57 m/s (left: top view; right: side view) 110

Figure 5-17 Layered half-space ground model 111

Figure 5-18 Displacement of the layered half-space for load speed 80 m/s 112

Figure 5-19 Maximum deflection for a moving load of amplitude 1 N for the layered half-space ground 113

Figure 6-1 Cuboid model; (a) fixed boundary; (b) fixed boundary with infinite elements 116

Figure 6-2 Element types; (a) 12-node infinite element (CIN3D12R); (b) 20-node brick element (C3D20) (ABAQUS, 2013b) 116

Figure 6-3 Midpoint displacement using different stretch factors for a load speed of 50 m/s 117

Figure 6-4 Rail midpoint displacement due to a moving load of 1 N for different load speeds; (a) *V*=40m/s; (b) *V*=50m/s; (c) *V*=57m/s; (d) *V*=60m/s; (e) *V*=70m/s; (f) *V*=80m/s; 119

Figure 6-5 Propagation of P- and S-wavefronts from a moving point source for (a) subsonic, (b) transonic and (c) supersonic convection. (Andersen et al., 2007) 120

Figure 6-6 The route of the reflection propagating from the side boundary when load speed at 80 m/s 120

Figure 6-7 Comparison of midpoint displacement for a moving load of 1 N between the models with and without the infinite elements; (a) *V*=40m/s; (b) *V*=50m/s; (c) *V*=57m/s; (d) *V*=60m/s; (e) *V*=70m/s; (f) *V*=80m/s; 122

Figure 6-8 The maximum displacements at each point along the rail found from a model with 20 m width and fixed boundaries; (a) V=40 m/s; (b) V=50 m/s; (c) V=57 m/s; (d) V=60 m/s; (e) V=70 m/s; (f) V=80 m/s 124

Figure 6-9 The maximum displacement at each position along the rail found by using models with fixed boundaries and different widths; (a) V=40 m/s; (b) V=50 m/s 125

Figure 6-10 Equivalent loss factor..126

Figure 6-11 Comparison of four different model with the first model; (a) α=0, β=0.000636 s, W=20 m; (b) α=3.925 s^{-1}, β=0, W=20 m; (c) α=0.98 s^{-1}, β=0.000159 s, W=20 m; (d) α=0.98 s^{-1}, β=0.000159 s, W=40 m 127

Figure 6-12 Displacements of the cuboid model when the load is at midpoint by stiffness damping β=0.000636 s (W=20 m) 128

Figure 6-13 Displacements of the cuboid model when the load is at midpoint by mass damping α=3.925 s (W=20 m)..128

Figure 6-14 Displacements of the cuboid model when the load is at midpoint by Rayleigh damping α=0.98 s^{-1}, β=0.000159 s (W=20 m)..128

Figure 6-15 Displacements of the cuboid model when the load is at midpoint by mass damping α=0.98 s^{-1}, β=0.000159 s (W=40 m)..129

Figure 6-16 Rail displacement obtained by using different widths of model when load speed is 60 m/s 130

Figure 6-17 The maximum displacements at each position along the rail from model with α=0.98 s^{-1}, β=0.000159 s and W=40 m; (a) V=40 m/s; (b) V=80 m/s; (c) V=57 m/s....131

Figure 6-18 Maximum displacements plotted against load speed obtained by using different values of Rayleigh damping and compared with the wavenumber FE/BE model....133

Figure 6-19 Maximum displacements plotted against load speed obtained by using wavenumber FE/BE method with different constant values of loss factor 133

Figure 6-20 Required distances for different load speeds by using different Rayleigh damping133

Figure 6-21 Displacement of the rail with different load speeds from ABAQUS and wavenumber FE/BE model (with loss factor 0.05); (a) V=40 m/s; (b) V=57 m/s; (c) V=80 m/s 134

Figure 6-22 Results for layered half-space ground. (a) Length of transient zone required for convergence to steady-state solution for different load speeds; (b) Maximum deflection of track during the passage of a unit load plotted as a function of speed 135

Figure 6-23. Comparison between the results from FE model and the results from wavenumber FE/BE for layered half-space; (a) V=50 m/s; (b) V=70 m/s; (c) V=80 m/s (d) V=100 m/s 136

Figure 6-24. Displacement of the layered half-space in the space domain for different load speeds (top view); (a) *V*=50 m/s; (b) *V*=70 m/s; (c) *V*=80 m/s (d) *V*=100 m/s 137

Figure 6-25 Point receptance on the rail for homogeneous half-space ground (α = 0.98 s^{-1}, β = 0.000159 s); (a) by using three different hemispherical models ; (b) when load applied at different locations for 40 m radius model 138

Figure 6-26 Point receptance on the rail for homogeneous half-space; (a) α = 0, β = 0.000636 s; (b) α = 0, β = 0.00265 s; (c) α = 3.925 s^{-1}, β = 0; (d) α = 0.98 s^{-1}, β = 0; (e) α = 0.98 s^{-1}, β = 0.000159 s 139

Figure 6-27 Receptance of layered half-space. Comparison of wavenumber FE/BE model (loss factor 0.05) with cuboid FE model with three different combinations of damping parameters 140

Figure 6-28 Maximum displacements plotted against load speed from track model using discrete sleepers and the continuous model for layered half-space 142

Figure 7-1 Maximum displacement as a function of load speed for different cases; (a) variation of c_{p1}, c_{p2} and c_{s2}; (b) variation of c_{s2}; (c) variation of layer depth 148

Figure 7-2 Receptance of the rail from seven different models; (a) Cases 1~4; (b) cases 5~8 . 149

Figure 7-3 Results from case 1 for different load speeds; (a) rail displacement spectrum; (b) rail displacement in the time domain 150

Figure 7-4 Results from case 2 for different load speeds; (a) rail displacement spectrum; (b) rail displacement in the time domain 151

Figure 7-5 Results from case 3 for different load speeds; (a) rail displacement spectrum; (b) rail displacement in the time domain 151

Figure 7-6 Results from case 4 for different load speeds; (a) rail displacement spectrum; (b) rail displacement in the time domain 151

Figure 7-7 Results from case 5 for different load speeds; (a) rail displacement spectrum; (b) rail displacement in the time domain 152

Figure 7-8 Results from case 6 for different load speeds; (a) rail displacement spectrum; (b) rail displacement in the time domain 153

Figure 7-9 Results from case 7 for different load speeds; (a) rail displacement spectrum; (b) rail displacement in the time domain 153

Figure 7-10 Results from case 8 for different load speeds; (a) rail displacement spectrum; (b) rail displacement in the time domain 153

Figure 7-11. Dispersion diagrams obtained from analytical model for case 1; (a) without track; (b) with track 154

Figure 7-12. Dispersion diagrams obtained with analytical results for case 2; (a) without track; (b) with track 155

Figure 7-13. Dispersion diagrams obtained with analytical results for case 3; (a) without track; (b) with track 155

Figure 7-14. Dispersion diagrams obtained with analytical results for case 4; (a) without track; (b) with track 156

Figure 7-15. Dispersion diagrams obtained with analytical results for case 5; (a) without track; (b) with track 156

Figure 7-16. Dispersion diagrams obtained with analytical results for case 6; (a) without track; (b) with track 156

Figure 7-17. Dispersion diagrams obtained with analytical results for case 7; (a) without track; (b) with track 157

Figure 7-18. Resonance frequency at different load speeds obtained by using three different methods; (a) Case 1; (b) Case 2; (c) Case 3; (d) Case 4; (e) Case 5; (f) Case 6; (g) Case 7 160

Figure 8-1 Shear-strain path during cyclic loading...164

Figure 8-2 Nonlinear soil characteristics obtained for different soil layers at Ledsgård (Costa et al., 2010) (a) shear modulus reduction curves; (b) damping ratio......................165

Figure 8-3 ABAQUS three-dimensional quarter model for cyclic triaxial test 168

Figure 8-4 Shear modulus reduction curve for four different soil properties obtained from FE model of triaxial test; (a) embankment; (b) crust; (c) organic clay; (d) clay...........169

Figure 8-5 Soil and railway embankment geometry and shear wave speeds at Ledsgård based on soil investigations; (a) cross-section; (b) shear wave speed 170

Figure 8-6 Three-dimensional track/ground model 171

Figure 8-7 Shear modulus reduction curve and damping ratio for organic clay layer; (a) shear modulus reduction; (b) damping ratio 173

Figure 8-8 Northbound displacement, comparison between linear, nonlinear models and measurement for load speed 50 m/s 174

Figure 8-9 Northbound displacement comparison between two nonlinear models for different load speeds; (a) V=19 m/s; (b) V=45 m/s; (c) V=50 m/s 175

Figure 8-10 Southbound displacement from linear model for two different speeds; (a) V=19 m/s; (b) V=56.7 m/s 176

Figure 8-11 Octahedral shear strain on the top surface of organic clay layer when train speed is 50 m/s for two different nonlinear models (northbound); (a) nonlinear model 1; nonlinear model 2 177

Figure 8-12 Octahedral shear strain variation below the rail on the top surface of the organic clay layer from two different nonlinear models 177

Figure 8-13 Octahedral shear strain at the top surface of the organic clay layer from linear and nonlinear model at load speed 56.7 m/s (northbound); (a) linear model; (b) nonlinear model 2 178

Figure 8-14 Octahedral shear strain in the y-z plane below the first and fourth axles for different load speeds (northbound); (a) V=19 m/s, 1st axle; (b) V=19 m/s, 4th axle; (c) V=56.7 m/s, 1st axle; (d) V=56.7 m/s, 4th axle 179

Figure 8-15 The maximum octahedral shear strain along the depth from northbound analysis for two different load speed; (a) V=19 m/s; (b) V=56.7 m/s 180

Figure 8-16. Maximum upward and downward sleeper displacements for different train speeds; -: northbound nonlinear model; □: southbound nonlinear model; --: linear model; o: northbound measurement data; *: southbound measurement data 181

Figure 8-17. Maximum octahedral strain level at various depths in the organic clay layer at different load speeds 181

Figure 8-18 Variation of shear modulus reduction and damping ratio with depth obtained using R_r=0.65 for two different load speeds, showing initial results and results after two iterations ; (a) shear modulus reduction; (b) damping ratio 184

Figure 8-19 Variation of shear modulus reduction and damping ratio with depth obtained using R_r =0.2 for two different load speeds, showing initial results and results after two iterations; (a) shear modulus reduction; (b) damping ratio 184

Figure 8-20 Cumulative distribution function of octahedral shear strain at load speed 56.7 m/s for the top surface of organic clay layer..185

Figure 8-21 Variation of maximum octahedral shear strain from two different speeds; (a) *V*=19 m/s; (b) *V*=56.7 m/s...186

Figure 8-22 Southbound displacement from equivalent linear model; (a) *V*=19 m/s; (b) *V*=56.7 m/s 186

Figure 8-23 Roughness spectrum for different load speeds; (a) *V*=19 m/s; (b) *V*=56.7 m/s......188

Figure 8-24 Rail roughness profile used for two different speeds; (a) *V*=19 m/s; (b) *V*=56.7 m/s189

Figure 8-25 Five degree of freedom vehicle model..189

Figure 8-26 Midpoint results with/without window from moving point load for load speed 19 m/s in the time domain; (a) *z*=0.7 m; (b) *z*=7.5 m 190

Figure 8-27 Results from moving point load with/without window for load speed 19 m/s in the space domain when load is applied at *x* = 4 m away from the centre; (a) *z*=0.7 m; (b) *z*=7.5 m...191

Figure 8-28 Results due to moving loads calculated by superposition in the space domain for two different load speeds; (a) 19 m/s; (b) 56.7 m/s 192

Figure 8-29 Results from ABAQUS at 7.5m from the track compared to the measurement (Sheng et al., 2003).; (a) load speed 19 m/s ; (b) load speed 56.7 m/s 193

Figure A-1 Single-layer support track model 204

Figure A-2 Double-layer support track model..204

Figure A-3 Winkler foundation with a moving load...205

Figure B-1. Cross-section of track and ground model in wavenumber FE/BE method.............209

Declaration of Authorship

I, Jou-Yi Shih declare that the thesis entitled, “Models of vehicle/track/ground interaction in the time domain” and the work presented in the thesis are both my own and have been generated by me as the result of my own original research. I confirm that:

1. This work was done wholly or mainly while in candidature for a research degree at this University.
2. No part of this thesis has previously been submitted for a degree or any other qualification at this University or any other institution.
3. Where I have consulted the published work of others, this is always clearly attributed;
4. Where I have quoted from the work of others, the source is always given. With the exception of such quotations, this thesis is entirely my own work.
5. I have acknowledged all main sources of help.
6. Where the thesis is based on work done by myself jointly with others, I have made clear exactly what was done by others and what I have contributed myself.
7. Parts of this work has been published as
    - Shih, J., Thompson, D. and Zervos, A. (2017) ‘The influence of soil nonlinear properties on the track/ground vibration induced by trains running on soft ground’ Transportation Geotechnics . vol. 11, pp. 1-16.
    - Shih, J., Thompson, D. and Zervos, A. (2016) ‘The effect of boundary conditions, model size and damping models in the finite element modelling of a moving load on a track/ground system’ Soil Dynamics and Earthquake Engineering , vol. 89, pp. 12-27.
    - Shih, J., Thompson, D. and Zervos, A. (2016) ‘Modelling of ground-borne vibration when the train speed approaches the critical speed’. In: 12th International Workshop on Railway Noise, IWRN12, 12th-16th September 2016, Terrigal, Australia.
    - Shih, J., Thompson, D. and Zervos, A. (2016) ‘Modelling scheme for railway vehicle/track/ground dynamic interaction in the time domain’. In: Proceeding of the 24th UK conference of the Association for Computational Mechanics in Engineering, 31st March-1st April 2016, Cardiff, Wales.

- Shih, J., Thompson, D. and Zervos, A. (2014) ‘Assessment of track-ground coupled vibration induced by high-speed trains’. In: The 21st International Congress on Sound and Vibration, 13-17 July, 2014, Beijing, China.

Signed: ……………………………………………………………………………

Date: 20/06/2017

List of Symbols

A_{total}	Total area of all elements around the node considered on the boundary
A_L	Area enclosed by the hysteresis loop
A_T	Area enclosed by the triangle defined by the maximum strain and the maximum stress
a	Constants for Ramberg-Osgood model
b	Constants for Ramberg-Osgood model
c	Correction to allow for load spreading beneath the sleeper in the direction along the track
c_p	Compressional wave (P-wave) speed
c_s	Shear wave (S-wave) speed
c_R	Rayleigh wave (R-wave) speed
c_p	Railpad damping coefficient for discrete sleeper model
c_b	Ballast damping coefficient for discrete sleeper model
C_{Ni}	Damping values for the normal direction for viscous or viscous-spring artificial boundary
C_{Ti}	Damping values for the tangential direction for viscous or viscous-spring artificial boundary
$\mathbf{C}$	Damping Matrices
D	Decay rate respect with distance
EI	Bending stiffness of the rail
E	Young’s modulus
E'_b	Ballast equivalent Young’s modulus for continuous sleeper model
E'_s	Sleeper equivalent Young’s modulus for continuous sleeper model
E_b	Ballast equivalent Young’s modulus for discrete sleeper model
E_s	Sleeper equivalent Young’s modulus for discrete model
E_f	Equivalent foundation stiffness using plan
F	Axle load
$\mathbf{F}_t$	Contact force vector
$f_{\max}$	The maximum frequency in the dynamic analysis
G	Shear modulus of soil

$G_{\max}$	Shear modulus at very low strain levels ($<10^{-6}$)
h	Normal distance between two specified contact surfaces
h_b	Height of the ballast
h_s	Height of the sleeper
H	Soil layer depth
I	Second moment of area
k_{Ni}	Stiffness values for the normal direction for viscous or viscous-spring artificial boundary
k_{Ti}	Stiffness values for the tangential direction for viscous or viscous-spring artificial boundary
K_1	Constants for granular material $K-\theta$ model
K_2	Constant for granular material $K-\theta$ model
K_3	Constant for modified $K-\theta$ model
$\mathbf{K}$	Stiffness Matrices
k	Wavenumber
L	Length of the model
L_s	Sleeper spacing
L_{sl}	Half length of the sleeper
L_{static}	Total length of the waveform for static analysis
l_e	Element length (maximum node spacing)
l_h	Element height
l_t	Element thickness
m_s'	Sleeper mass per unit length
m_s	Ballast mass per unit length
$\mathbf{M}$	Mass Matrices
p	Contact pressure
p_a	The non-uniform pressure at the left node
p_b	The non-uniform pressure at the right node
q	Deviatoric stress
R_r	Empirical factor for equivalent linear analsysis
R	The radial coordinate
s	Winkler foundation stiffness per unit length

s_b	Ballast stiffness per unit length
s_p	Railpad stiffness per unit length
u_r	Rail displacement
u_s	Sleeper displacement
$u_{1,i} \sim u_{6,i}$	Nodal displacements for beam element
$\dot{u}_x^i \sim \dot{u}_z^i$	Nodal velocity in *x,y,z* direction
$\mathbf{u}_{v,t}$	Vehicle displacement vector
$\dot{\mathbf{u}}_{v,t}$	Vehicle velocity vector
$\ddot{\mathbf{u}}_{v,t}$	Vehicle acceleration vector
V_{cr}	Critical speed
V	Load speed
W	Width of the model
w_{b1}	Half the top widths of the ballast layer
w_{b2}	Half the bottom widths of the ballast layer
x_i	location of node *i* in each element
y_0	Deflection at mid-span of a beam
α	Mass proportional value for Rayleigh damping
α_T	Tangential artificial boundary parameters
α_N	Normal artificial boundary parameters
β	Stiffness proportional value for Rayleigh damping
γ	Shear strain
γ_r	Reference shear strain
γ_{oct}	Octahedral shear strain
γ_{eff}	Effective shear strain
$\gamma_{\max}$	The maximum shear strain level
λ	Lamé’s first parameter
$\lambda_{\min}$	The minimum wavelength in the dynamic analysis
λ_s	Wavelength of S-wave
η	Foundation loss factor
η_r	Rail damping loss factor
η_b	ballast damping loss factor

η_p	Railpad damping loss factor
ρ	Material density
ρA	Rail mass per unit length
ρ_s'	Equivalent sleeper density for continuous sleeper model
ρ_s	Equivalent sleeper density for discrete model
ν	Poisson ratio of
ξ	Damping ratio
ξ_p	Damping ratio for railpad
ξ_b	Damping ratio for ballast
ω	Circular frequency
ω_n	*n*-th natural frequency of the beam
ω_{c1}	First resonance frequency for two-layer ballasted track
ω_{c2}	Second resonance frequency for two-layer ballasted track
θ	Sum of the effective principal stresses (bulk stress)
θ_0	reference value for granular material $K-\theta$ model
σ_1'	Effective stress in *x*-*x* direction
σ_2'	Effective stress in *y*-*y* direction
σ_3'	Effective stress in *z*-*z* direction
$\sigma_{xx}^i \sim \sigma_{zz}^i$	Stress at *x*-*x*, *y*-*y* , *z*-*z* direction
$\phi_{1,t,j}^{(s_i)} \sim \phi_{6,t,j}^{(s_i)}$	Six shape functions for a beam element
τ_f	Yield strength of the material
τ	Shear stress
$\varepsilon_{v,r}$	Volumetric strain
$\varepsilon_{s,r}$	Deviatoric strain

List of abbreviations

BEM	Boundary Element method
DSEM	Damping solvent extraction method
DEM	Discrete element method
FEM	Finite Element method
SBFE	Scaled boundary finite element method
TLM	Thin Layer Method

Acknowledgements

I would first like to express my sincere appreciation to my supervisors, Prof. David Thompson and Dr. Antonis Zervos. Especially to David who deserves the award of “the best supervisor”; who always has the answer to my doubts; who trusts me from the very beginning to the end even though I am a “trouble maker”. Thanks for all the support, encouragement, and concern. What I have been able to achieve has been beyond my expectation in terms of not only the results but also the attitude of being a good researcher.

I would like to thank Dr. Pedro Alves Costa from University of Porto for sharing the measurement data from Ledsgård. I would also like to thank Dr. Evangelos Ntotsios and Dr. Samuel Koroma for helping with the validation of the vehicle/track/ground dynamics.

My sincere thanks go to my lovely family, my dad, mom and my little brother. You are my energy source that makes me strong and lets me have the strength to go through every difficulty. You are my shelter that I know you are always there no matter what. Special thanks go to my dear dad who knows me the best and trusts me the most. Thanks for being the first person supporting me to complete my dream. Thanks for all the silly ideas like buying a super computer for me.

A very special gratitude goes to the EPSRC programme grant ‘Railway Track for the 21st Century’ for providing the funding for the work.

With a special mention to Sheng-Yu Tsai who encouraged me to achieve what I wanted and gave me a lot of support during the hardest time of my PhD. Without you, my dream would never come true.

And finally, I would like to thank all my friends in Taiwan especially Ruei-Shiang Hung who is always there when I need him. I would also like to thank Sonia, Lluis, Ana, Xianying, Toni, especially Xiaowan and all my colleagues in ISVR. Even though Southampton seems a very boring city, people make my life full of joy every day. Thanks for all the concern, encouragement and happiness.

Chapter 1: Introduction

1.1 Background

Nowadays the quality of public transportation has become very important due to the increased population density and growing environmental concerns. Carbon dioxide emission from airplanes is much higher than any other public transportation and private cars are less sustainable and more time consuming for longer journeys. The railway system offers many advantages because of its high capacity and its low carbon dioxide emissions. However, with the development of high-speed trains, many problems have to be solved such as the running stability of the trains, the increased cost of the railway maintenance, and railway noise including the aerodynamic noise, which becomes the dominant noise when the train speed is higher than 300 km/h. In addition, ground borne noise and vibration induced by high-speed trains has also become an important issue.

A very important aspect of the design of the track is known as the critical speed. As the train approaches the speed of waves in the ground and embankment, large displacements of the track and ground can occur. This has become an important issue due to the development of high-speed trains. Moreover, sometimes even normal operating speeds may reach the critical speed for soft soil sites. For example, large displacements of the track were found at Ledsgård for load speed of 50 m/s (180 km/h) (Madshus and Kaynia, 2000) and enhanced ground treatment was required in order to improve the safety and stability. As a result, good prediction of the track/ground interaction dynamics is not only required for better design of new railway lines but also to design the treatments that are required to improve the behaviour appropriately with the least cost for existing lines where the speed is to be raised.

Ballasted track is the most common conventional track form in which the rails are supported on sleepers which are embedded in a compact ballast layer up to 350 mm thick below the sleeper (Indraratna and Salim, 2005), as shown in Fig. 1-1. Such track is widely used throughout the world due to its resilience to repeated wheel loads, relatively low construction cost and ease of maintenance. However, ballast degradation, which is associated with particle breakage, fouling and ballast migration, as well as deformation of the subgrade, which may result in a small amount of permanent settlement under each wheel load, occurring due to the periodic forces induced by the trains. In the long term, this accumulated settlement will cause uneven track geometry which will lead to high dynamic stresses on critical track components, such as rails, sleepers and fasteners, and increase the track settlement and track deterioration further. Therefore, regular maintenance is required such as by ballast tamping machines. Although the cost of such maintenance is lower than that of replacing the whole system, it is still very high. Moreover, even though maintenance machines are used frequently, it is suspected that routine ballast tamping can lead to particle breakage. Therefore, a knowledge of the crush behaviour of railway ballast and the dynamic behaviour of the track system, including the deformation of the sleeper, ballast and subgrade and the dynamic stress distribution through the track components, is very important for better railway design that can reduce the cost of maintenance and increase the safety of high-speed train operation.

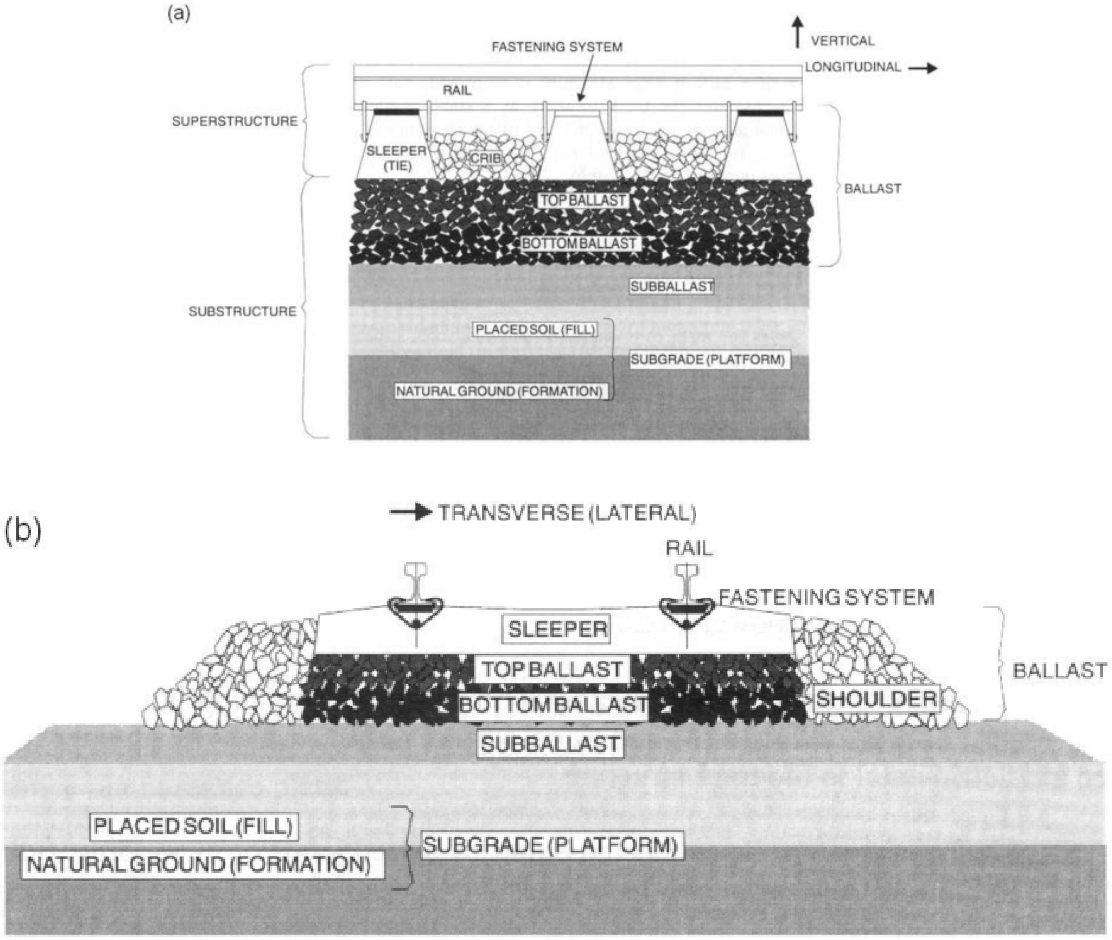

Figure 1-1 Ballast track (a) lateral viewl (b) longitudinal view (Selig and Waters, 1994)

A related issue is ground-borne vibration which has become a serious concern for nearby residents when passing trains cause buildings to vibrate. Ground-borne vibration is transmitted as P-waves (longitudinal waves), S-waves (shear waves) and Rayleigh waves (surface waves). The fastest wave is the P-wave; however, it has lower energy than surface waves and is attenuated more quickly away from the excitation region. In contrast, the slowest wave, the Rayleigh wave, can propagate over large distances and its amplitude is much higher than the others. Therefore, the surface waves are usually the most important for ground vibration, because of their amplitude and their influence area.

Figure 1-2 Three-dimensional vehicle-track-ground model

The vehicle, track, and ground systems are not independent; each system is coupled to the others. Therefore, to study ground-borne vibration and critical velocity effects and their dependence on ground properties, coupled vehicle-track-ground numerical simulations are required. Moreover, dynamic loads calculated through the simulations can be used to investigate the influence of dynamic stresses on the railway components, which can lead to increased understanding of ballast degradation and subgrade damage.

1.2 Aims of the current work and overview of thesis

The aim of the current work is to develop a method of modelling the vehicle-track-ground interaction that can be used for any desired condition including nonlinear behaviour. The model is visualised in Fig. 1-2. It uses a three-dimensional finite element model that describes the response of the track and ground to the moving dynamic loads of a train. The model should operate in the time domain and it is intended that it can account for nonlinear behaviour; it should include the dynamic behaviour of the vehicle (using a multi-body approach) and the wheel/rail contact as well as the track and the ground. Initially a three-dimensional linear dynamic model is constructed and then nonlinearities in the soil properties are included subsequently.

In Chapter 2 a detailed literature review is presented of critical speed, ground modelling, train-induced ground borne vibration and nonlinearity of railpads, ballast and soil. In Chapter 3 procedures for modelling the moving vehicle problem are discussed and the performance of the various alternative finite elements is assessed. In Chapter 4 two- and three-dimensional track models are introduced. Stationary harmonic loads, moving constant loads and moving dynamic loads including the vehicle model are compared with results from an analytical model. Differences between the two- and three-dimensional models and between discrete and continuous sleeper models are discussed.

In Chapter 5 a track/ground model using a hemispherical mesh surrounded by infinite elements is used to represent a homogeneous half-space. The results are validated against an existing wavenumber FE/BE model. Limitations of the infinite elements are investigated, transient effects are discussed and the required mesh and model size is determined. In Chapter 6 instead of the hemispherical model, a cuboid mesh is used for the homogeneous half-space and for a layered half-space. The effect of the boundaries is investigated and an appropriate damping model is introduced. In Chapter 7 a parametric study is performed for a layered half-space, in particular focussing on the oscillation frequency of the ground under a moving load. Chapter 8 applies the models of vehicle/track/ground interaction to the soft ground site of Ledsgård in Sweden. Soil nonlinearity is considered and results are compared with those from linear and equivalent linear models. Finally, Chapter 9 presents the conclusions of the work and recommendations for future research.

1.3 Original contributions of thesis

The original contributions of the thesis can be listed as follows:

(1) Distances required for moving load problems to reach steady-state

For the moving load problem it has been shown that the distance required to reach the steady-state solution becomes very large when the load speed is close to the critical speed of a homogeneous ground. Models of a track on a Winkler foundation, on a half-space, and on a layered half-space have been used to investigate the required distances. From this, general conclusions have been reached concerning the necessary length of model for the results to reach steady-state.

(2) Better understanding of the limitation of the use of infinite elements for moving load problems

Incorrect whole body displacements of the model have been found when the infinite elements are used with moving load problems due to the unconstrained boundary. In addition, even though the hemispherical model has good absorption at the boundary due to its geometry, small wave reflections can still be found. As a result, a specific cuboid model with fixed boundaries and appropriate damping has been shown to be preferable for modelling the moving load problems due to its acceptable accuracy and better efficiency. It is shown that a cuboid model with specific width and depth can be used to represent a semi-infinite ground more efficiently than a smaller model including infinite elements.

(3) Resonance phenomenon for a layered half-space

From the parametric studies of a moving load applied on a layered half-space it has been shown that the resonance frequency is mainly determined by the shear wave speed of the upper soil layer and the depth of this layer. Furthermore, the variation with load speed is found to be small. A formula is introduced to estimate the resonance frequency for a layered half-space.

(4) Modelling approach for soft ground when the load speed approaches the critical speed

A simple nonlinear soil model has been introduced and improved results for the track displacements have been found when soil nonlinearity is included compared with a linear model. From an analysis of the strain levels better understanding of the limitations of the linear and equivalent linear models has been obtained. Guidelines are given for whether the soil nonlinearity needs to be considered in studying the vibration of soft ground induced by moving trains. In addition, an appropriate factor is suggested for calculating the “effective” shear strain in order to obtain better predictions.

(5) Modelling guidelines for the time domain analysis for vehicle/track/ground system

Based on above contributions, general modelling guidelines are given in terms of requirement of model geometry, grid size, damping model, consideration of soil nonlinearity, and the used of the element type to be used.

Chapter 2: Literature review

2.1 Critical speed

As the train speed increases, the amplitude of the track vibration can become larger. In 1994, rail deflection measurements at various train passing speeds were carried out at Stilton Fen, England and a value of 12 mm, which was almost double the response at lower speeds, was found at a train speed of 185 km/h (Hunt, 1994). In 1998, extensive site measurements were carried out by the Swedish State Railways at a location with very soft soil ground in Ledsgård. The vibration of the rail, embankment and ground induced by an X-2000 passenger train showed very high levels when the train speed increased to 200 km/h, which was close to the wave speed in the ground. The maximum amplitude of track vibration was around 15~20 mm, which exceeded the limit for safety and stability (Kaynia, et al., 2000; Madshus and Kaynia, 2000). Assessment of the critical speed has become a very important issue for railway engineering due to the large vibration that can occur which may damage the track components and cause environmental impact for the neighbourhood (Sheng, et al., 2004a).

In early research on the subject of track vibration due to moving loads, the ground was usually neglected or considered as part of the supporting layer in the track model to form a continuous damped elastic Winkler foundation. For such a system, the critical speed can be derived by (Fryba, 1999; Kenney, 1954; Timoshenko, 1926)

$$V_{cr} = \sqrt[4]{\frac{4sEI}{(\rho A)^2}} \qquad (2\text{-}1)$$

where s is the foundation stiffness per unit length, EI is the bending stiffness of the rail (with E the Young's modulus and I the second moment of area) and ρA is the rail mass per unit length. Severe vibration can occur as the load approaches this value. However, this expression does not give realistic values for the critical speed. Using the common properties of the subgrade it gives a value around 500 m/s (Madshus and Kaynia, 2000).

An alternative estimate, instead of using the model with continuous springs, can be obtained by using a half-space ground to calculate the critical speed. In an elastic medium there are two fundamental wave speeds, of the compressional wave (P-wave) c_p and shear wave (S-wave) c_s , which are given by

Compressional wave (P-wave): $$c_p = \sqrt{\frac{\lambda + 2G}{\rho}} \tag{2-2}$$

Shear wave (S-wave): $$c_s = \sqrt{\frac{G}{\rho}} \tag{2-3}$$

where G is the shear modulus, v is the Poisson ratio, and λ is Lamé's first parameter which can be given as

$$\lambda = \frac{Ev}{(1+v)(1-2v)} \tag{2-5}$$

where $E = 2G(1+v)$ is Young's modulus. For a half-space, surface waves known as Rayleigh waves occur with a wave speed that is slightly lower than the shear wave speed:

Rayleigh wave (R-wave): $$c_R = \frac{0.87 + 1.12v}{1+v} c_s \tag{2-4}$$

A moving point load applied on the surface of a three-dimensional semi-infinite homogeneous isotropic elastic solid was studied by (Eason, 1965) who showed that the displacement became large when the load speed approached the Rayleigh wave speed. The results were obtained numerically by using single finite integrals which were reduced from the multiple integrals obtained from the basic equation. However, the results were found to be inadequate when the Rayleigh wave speed was approached. A more detailed model, which used an Euler-Bernoulli elastic beam to represent rail and sleeper, was developed by (Krylov, 1995, 1996) who indicated that severe rail displacement would occur when the load speed is close to or exceeds the Rayleigh wave speed. Two critical speeds were identified by Dieterman and Metrikine, 1996, 1997, by considering a beam on a homogeneous half-space. The beam was intended to represent the track and the embankment. The first critical speed was equal to the Rayleigh wave speed but the second one was slightly lower. This second critical speed was controlled by the bending stiffness and the mass of the beam (Dieterman and Metrikine, 1996, 1997).

A model of track on a layered ground was used by (Costa, et al., 2015) and two critical speeds were found when the stiffness of the upper layer was higher than the lower layer. The lower critical speed is close to the shear wave speed of the lower layer and the second critical speed is close to the Rayleigh wave speed of the upper layer.

The value of the Rayleigh wave speed in the soil is therefore important for the assessment of critical speeds. The typical range of the Rayleigh wave speeds in soil is 250~500 m/s (Krylov, 1998) but for very soft soil it can be less than 100 m/s (360 km/h). For example, Rayleigh wave speeds of peats and soft clays have been observed to be as low as 40~50 m/s (Madshus and Kaynia, 2000) which is much less than the operational speeds of high-speed trains. Table 2-1 illustrates how train speeds have increased over a period of 100 years by showing the record speeds achieved. Operational speeds now regularly exceed 300 km/h in several countries.

Table 2-1 Record speeds of high-speed trains

speed	Year	Country	Train
210 km/h	1903	Germany	AGE
230 km/h	1931	Germany	Schienenzeppelin
331 km/h	1955	France	Locomotive BB9004
380 km/h	1981	France	TGV
407 km/h	1988	Germany	ICE
515 km/h	1990	France	TGV-A
575 km/h	2007	France	TGV (modified)

2.2 Resonance phenomenon of layered half-space

When the speed of a moving load on a layered ground exceeds the Rayleigh wave speed of the upper layer a resonance phenomenon is observed (Dieterman et al., 1997; Lieb and Sudret, 1998; Sheng, et al., 1999a, 1999b). Wave propagation in a homogeneous half-space is non-dispersive and consequently no resonance frequency can be found for a moving point source (Shih, et al., 2016). This resonance frequency is usually called the cut-on frequency due to the fact that the waves begin to propagate in the upper soild layer above this frequency. This frequency is indicated in the literature as being related to the depth of the layer and the P-wave speed in the first layer (El Kacimi, et al., 2013; Kouroussis, et al., 2014; Yang, et al., 2003). However, because the oscillating wave occurs as a surface wave, a modified formula, based on the shear wave speed of the first layer and its depth with a cut-off factor, was introduced by (Mezher et al., 2015). However, the effect of load motion which may modify the frequency is not discussed in these papers.

2.3 Ground models

An ideal soil model includes a semi-infinite medium that allows waves to propagate away from the source without being reflected back by artificial domain boundaries. A common way to simulate an infinite domain is to use analytical solutions by using an integral transform over wavenumber. A general scheme to model the surface waves in the ground was developed by (Haskell, 1953; Thomson, 1950). However, it has difficulties for simulations at high frequencies or for thick layers (Dunkin, 1965). An improved closed-form solution was derived by (Kausel and Roësset, 1981) using the dynamic stiffness of layers of soil in the wavenumber domain. The Thin Layer Method (TLM) is another efficient semi-analytical method developed by (Waas, 1972) that is also commonly used for modelling infinite media. A semi-analytical method, called the scaled boundary finite element method (SBFE), was introduced by (Song and Wolf, 1997). This is an alternative scheme to model infinite media and achieve near-perfect absorption. However, this method suffers from the need to know the frequency of the incident wave at the boundary (Lane, 2007). The boundary element method (BEM) is a common numerical method to model an unbounded domain (Dominguez, 1993). However, these methods are usually based on continuous domains solved in the frequency domain, and cannot be used for modelling soil nonlinearity. Furthermore, the geometry is mostly limited to horizontal layers.

Consideration of soil nonlinearity may become necessary if the soil is very soft or the train speed approaches the critical speed. Therefore, to consider soil nonlinearity, the Finite Element Method (FEM) is often used. However, the way to define the boundaries to imitate the infinite domain is an important issue. Two kinds of boundaries that can approximate an infinite medium are introduced in this section: elementary (non-transmitting) boundaries and local (imperfect transmitting) boundaries.

2.3.1 Elementary (non-transmitting) boundaries

The elementary boundary consists of rigid constraints that actually reflect the incident waves from the boundary. To represent an infinite medium a large computational domain is required with sufficient material damping inside the domain to attenuate the energy before the waves reach the boundary (Kausel and Tassoulas, 1981). Rigid boundaries can also be used when wave transmission is not important, such as for shallow strata above a stiff foundation.

This approach can be adapted to introduce an extended layer to absorb the incident wave energy, as shown in Fig. 2-1. Instead of using the same material damping for the whole region, the extended layer is assigned a higher damping to absorb the incident waves. The ‘damping solvent extraction method’ (DSEM), proposed by (Wolf and Song, 1996), uses damping to weaken the incident wave energy. An equivalent viscoelastic artificial boundary was derived by (Gu, et al., 2007) based on the viscous-spring boundary (Liu et al., 2006). The model was extended and the material properties of the extended elements were defined to be equivalent to the viscous-spring.

These methods are relatively easy to implement in an FE model; however, the use of such methods can affect the dynamic system characteristics of the finite field unless the finite domain is large enough (Qiang et al., 2012).

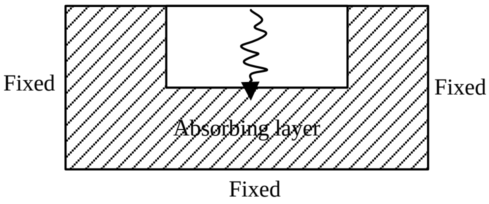

Figure 2-1 Equivalent viscoelastic artificial boundary

2.3.2 Locally absorbing (imperfect transmitting) boundaries

Locally absorbing boundaries are a good method of providing boundary absorption that can reduce the domain size of a model. They can be applied easily in the FE method in the time domain or in the frequency domain. There are a number of local boundaries that have been developed recently including viscous dashpot, viscous-spring artificial boundary, paraxial artificial boundary, multi-direction transmitting boundary, superposition artificial boundary, transmitting boundary and so on (Xu, et al., 2012). The method indicated by (Lysmer and Kuhlemeyer, 1969) is a typical local boundary method that uses viscous dashpots to absorb the incident waves at the boundary, as shown in Fig. 2-2.

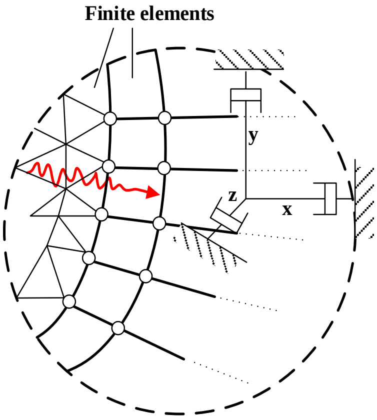

Figure 2-2 Viscous dashpot boundary

This has been applied, for example, in the commercial FE software ABAQUS in the form of infinite elements (Abaqus Theory Manual V6.12 2013). The damper coefficients (per unit area) are set as

$$\begin{cases} C_{Ni} = \rho c_p \\ C_{Ti} = \rho c_s \end{cases} \tag{2-5}$$

where C_{Ni} and C_{Ti} are the damping coefficients for the normal and tangential direction, respectively, ρ is the material density and c_p , c_s are the wave speeds of the P-wave (longitudinal wave) and the S-wave (shear wave) in the material.

This is a good absorber and can be used in both frequency- and time-domain analysis. However, even though it can be used for three-dimensional problems, errors can occur due to the fact that the theory is based one-dimensional plane waves. It only gives perfect absorption for an incident wave that is normal to the boundary. Therefore, it is not suitable for problems that involve arbitrary directions of wave propagation, particualrly at low frequencies. Furthermore, the model is subject to permanent displacement at low frequencies (Liu et al., 2006; Shih et al., 2016; Zdravkovic & Kontoe, 2008). Several local boundaries have been developed to overcome this disadvantage.

An alternative scheme using a 3D viscous-spring dynamic artificial boundary to overcome the instability at low frequencies was derived by (Liu et al., 2006). This is given by a spring and a damper in parallel for the normal and tangential directions:

$$\begin{cases} k_{Ni} = \dfrac{4G}{R} A; \qquad C_{Ni} = \rho c_p A \\ k_{Ti} = \dfrac{2G}{R} A; \qquad C_{Ti} = \rho c_s A \end{cases} \tag{2-6}$$

where A is the total area of all elements around the node considered on the boundary; R is the radial coordinate; G is the shear modulus. This was derived based on a spherical geometry. A more general model that can be used for a cuboid geometry was also introduced by Liu et al., 2006, as follows

$$\begin{cases} k_{Ni} = \dfrac{\alpha_N G}{R} A; \qquad C_{Ni} = \rho c_p A \qquad 1 \le \alpha_N \le 2 \\ k_{Ti} = \dfrac{\alpha_T G}{R} A; \qquad C_{Ti} = \rho c_s A \qquad 0.5 \le \alpha_T \le 1 \end{cases} \tag{2-7}$$

where α_T and α_N are tangential and normal artificial boundary parameters, the recommended values for which are 1.33 for α_N and 0.67 for α_T. However, even though the viscous-spring artificial boundary shows better results than the viscous dashpot boundary, the accuracy is very sensitive to the spring stiffness, which is related to the radial coordinate, *R*, and can result in severe oscillation under some conditions. Furthermore, the geometry of the boundary is still an important issue. Even though the above parameters are used for the artificial boundary to improve the results, errors may occur due to uncertainty in the choice of the appropriate parameters for a particular geometry.

Another possible method to model the infinite domain is by using an infinite element approach which uses displacement shape functions with the geometrical decay formulation (Bettess, 1977). However, this method limits the accuracy of the approximation in the radial direction and the boundary needs to have simple geometry, such as a circle in two dimensions (2D) or sphere in three dimensions (3D) (Gomez-Revuelto, et al., 2012). On the other hand, the paraxial artificial boundary and transmitting boundary only have good absorption when the incident angle is less than 45 degrees. The superposition artificial boundary and multi-direction transmitting boundary both have good absorption in any direction but they are considered to be too complicated to combine with the FE model and are inefficient (Qiang et al., 2012).

2.4 Train-induced ground-borne vibration

2.4.1 Analytical models

In early research on the subject of track vibration due to moving loads, the ground was usually neglected or combined with the track model to form a continuous damped elastic Winkler foundation. Moreover, the vehicle was simply represented by a multiple set of moving loads. An analytical method was developed for track dynamics based on a continuous model and results were obtained in the frequency domain (Fryba, 1999; Kenney, 1954; Timoshenko, 1926; Kenny, 1954). Knothe and Grassie, 1993 reviewed many works in this field and discussed three different types of track model in particular, as shown in Fig. 2-3. These consist of one-, two-, and three-layer support models, the latter including sleeper and ballast mass respectively.

The single-layer support model uses two parameters (stiffness and damping) to represent the connection between track and foundation. This is only sufficient to determine the dynamic response of an observation point directly under the excitation load (Knothe et al., 1993). A two-layer support model with railpad, rigid sleeper and ballast has a more representative dynamic response than a single-layer support. A three-layer support system which uses seven parameters to represent the ballast and subgrade gives further improvements (Zhai, et al., 2004). Furthermore, consideration of the subgrade model becomes very important for frequencies below 200 Hz (Knothe and Wu, 1998).

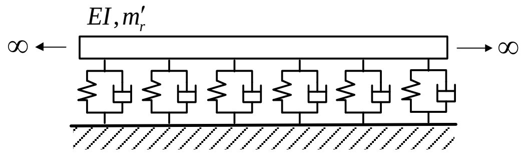

(a) One-layer support

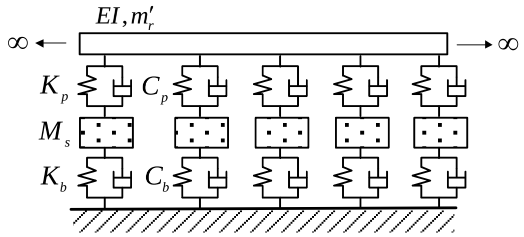

(b) Two-layer support with rigid sleepers

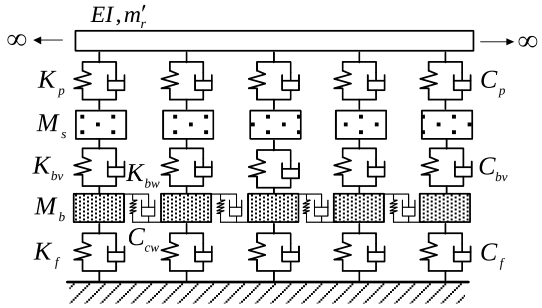

(c) Three-layer support

Figure 2-3 Track models with discrete track components (adapted from Knothe and Grassie, 1993)

If the vehicle model is neglected in the above methods this may mean that the response level is underestimated (Lai et al., 2000). In (Zhai and Sun, 1994) a 10 degree-of-freedom multi-body vehicle model was considered with a three-layer support track model.

Although the effect of the foundation was considered in the three-layer support model, the foundation spring is probably not sufficient to represent the soil. Furthermore, the large increase in vibration that occurs if the train reaches the velocity of Rayleigh surface waves in the ground cannot be simulated by that model (Krylov, 1995). An analytical method was introduced by (Krylov and Ferguson, 1994; Krylov, 1995, 1998) to calculate the train-induced vibration due to the quasi-static moving load. This vibration is developed by the deflection of the track when the force is transmitted from the rail to the sleepers based on the results from Euler-Bernoulli elastic beam on an elastic or viscoelastic foundation. The track deflection shape, which depends on the properties of track and soil and the magnitude of the axle load, was then applied to a half-space ground model to calculate the ground vibration spectra. Lamb’s approximate solution for the Green’s function of a half-space was used to represent the wave propagating in the soil in the frequency domain. However, the coupling of rail/wheel dynamics and excitation by the rail roughness was not taken into account; furthermore, the effects of the layering of the ground were not considered.

Dieterman and Metrikine used a moving load acting on a finite-width beam supported by an equivalent stiffness of the half-space ground model, which depends on the frequency and the wavenumber of the waves in the beam (Dieterman and Metrikine, 1996, 1997). Kaynia et al., 2000 developed a model based on Kausel and Roësset’s layered ground model and extended this by using Dieterman and Metrikine’s method to simulate the dynamic responses from a high-speed train. Good agreement between measurements and the results from the simulation were obtained.

In many papers the track system is assumed to be continuous as there is little difference in the response in the vertical direction, excited by the train, between uniformly distributed and discretely supported models (Vostroukhov and Metrikine, 2003). However, the continuous support models are strictly only valid when the calculation frequencies of the track vibration are less than 500 Hz for the vertical direction and 400 Hz for the horizontal direction (Knothe and Grassie, 1993).

A more complete analytical model that considered the coupling between a more complicated track system, including rail, railpads, sleepers and ballast, and a layered elastic ground was introduced by (Sheng et al., 1999a). It uses a scheme based on (Haskell, 1953; Thomson, 1950) to solve the solutions by an integral transform over wavenumber. The rails are modelled as Euler-Bernoulli beams on a multiple layer support attached to the ground over an area. The response to a moving load can be obtained in the frequency domain. Costa, et al., 2015 investigated the critical velocity based on Sheng’s model and found it to have good accuracy and computational efficiency (Pedro Alves Costa et al., 2015). A similar analytical model of a three-dimensional track/ground system, including rail, pad, sleeper, ballast, subgrade and semi-infinite layered ground, was developed by (Karlström and Boström, 2006). Euler-beam theory was again used for the rail but the sleepers were assumed to be an anisotropic Kirchhoff plate; furthermore, a layered ground was modelled using linear viscoelastic layers. The solution was obtained based on the Fourier transform in time and along the track. Embankment vibration in the transverse direction was developed as a Fourier series, and the vibration in the half-space was obtained by a Fourier transform.

The vehicle model was neglected in above methods, being replaced by dynamic excitation forces or quasi-static moving loads. A more complete analytical model, including wheel-rail interaction and a multi-body dynamic vehicle model was introduced by various authors (Sheng, et al., 2003, 2004a; Auersch, 2005; Xia, et al., 2010). Moreover, (Sheng, Jones, and Thompson, 2003) indicated that to calculate the ground vibration in the far field it is important to consider dynamic loads instead of only quasi-static loads. This is because the travelling speed is usually well below the speed of wave propagation in the ground and the dynamic component of excitation has more effect for the lower speeds (Sheng et al., 2004a). A field experiment was compared with the results from a similar approach and showed good agreement (Lombaert, et al., 2006). Although the track response is dominated by the quasi-static contribution, the ground response further away from the track is again dominated by the dynamic one (see also Sheng et al., 2003), indicating that for train speeds below the critical speed Krylov’s model is only suitable for predicting the ground responses in the immediate vicinity of the track (Lombaert and Degrande, 2009).

2.4.2 Numerical models

As well as these analytical methods, various numerical models have been developed for ground-borne vibration. A wavenumber FE/BE model was introduced by (Sheng, et al., 2005) and a similar method called 2.5D wavenumber FE/BE track-ground model was introduced by (François et al., 2010). The geometry is assumed to be invariant in the longitudinal direction and the results in this direction are solved by an inverse Fourier transformation with respect to the wavenumber. Only a 2D FE/BE mesh is required to represent the cross-section. These methods used boundary elements to model the soil and finite elements to model the track. As an alternative, a 2.5D finite/infinite element method, which is capable of dealing with more complex geometry and materials, was developed by (Yang and Hung, 2001) and used to study the transmission of vibration induced by trains moving at different speeds (Yang, et al., 2003). A 2.5D FE/BE was introduced and coupled with a vehicle model by (Costa, et al., 2012; Galvín, et al., 2010). However, the analysis mentioned above cannot consider the soil nonlinearity. A fully three-dimensional analysis of high-speed train-track-soil-structure dynamic interaction in the time domain was developed by Galvín using a coupled FE/BE method (Galvín, et al.d, 2010). However, soil nonlinearity was not considered.

A combination of the analytical model developed by Karlström with a numerical vehicle/track model (DIFF), was also introduced by (Karlström and Bostrom, 2006). This allowed analysis of the vehicle dynamics in the time domain using a multi-body vehicle model, including wheel, car body and bogie. Triepaischajonsak and Thompson (2015) introduced a hybrid method in which a time domain numerical model of wheel-rail interaction using an FE model of the track was combined with a frequency-domain analytical ground model (Triepaischajonsak and Thompson, 2015).

The finite element method has been commonly used for modelling ground-borne vibration induced by high-speed trains recently due to the requirement to consider soil nonlinearity. However, modelling of unbounded media is the most difficult issue for this problem. As discussed in Section 2.3 reflected waves will occur at the boundaries, which can influence the results, unless a very large model is applied.

A special technique, called the moving finite element method, was developed by Lane to model the track and ground response due to interaction with a multi-body vehicle model (Lane, et al., 2008). In this approach the soil material is moved relative to the FE mesh after a certain number of time steps, so that the vehicle does not need to move relative to the mesh. This allows for better efficiency and a smaller model size.

As discussed in Section 2.3, dashpot absorbing elements (Lysmer and Kuhlemeyer, 1969) have been commonly used in combination with the finite element method due to their simple theory and good absorption ability. Furthermore, even though a modelling approach in the frequency domain is more efficient, consideration of nonlinear behaviour cannot be included (see Section 2.4). Kouroussis, et al., 2009 use a special technique to calculate the vehicle/track and track/ground analysis separately by assuming a much larger stiffness of the soil, compared to the stiffness of the ballast. The ABAQUS infinite elements were used for the boundaries of the half-sphere ground model (see Fig. 2-4) were combined with a finite element model of the soil. Comparisons of numerical results in the time domain with measurements showed good agreement (Kouroussis et al. 2009; Kouroussis, et al., 2011). Recently, (Connolly, et al., 2013) used a method similar to that introduced by Kouroussis but implemented a moving load subroutine defined by FORTRAN code linked to ABAQUS. Furthermore, instead of a spherical model, as shown in Fig. 2-4, an elongated spherical model with infinite elements, as shown in Fig. 2-5, was used in order to have better absorption efficiency at the boundary. Vehicle/track/ground interaction was calculated in the time domain and the model has been verified using experimental data collected from the high speed line between Paris and Brussels. (El Kacimi, et al., 2013; Hall, 2003; Fu and Zheng, 2014) determined the dynamic response from a 3D finite element model coupled to a moving train model by using the same approach but using a cuboid ground model with absorbing boundary, as shown in Fig. 2-6.

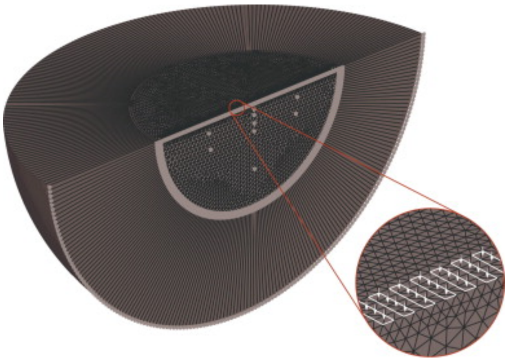

Figure 2-4 Spherical ground model (Kouroussis, Verlinden, et al., 2011)

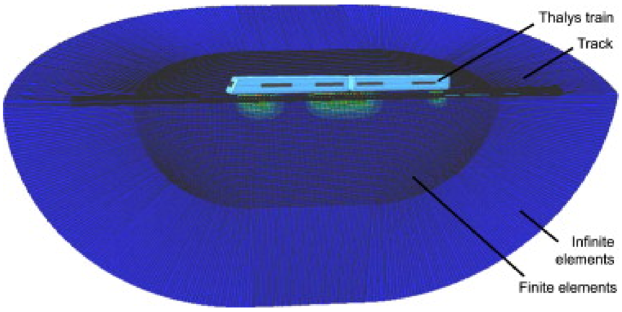

Figure 2-5 Elongated spherical ground model (Connolly et al., 2013)

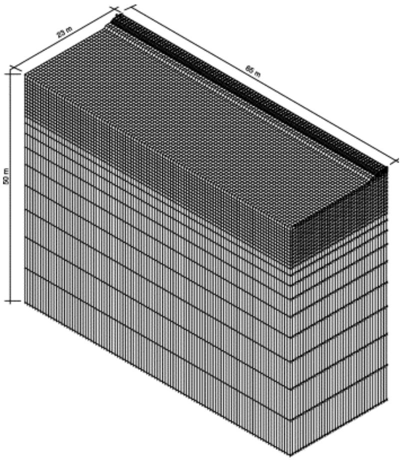

Figure 2-6 Cuboid ground model (Hall, 2003)

2.5 Railpad nonlinearity

The railpad is an important component of the track system that connects the rails and sleepers. The damage of track components can be reduced due to the resiliency of the railpad. Soft pads are now commonly used because of the reduction of the forces transmitted to the sleepers, which can lead to a reduction in the damage of track components such as sleepers and ballast. However, the stiffness of the railpad also influences the noise radiation and track vibration. A stiff pad can reduce the noise from the rail but increases the vibration transmitted into the ground. Furthermore, the sound radiated from the sleepers increases if stiff pads are used (Vincent et al., 1996).

Linear spring elements are usually used for modelling the railpad behaviour (see Section 2.3.1 on track models). However, the stiffness of the rail pads is strongly load-dependent and no longer linear due to geometrical effects (Fenander, 1997; Thompson, et al., 1998; Wu and Thompson, 1999). The stiffness increases with increasing deflection. For example, the static stiffness of a Pandrol natural rubber studded railpad is relatively constant for preloads below 25 kN but increases rapidly above this value (Thompson et al., 1998). In addition, the small strain dynamic stiffness of the railpad is usually higher than the static stiffness, in this case by a factor of 3.5. The dependence of stiffness on preload is more significant than that due to frequency (Fenander, 1997; Thompson et al., 1998). The effect on noise of using a nonlinear railpad model was investigated by (Thompson, et al., 1999). The track noise component predicted by using a linear railpad model was higher than that based on the nonlinear one. Better agreement was shown when a nonlinear railpad was used compared with measurement.

The influence of the frequency dependence can be neglected due to the small differences below 250 Hz. However, for a more complete railpad model, consideration of the frequency dependent stiffness and damping should be included for better prediction.

2.6 Ballast nonlinearity

2.6.1 Experiments

Monotonic and cyclic material testing, as shown in Fig. 2-7, are two common test procedures for understanding the material characteristics of soils that are also applied to ballast. Monotonic tests are applied to study the stress-strain behaviour, strength, and degradation. A large-scale triaxial test was proposed by (Indraratna, Ionescu, and Christie, 1998) to study the mechanical behaviour of railway ballast. The applied confining stress was from 15 kPa to 240 kPa which are typical of the confining pressures generated within ballasted track by the passage of unloaded to fully loaded trains. Large-scale cyclic triaxial tests can be used to investigate the permanent strain and particle degradation (Indraratna and Christie, 2005; Suiker, et al., 2005). (Lackenby, et al., 2007) showed that the axial strain was not only influenced by the magnitudes of maximum deviatoric stress but also by the confining pressure. Cyclic triaxial tests at frequencies from 10~40Hz, which are equivalent to the dynamic responses at train speeds from 73 km/h~291 km/h, were conducted by (Indraratna, et al., 2010). The results showed that ballast degradation and permanent deformation increases with the number of applied loading cycles and the frequency of the loading. Three zones were categorized, based on the level of confining pressure and maximum deviatoric stress acting on the specimen, to define the ballast degradation behaviour under cyclic loading. The resilience of the ballast under monotonic and cyclic loading can be found in paper (Anderson & Fair, 2008).

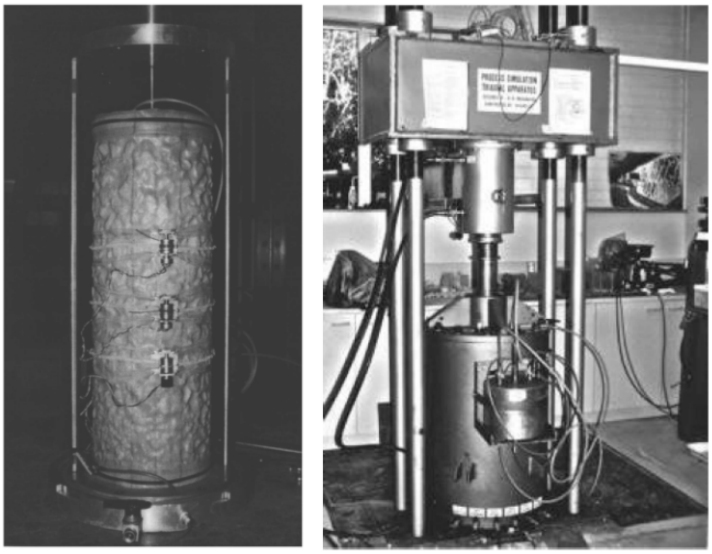

(a) (b)

Figure 2-7 Triaxial cells used for testing ballast material; (a) Triaxial cell used by Suiker, et al., 2005; (b) Triaxial cell used by (Buddhima, et al., 2011)

Even though ballast mechanical responses can be found by monotonic and cyclic triaxial tests, real site experiments on ballast in railway track are desirable for better understanding. However, it is very difficult to control the test parameters and to collect the data. Hence, various laboratory facilities have been introduced. A test facility as shown in Fig. 2-8, was introduced at the University of Nottingham by (Brown, Brodrick, Thom, & McDowell, 2007) in an attempt to simulate the conditions in a real track in a controlled way. It is a full-scale railway track model consisting of three sleepers housed in a concrete pit filled with subgrade material and ballast. However, the cost of the facility is high. The results from this facility were compared with the results from triaxial test apparatus to obtain the reliable variables from the triaxial test (Aursudkij, et al., 2009). In the triaxial test, a pressure of 200~250 kPa was applied as cyclic loading corresponding to the maximum contact pressure at the sleeper base (Shenton, 1975) and 30 kPa confining pressure was applied. Although the observed horizontal stress in ballast fluctuates it can eventually reach 30 kPa (Selig et al., 1994).

A test facility was developed at the University of Southampton, as shown in Fig. 2-9. A single sleeper bay of track is considered, contained between vertical steel sections 5 m long, 0.65 m high and 0.65 m apart, attached to a strong floor in order to maintain plane strain conditions. Investigation of ballast settlement and ballast lateral resistance have been carried out using this facility (Le Pen, et al., 2016; Le Pen & Powrie, 2011).

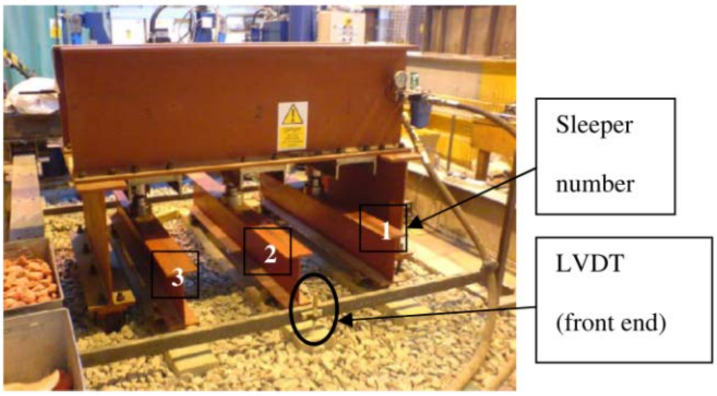

Figure 2-8 The railway test facility at University of Nottingham (Aursudkij et al., 2009)

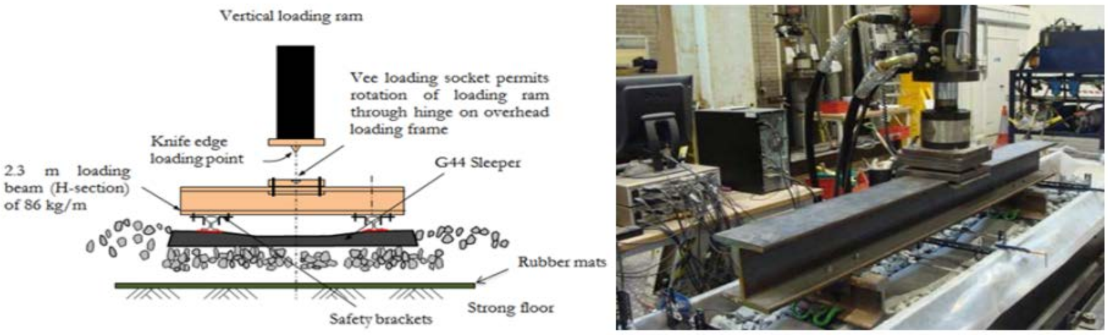

(a) (b)

Figure 2-9 Southampton Railway Testing Facility at University of Southampton (Abadi et al., 2016)

A larger railway test facility was developed at Heriot-Watt University, as shown in Fig. 2-10. This facility consists a full geopavement or railway trackbed constructed within a steel box with dimensions 1.06 m x 3 m and depth 1.15 m (Kennedy, et al., 2012).

Figure 2-10 Geopavement and railway accelerated fatigue testing facility at Heriot-Watt University (Kennedy, et al., 2012)

2.6.2 Modelling of ballast by continuous approach

Similar to granular materials, such as sand, ballast cannot resist a tensile stress. The stiffness is usually low because of the weakness of bonding. An example of the stress-strain behaviour of ballast during one cycle of compressive loading can be seen in Fig. 2-11 (Varandas, 2013). The resilient modulus can be derived by dividing the axial stress by the axial strain. An increment of resilient modulus can be found with increasing strain, as shown in Fig. 2-11(b). This is due to the increased contact surface leading to higher stiffness with higher applied pressure (Timoshenko and Goodier, 1951). Moreover, even though most of the deformation of the ballast is recoverable, some permanent strain occurs during the cyclic loading, as shown in Fig. 2-11(a). The resilient modulus generally increases with the number of applied load cycles and eventually reaches an approximately constant value after a certain number of repeated loads.

A no-tension constitutive law for modelling granular materials was proposed by (Nguyen, et al., 2003). Significant differences can be found compared with the results from a nonlinear elastic model. However, confining stress was not considered, which is an important factor for modelling the ballast mechanical responses (Anderson et al., 2008; Aursudkij et al., 2009; Indraratna and Christie, 2005; Indraratna and Salim, 2002; Lackenby et al., 2007).

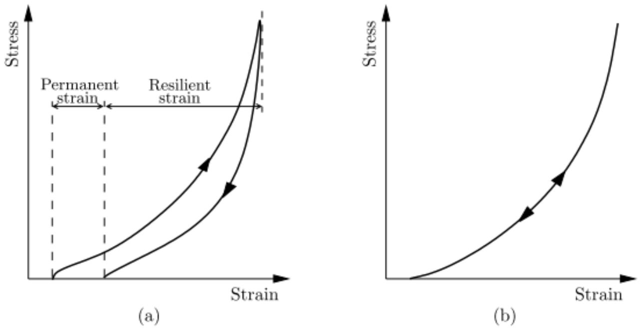

Figure 2-11 Nonlinear elastic strain behaviour during one cycle of compressive load application (Varandas, 2013); (a) elastoplastic; (b) nonlinear elastic

The most widely used model to describe the nonlinear resilient nature of unbounded granular material is the $K-\theta$ model (Hickes, 1970). The resilient modulus can be derived as

$$E = K_1 \left(\frac{\theta}{\theta_0} \right)^{K_2} \tag{2-8}$$

where θ is the sum of the effective principal stresses (bulk stress)

$$\theta = \sigma_1' + \sigma_2' + \sigma_3' \tag{2-9}$$

and θ_0 is a reference value, usually chosen equal to 100 kPa**.** K_1 and K_2 are constants which have to be determined from experimental results. A three-dimensional Finite element model of railway track considering the ballast nonlinearity based on the $K-\theta$ constitutive law was proposed by (Varandas 2013). Dynamic results from two different load speeds were compared with the results from a linear model. The displacements for the lower speed, 22% of critical speed, were approximately coincident. A small difference was found for the higher speed, 75% of critical speed.

The resilient modulus not only depends on the bulk stress but also on the shear strain induced by the deviatoric stress and from experiments the Poisson's ratio is found not to be constant (Fernandes, 2014). A modified $K-\theta$ model was proposed by (Uzan, 1985)

$$E = K_1 \left(\frac{\theta}{\theta_0} \right)^{K_2} \left(\frac{q}{\theta_0} \right)^{K_3} \tag{2-10}$$

where q is the deviatoric stress

$$q = \sigma_1' - \sigma_3' \tag{2-11}$$

This model can capture better variations of the resilient modulus and was adopted for soil for assessing the critical speed by (Woodward, et al., 2015).

A nonlinear elastic model in which the resilient deformation is split into volumetric $\varepsilon_{v,r}$ and deviatoric $\varepsilon_{s,r}$ components was proposed by (Boyce, 1980). This model requires three parameters to account for different volume behaviour depending on the stress path. An anisotropic model was proposed by (Hornych, et al., 1998). This followed the same Boyce model but the effective mean normal stress and deviatoric stress used are different.

Models that consider the factors of initial state, volume behaviour, drainage conditions, stress-strain behaviour and possibly rotation of principal stress axes are called advanced constitutive models (Kramer, 1996). An elastoplastic constitutive model for coarse granular aggregate ballast incorporating particle breakage was proposed by (Indraratna et al., 2002), which considered the degradation of particles due to shearing. The model was based on the ratio between the deviatoric and mean stresses as a function of dilatancy, strength and particle breakage. A theory based on plasticity considering the strain hardening and yield surface were then derived by (Salim and Indraratna, 2004) based on the previous model of (Indraratna et al., 2002). Due to the fact that the resilience is related to the number of load cycles, a cyclic densification model was then proposed by (Indraratna, et al., 2012). At Ecole Centrale de Paris (ECP) a model was proposed by (Aubry, et al., 1982). This is an elastoplastic multi-mechanism model that is based on a Coulomb-type failure criterion and the concept of critical state. The required model parameters were classified by (Lopez-Caballero, et al., 2008). Another alternative is the extended Drucker-Prager model with hardening which has been used by several authors to model the behaviour of ballast (Indraratna, et al., 2007; Leshchinsky and Ling, 2013; Suiker and Borst, 2003)

2.6.3 Discrete element method (DEM)

The discrete element method (DEM) was first developed by (Cundall and Strack, 1979), based on the normal and transverse contact forces between a collection of rigid particles in an explicit scheme. The main advantage of this method is that the micromechanics of the ballast layer are well represented, this approach being particular suitable for studying granular thin layers and the localized rigid structures appearing during loading. A material constitutive law is not needed for the simulation. However, the calculation time required is significant.

Modelling of ballast mechanical behaviour during train loading by using DEM has been carried out by several authors recently. However, DEM implementation does not allow particle breakage. Agglomerates, which are made by bonding elementary spheres have been used to imitate the particle breakage behaviour (Cheng, et al., 2003; Lim and McDowell, 2005). Particle breakage can be arranged to occur at a predefined condition or by using bonds with restricted resistance. A more angular particle was considered by (Lu and McDowell, 2006) and the results showed more realistic load-deformation response than the spheres. Clumps of spheres with many very small asperities were used to model monotonic and cyclic tests by (Lu and McDowell, 2010) and showed good agreement with the measurement. Asperities were shown to play an important role in governing the strength and volumetric strain under monotonic loading, and on permanent strains under cyclic loads. Instead of spherical particles, spheres with flats were used to model the railway ballast (Harkness, 2009). A new contact law modelling damage at the contacts between particles is introduced by (Harkness, et al., 2016), which is able to replicate the behaviour of laboratory test without changing the material stiffness and the inter-particle friction.

2.7 Soil and subgrade nonlinearity

Soil is similar to ballast material; however, the particle size is much smaller than ballast and consideration of undrainage is not necessary for ballast. According to laboratory tests, soil stiffness is related to cyclic strain amplitude, void ratio, mean principal effective stress, plasticity index, over-consolidation ratio, and the number of loading cycles (Kramer, 1996). The most important parameter for modelling nonlinear soil behaviour, especially at shear strains larger than ~10^{-5} to 10^{-4}, is the shear modulus (Beresnev and Wen, 1996). The shear modulus is found to decrease with increased shear strain above this level. This is known as shear modulus degradation. Zhang et al. (2005) indicated that the key factors for shear modulus degradation are the shear strain, mean effective confining stress, soil type and plasticity index, whereas they indicated that the frequency of the loading and number of loading cycles, over-consolidation ratio, void ratio, degree of saturation, and grain characteristics are less important (Zhang, et al., 2005). On the other hand, an increment of damping ratio is found with increasing shear strain and the most important factors are not only shear strain level, confining stress, soil type and plasticity index but also frequency of loading and number of loading cycles (Kumar, et al., 2013; Zhang et al., 2005).

Linear-elastic models are usually used for ground vibration due to railway. However, when the train speed is close to the critical speed, nonlinear behaviour of the soil occurs, especially in the region near the track. Soil degradation cannot be simulated by linear models. Soil nonlinearity therefore needs to be taken into account for improved predictions.

2.7.1 Experiments

The nonlinearity of the shear stiffness and damping ratio with increasing shear strain can be seen from measurement data of shear-stress behaviour under a cyclic loading, such as shown in Fig. 2-12. Stress-strain curves with seven different maximum strain levels, indicated as I~VII, are shown in Fig. 2-12(a). Soil stiffness and damping are then plotted against the maximum strain level, as shown in Fig. 2-12(b). As shown, the shear modulus decreases with the increase of the strain level whereas the damping ratio increases as the shear strain becomes higher. The damping ratio can be derived by (Hardin and Drnevich, 1972)

$$\xi = \frac{A_L}{4\pi A_T} \tag{2-12}$$

where A_L is the area enclosed by the hysteresis loop and A_T is the area enclosed by the triangle defined by the maximum strain and the maximum stress. The shear modulus reduction curve can be derived from stress-strain behaviour, as shown in Fig. 2-13, by normalizing the shear modulus G by its maximum value G_{max}. where G_{max} is the shear modulus at very low strain levels ($<10^{-6}$), which can be derived from different laboratory results such as listed by (Kramer, 1996).

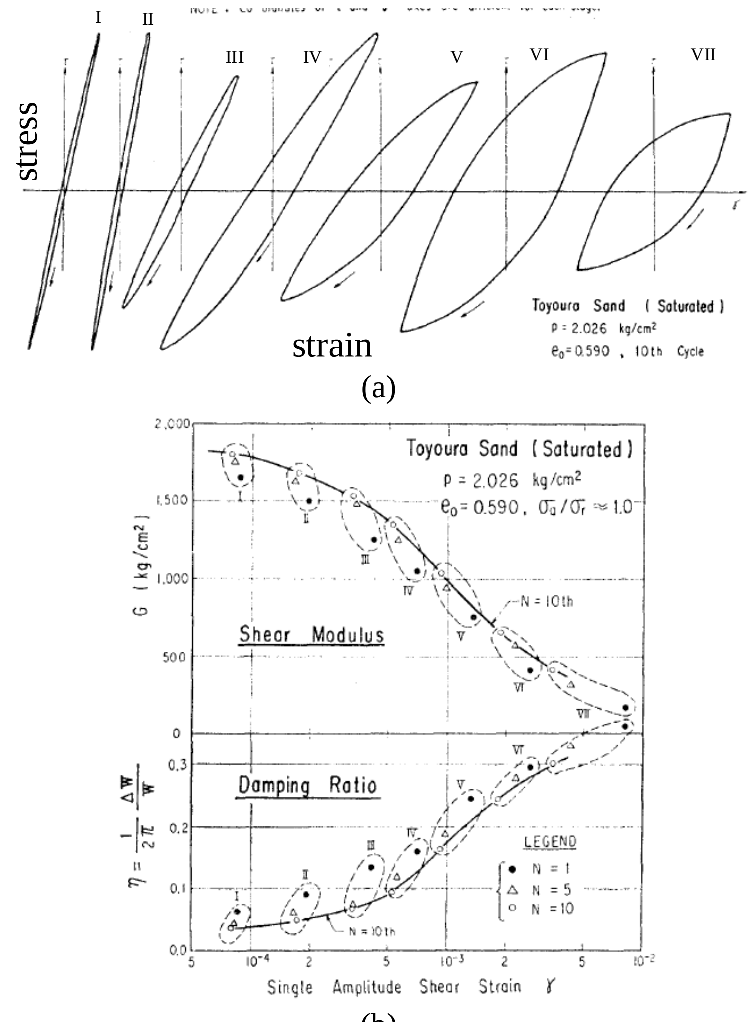

(a)

(b)

Figure 2-12 Drained torsional shear test on Toyoura sand; (a) stress-strain behaviour; (b) shear moduli and damping ratio (Iwasaki, et al., 1978)

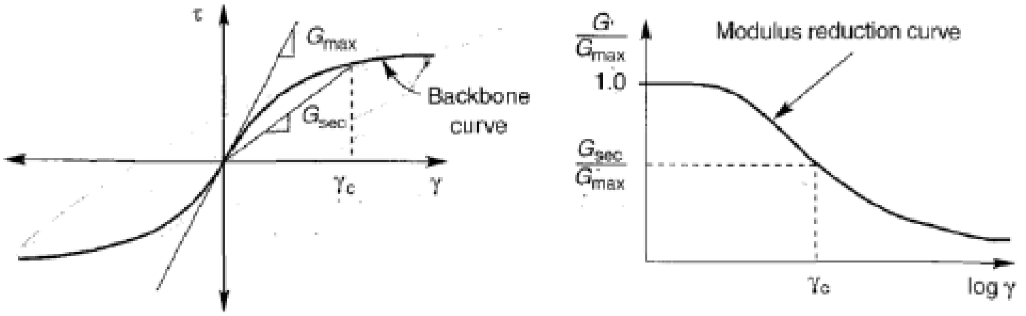

(a) (b)

Figure 2-13 Reduction curve of shear modulus versus shear strain (a) Stress-strain curve with variation of shear modulus; (b) modulus reduction curve (Kramer, 1996)

The shear modulus and damping ratio are significantly influenced by the confining pressure, particularly for soils of low plasticity. This can be seen in Fig. 2-14, which shows shear modulus reduction curves for dense sand at different confining pressures (Ishibashi and Zhang, 1993; Kokusho, 1980). As the confining pressure increases, the shear modulus increases and the damping ratio decreases. The rate of gain in cyclic strength due to over-consolidation increases with an increase in fines or decrease in mean grain size of the soil specimens, as shown in Fig. 2-15 (Ishihara, et al., 1978). Vucetic and Dobry (1991) indicated the influence of plasticity index (*PI*) on the cyclic stress-strain parameters of normally consolidated and over-consolidated clay (over-consolidation ratio, OCR=1-15), as shown in Fig. 2-16 (Vucetic and Dobry, 1991). Soils with higher plasticity tend to have a more linear cyclic stress-strain response at smaller strains and degrade less at larger shear strain, as shown in Fig. 2-16(a). On the other hand, soils with higher plasticity index have a smaller damping ratio at higher shear strain than those with lower plasticity index, as shown in Fig. 2-16(b). The frequency of cyclic loading does not significantly affect the shear modulus, but the influence is significant for the damping ratio, as shown in Fig. 2-17 (Lin & Huang, 1996).

A summary of the results of the influence of the shear strain amplitude on cyclic load from different laboratory results with fine and granular soils, at different confining pressures can be seen in Fig. 2-18 (Seed and Idriss, 1970).

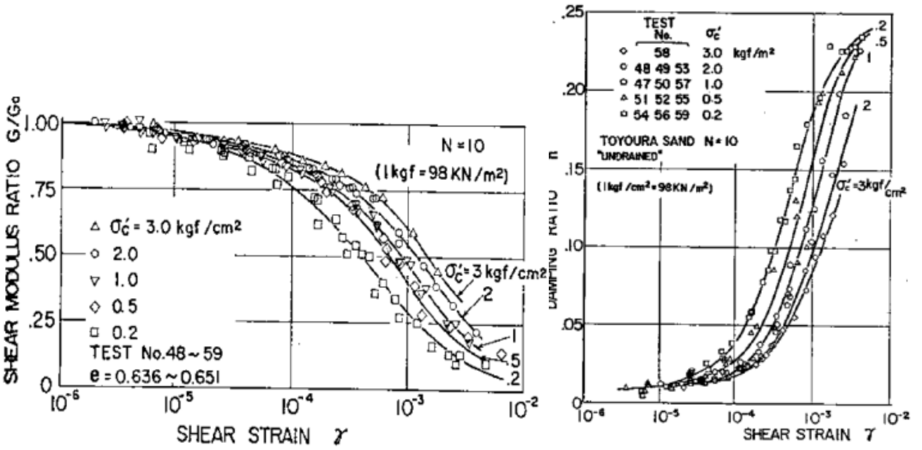

(a) (b)

Figure 2-14 Tri-axial cyclic test strain for dense sand with different confining pressures; (a)Variation of shear modulus ratio and shear strain (b) Variation of damping ratio and shear strain (Kokusho, 1980)

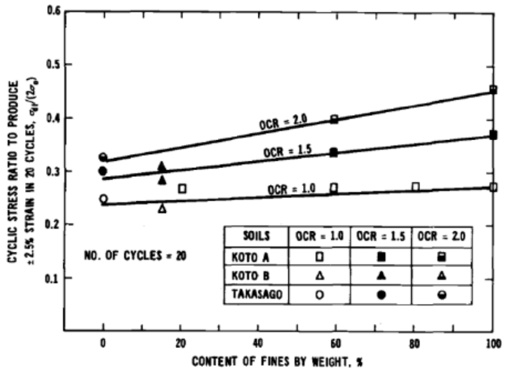

Figure 2-15 Relationship between cyclic strength and content of fines in soils (Ishihara et al., 1978)

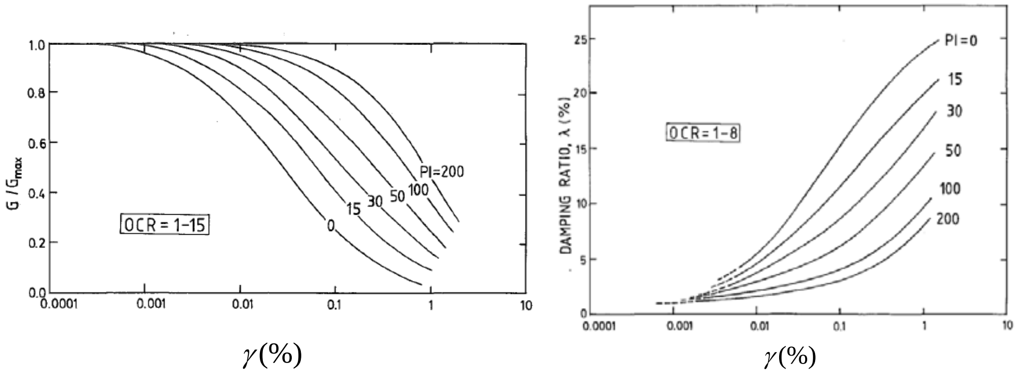

(a) (b)

Figure 2-16 Results for fine-grained soils of different plasticity; (a) modulus reduction curve; (b) damping ratio (Vucetic et al., 1991)

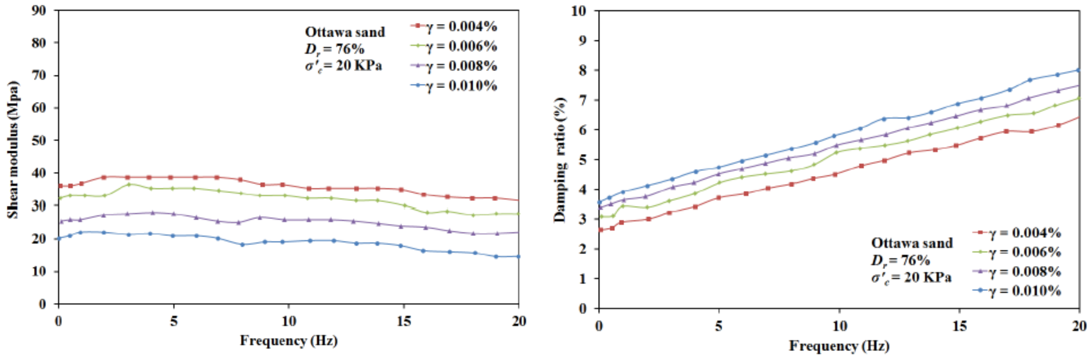

(a) (b)

Figure 2-17 Results from Ottawa sand; (a) variation of shear modulus with frequency; (b) variation of damping ratio with frequency (Lin et al., 1996)

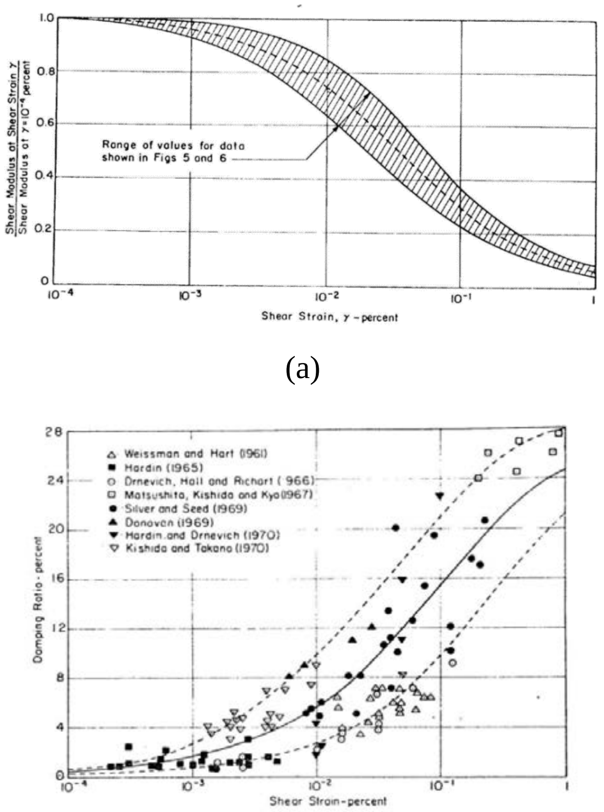

(a)

(b)

Figure 2-18 Influence of the shear strain amplitude on cyclic load; (a) shear modulus; (b) damping ratio (Seed et al., 1970)

2.7.2 Equivalent linear model

An equivalent linear model is a simple procedure that can approximate nonlinear behaviour more efficiently than a fully nonlinear calculation. Several authors have used equivalent linear models in studying the loading due to a train pass-by to include soil nonlinear effects of the track and ground (Costa, et al., 2010; Hall, 2003; Kaynia et al., 2000; Madshus et al., 2000; Thach, et al., 2013). These involve an iterative procedure that can approximate nonlinear behaviour efficiently. From an initial calculation based on the maximum shear modulus and smallest damping ratio, an ‘effective’ shear strain amplitude is determined as a certain proportion of the maximum shear strain from the time-varying strains. This is then used to calculate an updated value of the shear modulus and damping ratio based on the measured curves, as shown in Fig. 2-18. The model is run again until the corresponding modulus is close to the assumed modulus from the previous iteration. In order to characterise the motion, the value used for the effective shear strain in this process is chosen as a certain proportion of the maximum strain. It is important to determine this factor appropriately if the correct results are to be obtained from the equivalent linear model (Miura, et al., 2000; Yoshida, et al., 2002). Different values for this factor have been found empirically; for example 0.65 is usually recommended for seismic analysis (Kramer, 1996). However, overestimation of the amplitude, sometimes by more than 50%, has been found when using the value of 0.65 in situations where particularly large strains occur (Yoshida et al., 2002). Depending on the situation, values between 0.2 and 1 have been found to give the best results (Katayama, et al., 1992; Yoshida et al., 2002). As the dynamic characteristics of the vibration induced by high-speed trains differ from those of earthquakes, further investigation is required.

In (Hall, 2003; Kaynia et al., 2000; Madshus et al., 2000) such equivalent linear models were used for the soft soil site of Ledsgård. In these models the stiffness reduction, based on an approximate effective strain level, was applied to all elements within a given soil layer. A more advanced approach was implemented by Costa et al. (Costa et al., 2010) in which the shear modulus was adjusted according to the maximum effective shear strain in each element of the 2D cross-section, resulting in a transverse inhomogeneity in the ground. It was found that a number of iterations were required to reach a value of shear modulus that was consistent with the corresponding strain level.

However, it is restricted to the linear approach which is unable to capture the real strain variation and the changes of soil properties during dynamic loading. Furthermore, it is not able to predict settlement and failure. In general there are some disadvantages.

- It is incapable of representing the changes in soil stiffness that actually occur during the excitation (Kramer, 1996)

- It is still a linear model that cannot represent the change of the soil properties that actually occurred during the dynamic responses (Kramer, 1996)
- It cannot be used directly for problems involving permanent deformation or failure (Kramer, 1996)
- The damping ratio is constant, independent of frequency. In particular low-amplitude and high-frequency components of strain should have much less damping (Yoshida & Iai, 1998)
- It may overestimate the resonance-frequency amplitude and shear stress compared to a nonlinear analysis due to variations of the soil stiffness as a function of time in the nonlinear analysis (Yoshida et al., 1998)

2.7.3 Cyclic nonlinear model

The nonlinear stress-strain behaviour of soils can be represented more accurately by cyclic nonlinear models that follow the actual stress-strain path during cyclic loading. These are characterized by a backbone curve, as shown in Fig. 2-19, and a series of rules that govern the unloading-reloading behaviour, stiffness degradation, and other effects such as irregular loading, densification, pore pressure generation, or so on. Four steps are used for defining the cyclic nonlinear models (Kramer, 1996).

1. Define the initial loading (or unloading) backbone curve

   There are many models can be used to model the initial loading backbone curve. Three example models are:

   a. Ramberg-Osgood model: $\gamma = \frac{\tau}{G_{\max}}\left(1 + a\left(\frac{\tau}{\tau_f}\right)^{b-1}\right)$ *(2-13)*

   where τ_f is the yield strength of the material; *a* and *b* are constants that depend on the material being considered.

   b. Pyke Method: $\tau = f\left(\gamma\right) = \frac{G_{\max}\gamma}{1+\left|\gamma\right| / \gamma_r}$ (or unloading case) *(2-14)*

   c. Hardin-Drnevich hyperbolic model: $\tau = \frac{G_{\max}\gamma}{1+\left|(\gamma / \gamma_r)\right|}$ *(2-15)*

   where $G_{\max}$ and γ_r are the largest shear modulus and reference shear strain respectively.

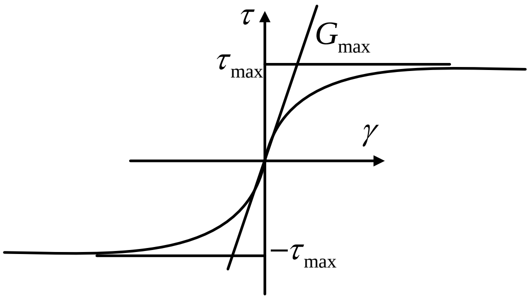

Figure 2-19 Backbone curve of shear modulus versus shear strain

2. If the stress reversal occurs at a point defined by $\left(\gamma_r, \tau_r\right)$, the stress-strain curve follows a path given by

$$\frac{\tau-\tau_r}{2}=\frac{G_{\max}\dfrac{\gamma-\gamma_r}{2}}{1+\left|(\gamma-\gamma_r/2\gamma_r)\right|} \text{ (Masing rule)} \qquad \textit{(2-16)}$$

   and the unloading and reloading curves have the same shape as the back-bone curve but enlarged by a factor of 2 (Kramer, 1996).

3. If the unloading or reloading curve exceeds the maximum previous strain and intersects the back-bone curve, it follows the backbone curve until the next stress reversal.
4. If an unloading or reloading curve crosses an unloading or reloading curve from the previous cycle, the stress-strain curve follows that of the previous cycle.

The dynamic results and the stress-strain behaviour obtained by using a cyclic model are illustrated in Fig 2-20.

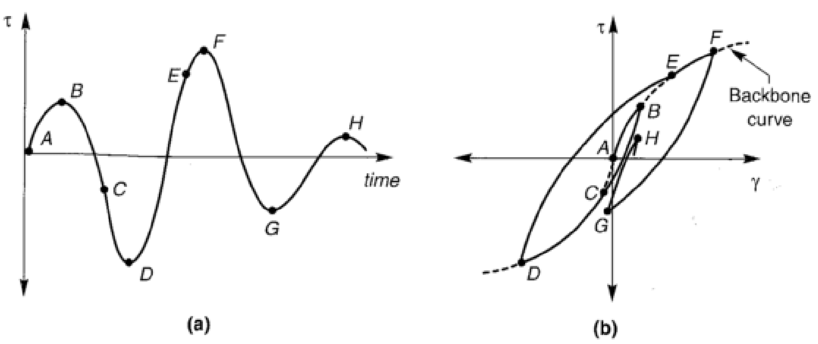

Figure 2-20 Extended Masing rules; (a) variation of shear stress with time; (b) resulting stress-strain behaviour (Kramer, 1996)

A popular cyclic model for soil is that given by Iwan (Iwan, 1967). This used a series of parallel Jenkin elements, which consist of a linear spring in series with a frictional slider, to describe the backbone curve and the yield level. This model was adopted by Gomes Correia and Cunha (Gomes Correia & Cunha, 2014) to study the effect of subgrade nonlinearity on the track response induced by a high-speed train.

Cyclic models are able to represent the development of permanent strains and allow the determination of shear-induced volumetric strains that can lead to hardening under drained conditions or to pore pressure development with attendant stiffness degradation under undrained conditions. Furthermore, they are able to compute changes in pore pressure, hence also changes in effective stress. However, some disadvantages exist. In particular, they cannot model the general soil behaviour and do not consider the yield surface and hardening law (see below).

2.7.4 Advanced constitutive model

The so-called advanced constitutive model requires a yield surface that describes the limiting stress conditions for which elastic behaviour is observed, a hardening law that describes changes in the size and shape of the yield surface as plastic deformation occurs, and a flow rule that relates increments of plastic strain to increments of stress.

An early implementation of a nonlinear model for railway dynamics was that introduced by Sadeghi (Sadeghi, 1997). A nonlinear stress-strain model was developed including consideration of permanent strain and failure criteria using an extended Drucker-Prager plasticity model. The rail displacements from a nonlinear model were found to be 20% greater than those from a linear model due to the plastic strain in the substructure layer. However, this was a two-dimensional model which did not consider the moving load effect.

The advantages of using such an advanced constitutive model are that it allows considerable flexibility and generality in modelling the response of soils to cyclic loading for general initial stress condition, wide variety of stress paths, rotating principal stress axes, cyclic or monotonic loading, high or low strain rates, and drained or undrained conditions. However, they are very complicated and requires many parameters, which may be difficult to evaluate.

2.8 Summary of literature review and overview of thesis

As has been seen, most of the vehicle/track/ground interaction models to date involve calculations of the dynamic response in the frequency domain or involve a transfer from the frequency to the time domain by means of a Fourier transform. This approach is restricted to linear simulations. However, in order to include non-linear effects, a time domain approach is required. Although boundary element and analytical methods are more efficient than the finite element method, complex geometric and non-linear effects require the use of the FE method. However, the correct representation of the boundary of the finite element model for the ground system to avoid unphysical reflections is a very important issue for the simulation accuracy.

The infinite element method, which was developed by (Lysmer et al., 1969), can be used to solve this problem and it is a simple approach that can easily be combined with the finite elements. Furthermore, it can be used both in the time and frequency domain and soil nonlinearity can be considered in the FE region by using this method. It has been implemented in the commercial FE software ABAQUS, and extended by (Connolly et al., 2013; Kouroussis et al., 2009). However, even though incident waves can be absorbed by using infinite elements, a small reflected component may still exist due to its non-perfect absorption ability. An alternative scheme is to consider using an elementary boundary with appropriate damping model. On the other hand, a larger model will be required for better accuracy that is more expensive than the model without the infinite elements.

Commercial FE software, ABAQUS, is used in the present work due to the fact it includes extensive nonlinear material capabilities and a user-defined subroutine can be used to develop a new material constitutive law. Furthermore, infinite elements and parallel analysis, which are important for the present work in terms of simulation efficiency, have been built in the program. In order to account for vehicle/track dynamics, two different coupling approaches are introduced and discussed first in Chapter 3. Two- and three-dimensional track models with stationary harmonic load, moving load and moving dynamic load are considered and compared in Chapter 4 in order to validate the modelling of vehicle/track interaction dynamics. Various approaches for modelling the ground are compared in Chapters 5 and 6 using different meshing strategies and boundary conditions. Resonance phenomena in layered ground are then discussed in Chapter 7.

Finally in this chapter various approaches for introducing nonlinearity have been reviewed. Soil nonlinearity is considered in the FE model in Chapter 8 and a case study from Ledsgård in Sweden is assessed. Railpad and ballast nonlinearity is not considered here due to the fact that the interest of the present work is the effect of the critical condition when train running on the ground where the soil plays the key role for the whole system but a similar approach could be used for this.

Chapter 3: Modelling of the moving vehicle coupled with the track

3.1 Introduction

In order to model the track/ground vibration induced by a high-speed train, in this work the commercial FE (Finite Element) software ABAQUS is used. Separate models are used to represent the vehicle and the track/ground system. Rigid-body elements are used for the vehicle components (car body, bogies and wheelsets), while the primary and secondary suspensions are modelled by springs and dampers connecting the rigid bodies. Only vertical (and pitch) dynamic behaviour is considered. The track and ground models are developed by using solid elements in ABAQUS (these will be described in Chapter 4 and Chapter 5 respectively). Motion of the vehicle along the track is taken into account. However, the consideration of a moving dynamic load coupled with deformable bodies is not supported automatically in ABAQUS. The response of a finite element system to a moving load can be readily calculated by specifying the nodal forces corresponding to the moving load as a function of time. However, for a moving vehicle problem, the loads depend on the dynamic response of the vehicle as well as the track system. Therefore, a user-defined subroutine is often used to combine a vehicle multi-body model with the FE model of the deformable object. This requires more time to complete the simulation due to the interaction between the two different programs. An alternative approach has been adopted here, using the large (finite) sliding contact model in (ABAQUS, 2013b) to connect the whole system. This allows the multi-body vehicle model to be represented directly by finite elements in ABAQUS. This could also allow the inclusion of the flexibility of the vehicle structure, although this is not considered here.

3.2 Simulation procedure

3.2.1 Contact model

The same procedure has been followed as (Saleeb & Kumar, 2011; Shih, Thompson, & Zervos, 2014) in which the sliding contact model in ABAQUS is used to connect the vehicle and track without the need for coupling with an external subroutine. The approach has been tested first on a simple moving vehicle-bridge interaction problem. An appropriate contact model is the key to ensure that this simulation correctly represents the interaction between the two systems. One has to be chosen as the primary system (here this is the track system) and the other as the secondary system (the vehicle). The slave surface is treated as collection of discrete points and cannot penetrate the master surface facets. Furthermore, a more-refined surface is usually required for the slave surface. On the other hand, the stiffer body should act as the master surface for which a coarser mesh is allowed.

In the large sliding contact model in ABAQUS, the normal contact pressure resists penetration, while in the tangential direction frictional stress resists sliding. In addition, contact damping, electrical, and thermal interactions can all be considered. However, only the normal contact problem is considered here, while the other effects including friction are neglected. Two main contact formulation aspects have to be defined for a contact simulation in ABAQUS: contact discretization and contact enforcement.

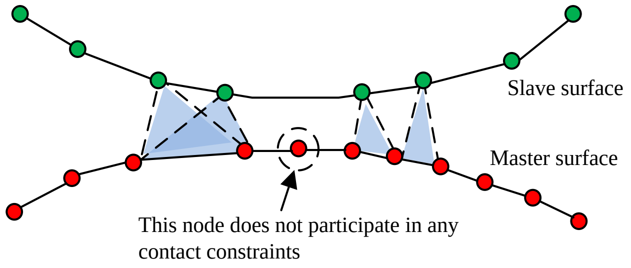

(a)

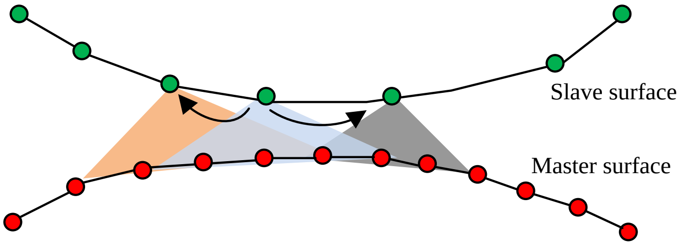

(b)

Figure 3-1. ABAQUS contact model; (a) Node-to-Surface contact discretization; (b) Surface-to-Surface contact discretization

There are several methods of contact discretization available in (ABAQUS, 2013b). Each is based on attempting to match points on the “slave” surface to the closest point on the “master” surface. These two discretized surfaces have to be defined first. Three contact discretization methods are available: node-to-surface, surface-to-surface, and edge-to-surface. One of these should then be selected to determine the way to calculate gap or penetration distances between the two surfaces from the nodal positions. Node-to-surface contact discretization is based only on the relative position between nodes on the slave surface and the closest elements on the master surface as shown in Fig. 3-1(a). On the other hand, the surface-to-surface constraint method averages the overall region as shown in Fig. 3-1(b), which can reduce the sensitivity of the results to the influence of individual master and slave nodes and gives a more correct contact stress and better convergence. Similar to the surface-to-surface method, the edge-to-surface method has a better resolution of the contact and needs fewer increments and iterations during the simulation. However, it can only be used with 3D solid edges and is not supported in ABAQUS/CAE.

The node-to-surface contact feature is used in the present work to simulate the sliding motion on a frictionless surface. The default contact property “hard contact”, as explained below, without contact damping, is used in ABAQUS/Standard. The secondary system has been defined as the first surface (the “slave” surface) and the connected primary system, is defined as the “master” surface. Then the hard pressure-overclosure relationship (penetration of the point on the surface) is applied between the two contacting surfaces to determine the kinematic equilibrium using appropriate Lagrange multiplier techniques. The hard pressure-overclosure relationship is a strict constraint, which only allows the contact pressure to be transmitted when there is penetration of the slave nodes into the master surface; the contact pressure can be infinite. However, tensile stress across the interface is not considered. The contact pressure can be calculated by

$$\begin{aligned} &p = 0 \quad \text{for} \quad h < 0 \quad \text{(open), and} \\ &h = 0 \quad \text{for} \quad p > 0 \quad \text{(closed).} \end{aligned} \tag{3-1}$$

where p is the contact pressure and h is the normal distance between two specified contact surfaces.

Implicit dynamic analysis of the FE time-stepping procedure is used for this problem due to a better convergence than the explicit approach. The location of the moving object in the direction of travel is defined at each time step. However, an initial static analysis is required before executing the dynamic calculations in order to obtain the starting conditions to ensure convergence during the initial contact calculation. Furthermore, this initial static analysis can minimise starting transient effects.

3.2.2 User-defined subroutine

An alternative method can be used for modelling moving load and moving vehicle problems in ABAQUS, based on user-defined subroutines. This approach was used by (Connolly et al., 2013) and will be compared with the above contact model. A user-defined subroutine (VDLOAD) can be used to define the variation of the distributed load amplitude as a function of position, time, element number, and load integration point number. An additional user-defined subroutine (VUFIELD) is required in order to access the rail deflection in each time step to calculate the coupling between wheel and rail. The explicit integration scheme was used by (Connolly et al., 2013).

Here an implicit integration scheme is used in order to have better convergence, as mentioned in Section 3.2.1. Instead of the user-defined subroutines VDLOAD and VUFIELD, the subroutines DLOAD and URDFIL are used. User-defined subroutine DLOAD has the same functionality as VDLOAD but is intended for use in implicit analysis. The subroutine URDFIL is used to access the results file, here the rail displacement under the moving wheel, during the analysis. Three procedures need to be implemented to simulate the moving vehicle problem. The first is the definition of the non-uniform distributed load acting on each element; the second is the contact force calculation; the final step is the vehicle dynamic analysis.

An element-based non-uniform distributed load is defined in the user-defined subroutine DLOAD at each load integration point, as shown in Fig. 3-2. The non-uniform pressure at each node point can be calculated by

$$\begin{cases} p_a = \dfrac{-2F}{l_e^2}\left(Vt - x_i\right) + \dfrac{2F}{l_e} \\ p_b = \dfrac{2F}{l_e^2}\left(Vt - x_i\right) \end{cases} \tag{3-2}$$

where F is the axle load for a moving load analysis or the contact force for a moving vehicle analysis, V is the moving load speed, l_e is the element length and x_i is location of node *i* in each element. A non-uniform distributed load function for an element can be derived to apply at each integration point, as shown in Fig. 3-2.

A linear contact spring is used and the contact force, F_t, can be calculated in terms of the relative displacement between the wheel and rail multiplied by the stiffness of the contact spring. For a beam element the rail displacement under the wheel can be calculated by

$$u_{w,t} = u_{1,i}\phi_{1,t,i}^{(s_i)} + u_{2,i}\phi_{2,t,i}^{(s_i)} + u_{3,i}\phi_{3,t,i}^{(s_i)} + u_{4,i}\phi_{4,t,i}^{(s_i)} + u_{5,i}\phi_{5,t,i}^{(s_i)} + u_{6,i}\phi_{6,t,i}^{(s_i)} \tag{3-2}$$

where $u_{1,i} \sim u_{6,i}$ are the nodal displacements for beam element *i*, as shown in Fig. 3-3.

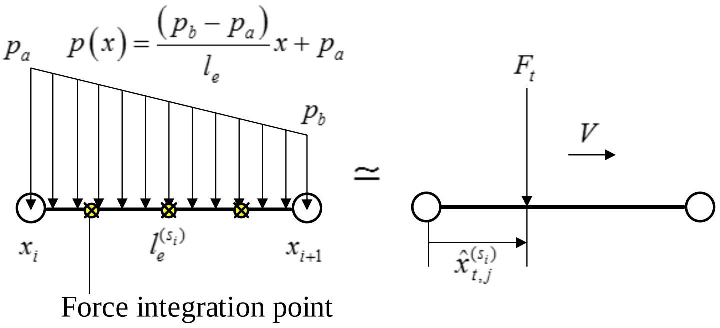

Figure 3-2. Non-uniform distributed load in each element during analysis

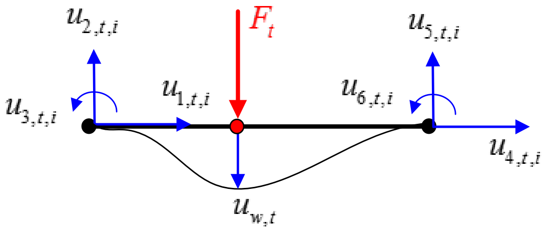

Figure 3-3. Nodal displacement for *i* element

Six shape functions are used for a beam element:

$$\phi_{1,t,j}^{(s_i)} = 1 - \eta_{t,j}^{(s_i)} \tag{3-3}$$

$$\phi_{2,t,j}^{(s_i)} = \phi_{3,t,j}^{(s_i)} = 1 - 3\xi_{t,j}^{(s_i)2} + 2\xi_{t,j}^{(s_i)3} \tag{3-4}$$

$$\phi_{5,t,j}^{(s_i)} = \phi_{6,t,j}^{(s_i)} = (\xi_{t,j}^{(s_i)} - 2\xi_{t,j}^{(s_i)2} + \xi_{t,j}^{(s_i)3})l_e^{(s_i)} \tag{3-5}$$

$$\phi_{7,t,j}^{(s_i)} = \eta_{t,j}^{(s_i)} \tag{3-6}$$

$$\phi_{8,t,j}^{(s_i)} = \phi_{9,t,j}^{(s_i)} = 3\xi_{t,j}^{(s_i)2} - 2\xi_{t,j}^{(s_i)3} \tag{3-7}$$

$$\phi_{11,t,j}^{(s_i)} = \phi_{12,t,j}^{(s_i)} = (-\xi_{t,j}^{(s_i)2} + \xi_{t,j}^{(s_i)3}) l_e^{(s_i)} \tag{3-8}$$

where $\xi_{t,i}^{(s_i)} = \frac{\hat{x}_{t,i}^{(s_i)}}{l_e^{(s_i)}} = \eta_{t,i}^{(s_i)}$, $l_e^{(s_i)}$ is the length of the i^{th} element and $\hat{x}_{t,i}^{(s_i)}$ is the distance between the moving axle load and left node of the i^{th} element, as shown in Fig. 3-2.

Once the rail displacement is obtained the contact force can be derived and the vehicle dynamic response can be derived using the implicit integration procedure (Newmark integration scheme) (Chopra, 2007) by solving $\mathbf{u}_{v,t+dt}$ in the user-defined subroutine DLOAD by solving equation

$$\mathbf{M}\ddot{\mathbf{u}}_{v,t+dt} + \mathbf{K}\mathbf{u}_{v,t+dt} + \mathbf{C}\dot{\mathbf{u}}_{v,t+dt} = \mathbf{F}_{t+dt} \tag{3-9}$$

where $\mathbf{F}_t$ is contact force vector in which only vertical force, F_{t+dt}, is considered. **K**, **C**, **M** are the stiffness, damping and mass matrices of the vehicle system. Finally, the vehicle displacement can be derived with $\gamma = 1/2$ and $\beta = 1/4$ from

$$\mathbf{u}_{v,t+dt} = \mathbf{u}_{v,t} + dt\dot{\mathbf{u}}_{v,t} + dt^2\left(\left(\frac{1}{2} - \beta\right)\ddot{\mathbf{u}}_{v,t} + \beta\ddot{\mathbf{u}}_{v,t+dt}\right) \tag{3-10}$$

where

$$\dot{\mathbf{u}}_{v,t+dt} = \dot{\mathbf{u}}_{v,t} + dt\left((1-\gamma)\ddot{\mathbf{u}}_{v,t} + \gamma\ddot{\mathbf{u}}_{v,t+dt}\right) \tag{3-11}$$

3.3 Simply supported beam with moving sprung mass

To demonstrate the validity of the method introduced in Section 3.2, the two schemes, contact model and user-defined subroutine, are applied to a simple model and the results are compared and discussed. The model consists of a sprung mass moving along a simply supported beam, as shown in Fig. 3-4. The same validation procedure using the contact model (see Section 3.2.1) is also given in (Saleeb et al., 2011).

The material parameters adopted for the beam are: Young's modulus E=2.87 GPa, Poisson's ratio v=0.2, second moment of area I=2.9 m^4, mass per unit length ρA=2303 kg/m. The vehicle suspension stiffness is 1595 kN/m, the damping is c_v=0 Ns/m, and the mass is m_v=5750 kg, m_w=0 kg. The vehicle speed is 27.78 m/s and the length of the beam, *L*, is 25 m. Fifty Euler-Bernoulli beam elements, without consideration of shear flexibility (type B23), are used.

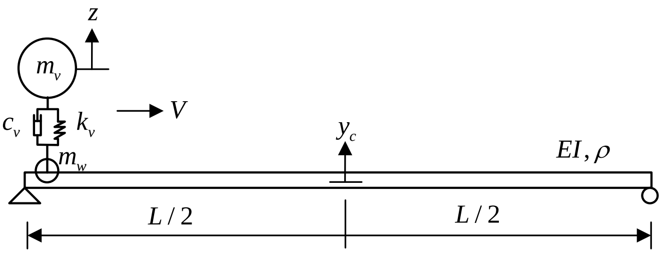

Figure 3-4. Moving oscillator with a simply support beam

For the simpler case of a moving constant load *F* (ignoring the dynamics of the moving vehicle), the analytical solution for the displacement of a simply supported beam with no damping can be derived as (Fryba, 1999)

$$y(x,t) = y_0 \sum_{n=1}^{\infty} \sin \frac{n\pi x}{L} \frac{1}{n^2\left(n^2-\alpha^2\right)} \left(\sin n\omega t - \frac{\alpha}{n} \sin \omega_n t \right) \tag{3-12}$$

where y_0 represents the deflection at mid-span of a beam loaded with static force *F* at the midpoint

$$y_0 = \frac{FL^3}{48EI} \tag{3-13}$$

L is the length of the beam, α is the dimensionless parameter

$$\alpha = \frac{\omega}{\omega_1} \tag{3-14}$$

and the circular frequency ω is given by

$$\omega = \frac{\pi V}{L} \tag{3-15}$$

V is the speed of the moving load, and the *n*-th natural frequency of the beam is given by

$$\omega_n = \sqrt{\frac{n^4 \pi^4}{L^4} \frac{EI}{\rho A}} \tag{3-16}$$

where E is Young’s modulus, I is the second moment of area, and ρA is the mass per unit length of the beam.

For the case of a moving spring-mass system with no damping, the midpoint displacement of a simply supported beam can be found approximately by considering only the first mode of vibration of the beam by solving the following two-degree system (Biggs, 1964) by a numerical procedure.

$$\begin{bmatrix} \frac{1}{2}\rho AL + m_w \sin^2\left(\frac{\pi Vt}{L}\right) & 0 \\ 0 & m_v \end{bmatrix} \begin{Bmatrix} \ddot{y}_c \\ \ddot{z} \end{Bmatrix} + \begin{bmatrix} \frac{mL\omega_1^2}{2} + k_v \sin^2\frac{\pi Vt}{L} & -k_v \sin\frac{\pi Vt}{L} \\ -k_v \sin\frac{\pi Vt}{L} & k_v \end{bmatrix} \begin{Bmatrix} y_c \\ z \end{Bmatrix} = \begin{Bmatrix} -(m_v + m_w)g \\ 0 \end{Bmatrix} \tag{3-17}$$

The dynamic responses of the moving load and moving vehicle problems obtained using ABAQUS with the specific contact model of Section 3.2.1 have been compared with the above analytical solutions (Biggs, 1964; Fryba, 1999) and with the numerical solution obtained by (Yang and Yau, 1997). The displacement of the beam and the sprung mass are shown in Fig. 3-5 and Fig. 3-6. Numerical results are also shown for a moving load, i.e. omitting the vehicle dynamics. The displacements of the beam show good agreement with the analytical results and the difference in the beam response introduced by the dynamics of the sprung mass can also be seen by comparison with the results for a moving load in Fig. 3-5.

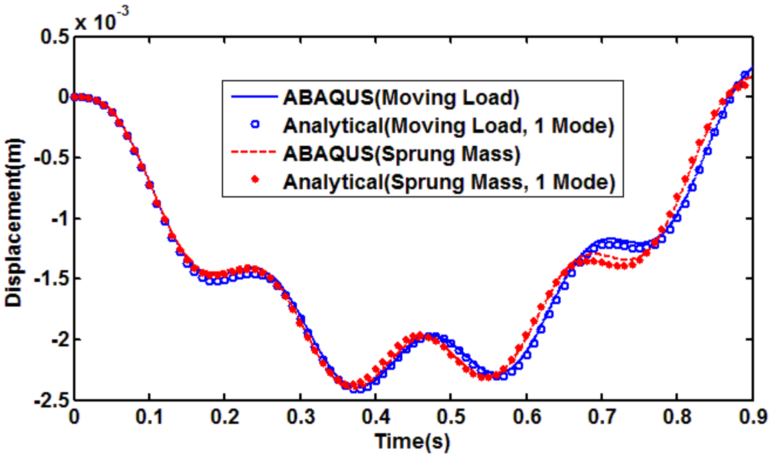

Figure 3-5. Vertical displacement of the beam at its midpoint for a moving load and a moving sprung mass

However, there are some differences between the sprung mass results from ABAQUS and the analytical results, as shown in Fig. 3-6. This is due to the neglect of higher order beam modes in the analytical results. Nevertheless, the displacements of the sprung mass agree well with the numerical results from (Yang and Yau, 1997).

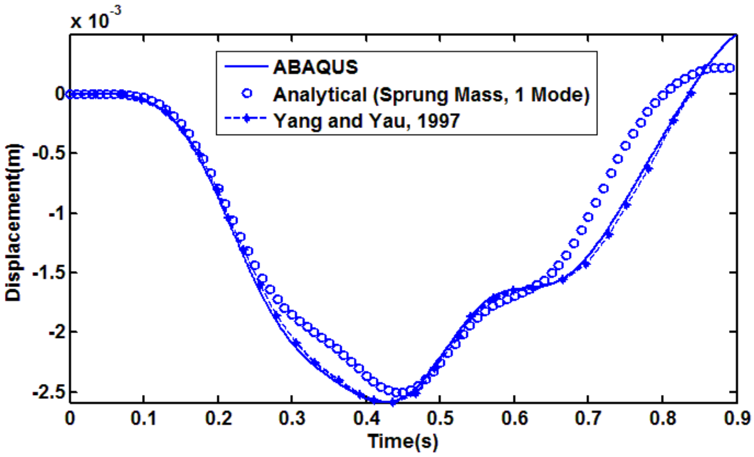

Figure 3-6. Vertical displacement of the sprung mass

Finally, the results from the two different coupling schemes are compared, as shown in Fig. 3-7. Good agreement between the results of the two coupling schemes can be seen for both the middle point displacement and the sprung mass displacement. Total simulation times for the moving load and moving vehicle analysis are listed in Table 3-1. As shown, the simulation by using the user-defined subroutine is less efficient for both cases due to the need to couple two programs (FORTRAN and ABAQUS), especially for the moving vehicle problem. As a result, the contact model is used for coupling between the wheel and rail for all further simulations.

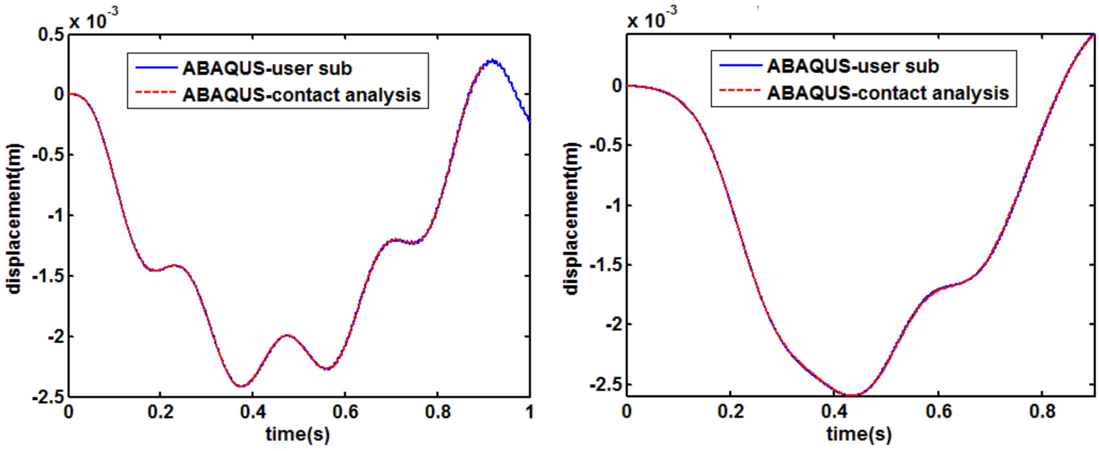

(a) (b)

Figure 3-7. Comparison of midpoint and vehicle displacement between two schemes

Table 3-1 Simulation CPU cost comparison between two schemes for a typical desktop computer. Times given in seconds.

	Contact model	User-subroutine
Moving load	35	80
Moving vehicle	35	120

3.4 Use of solid elements to represent simply supported beam subjected to a moving sprung mass

3.4.1 Element types

For the vehicle/track/ground system in subsequent chapters, the rail will be modelled using solid elements. Three-dimensional beam elements would be required in order to be combined with a three-dimensional ground model. However, the three-dimensional beam surface can only be used as a slave surface in the contact definition in ABAQUS. Therefore, solid elements, with a cross-section equivalent to the beam section, will be used. In this section the above problem is modelled using solid elements to represent the simply supported beam.

Three types of hexahedral element can be considered in ABAQUS: the fully integrated elements, the reduced-integration elements, and the incompatible mode elements. Moreover, both fully-integrated and reduced-integration elements can be defined to be linear or quadratic and each element type has its specific characteristics in the simulation (ABAQUS, 2013b).

Hexahedral reduced-integration elements (C3D8R, C3D20R) are the default element types in ABAQUS due to their efficiency and high tolerance of distortion. However, one of the main problems which may occur is hour-glassing, which results in mesh instability. Therefore, fine meshes are usually required with this type of element, especially the number of elements through the thickness for any simulation including bending behaviour. Furthermore, they are not suitable for large-displacement simulations involving very large strains and for some types of contact analysis (ABAQUS, 2012).

On the other hand, the use of the linear fully integrated brick elements (C3D8) may result in shear-locking problems, as they are overly stiff in bending applications due to incorrect artificial shear stress. This is because the edges of the fully integrated linear element are not able to curve in bending. Therefore, a higher order element formulation (C3D20) should usually be used in order to avoid this problem. In addition, reduced-integration elements can also be used in ABAQUS to overcome the shear-locking problem (ABAQUS, 2012).

Incompatible mode elements (C3D8I) were developed in ABAQUS in order not only to avoid the artificial stress caused in pure bending but also because they have less sensitivity to the mesh density and better accuracy. However, this element is very sensitive to element distortions (ABAQUS, 2012).

A table summarising the various elements including the main advantages and disadvantages is given in Table 3-2. The results of using these different element types will be compared in the next section.

Table 3-2 Element description

Element code	Element type	Advantage	Disadvantage
C3D8	Linear fully integrated brick elements	Relatively good efficiency	Overly stiff in bending applications due to shear-locking problems
C3D8R	Reduced-integration brick elements	Good efficiency and high tolerance of distortion	Mesh instability due to hour-glassing
C3D8I	Incompatible mode brick elements	Good accuracy and less sensitivity to the mesh density	Sensitive to element distortions and relatively poor efficiency
C3D20	Higher order with fully integrated brick element	Good accuracy and less sensitivity to the mesh density	Relatively poor efficiency

3.4.2 Simply supported beam

Using the same parameters as in Section 3.3, the beam is represented by four different meshes, as shown in Fig. 3-8, and four different element types, C3D8, C3D8R, C3D8I, C3D20. Only one element is used across the width because the influence of this coordinate is very small. However, due to the fact that the boundary condition for the simply supported beam is based on fixing the centroid of the beam cross-section, a minimum of two elements through the thickness in the solid element model are used. Fifty elements are used along the axial direction in each case.

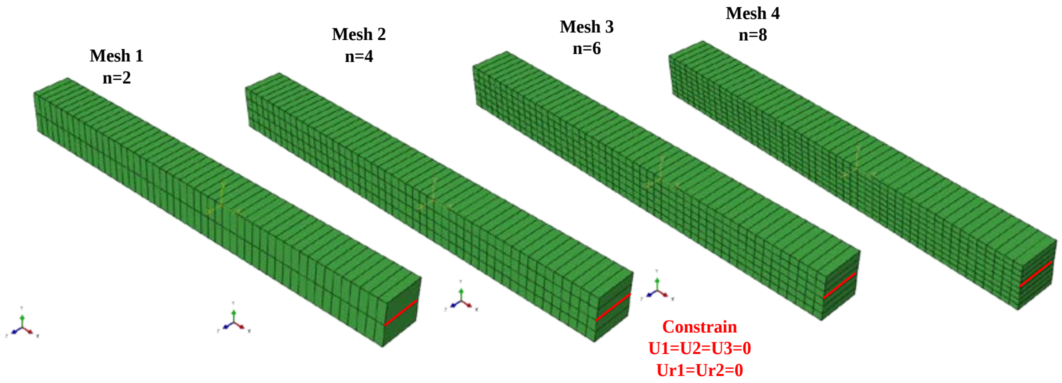

Figure 3-8. Four different meshes for a simply supported beam using solid elements

Before considering a moving load problem, the natural frequencies of the first five modes of these simply supported beams are calculated. The ratio of the natural frequency found using the solid elements and that found using the Euler-Bernoulli beam elements is plotted versus the mode number in Fig 3-9. The results from the incompatible mode elements and the higher-order fully-integrated elements all show good agreement even with only two elements in the thickness direction, as seen in Fig. 3-9(a). The influence of the mesh density in the thickness direction is very small for these two element types. For the fully integrated elements the natural frequency becomes slightly larger with more elements through the thickness. This is because of shear locking that causes the stiffness of the solid beam to increase. However, significant differences can be seen between the four different meshes for the reduced-integration elements. Better results can be seen with finer meshes, but small differences still can be found even for the lower modes as seen in Fig. 3-9(d). As a result, for element type C3D8I and C2D20 it is sufficient to have two elements in the thickness direction, although better results are found with increasing numbers of elements. On the other hand, at least four elements should be used for element type C3D8. Moreover, the results do not improve when the number of elements is increased for this element type. Element type C3D8R gives the worst results and requires a larger number of elements to achieve reasonable predictions.

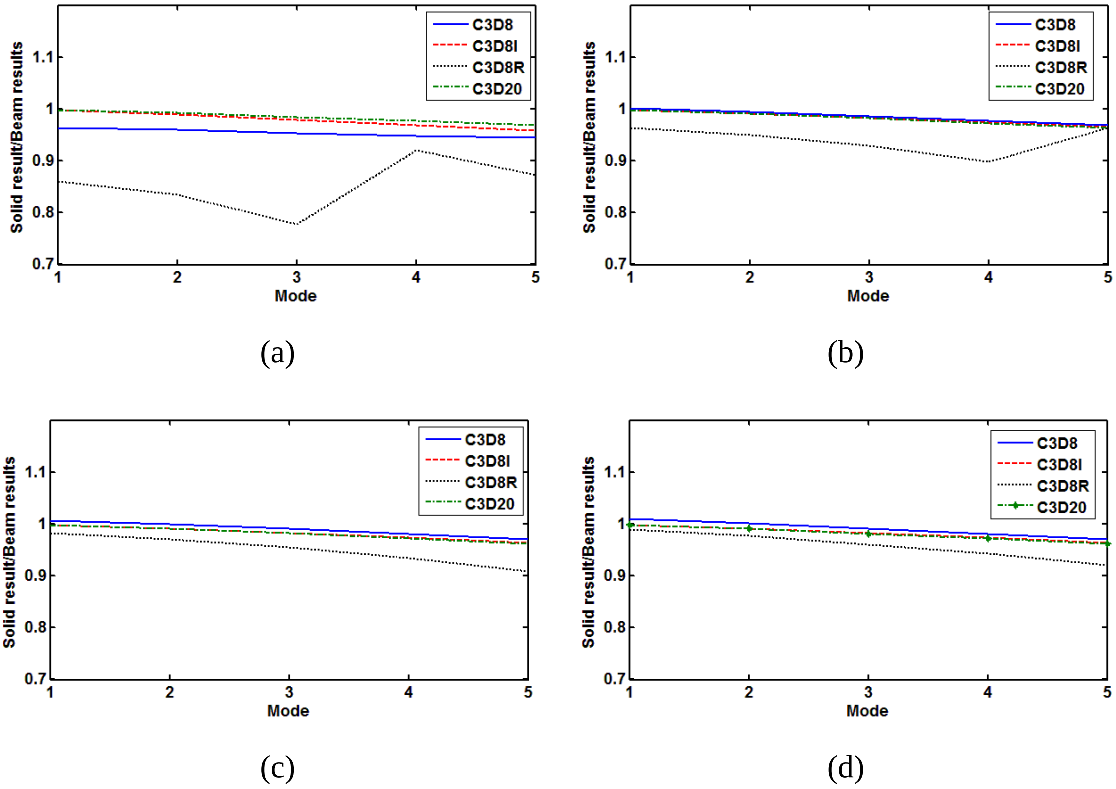

Figure 3-9. Effect of mesh density with three types of element; (a) mesh 1, *n*=2; (b) mesh 2, *n*=4; (c) mesh 3, *n*=6; (d) mesh 4, *n*=8

3.4.3 Moving sprung mass

In this section the various different types of solid element are used to represent the beam to study the moving sprung mass. Fig 3-10 shows the midpoint displacements and the sprung-mass displacements obtained from the fully integrated elements (C3D8) with different numbers of elements across the thickness. The results are compared with those obtained using beam elements (from Section 3.3). The results from the solid elements show differences when only two elements are used across the thickness. Even though the results become better when the number of elements increases, slight differences still can be found. This is because shear locking occurs when the number of elements increases through the thickness, as also found in Fig 3-9.

The results from reduced-integration elements (C3D8R) are shown in Fig. 3-11. These show quite large differences when using only two elements through the thickness. Furthermore, even when the number of elements in the thickness direction increases, small differences still can be found.

The results from incompatible mode elements (C3D8I) and higher-order fully integrated elements (C3D20) with different meshes all show good agreement with the beam elements as shown in Fig. 3-12 and Fig. 3-13.

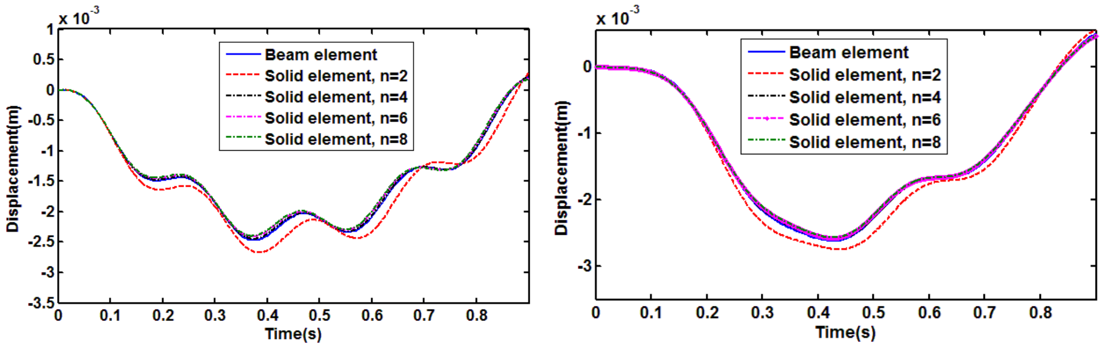

(a) (b)

Figure 3-10. Vertical displacement by using fully integrated C3D8 element; (a) midpoint displacement; (b) sprung-mass displacement

Therefore, although the reduced-integration elements cost less simulation time, they are too sensitive to the mesh density. Furthermore, small differences still can be found with a finer mesh. The results from the fully integrated elements show better agreement with the beam elements; however, small differences still remain. The incompatible mode elements and higher-order fully integrated elements both show very good agreement and are less sensitive to the mesh density. The higher-order fully integrated elements (C3D20) will be used for further simulations due to their better accuracy and better efficiency compared with the incompatible mode elements.

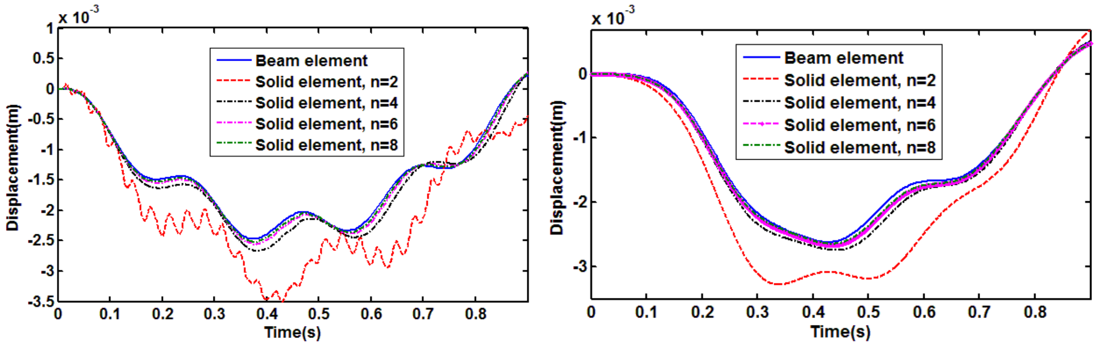

(a) (b)

Figure 3-11. Vertical displacement by using reduced-integration C3D8R element; (a) midpoint displacement; (b) sprung-mass displacement

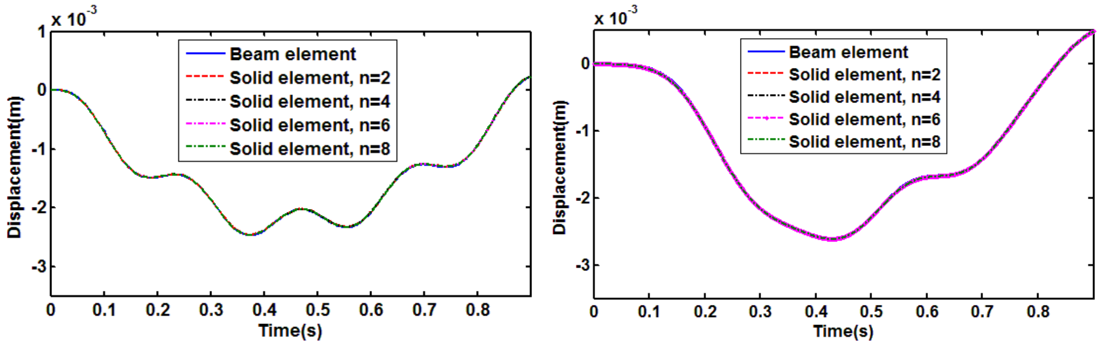

(a) (b)

Figure 3-12. Vertical displacement by using incompatible mode C3D8I element; (a) midpoint displacement; (b) sprung-mass displacement

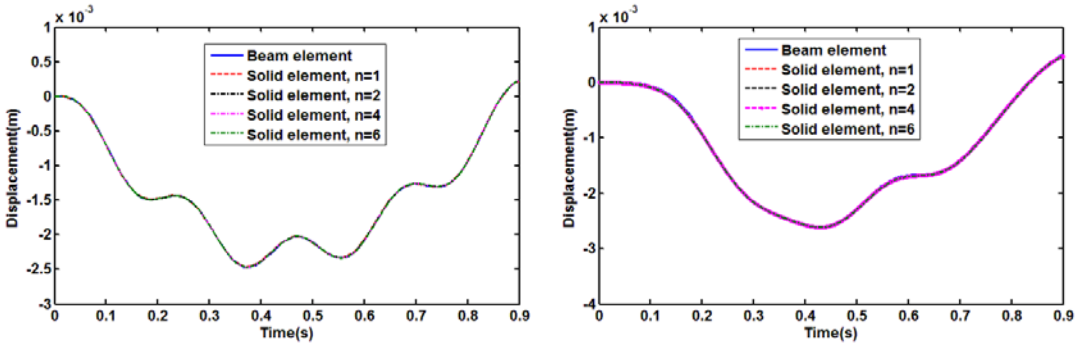

(a) (b)

Figure 3-13. Vertical displacement by using higher-order fully integrated C3D20 element; (a) midpoint displacement; (b) sprung-mass displacement

3.5 Summary

Modelling of vehicle-track interaction with and without the need for a user-defined subroutine has been demonstrated and good agreement has been found using both approaches compared with analytical results for a problem of a load or a mass-spring moving along a beam. The sliding contact model is used for further simulation due to its better efficiency. Furthermore, the use of three-dimensional solid elements for the beam has been shown to give good results provided appropriate elements are used. The higher-order fully integrated element (C3D20) has been shown to avoid shear locking and hour-glassing problems and will be used in subsequent calculations.

Chapter 4: Ballasted track model

4.1 Introduction

The cross-section of the typical ballasted track system is shown in Fig. 4-1. The rails are supported on railpads and attached by clips to the sleepers. These are commonly made of concrete or wood but may also be made of steel or plastic. The sleepers are supported in a layer of ballast as can be seen in Fig. 4-1. Furthermore, the ballast is supported on a subgrade layer. This may be the top of an embankment or material stabilized by the addition of asphalt, lime, Portland cement or other modifiers. This is intended to help maintain the track geometry and prevent deflections from being too large.

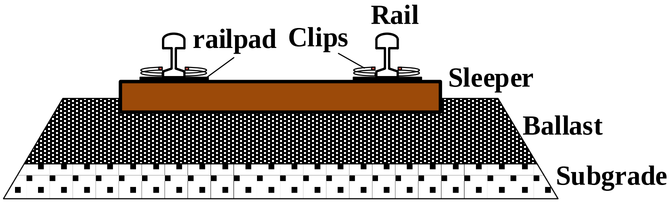

Figure 4-1. Typical ballasted track system

In this chapter, the modelling of ballasted track by using commercial FE software is introduced and various element types are compared. The ground beneath the ballast is assumed to be rigid, the flexible ground being introduced in the next chapter. In Section 4.2 various models of a beam on a one- and two-layer support are introduced and the rail receptance (displacement for a unit harmonic load as a function of frequency) is compared with analytical results. Then in Section 4.3 the response of a beam on a Winkler foundation to a moving point load is studied in the time domain and compared with analytical results. A moving vehicle model is introduced in Section 4.4; this is connected to the track by using the contact model discussed in Section 3.2.1. The results are compared with a moving frame approach (Nguyen and Duhamel, 2008). Finally, three-dimensional models of the track are introduced in Section 4.5 and results for continuous and discrete supports are compared.

4.2 Analysis of one and two-layer track with stationary harmonic load

In this section simple beam models of the track are studied, excited by a stationary harmonic load. Analytical models of an infinite beam on a single layer support, as shown in Fig. 4-2, or a two-layer support, as shown in Fig. 4-3, are presented in (Thompson, 2009). These are summarised in Appendix A.1. The rail is represented by an Euler-Bernoulli beam. In the single layer model, known as a Winkler foundation, the rail is supported by a continuous layer of elastic springs (and dampers). In the two-layer support model the upper elastic layer represents the railpads, the sleepers are represented by a layer of mass and the ballast is also assumed to be an elastic layer.

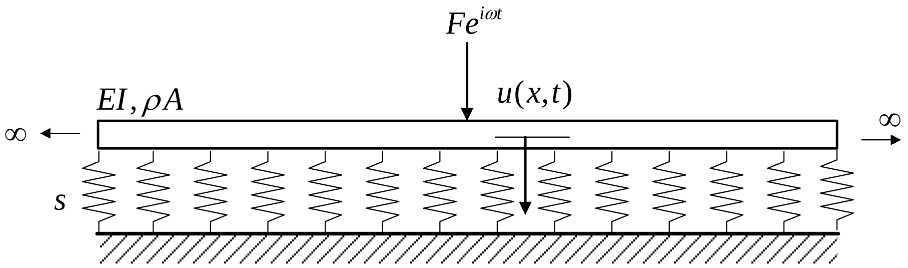

Figure 4-2. Track model with single-layer support

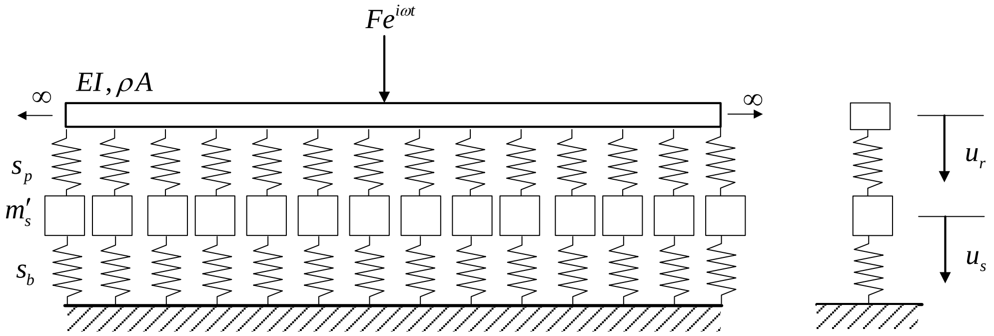

Figure 4-3. Track model with two-layer support

In order to represent a continuous support using finite element method, a two-dimensional plane stress element is used. For convenience, a constraint condition is used to connect the beam elements (rail) and plane elements (foundation), as shown in Fig. 4-4. This can be achieved in ABAQUS by partially or fully eliminating degrees of freedom of a group of nodes and coupling their motion to the motion of a set of master nodes (ABAQUS, 2013b). Tie constraints are used in this analysis, which provide a simple way to bond surfaces together by setting master-slave formulations. This constraint prevents the slave nodes from separating or sliding relative to the master surface; therefore, there are no relative displacements between the two surfaces. In this analysis, the beam elements were set to be the master surface controlling the displacement of the plane elements, because the excitation load is applied to the rail.

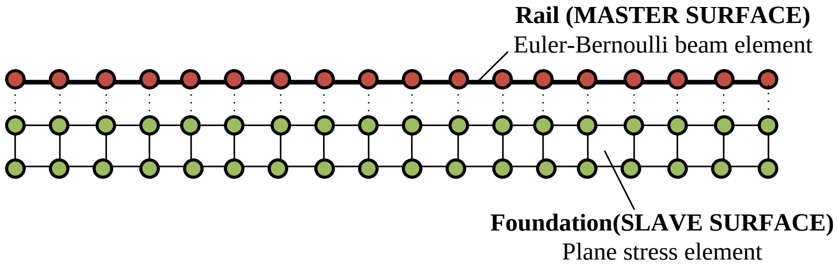

Figure 4-4. Track model in ABAQUS with constraint function

Euler-Bernoulli beam elements are used to represent the rail. The foundation, consisting of the pad, sleeper and ballast, is modelled by plane stress membrane elements to represent continuous spring stiffness and mass per unit length. Assuming that the track is modelled in the *x*-*z* plane, the only non-zero stress components in the membrane are those parallel to the middle surface, σ_{xx} , σ_{zz} and τ_{xz}. Isotropic elements are used with very small second moment of inertia in order to represent the continuous support such as Winkler foundation. Here the Poisson's ratio is assumed to be zero due to the fact that the foundation is modelled as a continuous support and Poisson's ratio effects are not considered. The analysis method used in ABAQUS is the direct steady-state dynamic analysis in the frequency domain. Structural damping with a constant loss factor is used.

As it is not possible to model an infinite beam in ABAQUS, finite length models were constructed and their results are compared with the analytical model in the following sections to investigate the effect of the finite length.

4.2.1 Static analysis

The single-layer support track model constructed in ABAQUS is shown in Fig. 4-5. The parameters used are listed in Table 4-1. The Young's modulus of the foundation in the FE model is related to the stiffness by

$$E_f = \frac{s \times l_h}{l_t} \tag{4-1}$$

where *s* is the foundation stiffness, l_h is the element height and l_t is its thickness. By choosing $l_h = l_t$, the Young's modulus is identical to the required stiffness per unit length; the cross-section of the elastic layer is thus given as 0.1 × 0.1 m.

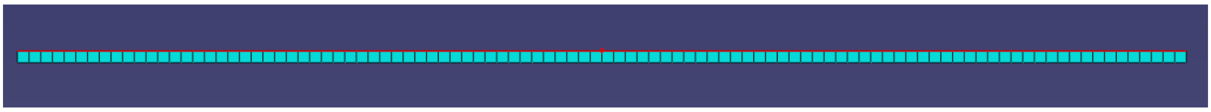

Figure 4-5. 10 m long track model with single-layer support modelled in ABAQUS

First a static analysis is considered to check the stiffness of the foundation in the FE model and test the application of this formula A static vertical load of 100 N is applied at the centre of a 10 m length of track, *x*=0. The theoretical deflection at a position *x*=0 is given by (Esveld, 2001)

$$w = \frac{F}{8EI\lambda^3}\varphi_1(\lambda x) = \frac{100}{8\times 6.42\times(1.405)^3} = 0.7024\mu\text{m} \tag{4-2}$$

where $\lambda = 1/\sqrt[4]{s/(4EI)}$ and $\varphi_1(\lambda x) = e^{-\lambda x}(\cos\lambda x + \sin\lambda x)$ so that $\varphi_1 = 1$ for $x = 0$. Furthermore, the total length of the waveform can be calculated by

$$L_{static} = 2\pi/\lambda \tag{4-3}$$

Table 4-1 Single-layer support track parameters

	Analytical model parameter (D. J. Thompson, 2009)	FE parameter in ABAQUS	
Rail bending stiffness, *EI*	6.42 MNm^2	E	210 GPa
		I	3.055×10^{-5} m^4
		v	0.3
Rail mass per unit length, ρA	60 kg/m	A_r	0.00763 m^2
		ρ_r	7850 kg/m^3
Foundation stiffness per unit length, *s*	100 MN/m^2	E_s	100 MPa
		v_s	0
		A_s	0.1 x 0.1 m
		ρ_b	0.01 kg/m^3
Rail damping loss factor, η_r	0.02	0.02	
Foundation loss factor, η	0.1/0.2/0.5	0.1/0.2/0.5	
Model length, *L*	Infinite	10 m / 30 m	

The displacements at the forcing point are shown in Table 4-2 for different values of l_h, l_t and *dx*. Although the Young's modulus of the foundation in the FE model can be calculated by Eq. (4-1), the results shown in Table 4-2 with different plane thickness and height differ from the theoretical result. It appears that the large errors occurring for the 1 m height are due to horizontal displacements that are allowed in the FE model, but are not considered in the analytical model. The 0.1 × 0.1 m cross-section was chosen for subsequent use in the FE track model.

Table 4-2 Displacement of the beam at the midpoint

Thickness of the foundation, l_t	Height of the foundation, l_h	Mesh element size, *dx*	Deformation at the midpoint	Error
1 m	1 m	0.2 m	0.6175 μm	-12.1%
0.1 m	0.1 m	0.1 m	0.7034 μm	-0.14%
0.1 m	0.1 m	0.2 m	0.7086 μm	0.88%

In addition, the number of plane elements needs to be sufficient to represent the continuous foundation. Therefore, a mesh element size of *dx* = 0.1 m was used with a total of 100 elements for the 10 m length. This case showed good agreement with the analytical result, as can be seen in Table 4-2. The deformation of the one-layer track model is shown in Fig. 4-6, which shows good agreement compared with analytical results.

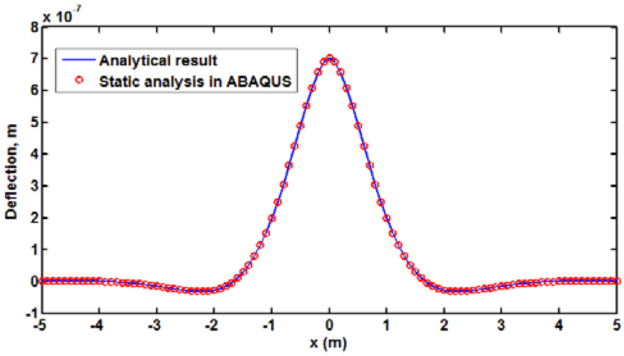

Figure 4-6. Comparison of rail deflection from ABAQUS with analytical results

4.2.2 Single–layer support analysis

For a point harmonic load, the receptance magnitude for a 10 m long model is compared with the analytical results in Fig. 4-7~4-9 for three different damping values. The corresponding results for a 30 m long model are shown in Fig. 4-10.

In each case the receptance has a constant value at low frequency, corresponding the stiffness-controlled region. A resonance peak is seen at 200 Hz. This frequency is called the cut-on (or cut-off) frequency of bending waves in the rail due to the fact that the waves start to propagate above this frequency (Thompson, 2009). As can be seen, the dynamic responses below and up to the cut-on frequency at 200 Hz agree well with the analytical results. Moreover, the behaviour at the resonance is predicted well for different damping loss factors of the foundation. However, above the cut-on frequency, the influence of the finite length of the model can be seen in the figures as a series of peaks and dips at high frequency. The oscillations are bigger for the 10 m model than for than 30 m model. Increased damping reduces their amplitude. Therefore, either a longer model or a higher foundation damping loss factor is required to approximate the infinite behaviour. In addition, the accuracy of the dynamic results depends on the mesh density, in particular the number of nodes per shortest wavelength. Kuhlemeyer and Lysmer, 1973 suggested a maximum element size of one-eighth of the shortest wavelength, related to the maximum frequency in the dynamic analysis, which can be calculated by

$$f_{\max} = \frac{1}{2\pi}\sqrt{\frac{k_{\max}^4 EI}{\rho A}} \tag{4-4}$$

where $k_{\max} = 2\pi / \lambda_{\min}$, and $\lambda_{\min} \approx 8l_e$, l_e is the maximum node spacing, which gives around 3200 Hz for the node spacing of 0.1 m. Since the focus is on frequencies below 100 Hz, the mesh used is more than sufficient.

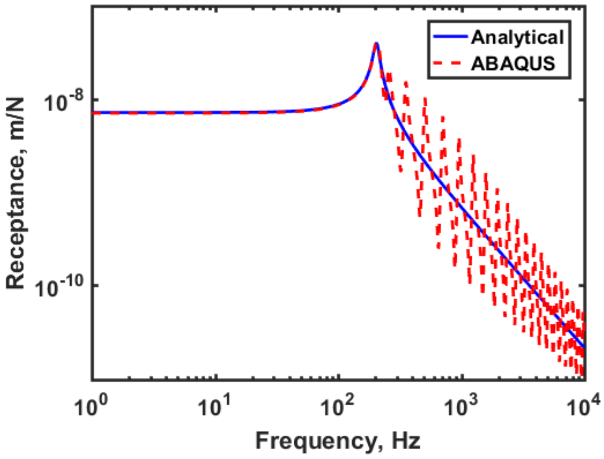

Figure 4-7. Point receptance magnitude of single-layer track model for $\eta = 0.1$ (10 m model)

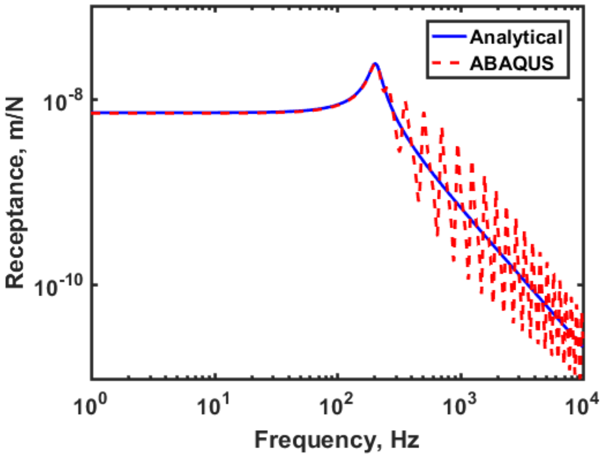

Figure 4-8. Point receptance magnitude of single-layer track model for $\eta = 0.2$ (10 m model)

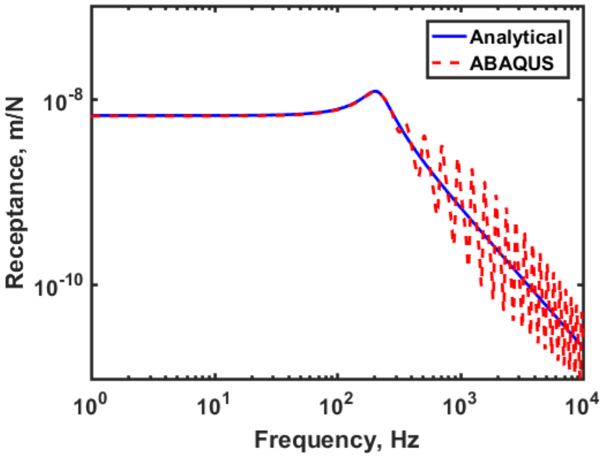

Figure 4-9. Point receptance magnitude of single-layer track model for $\eta = 0.5$ (10 m model)

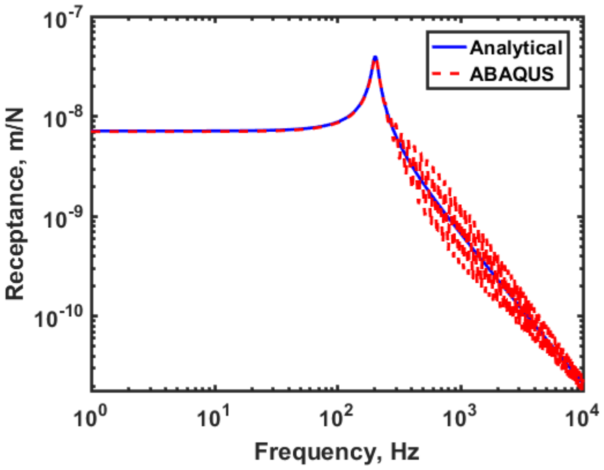

Figure 4-10. Point receptance magnitude of single-layer track model for $\eta = 0.1$ (30 m model)

4.2.3 Two–layer support analysis

Next the model is extended to a track with a two-layer support by the introduction of a sleeper layer as shown in Fig. 4-11. The length is again 10 m. Two elastic layers are considered which represent the railpads and ballast. They are modelled in a similar way to the single-layer foundation layer, but with different parameters, as given in Table 4-3.

Table 4-3 Two-layer support track parameters

	Analytical model parameter (D. J. Thompson, 2009)	FE parameter in ABAQUS	
Rail bending stiffness, EI	6.42 MNm^2	E_r	210 GPa
		I	3.055×10^{-5} m^4
		v	0.3
Rail mass per unit length, ρA	60 kg/m	A_r	0.007687m^2
		ρ_r	7805.4 kg/m^3
Rail damping loss factor, η_r	0.02	0.02	
Railpad stiffness per unit length, s_p	300 MN/m^2	E_p	300 MPa
		A_p	0.1 x 0.1 m
		v_p	0
		ρ_p	0.01 kg/m^3
Railpad damping loss factor, η_p	0.2	0.2	
Sleeper mass per unit length, m'_s	250 kg/m	E_s	10 GPa
		A_s	0.1 x 0.1 m
		v_s	0
		ρ_s	25000 kg/m^3
Ballast stiffness per unit length, s_b	100 MN/m^2	E_b	100 MPa
		A_b	0.1 x 0.1 m
		v_b	0
		ρ_b	0.01 kg/m^3
Ballast damping loss factor, η_b	1.0	1.0	
Model length, L	Infinite	10m	

The sleeper layer must be rigid (no compression) but should have no bending stiffness along the length of the track. Therefore, a sufficiently large Young's modulus is used for the sleeper layer in the FE model. The sleepers should ideally be orthotropic because there should be no bending stiffness along the track. However, an isotropic material is used for the sleepers. The effect of bending along the track direction can be neglected as it has a very small second moment of area even though it has a large Young's modulus. Due to its very small cross section, the mass density of sleeper is also very large, as shown in Table 4-3.

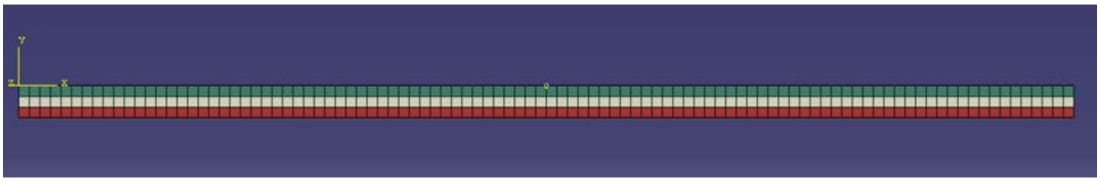

Figure 4-11. 10 m long track model with two-layer support modelled in ABAQUS

Dynamic results calculated in the frequency domain are shown in Fig. 4-12. The receptance for a 10 m long FE model is again compared with the corresponding analytical results. Two resonance peaks are found and these agree well with the cut-on frequencies in the analytical results. The first resonance frequency is dominated by the ballast stiffness, which is mainly the whole track bouncing on the foundation and the second mode is mainly the rail bouncing on the railpad (Thompson, 2009). Again, oscillations occur at high frequency for the same reason as in the single-layer track model but these are outside the frequency range of interest.

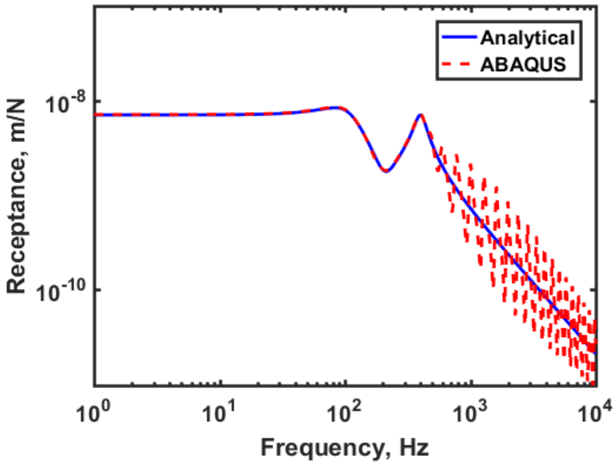

Figure 4-12. Point receptance magnitude of two-layer support track model

4.3 Analysis of single-layer track with a moving point load

In this section a moving point load is introduced on the track model. Similar to the approach mentioned in Section 4.2, a continuous single-layer support is used. However, solid elements are used here for the rail and the elastic layer due to limitations of the FE software for three-dimensional moving load analysis, as mentioned in Section 3.4. Time domain results are compared with the corresponding analytical results (see Appendix A.2).

A three-dimensional FE model of a rail on a Winkler foundation has been created using ABAQUS, as shown in Fig. 4-13. 20-node brick elements (C3D20) are used to model the rail and foundation to avoid shear locking and hour-glassing (see Section 3.4). The model is based on a UIC60 rail section, but this is represented by an equivalent rectangular cross-section with the same mass and vertical bending stiffness as the UIC60 section. This gives a rectangular cross-section of height 218 mm and width 35 mm. The parameters used for the single-layer track support are listed in Table 4-4.

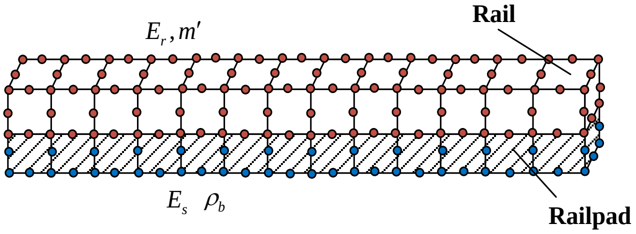

Figure 4-13. Three-dimensional single-layer support track model by using ABAQUS

One parameter commonly used to describe damping is the loss factor. However, a constant loss factor model can only be used in the frequency domain. Rayleigh damping, which is a form of viscous damping, is used here to introduce damping in the time-domain simulations. Rayleigh damping is a form of proportional in which the damping matrix is assumed to be proportional to the mass and stiffness matrices,

$$\mathbf{C} = \alpha\mathbf{M} + \beta\mathbf{K} \tag{4-5}$$

where α and β are constants for the mass and stiffness terms. These can be defined by equating the damping ratio for a certain frequency region or for a certain circular frequency ω. The damping ratio depends on frequency and is given by

$$\xi = \frac{\alpha}{2\omega} + \frac{\beta\omega}{2} = \frac{\eta}{2} \tag{4-6}$$

In the present case the parameters α and β are set to

$$\alpha = 0; \quad \beta = \frac{2\xi}{\omega_0} = 2\xi\sqrt{\frac{\rho A}{s}} \tag{4-7}$$

which gives results which are equivalent to the analytical results with a damping ratio, ξ at the frequency of the resonance of the rail on the support stiffness, ω_0. The resonance frequency is around 200 Hz (1291 rad/s) when the foundation stiffness is 100 MN/m^2, and 91.8 Hz (577 rad/s) when the foundation stiffness is 20 MN/m^2. Therefore, to obtain a damping ratio of 0.1, β is set to 1.55×10^{-4} when the foundation stiffness is 100 MN/m^2 and 3.47×10^{-4} when the foundation stiffness is 20 MN/m^2. Additionally, a lower damping ratio, 0.045, is also considered here with the foundation stiffness 20 MN/m^2 for comparison. This gives three different foundation properties, as shown in Table 4-4.

Table 4-4 One-layer support track parameters

	Analytical model parameter		FE parameter in ABAQUS	
Rail bending stiffness, EI		6.42 MNm^2	E_r	210 GPa
			I	3.055×10^{-5} m^4
			v	0.3
Rail mass per unit length, ρA		60 kg/m	A_r	0.035 × 0.218 m^2
			ρ_r	7805.4 kg/m^3
Foundation area, A_s		-		0.035 × 0.035 m
Foundation density, ρ_b		-		0.01 kg/m^3
Foundation stiffness per unit length, s	1	100 MN/m^2	1	$E_s = 100$ MPa
	2	20 MN/m^2	2	$E_s = 20$ MPa
	3	20 MN/m^2	3	$E_s = 20$ MPa
Foundation damping ratio, ξ	1	0.1	1	$\alpha = 0, \beta = 1.55\times10^{-4}$
	2	0.045	2	$\alpha = 0, \beta = 1.55\times10^{-4}$
	3	0.1	3	$\alpha = 0, \beta = 3.47\times10^{-4}$
Model length, L		Infinite		12 m (Static) 80 m (Dynamic, $E_s = 100$ MPa) 120 m (Dynamic, $E_s = 20$ MPa)

4.3.1 Static analysis of Winkler foundation

First a static analysis is carried out to check the stiffness of the foundation in the FE model and the influence of the element size. For this a load of 1000 N is applied to the centre of the track model. The parameters of the track with single-layer support were given in Table 4-4. As can be seen in the table, the cross-section of the foundation is given as 0.035 m x 0.035 m. As before, the foundation Young's modulus was derived from Eq. (4-1) with $l_h = l_t$.

The element size along the length direction needs to be sufficiently small to represent the continuous foundation. Results are shown in Fig. 4-14 and Fig. 4-15 for various element sizes in comparison with the analytical result. From this it can be concluded that an element length of 0.5 m is sufficiently small to give good agreement with the analytical results whereas a length of 1 m is too long. The differences between the results from ABAQUS with the results from analytical model (see Eq. 4-2) are shown in Table 4-5.

Table 4-5 Percentage differences between rail midpoint deflection from FE model compared with analytical solution

	l_e=1 m	l_e=0.5 m	l_e=0.2 m	l_e=0.1 m
E_s=100 MPa	-8.85%	1.00%	2.99%	3.27%
E_s=20 MPa	-5.23%	0.22%	1.11%	1.20%

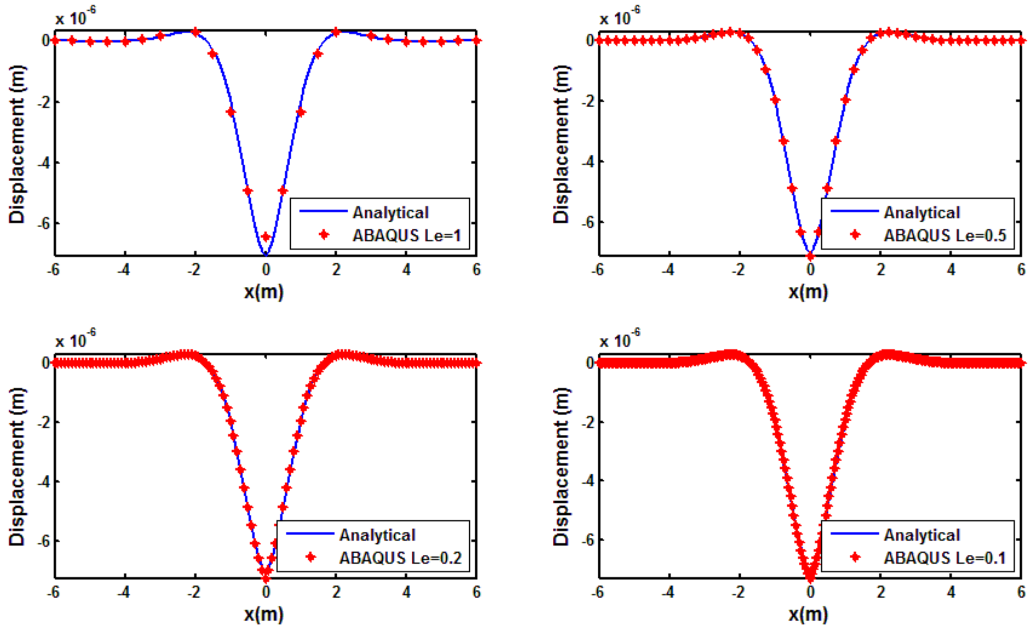

Figure 4-14. Static deflection of the solid beam model with different element size *dx* (E_s=100 MPa)

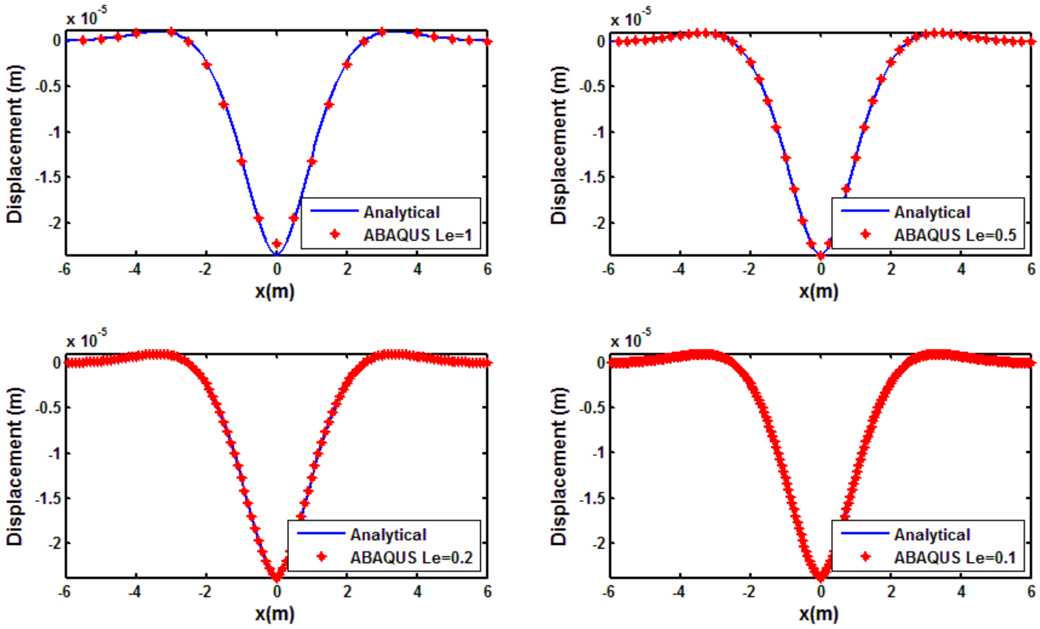

Figure 4-15. Static deflection of the solid beam model with different element size *dx* (E_S=20 MPa)

4.3.2 Moving load applied on Winkler foundation

The displacements of the Winkler foundation for different speeds of moving load are shown in this section. The parameters used are shown in Table 4-4. The beam and its support are represented by 0.5 m long quadratic elements, based on the static results presented in Section 4.3.1. Two different support stiffnesses, 100 MN/m^2 and 20 MN/m^2, are again considered. A moving load of 1000 N is applied at various speeds.

The maximum frequency of validity of the dynamic results can be calculated by Eq. (4-4). For the chosen node spacing of 0.25 m (half the length of the quadratic elements), which should be sufficient up to 513 Hz based on 8 nodes per wavelength. Since the focus is on frequencies below 200 Hz, the mesh used should give acceptable results.

The numerical model in ABAQUS has a finite length with free ends; therefore, the model needs to be long enough to represent the infinite domain. Furthermore, a relatively long transient is generated in the numerical model, which also needs time to achieve the steady-state results derived from the classical formula from the analytical model. Investigation of the minimum size is discussed in this section. An 80 m long model is used for the foundation stiffness of 100 MPa and a 120 m long model for the foundation stiffness of 20 MPa.

Displacements of the rail for different moving load speeds are plotted in Figs 4-16~18. The results in each case are the displacement at the midpoint of the track, plotted as a function of the load position x. The results for the three different sets of foundation properties are compared with the analytical results. Good agreement can be seen even when the load speed is close to the critical speed, which is around 918 m/s for 100 MPa and 614 m/s for 20 MPa, respectively (see Appendix A.2). The displacement of the track increases when the load speed becomes higher.

The lengths of the waveform and of the transient zone are two main factors used to assess the size of the model required. The length of the waveform, L_{static}, can be calculated by Eq. (4-3). As shown in Fig. 4-16(a)~(e), the waveform is around 8 m long when the load speed is below 800 m/s. However, as shown in Fig. 4-16(f), it becomes much longer, around 20 m, when the load speed is 900 m/s, which is close to the critical speed. Therefore, the model size needs to be larger than 20 m for this case when the load speed is 900 m/s. On the other hand, the waveform is around 10m long for speeds up to 500 m/s when the foundation stiffness is 20 MPa as shown in Fig. 4-17(a)~(e). The length of the waveform becomes about 40 m when the speed approaches the critical speed, as shown in Fig. 4-17(f). Therefore, when the stiffness of the foundation is 20 MPa, the model should be at least 40 m long for speeds up to 600 m/s. Similarly, the results with the same foundation stiffness, 20 MPa, but with lower damping show that the model should be at least 30 m long to include the whole wave form, as can be seen in Fig. 4-18(f).

In addition, the maximum displacements of each node along the track during the simulation are presented in Fig. 4-19~21 for these three cases. This shows the extent of the transient zone at the left-hand end of the track. If the responses of the nodes along the track have not reached steady state, the amplitude of the maximum displacement will vary. The maximum displacements are almost the same along the track when the load speed is very low, as shown in Fig. 4-19(a)~(b), Fig. 4-20(a)~(b), and Fig. 4-21(a)~(b). However, as the load speed increases, the responses require more time to arrive at a steady state, as shown in Fig. 4-19(c)~(f), Fig. 4-20(c)~(f), and Fig. 4-21(c)~(f).

The points are identified at which steady state is reached and these are marked on the graphs. To identify these points an algorithm has been developed. The amplitude of the steady-state displacement is determined first and the distance required from the left-hand end is then found based on this value.

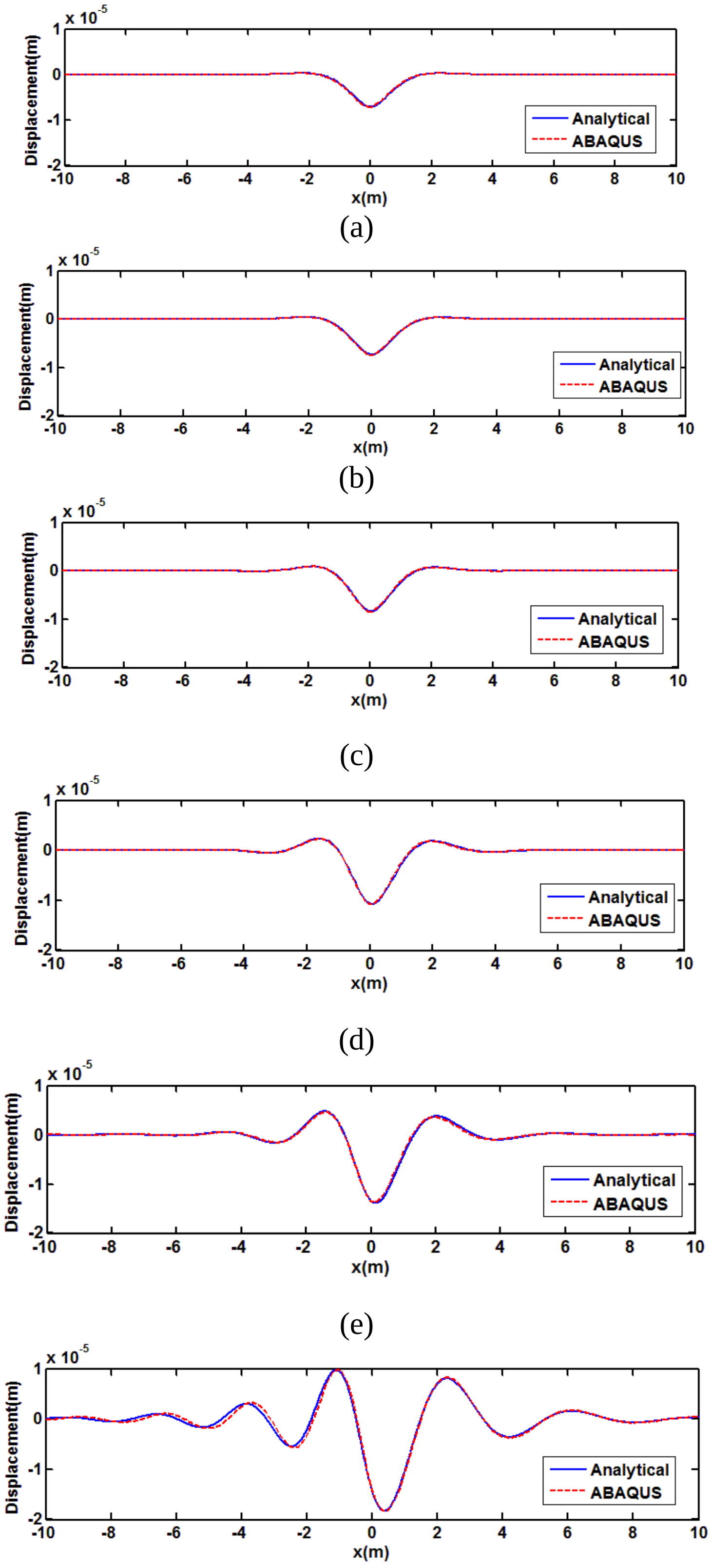

(a)

(b)

(c)

(d)

(e)

(f)

Figure 4-16. Displacement of the rail on Winkler foundation with different load speeds, E_s=100 MPa, $\xi = 0.1$ (a) 50 m/s; (b) 250 m/s; (c) 500 m/s; (d) 700 m/s; (e) 800 m/s; (f) 900 m/s

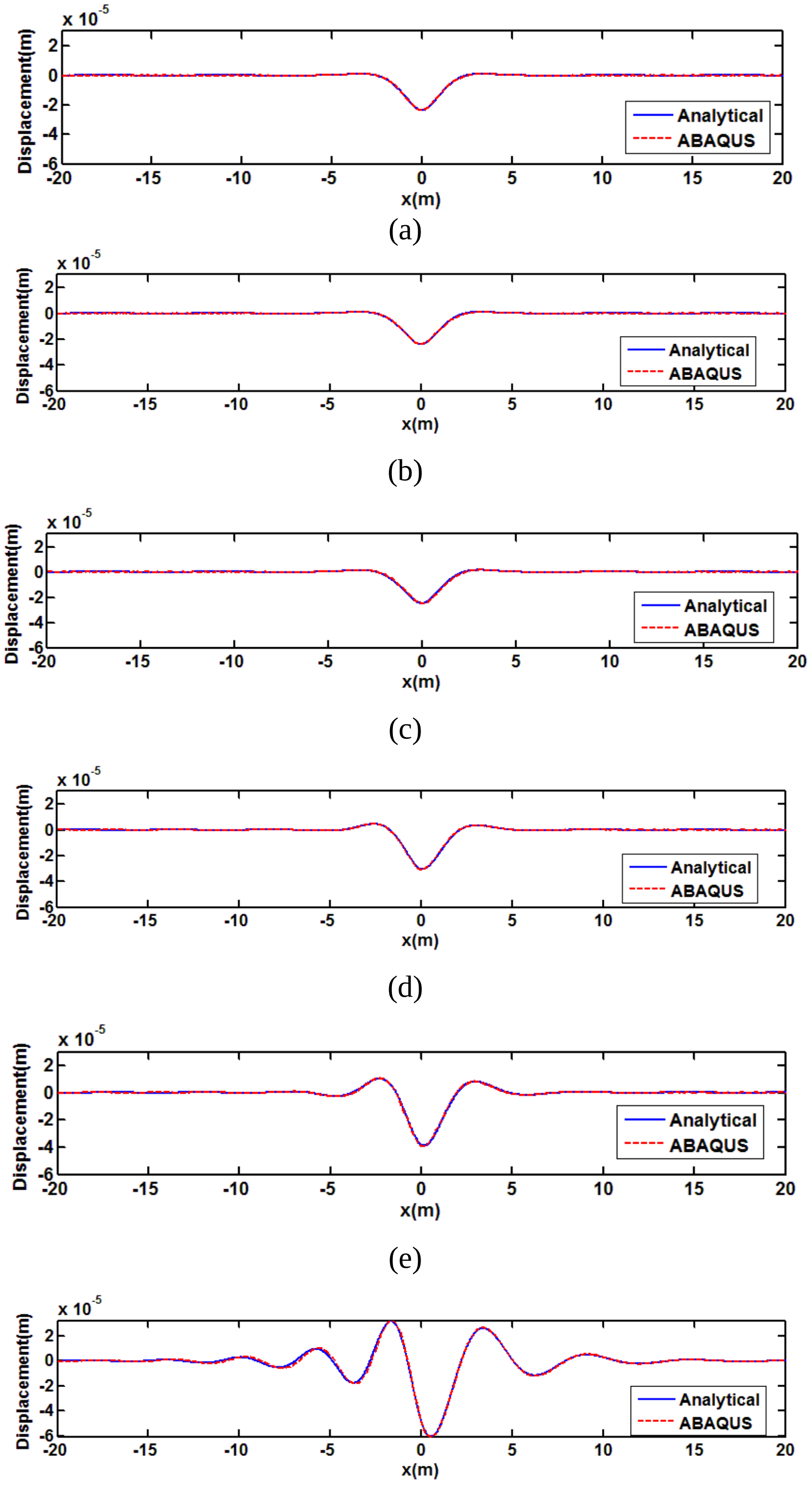

(a)

(b)

(c)

(d)

(e)

(f)

Figure 4-17. Displacement of the rail on Winkler foundation with different load speeds; E_s=20 MPa, $\xi = 0.1$; (a) 50 m/s; (b) 100 m/s; (c) 200 m/s; (d) 400 m/s; (e) 500 m/s; (f) 600 m/s

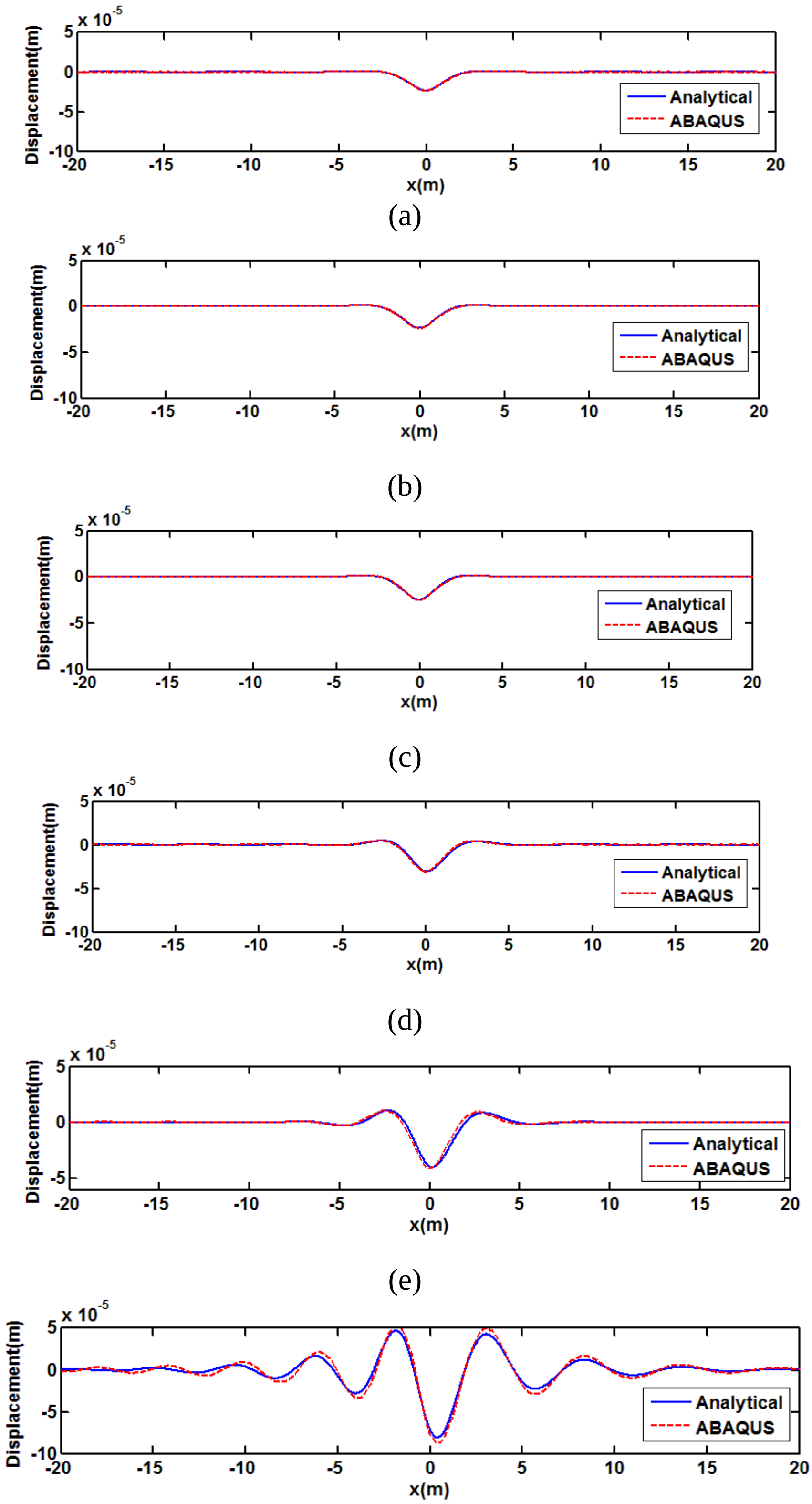

(a)

(b)

(c)

(d)

(e)

(f)

Figure 4-18. Displacement of the rail on Winkler foundation with different load speeds; E_s=20MPa, $\xi = 0.045$ (a) 50 m/s; (b) 100 m/s; (c) 200 m/s; (d) 400 m/s; (e) 500 m/s; (f) 600 m/s

As can be seen from Figs 4-19~4-21, the results near the ends change severely so they cannot be used as the convergence point. Therefore, 20% of the nodes from the right-hand end are neglected to determine the steady state. Omitting these points, the amplitude of the steady-state displacement is determined as the average over eight nodes that are 20% away from the end.

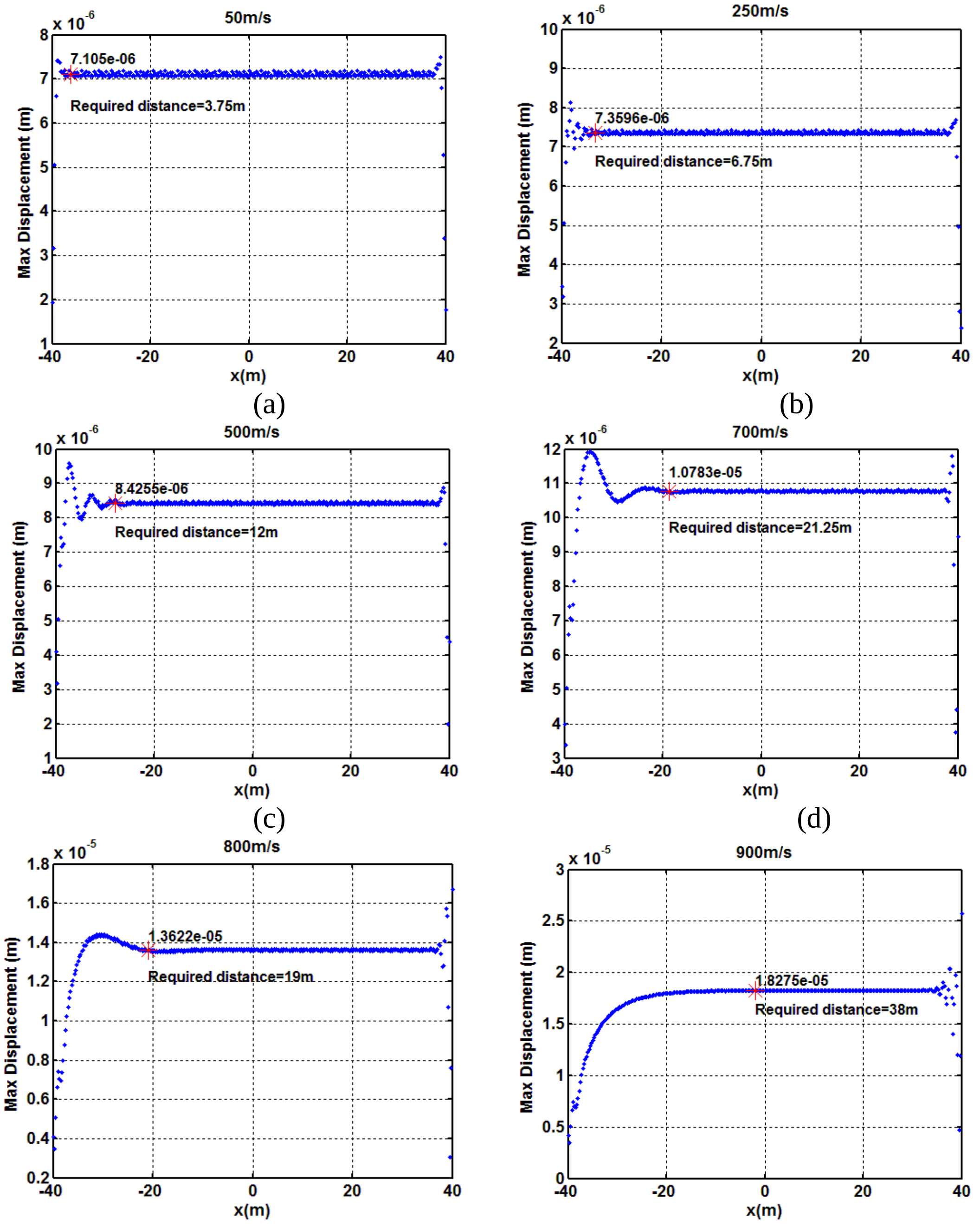

(a) (b)

(c) (d)

(e) (f)

Figure 4-19. Maximum displacement at different positions along the track during the simulation with E_s=100 MPa, for different load speeds; (a) V=50 m/s; (b) V=250 m/s; (c) V=500 m/s; (d) V=700 m/s; (e) V=800 m/s; (f) V=900 m/s

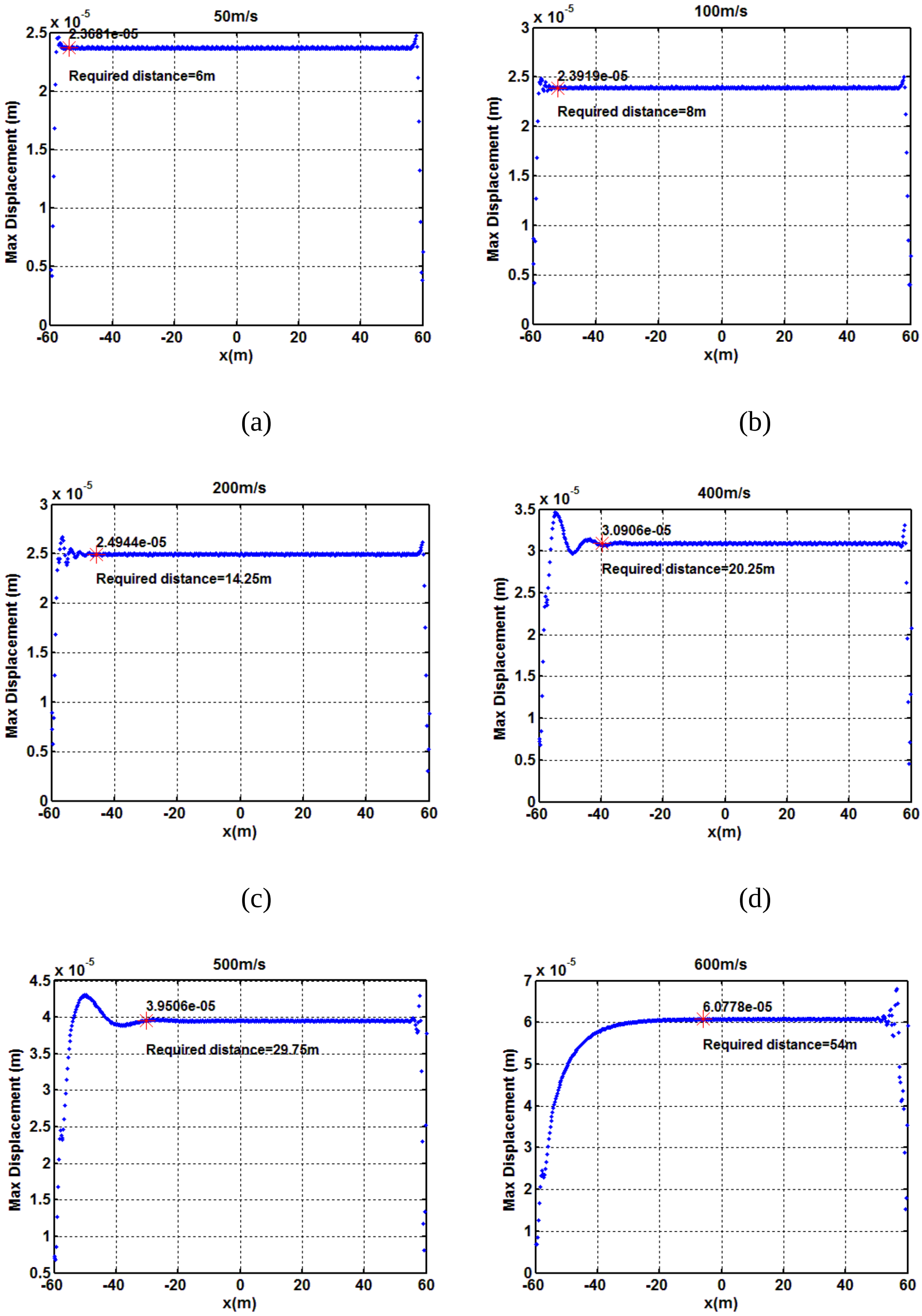

(a) (b)

(c) (d)

(e) (f)

Figure 4-20. Maximum displacement at different positions along the track during the simulation with E_s=20 MPa, $\xi = 0.1$, for different load speeds. (a) V=50 m/s; (b) V=250 m/s; (c) V=500 m/s; (d) V=700 m/s; (e) V=800 m/s; (f) V=900 m/s

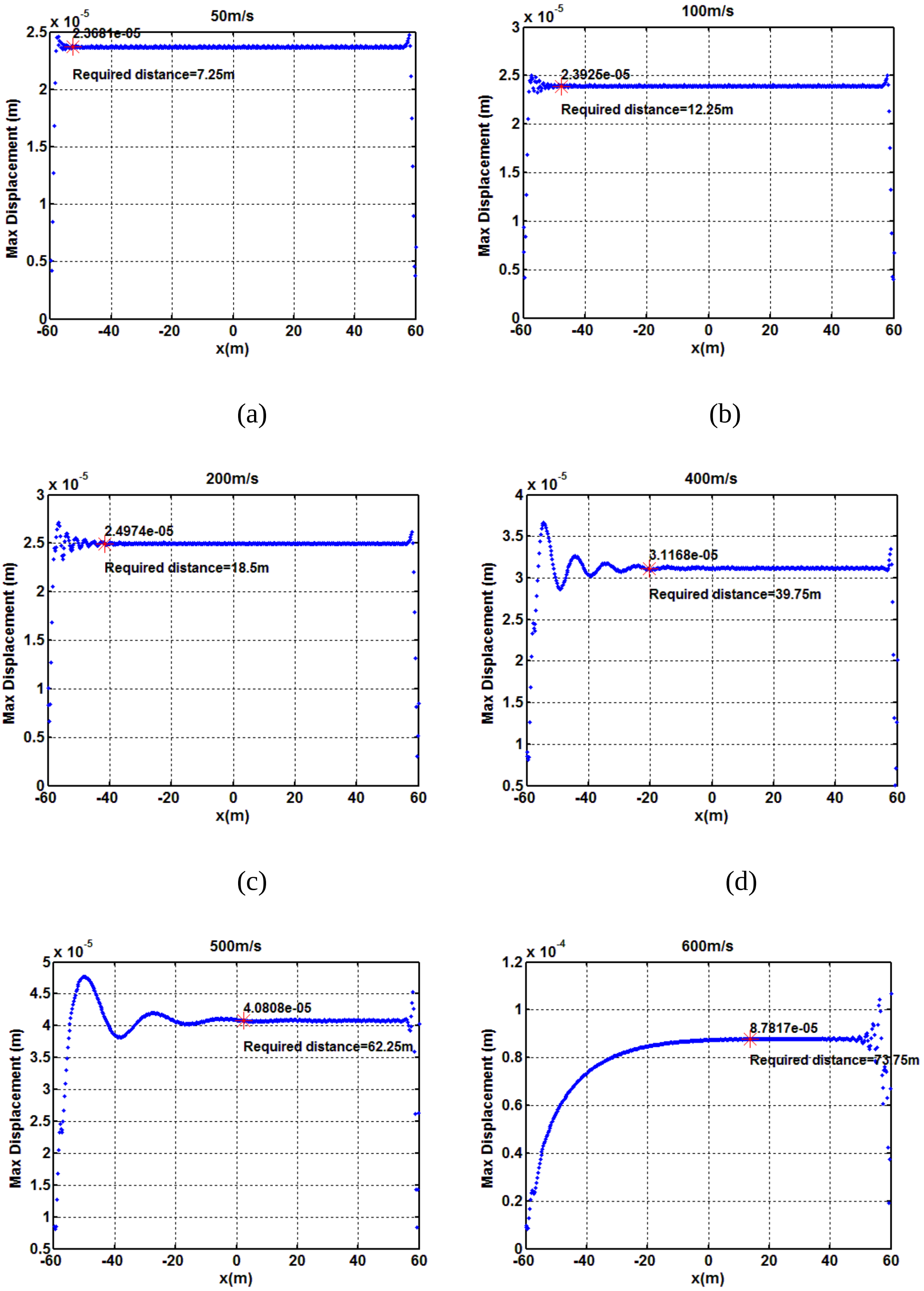

(a) (b)

(c) (d)

(e) (f)

Figure 4-21. Maximum displacement at different positions along the track during the simulation with E_s=20 MPa, $\xi = 0.045$, for different load speeds. (a) V=50 m/s; (b) V=250 m/s; (c) V=500 m/s; (d) V=700 m/s; (e) V=800 m/s; (f) V=900 m/s

As can be seen from Figs 4-19~4-21 even when the results have already converged, small oscillations still exist in the steady-state region. This is due to the fact the moving axle load is applied at the middle of the top surface of the rail; therefore, small differences occurs between the points at two edges and the middle of the rail top surface. The maximum and minimum value are therefore identified in the steady-state region. The position at which steady state is reached is then determined by comparing the mean of 8 consecutive nodes with the results in steady state. Steady state is assumed to have been reached when this difference is smaller than half the difference between the maximum and minimum values in the steady-state region.

These results are plotted in Fig. 4-22, in the form of the required distance from the left-hand end (i.e. the length of the transient zone), against the ratio of the load speed to the critical speed. Also plotted in Fig. 4-22(a)~(c) is the length of the waveform identified from Figs 4-16~18. The lengths of the transient zone from the three different track models are compared in Fig. 4-22(d).

At higher load speeds the required distances determined from the transient zone are greater than the length of the waveform, especially for the damping ratio of 0.045. These distances increase with increasing load speed. However, at low load speeds the length of the waveform tends to a constant value (see Eq. (4-2)) whereas the length of the transient zone tends to zero.

Large distances are required near the critical speed, especially for the model with the smaller damping ratio. However, the results for the two different foundation stiffnesses with damping ratio 0.1 differ by less than a factor of 1.5, as seen in Fig. 4-22(d).

This indicates that the required distance is more sensitive to the damping ratio than to the support stiffness. Furthermore, the effect of the transient is more important than the length of the waveform for most load speeds. Nevertheless, the length of the waveform has to be considered when the load speed is very low.

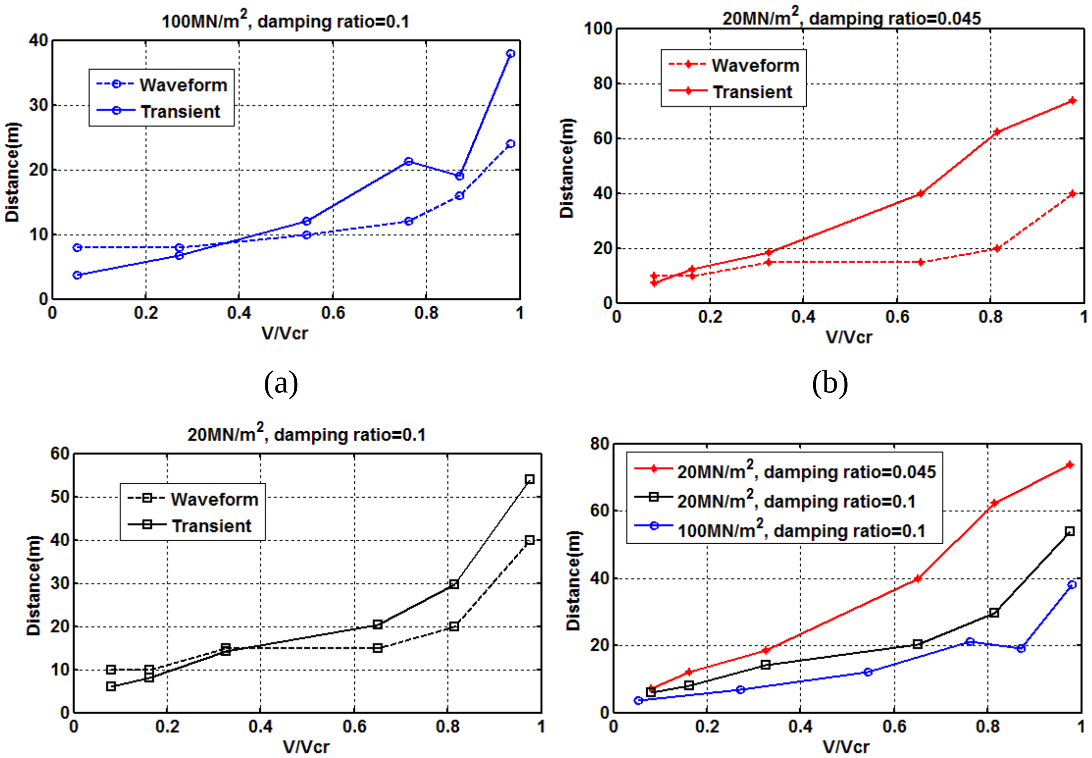

(a) (b)

(c) (d)

Figure 4-22. Distance requirements of the moving load problem: length of transient zone required for convergence to steady-state solution and length of waveform in the rail; (a) E_s=100 MPa, $\xi = 0.1$; (b) E_s=20 MPa, $\xi = 0.045$; (c) E_s=20 MPa, $\xi = 0.1$; (d) comparison of lengths of transient zone three different track models

4.4 Analysis of two-layer ballast track with moving dynamic loads

Due to the limitation of the commercial software for contact analysis in the space domain, as mentioned in Section 3.4.1, solid elements are used for modelling the rail. As a result, consideration of shear flexibility cannot be avoided when solid elements are used. However, beam elements have been commonly used for modelling the rail especially for lower frequency. The results up to this point have involved moving loads, which are restricted to very low frequencies. In this section, a 10 degree of freedom vehicle model, as shown in Fig. 4-23, is introduced running on the track in order to assess the results at higher frequencies. Vehicle/track dynamic interaction including rail irregularities is considered and compared against the results from a moving frame analysis (Nguyen et al., 2008) in order to further validate the contact procedure introduced in Section 3.2.2. Furthermore, two different beam elements, Euler-Bernoulli beam and Timoshenko beam, are compared in order to identify the influence of the consideration of shear flexibility.

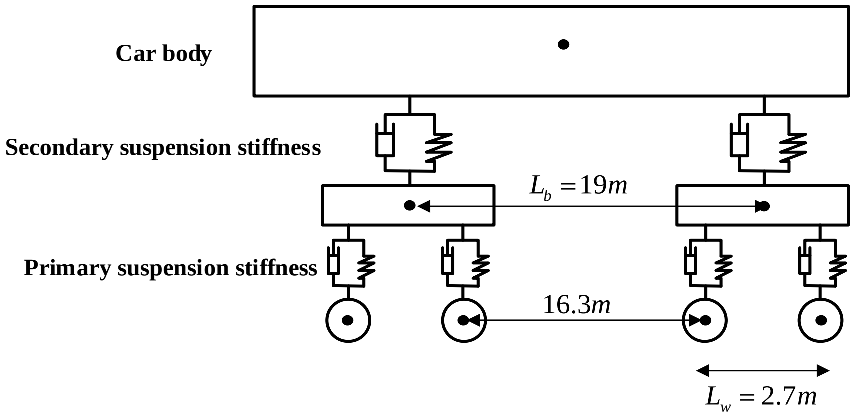

Figure 4-23. 10 degree of freedom vehicle model

The track model considered has a two-layer support, as shown in Fig. 4-11. The parameters of the vehicle model are shown in Fig. 4-23 and Table 4-6. The moving vehicle simulation is implemented here using the method introduced in Section 3.2 which does not require a user-defined subroutine. A 100 m long model is used and two moving load speeds, 19 m/s and 56 m/s, are considered. The element sizes for railpad, sleeper and ballast are 0.4 m, which are sufficient for frequencies up to 200 Hz (based on Eq. (4-4)). An implicit analysis is used with time step 0.001 s, which is more than sufficient for the maximum frequency of interest of 200 Hz.

Table 4-6 Vehicle properties

Vehicle components	value s	units
Mass of car body, M_c	40000	kg
Moment of inertial of car body, J_c	2x10^6	kgm^2
secondary suspension stiffness, K_2	600	kN/m
secondary suspension damping, C_2	20	kNs/m
primary suspension stiffness, K_1	2400	kN/m
primary suspension damping, C_1	30	kNs/m
Mass of bogie M_b	5000	kg
Moment of inertial of bogie, J_b	6000	kgm^2
Mass of wheel, M_w	1800	kg

As well as the moving loads, a random rail roughness is introduced, with frequency content between 2 and 200 Hz. Random roughness is generated as the superposition of cosine functions with random phase angles in the interval [-π π]. Rail roughness generated for two different speeds in the spatial domain and displacement spectrum can be seen in Fig. 4-24~25. It is implemented in the FE model by adding the height of the roughness to the vertical coordinates of the nodes at the top of the rail. A Python code has been developed in order to generate the rail roughness. In order to give sufficient spatial resolution to represent the roughness, the rail element size is set to 0.019 m for the speed of 19 m/s, and 0.056 m for 56 m/s. The results are compared with those obtained using a moving frame model with discrete sleeper support, which has less influence from the boundary than other FE models (Nguyen et al., 2008). [1]

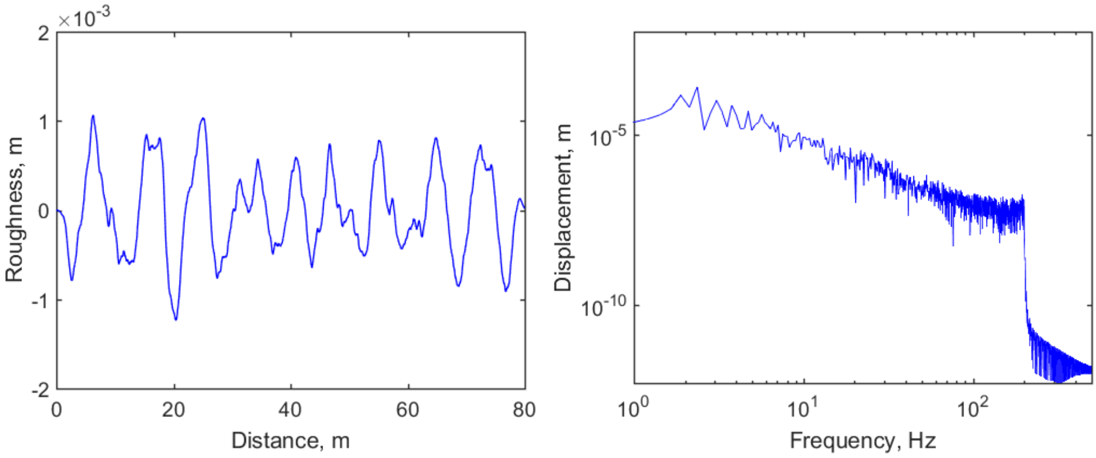

Figure 4-24. Rail roughness used for load speed 19 m/s; (a) roughness in spatial domain; (b) roughness spectrum

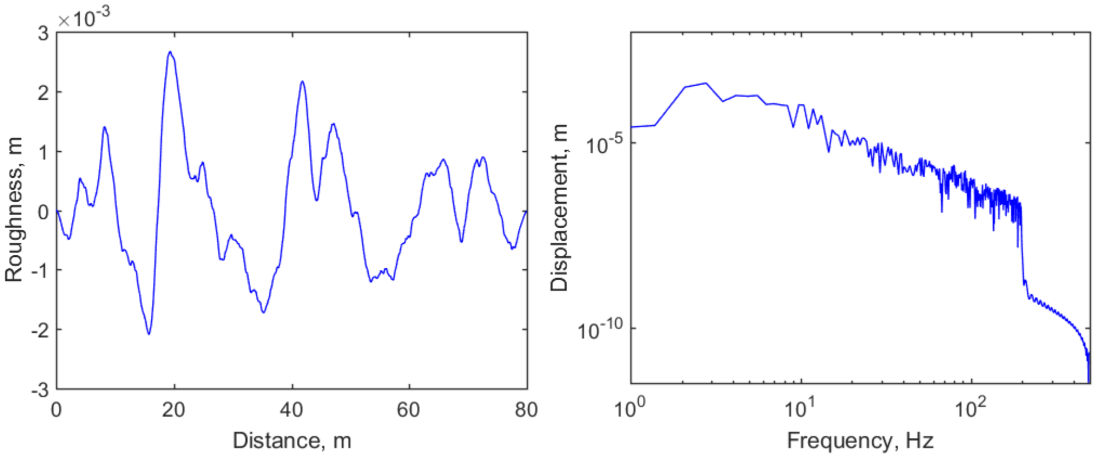

Figure 4-25. Rail roughness used for load speed 56.67 m/s; (a) roughness in spatial domain; (b) roughness spectrum

The parameters used for the two different track models are listed in Table 4-7. The two rails are represented by a single beam in these models. To convert from the parameters used for the model with discrete sleepers to those for the continuous support, the

---

[1] Simulations using moving FEM have been done by Dr. Samuel Koroma, former research fellow at University of Southampton.

equivalent ballast and railpad stiffness and mass per unit length are obtained by dividing by the sleeper spacing. Non-proportional viscous damping is used in the discrete sleeper track model whereas Rayleigh damping is used for continuous sleeper track model. To equate these, the damping ratio for the viscous damping model can be determined approximately at the resonance frequencies. The two resonance frequencies can be estimated by (Thompson, 2009)

$$\begin{aligned}\omega_{c1} &= \sqrt{\frac{s_b}{m_s' + \rho A}} \\ \omega_{c2} &= \sqrt{\frac{s_p}{\rho A}}\end{aligned} \tag{4-8}$$

where s_b is the ballast stiffness per unit length; s_p is the railpad stiffness per unit length; ρA is the rail mass per unit length; m_s' is the sleeper mass per unit length. Based on the first cut-on frequency, an equivalent ballast damping ratio can be calculated by

$$\xi_b = \frac{c_b}{2L_s(m_s + m_b)\omega_{c1}} \tag{4-9}$$

where, c_b is the damping coefficient for discrete sleeper model and L_s is the sleeper spacing. Similarly for the railpad damping coefficient, the damping ratio can be calculated by

$$\xi_p = \frac{c_p}{2L_s \rho A \omega_{c2}} \tag{4-10}$$

where c_p is the damping coefficient for discrete sleeper model. To define the Rayleigh damping, the two parameters α , β , are defined using

$$\alpha = \frac{2\xi_i \omega_{c1}\omega_{c2}}{\omega_{c1} + \omega_{c2}}; \beta = \frac{2\xi_i}{\omega_{c1} + \omega_{c2}} \qquad i = b, p \tag{4-11}$$

where ω_{c1} and ω_{c2} are two frequencies used for the fitting. Here 2 and 200 Hz are used to cover the frequency range from the rail roughness. Railpad and ballast Rayleigh damping can then be determined by combining Eq. (4-9) and Eq. (4-11), and Eq. (4-10) and Eq. (4-11), respectively.

The results are presented for four wheelsets moving over the track. However, due to the fact that the model is assumed to be linear, the simulation results for moving dynamic loads are determined by combining the results from moving quasi-static axle loads and moving dynamic loads in order to increase the efficiency. The vehicle system is not considered for the moving quasi-static load analysis. The axle loads, which are each one-quarter of the total weight of the vehicle, are applied on the rail at the position of the four wheelsets. On the other hand, the vehicle system and the rail roughness are considered for the dynamic load analysis but without consideration of the axle load. This allows the response to the two components of load to be studied separately.

Table 4-7 Two-layer support properties for continuous and discrete sleeper models (models represent two rails)

	Continuous sleeper model		units	Discrete sleeper model	units
Railpad stiffness	350×10^6		N/m^2	210×10^6	N/m
Railpad damping	α	76		18.4×10^3	Ns/m
	β	6.182×10^{-5}			
Ballast stiffness	315×10^6		N/m^2	189×10^6	N/m
Ballast damping	α	253	Ns/m^2	132×10^3	Ns/m
	β	2.06×10^{-4}			
Ballast mass	580		kg/m	1044	kg
Sleeper mass	490		kg/m	294	kg
Sleeper Young's modulus	10^{10}		N/m^2	-	
Sleeper spacing	-		-	0.6	m

4.4.1 Numerical results from moving vehicle simulation

The time domain results obtained using the current FE model with either Euler-Bernoulli beam elements or Timoshenko beam elements are compared with the results from the moving frame approach (which uses Euler-Bernoulli beam elements). Figs 4-26~27 show the rail displacement obtained from the moving quasi-static and moving dynamic loads at load speeds 19 m/s and 56 m/s when Euler-Bernoulli beams are used. Good agreement is found for in each case. The corresponding results obtained with Timoshenko beam elements are compared with the moving FEM in Figs 4-28~29. Again good agreement is found.

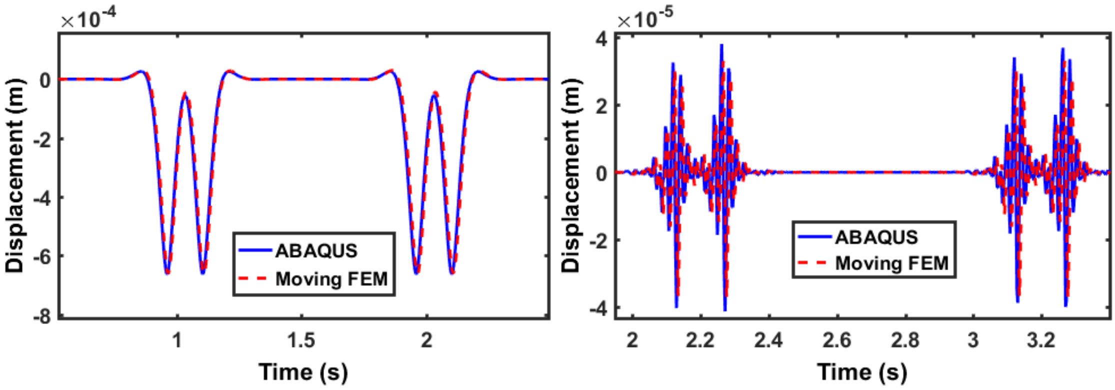

(a) (b)

Figure 4-26. Comparison with moving frame results in the time domain at load speed 19 m/s (Euler-Bernoulli beam) (a) quasi-static loads; (b) dynamic loads

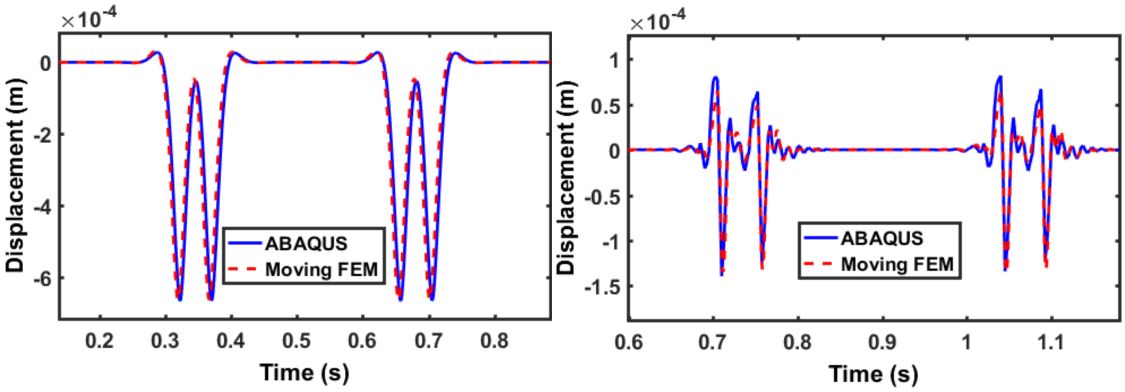

(a) (b)

Figure 4-27. Comparison with moving frame results in the time domain at load speed 56 m/s (Euler-Bernoulli beam) (a) quasi-static loads; (b) dynamic loads

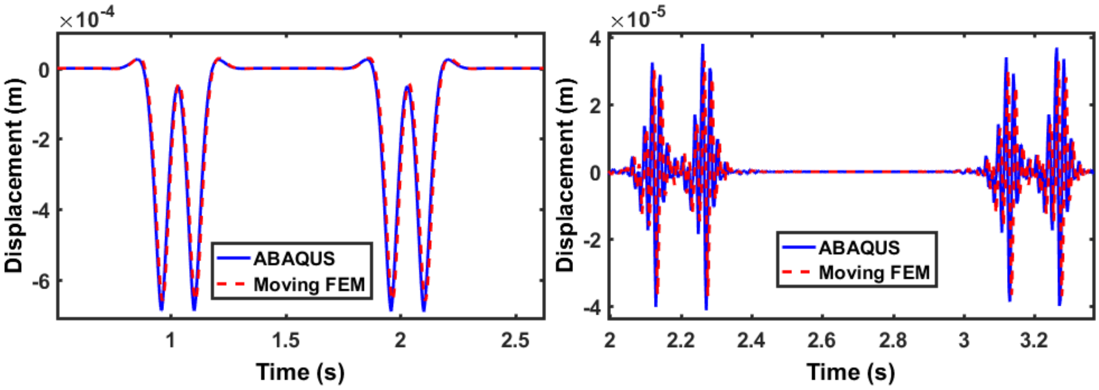

(a) (b)

Figure 4-28. Comparison with moving frame results in the time domain at load speed 19 m/s (Timoshenko beam) (a) quasi-static loads; (b) dynamic loads

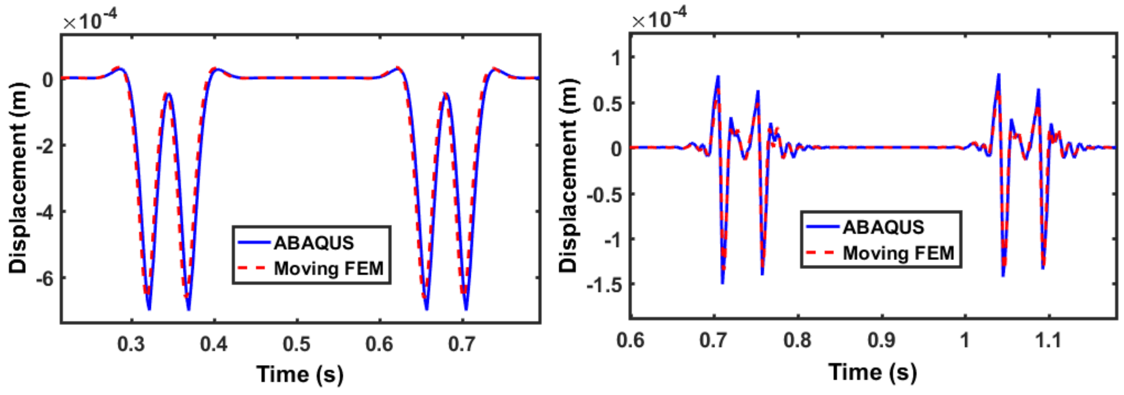

(a) (b)

Figure 4-29. Comparison with moving frame results in the time domain at load speed 56 m/s (Timoshenko beam) (a) quasi-static loads; (b) dynamic loads

The results obtained in the time domain are also transformed to the frequency domain using a Fast Fourier transform (FFT). The results are shown in Figs 4-30~31. Good agreement is found between the various results up to about 20 Hz for 19 m/s and 60 Hz for 56 m/s. A clear dip can be found in the frequency domain results for the moving axles loads at around 30 Hz for a load speed of 19 m/s and 100 Hz for a load speed of 56 m/s for the discrete sleeper model. These frequencies correspond approximately to the sleeper passing frequency in each case. The result from ABAQUS does not show this feature because continuous sleeper are used.

Although the time domain results are almost identical when using the two different beam elements, the results from the moving load analysis are different at higher frequency. The results obtained using the Timoshenko beam tend to increase above a certain frequency. Furthermore, at higher speeds, the frequency at which the models diverge tends to increase, as can be seen by comparing Fig. 4-30(a) and Fig. 4-31(a). This difference is surprising as the differences between the two models are usually considered to be significant only above 500 Hz.

In the spatial domain the difference between the two results occurs in the region close to load point. Fig. 4-32 shows an example of the rail deflection in the vicinity of the load point. The Timoshenko beam theory allows a discontinuity in the second derivative of the displacement at the load point which leads to a sharp dip in the response. This is responsible for the high frequency component seen in the Fourier transform in Fig. 4-30(a) and Fig. 4-31(a). However, it is believed that this behaviour should be not realistic, especially when the wheel/rail contact force is applied over a contact area rather than at point. As a result, the Euler-Bernoulli beam is suggested for this type of simulation.

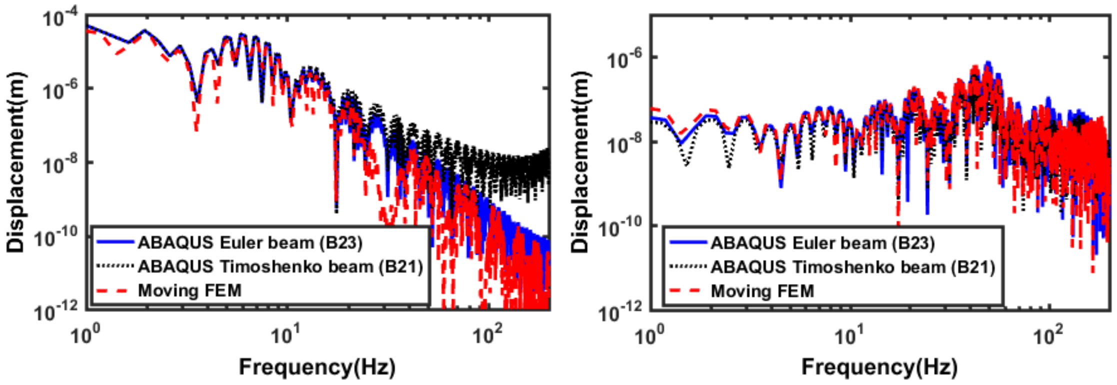

(a) (b)

Figure 4-30. Comparison with moving frame results after FFT at load speed at 19 m/s (a) Quasi-static loads; (b) dynamic loads

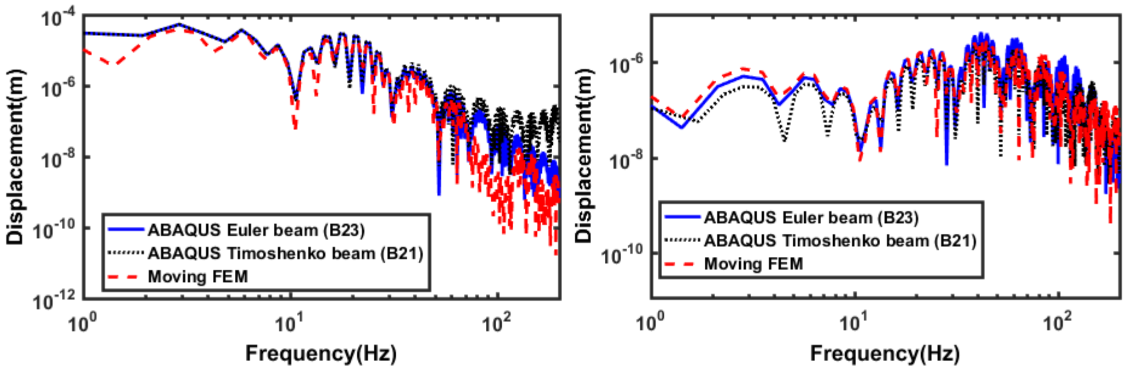

(a) (b)

Figure 4-31. Comparison with moving frame results after FFT at load speed 56 m/s (a) Quasi-static loads; (b) dynamic loads

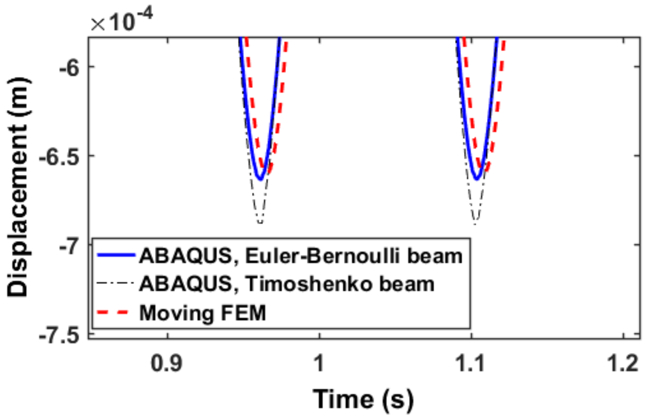

Figure 4-32. Rail deflection at position of applied axle load for load speed 19 m/s

Fig. 4-33 shows the ratio between the results from Timoshenko and Euler-Bernoulli beams for the moving axle loads plotted against the deflection wavelength, i.e. *V*/*f*. From this, it can be seen that the differences between the models occur when the wavelength is smaller than around 1 m for both speeds. This confirms that it is related to the deformation under the load and not to any dynamic effects.

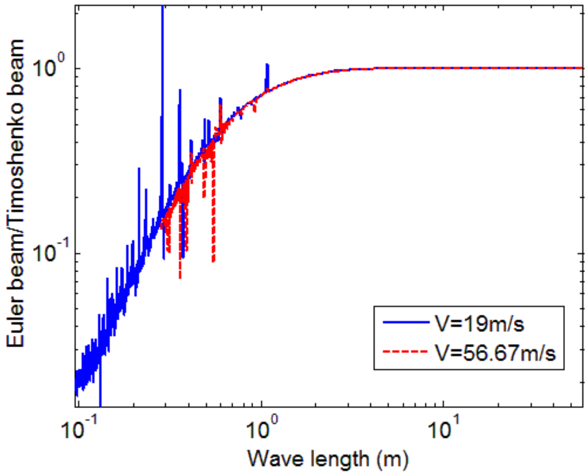

Figure 4-33. Ratio between the results from Timoshenko and Euler-Bernoulli beam models for moving axle loads plotted against deflection wavelength

Small differences are found between the results from the Euler-Bernoulli and Timoshenko beam in the time domain for both moving constant loads and moving dynamics loads. However, significant differences can be found in the frequency domain above a certain frequency for moving load analysis. As a result, in further simulations care is needed in order to avoid the artificial high frequency components.

4.5 Three-dimensional ballasted track model using ABAQUS

The results presented so far in this chapter have involved static harmonic loads, moving constant loads and moving dynamic loads for one-layer and two-layer support. However, the ballast has been represented by a continuous elastic layer which is difficult to capture the real stress distribution from the excitation force. A more realistic three-dimensional track model is introduced here which will form the basis of the models used with the ground in subsequent chapters.

The focus of the present section is to validate the three-dimensional model for further simulation. Only static harmonic loading is considered. Results for moving loads and moving dynamic loads will be presented for the track in combination with ground models in the following chapters.

Two different three-dimensional track models are considered here. These are a continuous sleeper track model (See Fig. 4-34), and a discrete sleeper track (See Fig. 4-35). In each case only a single rail is included, with a symmetry plane assumed along the track centreline. The results are compared with the results from a two-layer support analytical model as discussed in Section 4.2 with the parameters listed in Table 4-3. In order to compare the results with those from the analytical model, which is a 2D continuous model, equivalent parameters need to be specified for these three 3D ballasted track models, which will be discussed in the following sections. Results are shown for both the continuous and discretely supported track models with lengths of 20 m. A harmonic force is applied at the centre of the track length.

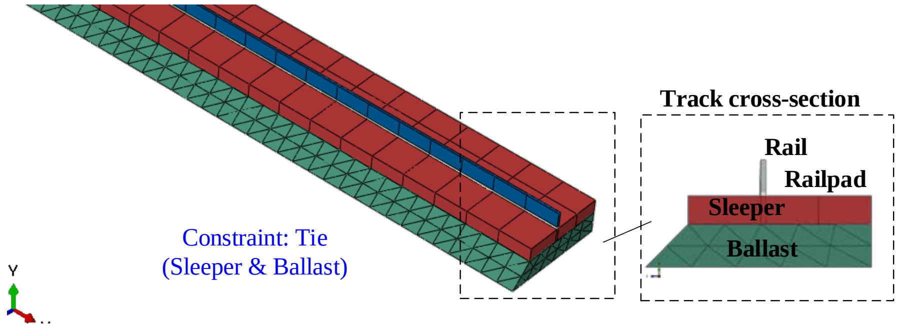

Figure 4-34 Three-dimensional continuous ballasted track model

4.5.1 Three-dimensional ballasted track model with continuous sleepers

For the 3D continuously supported track model, shown in Fig. 4-34, the railpads and sleepers are represented by equivalent continuous models. 20-node fully integrated brick elements (C3D20) are used for the rail, railpad and sleeper, as discussed in Section 3.4. The largest node spacing is 0.25 m, which is sufficient for frequencies up to around 1280 Hz for rail and 877 Hz for sleeper, based on Eq. (4-4). Four-node tetrahedral elements (C3D4) are used for the ballast for compatibility with the spherical ground model used in Chapter 5. Tie constraints are used between the railpad and sleeper and between the sleeper and ballast as this provides a simple way to bond the surfaces together by setting master-slave formulations when the element geometry does not match, e.g. when combining track and hemispherical ground models (see Chapter 5). This constraint prevents the slave nodes from separating or sliding relative to the master surface; therefore, there are no relative displacements between the two surfaces. The geometry of the rail and railpad is the same as introduced in Section 4.3.1, in which the rail is represented by an equivalent rectangular cross-section with the same mass and bending stiffness as the UIC60 rail. Isotropic materials are used for the whole track model except for the sleepers and railpad. Although the equivalent sleeper layer is continuous along the axial direction, it should have no bending stiffness in this direction. Therefore, it is modelled using an orthotropic material. On the other hand, an isotropic material is used for the railpad in the continuous sleeper model but orthotropic elements are used in the discrete sleeper model. A more detailed discussion is given in Section 4.5.3.

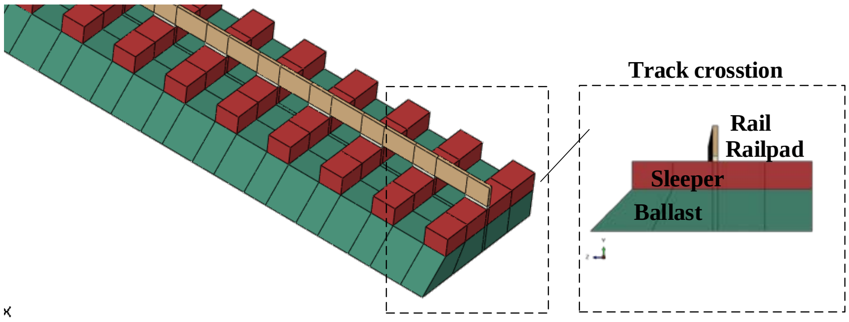

Figure 4-35 Three-dimensional discrete support ballasted track model using solid element for railpad

The same parameters listed in Table 4-3 are used here except those used for the sleepers and ballast. The equivalent sleeper density can be easily calculated by

$$\rho_s' = m_s' / (h_s L_{sl}) \tag{4-12}$$

where m_s' is the sleeper mass per unit length ($\rho_s h_s L_{sl} L_w / L_s$) and h_s, L_{sl} are the height and half length of the sleeper. The equivalent Young's modulus of the sleeper E_s' is calculated by multiplying the Young's modulus by the width of the sleeper and dividing by the sleeper spacing. For the ballast, the equivalent Young's modulus can be determined by

$$E_b' = \frac{2 s_b h_b}{w_{b1} + w_{b2}} \tag{4-13}$$

where s_b is the ballast stiffness per unit length, L_w is the sleeper spacing, w_{b1} and w_{b2} are half the top and bottom widths of the ballast layer. Furthermore, ballast mass is included. The parameters of the continuous 3D ballasted track are listed in Table 4-8.

Table 4-8. 3D continuous ballasted track properties

Parameter	Value	Units
Rail mass density, ρ_r	7850	kg/m^3
Rail Young's modulus, E_r	2.1x10^{11}	N/m^2
Rail area, A_r	0.00763	m^2
Rail second moment inertia, I	3.055 x10^{-5}	m^4
Railpad Young's modulus, E_p'	300x10^6	N/m^2
Railpad loss factor, η_p	0.2	
Sleeper equivalent mass density, ρ_s'	961.5	kg/m^3
Sleeper equivalent Young's modulus (E_{sy} , E_{sz})	1.15x10^{10}	N/m^2
Sleeper E_{sx}	0	N/m^2
Sleeper Poisson's ratio, v_s	0.15	
Sleeper height, h_s	0.2	m
Sleeper length (half), L_{sl}	1.3	m
Ballast Young's modulus, E_b'	20.69x10^6	N/m^2
Ballast Poisson's ratio, v_b	0.33	
Ballast top length (half), w_{b1}	1.3	m
Ballast bottom length (half), w_{b2}	1.6	m
Ballast height, h_b	0.3	m
Ballast mass density, ρ_b	2000	kg/m^3
Ballast loss factor, η_b	1.0	
Rail gauge (half)	0.7	m

4.5.2 Three-dimensional ballasted track model with discrete sleepers

A discretely supported ballasted track can be readily developed by following a similar approach but including discrete sleepers, as shown in Fig. 4-35. 20-node fully integrated brick elements (C3D20) are used with a maximum node spacing of 0.25 m (this size should be sufficient for frequencies up to 1280 Hz for rail and 877 Hz for sleeper). The parameters of the 3D discrete sleeper track are listed in Table 4-9.

The Young's modulus for the railpad can be determined from the value used in the continuous model divided by the width of the sleeper and multiplied by the sleeper spacing. The sleeper mass density can be calculated by dividing its mass by its volume. For the ballast, the equivalent Young's modulus can be calculated by

$$E_b = \frac{2s_b h_b L_s}{(L_w + c)(w_{b1} + w_{b2})} \tag{4-14}$$

Table 4-9. 3D discrete sleeper ballast track properties

Parameter	Value	Units
Rail mass density, ρ_r	7850	kg/m^3
Rail Young's modulus, E_r	2.1x10^{11}	N/m^2
Rail area, A_r	0.00763	m^2
Rail second moment inertia, I	3.055x10^{-5}	m^4
Railpad Young's modulus, E_p	780 x10^6	N/m^2
Railpad damping loss factor, η_p	0.2	
Sleeper mass density, ρ_s	2500	kg/m^3
Sleeper Young's modulus, E_s	3x10^{10}	N/m^2
Sleeper Poisson's ratio, v_s	0.15	
Sleeper width, L_w	0.25	m
Sleeper height, h_s	0.2	m
Sleeper length (half), L_{sl}	1.3	m
Sleeper spacing, L_s	0.65	m
Ballast Young's modulus, E_b	2.6 E_b' (c=0)	N/m^2
	1.18 E_b' (c=0.3)	
	E_b' (c=0.4)	
Ballast Poisson's ratio,	0.33	
Ballast top width (half),	1.3	m
Ballast bottom width (half),	1.6	m
Ballast height,	0.3	m
Ballast mass density,	2000	kg/m^3
Ballast loss factor,	1.0	
Rail gauge (half)	0.7	m

where L_s is the sleeper spacing, s_b is the ballast stiffness per unit length of track. L_w is the width of the sleeper in the direction along the track, w_{b1} and w_{b2} are half the top and bottom length of the ballast in the direction perpendicular to the track. h_b is the height of the ballast. *c* is a correction to allow for load spreading beneath the sleeper in the direction along the track, different values of which will be considered.

4.5.3 Numerical results

The three-dimensional track model is validated against the analytical model (Thompson, 2009). However, ballast mass and sleeper bending stiffness are not considered in the analytical model. As a result, in order to compare with the results from the analytical model, a smaller mass density for ballast and a stiffer sleeper are required to achieve better agreement. Firstly, the results from the continuous sleeper model are compared with the results from the analytical model. Investigation of the ballast density and the sleeper flexibility is discussed in Section 4.5.3.1. The results from the model with discrete sleepers with consideration of ballast density and sleeper flexibility are then compared with the results from the continuous sleeper model in Section 4.5.3.2. Finally, investigation of the correction factor, *c*, is discussed and this model is then used for further simulations.

4.5.3.1 Results from continuous sleeper model

Fig. 4-36 shows the point receptance for the continuous track model (red dashed line) which is compared with the receptance obtained from the analytical model (Thompson, 2009). Good agreement can be seen at low frequency, below around 80 Hz. However, the first cut-on frequency occurs at about 80 Hz, which is lower than the result from the analytical model. This is because the ballast density is not considered in the analytical model. Better agreement can be seen if the ballast density is set to a very low value in the 3D model, as shown by the black dash-dot line. However, the second cut-on frequency at around 350 Hz still does not match well. This is due to the bending of the sleeper. If a much stiffer sleeper model is used to avoid this behaviour (by multiplying the Young's modulus of the sleeper by 100, as shown by the pink line) better agreement can be found.

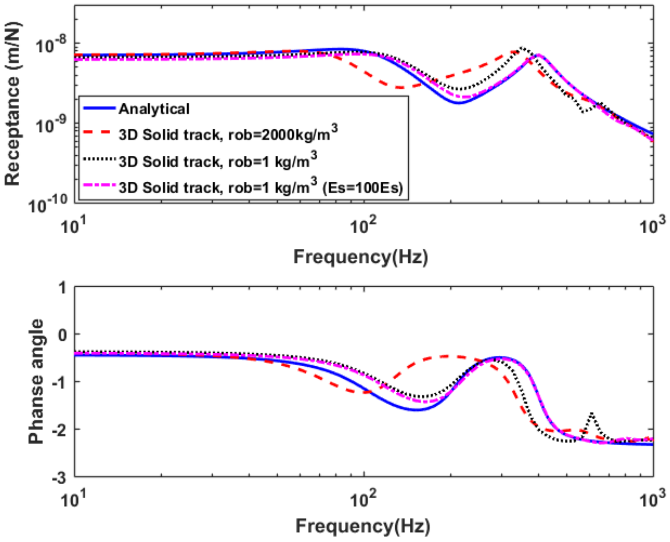

Figure 4-36. Point receptance from 3D continuous sleeper ballast track compared with analytical results

4.5.3.2 Results from discrete sleeper model

The results from the discrete sleeper model using two different values of ballast stiffness are shown in Fig. 4-37. These values are chosen by assigning different values to the correction term *c*. Compared with the analytical model, the ballast tends to be too stiff if *c*=0 is used in Eq. (4-14). Small differences can be found when *c*=0.4 is used. Better agreement can be seen when the correction is set to *c*=0.3, which corresponds to 63.4° “cone angle” in the ballast. Furthermore, by using *c*=0.3 the ballast Young’s modulus becomes very close to the value used for the continuous model. The results below 100 Hz are almost identical. However, some differences can be found between 140~320 Hz. From this it can be concluded that the parameters listed in Table 4-9 can be used for the further investigations, with the ballast Young’s modulus determined using the correction *c*=0.3, giving a similar value to that used in the continuous model.

Fig. 4-38 compares results for the discrete sleeper model in which two different element types are used for the railpad, isotropic and orthotropic. When the orthotropic elements are used for the railpad, only the vertical stiffness has its original value, with the stiffness in the other directions set to very small values. The results are almost identical. In order to investigate further the difference between isotropic and orthotropic railpad models, results are shown in Fig. 4-39 for different ballast stiffnesses and railpad stiffnesses. Very small differences are found between the results for orthotropic and isotropic elements in all cases. As a result, it appears to be sufficient to use isotropic elements for the railpad. Nevertheless, as will be discussed in Section 6.6, significant differences are found for track/ground interaction modelling.

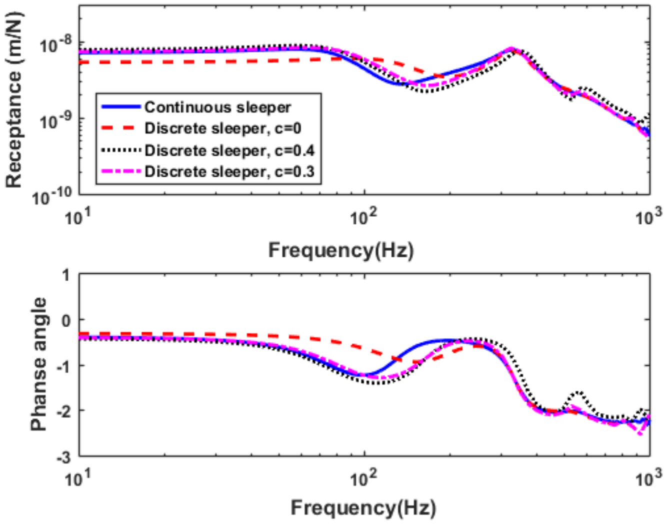

Figure 4-37. Comparison between continuous and discrete sleeper track model with different correction factors for the ballast stiffness

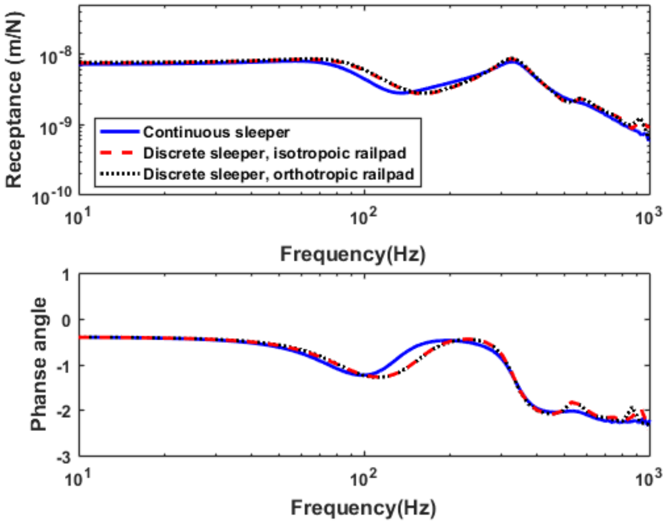

Figure 4-38. Comparison between results for discrete sleepers with orthotropic and isotropic elements for the railpad against the continuous sleeper model (c=0.3)

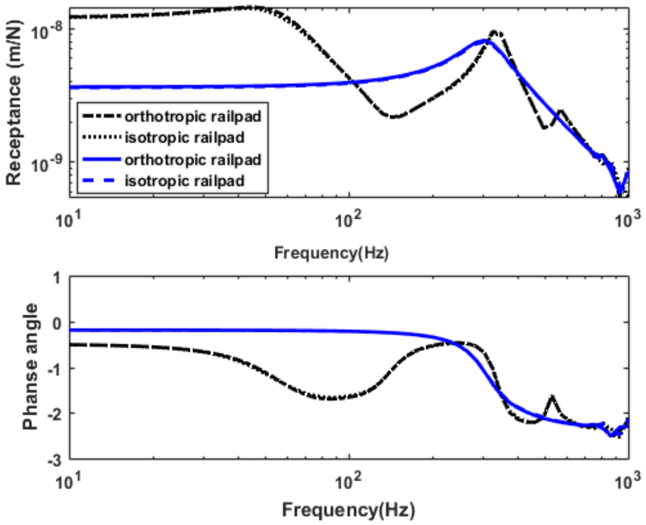

Figure 4-39. Comparison between results for orthotropic and isotropic railpad elements

The first and second cut-on frequencies of the various models are obtained by identifying the peaks in the receptance curves. Two cut-on frequencies from various models are listed in Table 4-10. The cut-on frequencies from the 3D ballast models are lower than those from the analytical results. The cut-on frequencies from the 3D discrete ballast model with either orthotropic or isotropic railpad elements are similar to the results from the continuous model, with only a slight difference for the first cut-on frequency.

Table 4-10. Cut-on frequencies from different track models

	First cut-on frequency, Hz	Second cut-on frequency, Hz
Analytical model	83	403
3D solid continuous model	56	330
3D solid discrete model (isotropic railpad)	61	330
3D solid discrete model (orthotropic railpad)	61	330

4.6 Summary

In this chapter, a method of modelling the track system in ABAQUS has been introduced. The dynamic responses for an Euler-Bernoulli beam with a single-layer and two-layer support excited by a stationary harmonic load have been compared with results from an analytical model. Good agreement is found for frequencies up to around 200 Hz. The length of the track model required to prevent influence from the reflections at the boundary has been investigated. A 10 m long model gives acceptable results up to 200 Hz. The first and second cut-on frequencies agree very well with the analytical model.

The response to a moving load has been studied for the track with a single-layer support. The minimum length of track required for convergence of the moving load problem in the time domain has been investigated. This shows that allowing for the transient effect requires a greater length of model than the length of the waveform at higher speeds. The required model size will be considered further in the next chapter for modelling the ground/track interaction.

To study a moving dynamic load, a 10 degree of freedom vehicle model has been coupled to a track with a two-layer support. The results are compared with those from a moving FEM model. Relatively good agreement is found. A comparison of Euler-Bernoulli and Timoshenko beam formulations indicates that the Timoshenko beam introduces some unrealistic higher frequency components associated with deflection wavelengths smaller than 1 m.

Two three-dimensional models of the track, with continuous and discrete sleepers, have been developed and compared. Good agreement is found between the results with continuous sleepers and the analytical results for a two-layer support provided that the ballast density in the FE model is neglected. However, inclusion of the ballast mass has a significant effect for frequencies between 80 and 400 Hz. The first and second cut-on frequencies of the rail are reduced if the ballast mass is included. Furthermore, some differences are identified as being related to the flexibility of the sleeper in the FE model.

Small differences are found between the results from the continuous and discrete sleeper models. The results below 100 Hz are almost identical provided that appropriate values are used for the support parameters. In particular, it is found that the Young’s modulus for the ballast should be similar in the two models. For the railpads, the results are identical when using isotropic or orthotropic elements.

These two 3D track models, with discrete sleepers and continuous sleepers, including the ballast density and sleeper flexibility, will be included in the track/ground interaction model with moving load in Chapters 5~7.

Chapter 5: Three-dimensional ground/track model based on hemispherical mesh

5.1 Introduction

The numerical simulation of the dynamic response of an infinite ground requires suitable boundaries to avoid spurious reflections from the edges of the model. Finite elements together with infinite elements are used here for modelling the response to moving loads. The concept of infinite elements was first introduced in Section 2.3.2. They are described in more detail in Section 5.2 and the method of combining infinite elements with finite elements in ABAQUS is presented in Section 5.3. Factors that influence the accuracy of the simulations, such as the size of the model and meshing strategy used are then discussed in Section 5.4~5.8. Finally, the results will be compared with the results from the wavenumber FE/BE method (Sheng, Jones, and Thompson, 2005).

5.2 Infinite elements

Finite elements can be used in combination with infinite elements to allow unbounded problems to be modelled without reflections from the domain boundaries. P-waves, S-waves, and even Rayleigh surface waves and Love waves, that are incident on the boundary can be modelled properly for plane and non-plane wave problems. Nevertheless, non-linear behaviour cannot be considered in the far field using infinite elements; if non-linear effects are present they should be included in the finite domain by using finite elements (“Abaqus Theory Manual v6.12,” 2013; “Abaqus 6.13-Analysis User’s Guide: Volume IV: Elements”).

The locally absorbing boundary based on the formulation by (Lysmer et al., 1969) is used for the infinite elements in ABAQUS. The incident waves are absorbed on the boundary by many infinitesimal dashpots which are orientated normal and tangential with respect to the boundary. To define the distributed equivalent dampers on the boundary, incident propagating waves are considered normal to the boundary, including compressional (P-) waves and shear (S-) waves. The dampers can then be derived in terms of particle motion in the local coordinates (x, normal and y, z tangential) as

$$\begin{cases}\sigma_{xx}^{i}=-C_{Ni}\dot{u}_{x}^{i}\\ \sigma_{xy}^{i}=-C_{Ti}\dot{u}_{y}^{i}\\ \sigma_{xz}^{i}=-C_{Ti}\dot{u}_{z}^{i}\end{cases} \tag{5-1}$$

where σ_{xx} etc are stresses, $\dot{u}_x$ etc are velocities and the equivalent damping coefficient, C_{Ni}, C_{Ti} are given in Eq. (2-5). These expressions can be derived by the assumption of linear elastic stress-strain relations and zero wave reflection at the boundary for a normally incident plane wave.

5.3 Modelling the ground using finite/infinite elements in ABAQUS

A track/ground model is introduced in this section. It uses the three-dimensional track model with continuous sleepers from Chapter 4. The track properties with isotropic railpad are listed in Table 4-8 but the railpad stiffness is 5×10^8 N/m^2 and ballast Young's modulus is 4.8×10^8 N/m^2. This is coupled to the ground which is assumed initially to be a homogeneous half-space, as shown in Fig 5-1(a). Due to the interest later in soil nonlinearity, which is likely to be more significant if the ground is very soft, the ground properties, as shown in Table 5-1, are chosen to correspond to a very soft ground.

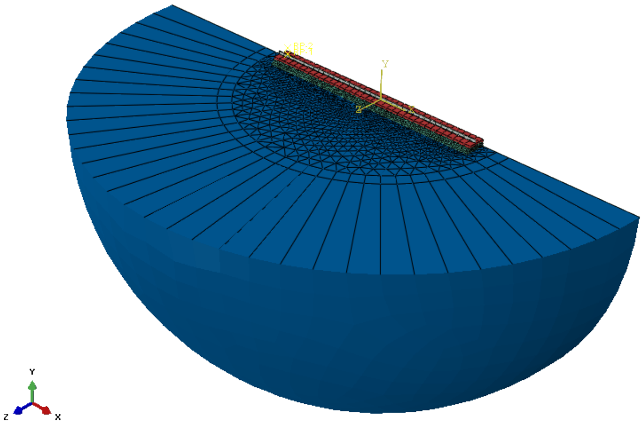

Figure 5-1 Half-space ground model

The ground is represented as a quarter sphere of finite elements surrounded by a layer of infinite elements, as shown schematically in Fig. 5-2. The track is arranged along the *x*-axis and use is made of symmetry in the *x*-*y* plane where *y* is the vertical direction. Eight-node brick elements (C3D8) and four-node tetrahedral element (C3D4) are used for the ground model and eight-node linear, one-way infinite elements (CIN3D8) are introduced on the boundary.

Table 5-1 Half-space Ground model properties

Young's Modulus, *E*	19.2 MN/m^2
Poisson's ratio, *v*	0.333
Rayleigh damping	$\alpha = 0,\ \beta = 0.000159\,\mathrm{s}$
Mass density, ρ	2000 kg/m^3
P-wave speed, c_p	120 m/s
S-wave speed, c_s	60 m/s

A hemispherical model is used due to the importance of the position of the nodes in the infinite elements with respect to the origin. Infinite elements only give perfect absorption for waves that impinge perpendicularly to the boundary ("Abaqus Theory Manual v6.12," 2013; Kouroussis, et al., 2011) Therefore, the hemispherical shape is usually preferred to a cuboid shape as it ensures that the vectors of the circular propagating wavefronts due to a point load are almost normal to the boundary, as shown in Fig. 5-2.

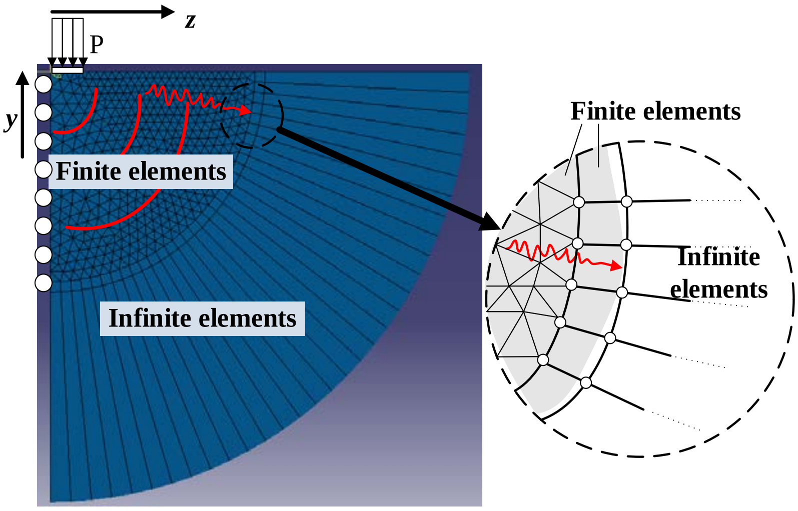

Figure 5-2 Schematic view of model geometry

For the hemispherical model tetrahedral elements are used in order to ensure better mesh quality. However, the infinite elements are brick elements which cannot be combined with tetrahedral elements. A layer of brick elements has therefore been created around the perimeter, as shown in Fig. 5-1. Additional constraints are applied between the surface of the region containing tetrahedral elements and the brick elements. It is time consuming to generate the whole model in ABAQUS/CAE and furthermore, the infinite elements are not supported in ABAQUS/CAE; they can be only specified by keyword. Therefore, a Python code has been developed to construct the geometry of the track, including rails, railpads, sleepers and ballast, and the ground. As well as the mesh, the material property definition is assigned via the Python code. The infinite elements are defined and combined with the finite element ground model automatically in the python code. The boundary and constraint conditions and the applied moving load with specific contact model are also implemented through the Python code.

Damping of the ground is often expressed in terms of a constant loss factor. However, for time domain models, such a model is non-causal. Here, therefore, a viscous damping model is used. The viscous damping in the FE models is modelled by Rayleigh damping, based on two parameters α , β . The mass damping can be derived by using $\beta = 0$ and it dominates the damping at lower frequencies, as shown in Fig. 5-3(a). On the other hand, the damping at higher frequencies is dominated by the stiffness damping, with $\alpha = 0$. Therefore, a constant damping ratio for a certain frequency can be approximately modelled by either taking α or β as zero, as shown in Fig. 5-3(a). Here the stiffness damping is used, as shown in Fig. 5-3(b). However, a constant loss factor was used in the wavenumber FE/BE method (Sheng et al., 2005) and will be used here for comparison with the current FE model. These two damping models are equivalent at only one frequency. A frequency of 50 Hz is used here in order to match the two damping models. The parameter β used in the FE model can be determined by

$$\alpha = 0, \qquad \beta = \frac{\eta}{\omega} \tag{5-2}$$

where ω is the frequency at which the loss factor η applies, in this case $2\pi \times 50$ rad/s. For $\eta = 0.05$ this gives β=0.000159 s.

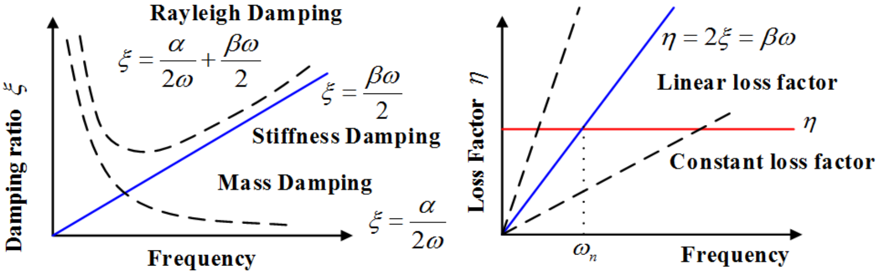

Figure 5-3 Relationship between Rayleigh damping parameters and loss factor

5.4 Additional displacement due to the unconstrained model

The results from three different sized models, with radius 10 m, 20 m, and 40 m, are compared. A moving load is applied on the rail and runs from the left to the right.

However, in order to have better initial contact condition between the moving node and rail surface, the moving load does not start from the end of the model. The starting points chosen are listed in Table 5-2. As can be seen these are different for different load speeds and model sizes. The reason for this is that, for lower speeds the calculation times become excessive if the whole length is used, whereas for higher speeds longer running lengths are needed to overcome transient effects.

Table 5-2 Starting point for different model sizes (radius *r*) and different load speeds

Load speed	*r*=10 m	*r*=20 m	*r*=40 m
10 m/s	-8 m	-8 m	-8 m
25 m/s	-8 m	-17 m	-17 m
40 m/s	-8 m	-17 m	-17 m
50 m/s	-8 m	-17 m	-37 m
57 m/s	-8 m	-17 m	-37 m
60 m/s	-8 m	-17 m	-37 m
70 m/s	-8 m	-17 m	-37 m
80 m/s	-8 m	-17 m	-37 m

The maximum downward displacements of each node along the rail during the movement of the load at different speeds are shown in Fig. 5-4. It can be seen that the overall displacement increases when the load speed becomes higher. As can be seen, the results from the smallest model increase significantly towards the boundary, whereas the maximum displacements are almost constant along the track for the larger size model. Other effects seen in these figures are discussed later.

Due to the characteristic of the infinite elements, which as has been seen correspond to viscous dampers, the ground model is unconstrained statically. Consequently, it is found that a moving constant load causes the whole ground to rotate and translate, as shown schematically in Fig. 5-5. However, this behaviour is not real and can give misleading results.

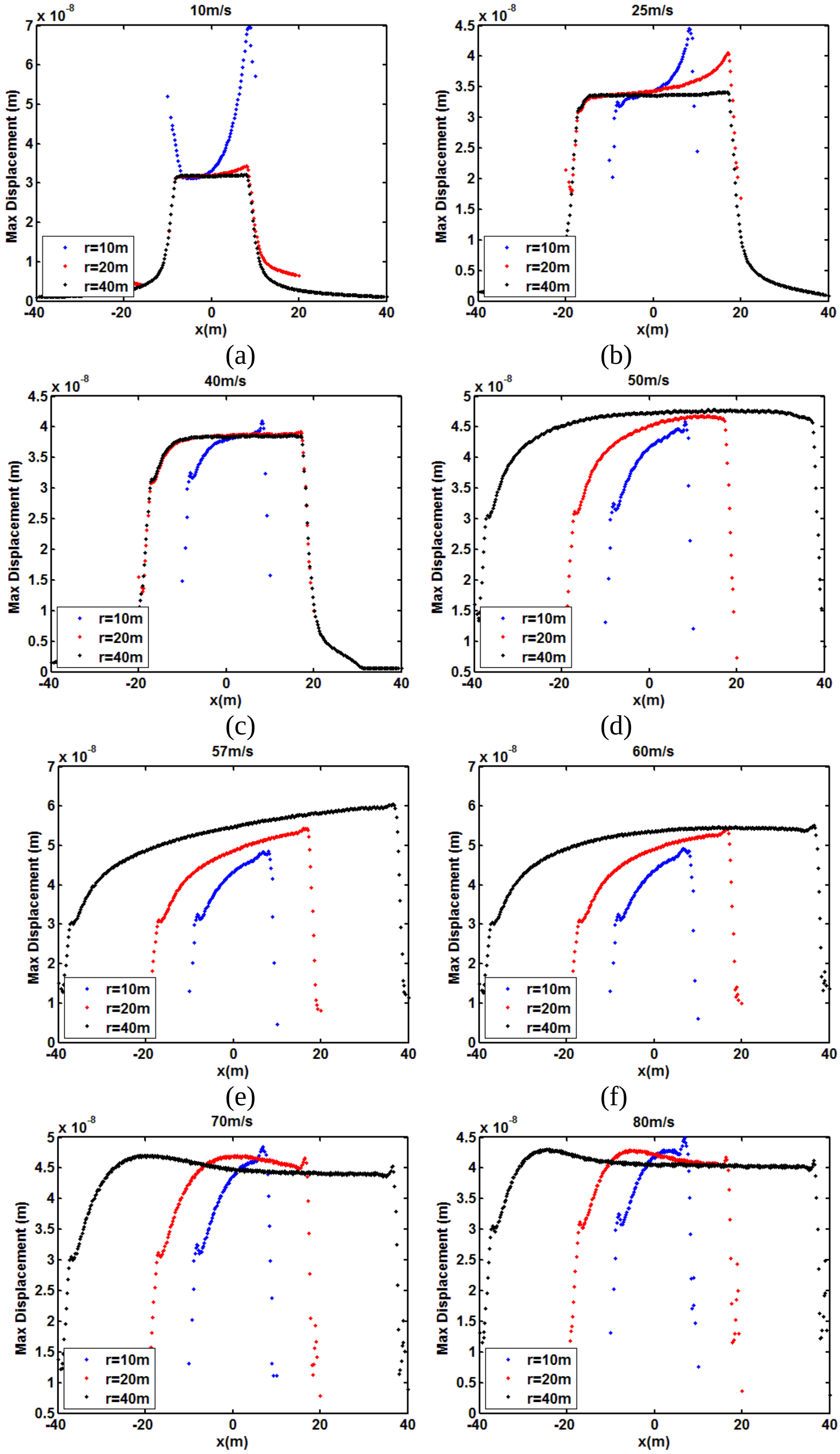

(a) (b) (c) (d) (e) (f) (g) (h)

Figure 5-4 The maximum displacements at each position along the rail due to moving load; (a) V=10 m/s; (b) V=25 m/s; (c) V=40 m/s; (d) V=50 m/s; (e) V=57 m/s; (f) V=60 m/s; (g) V=70 m/s; (h) V=80 m/s

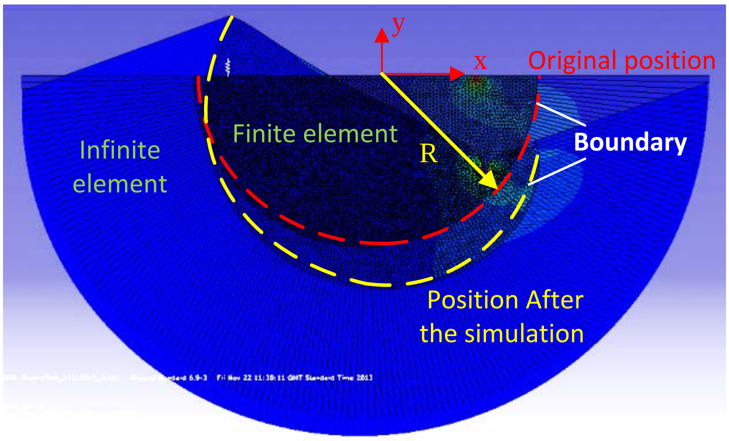

Figure 5-5 Incorrect displacment occuring due to the motion of the moving load (exaggerated)

The size of the model and the speed of the moving load are the main factors influencing this artificial displacement. Therefore, using a larger model can reduce the influence of the boundary on the results. When the critical speed is assessed in Section 5.8, the results at the midpoints of the model will be used as they are less influenced by the incorrect displacement and the boundary effects. Moreover, better absorption can be expected for excitation at the midpoint as the waves propagate normal to the boundary.

5.5 Static analysis of half-space ground model

Although the maximum element size is usually chosen according to the required frequency range, the element size also needs to be small enough in order to capture the deflection shape due to static or quasi-static loading. In this section, a study of the ground deflection due to static loading is introduced. The ground is assumed to be the same homogeneous half-space as before but the track is not considered here.

When a uniform pressure p is applied to a circular area of radius a on the surface of a half-space, as shown in Fig. 5-6, the vertical displacement of the surface at distance r from the centre is given by (Verruijt, 2009)

$$u_z = \frac{2pa(1-v)}{\pi G}\int_0^\infty \frac{J_1(\xi a)J_0(\xi r)}{\xi}d\xi \tag{5-3}$$

where p is the pressure, a is the radius of the circular area, v is the Poisson's ratio of the half-space, and G is the shear modulus. The integral is given by

$$\int_0^\infty \frac{J_1(\xi a) J_0(\xi r)}{\xi} d\xi = \begin{cases} \dfrac{2}{\pi} E\left(\dfrac{r^2}{a^2}\right) & \mathrm{r} < a \\ \dfrac{2r}{\pi a}\left\{E\left(\dfrac{r^2}{a^2}\right) - \left(1 - \dfrac{r^2}{a^2}\right) K\left(\dfrac{r^2}{a^2}\right)\right\} & \mathrm{r} > a \end{cases} \tag{5-4}$$

where the functions $K(x)$ and $E(x)$ are elliptic integrals of the first and second kind, respectively.

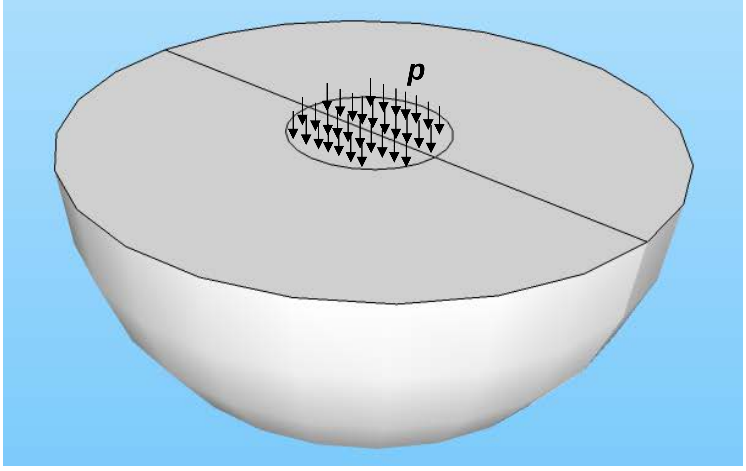

Figure 5-6 A uniform load applied to a half-space ground model

A quarter sphere model with radius 5 m modelled using finite/infinite elements is used for modelling the half-space. Again tetrahedral elements are used. Ground properties can be seen in Table 5-1. The pressure p is 1000 N/m^2, and the radius of the circular loading area a is 1 m.

The static results obtained from FE meshes with four different maximum element sizes for the region close to the track, 1 m, 0.5 m, 0.25 m, and 0.125 m, are shown in Fig. 5-7. The mesh with 0.25 m elements gives good results and is used subsequently for the ground surface in the region close to the track. In addition, the size of the finite elements needs to be small enough to account for wave propagation in the ground. This is considered in the next section.

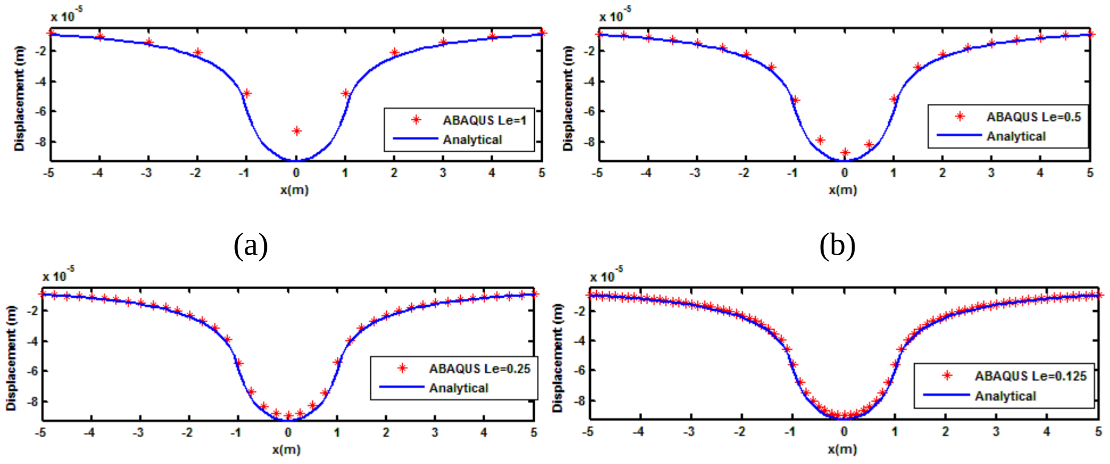

(a) (b)

(c) (d)

Figure 5-7 Surface deflection of the half-space ground model due to a uniform pressure over 1 m radius

5.6 Investigation of mesh required for half-space ground/track model with a moving load

In wave propagation problems, the element size is selected according to the highest frequency in the simulation. Higher frequencies correspond to smaller wavelengths; therefore, a smaller element size is required to obtain the correct results. The maximum element size is controlled by the shear wavelength λ_s (Kuhlemeyer, 1973; Lysmer, Ukaka, Tsai, & Seed, 1975).

Therefore, the maximum node spacing size, which here is the same as the element size, should satisfy the following inequality.

$$l_e \le \frac{1}{N}\lambda_s \tag{5-5}$$

where N is usually taken between 5 and 8. Consequently, due to the relationship between wavelength and frequency, the upper limit of the frequency range can be derived as

$$f_{\max} \le \frac{1}{N}\frac{c_s}{l_e} \tag{5-6}$$

However, the moving load problem is a transient problem which does not have a well-defined frequency range from which to determine the element size. Furthermore, the waves are attenuated outward from the load position into the infinite medium. Elements which are very far from the excitation point have less contribution to the results close to the track. Moreover, higher frequencies are attenuated more rapidly than low frequencies. (Zerwer, Cascante, & Hutchinson, 2002) indicated that a graded mesh can provide better accuracy for wave attenuation problems than a uniform mesh. This is due to the fact that the graded mesh gives a better representation of Rayleigh waves than the uniform mesh for a wider frequency range, because the wave energy is located within one wavelength of the surface. Therefore, a graded mesh is used here for these reasons and because it allows reduced simulation times.

Nevertheless, it is important to take account of the fact that the waveforms in the ground change with different load speeds. To illustrate this, Fig. 5-8 shows the instantaneous ground displacement induced by moving point load at different load speeds. The displacement is shown as positive upwards for ease of visualisation. The results are obtained from a semi-analytical model of a moving load on a track on a ground, developed by Sheng, 1999. This model will be introduced in more detail in Chapter 7. Here it is used with the same parameters as the FE model as it allows a larger domain to be considered than is possible in the FE model. When the load speed is low, as shown in Fig. 5-8(a) for 10 m/s, the deflection is attenuated quickly with lateral distance. On the other hand, as shown in Fig. 5-8(b), a much wider waveform is found for a load speed of 57 m/s, which is close to the critical speed as will be shown in Section 5.8. As it shown, very long wavelength is found in the transversal direction. As a result, although the deformation spreads out in the lateral direction, the wavelength is quite long and the element size for the transverse direction can be relatively large. For the depth direction, the surface waves penetrate to a depth that depends on the frequency, with higher frequencies penetrating much less than low frequencies (Thompson, 2009). Consequently, the mesh size can be allowed to increase further from the surface in the vertical direction.

Six different FE meshes are used here, as shown in Fig. 5-9, to investigate different meshing strategies for the moving load problem. In each case a 10 m radius ground model is used to investigate the effect of the different meshing strategies. Three parameters, *dx*, *dy*, and *dz*, are used to define the whole mesh for the ground model due to different requirements in different directions. *dx* is the minimum element size, which is used for the area close to the track, whereas *dy* is the maximum element size in the vertical direction, and *dz* is the maximum element size in the transverse direction. Thus the element size increases from *dx* at the track to *dy* at the bottom boundary and *dz* at the transverse boundary. Table 5-3 lists these values for the six different mesh types.

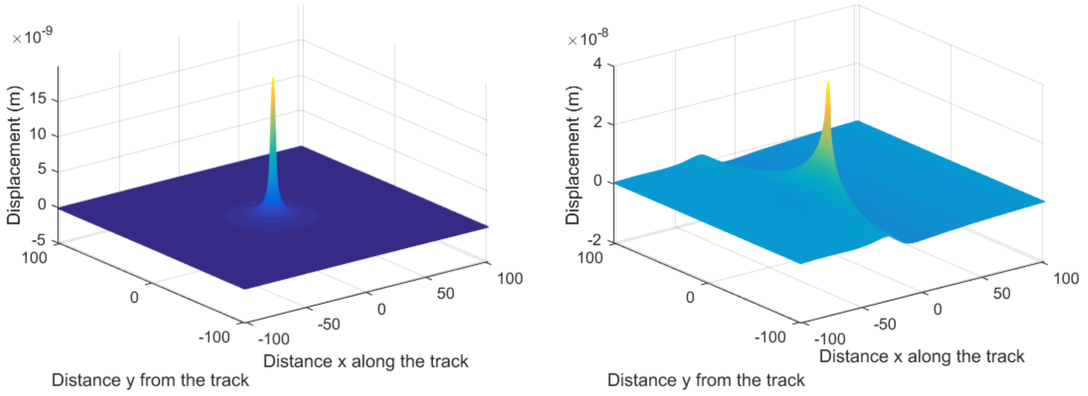

(a) (b)

Figure 5-8 Ground displacement for a constant load of 1 N moving at different load speeds; (a) *V*=10 m/s; (b) *V*=57 m/s. Results obtained using semi-analytical model, (Sheng, 1999)

Table 5-3 Six different mesh types

	Mesh1	Mesh2	Mesh3	Mesh4	Mesh5	Mesh6
Smallest element size, m	0.25	0.25	0.25	0.125	0.125	0.0625
Element size at bottom, *dy*, m	1.0	0.5	0.25	1.0	1.0	1.0
Element size at transverse boundary, *dz*, m	1.0	0.5	0.25	1.0	0.5	0.5

Mesh 1, 2 and 3 have the same value of *dx*, which is equal to 0.25 m, which was found sufficient in Section 5.5. The maximum element size is set to be the same for the transverse and vertical directions, with values of 1 m, 0.5 m and 0.25 m for the three different meshes. Mesh 4 and mesh 5 have the same minimum element size, which is half of that for mesh 1~3. They have the same maximum element size in the vertical direction, but a different maximum element size in the transverse direction. Finally, a smaller minimum element size is used for mesh 6 but with the same maximum element sizes as mesh 5. Note that mesh 3 is a uniform mesh whereas the others are all graded.

The maximum rail displacements at the midpoint of the model are shown in Fig. 5-10 for different speeds of a load of magnitude 1 N. The midpoint displacement is used as this minimises the effect of the fictitious overall motion. The trends of these results are almost the same for the six different mesh types. In all cases the displacement reaches a maximum at around 60 m/s.

There are only small differences between the results obtained using mesh 1~3, indicating that the element size far from the track has only a small contribution to the rail deflection. Similarly, the differences between mesh 4 and mesh 5 are small.

However, the maximum displacement becomes slightly larger for all speeds when the minimum element size becomes smaller. Nevertheless, the differences are only around 2.5% to 5%. A similar effect was seen in Fig. 5-7. Therefore, while recognising that the deflection may be underestimated, the strategy used in mesh 1 is considered to be sufficient for use in further simulations.

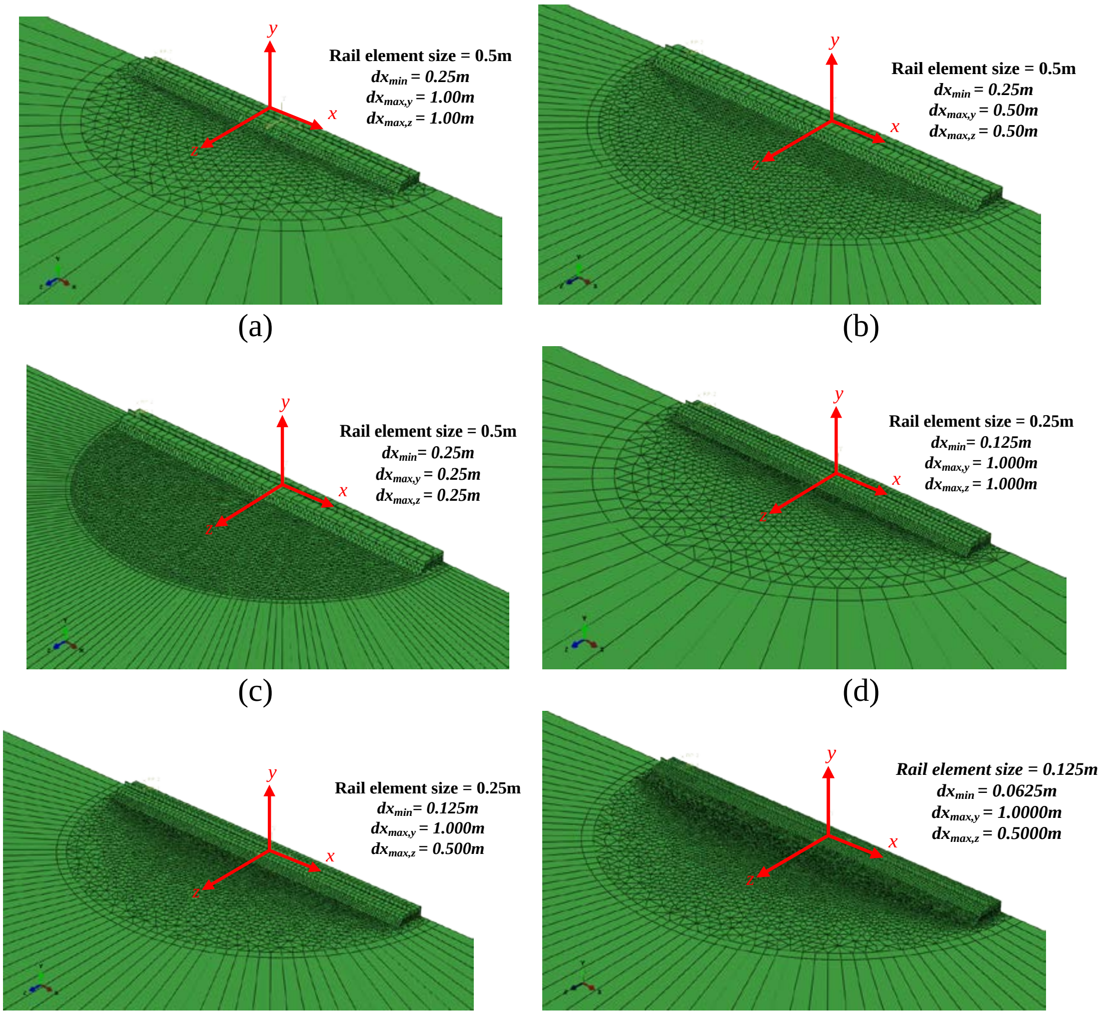

(a) (b)

(c) (d)

(e) (f)

Figure 5-9 Six different mesh types for radius 10m; (a) Mesh1; (b) Mesh2; (c) Mesh3; (d) Mesh4; (e) Mesh5; (f) Mesh6

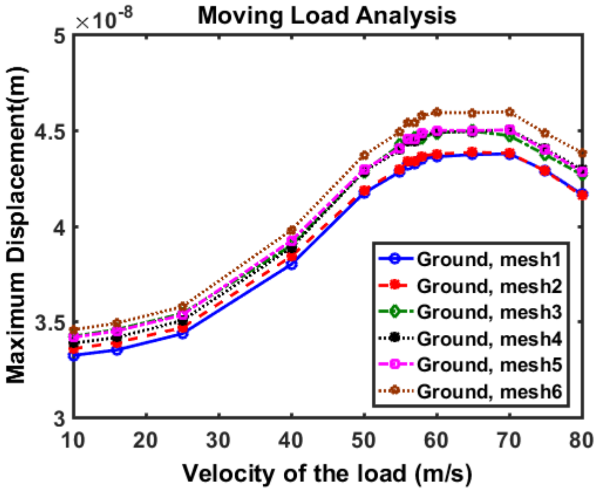

Figure 5-10 Mid-point maximum rail displacement for moving load of amplitude 1 N on homogeneous half-space at different speeds

5.7 Investigation of model size for homogeneous half-space ground model with a moving load

To investigate the required model size for the half-space ground model, consider the maximum displacements at each node along the track during the simulation previously shown in Fig. 5-4. The results from three different sized models were compared for different load speeds. Similar to the results from the Winkler foundation in Section 4.3.2, the maximum displacements are almost the same at different positions along the track when the load speed is very low, provided that the mesh is large enough to avoid significant fictitious overall motion. However, the results from the load speed of 57 m/s increase continuously and do not reach a steady state even when the 40 m radius model is used. This suggests that a larger size is required for speeds close to the critical speed. However, for the speeds that are lower, or even higher than the critical speed, a 40 m model is sufficient to reach steady state.

Due to the high computational requirements of the hemispherical model for larger radii, further discussion of the convergence will be left until Chapter 6 where cuboid models will be considered.

In order to investigate the required model size for specific speeds, the results are compared with the result from a wavenumber FE/BE model (Sheng, Jones, & Thompson, 2006). This approach models the infinite soil directly using boundary elements, without any need for specific boundary treatment (see also appendix B). It directly predicts the steady-state response to a moving load, in this case a constant load. The displacements from three FE models of different sizes for different load speeds are presented in Fig. 5-11. These are the displacements at the midpoint of the track and are plotted as a function of load position *x*. The results are compared with displacements obtained from the wavenumber FE/BE model WANDS (Nilsson & Jones, 2007) using the same parameters (except for the damping). The results in Fig. 5-11(a), (b), (e), (f) show good agreement. For these speeds the model size used is big enough to achieve the steady-state results. However, the agreement is less good for speeds close to the critical speed, Fig. 5-11(c)~(d), when the model is not long enough for steady state to be reached. Nevertheless, good agreement can be found when the load speed is higher than the critical speed, Fig. 5-11(e)~(f). As a result, larger model size is only required when the load speed is close to the critical speed. Further discussion about the required model size for moving loads will be given in Chapter 6.

In order to investigate how deep the model should be to avoid reflections from the bottom, the displacements at different depths are shown in Fig. 5-12. As shown in Fig. 5-12(a)~(d), for speeds lower than 57 m/s, the displacement at 20 m depth is already very small. However, the displacement at 20 m depth is still significant for higher speeds, as shown in Fig. 5-12(e)~(f). This indicates that a greater depth of model is required for speeds higher than the critical speed, which is 57 m/s in this case (see Section 5.8). Nevertheless, even at these higher speeds, by a depth of 30 m the response has reduced to a negligible level. The same phenomena can be also observed from the ground displacements in the spatial domain, as shown in Fig. 5-13 for speed of 25 m/s and 80 m/s.

Considering the transverse direction, the displacements at *x*=0 and different positions *z* in the transverse direction are shown in Fig. 5-14 when the load is applied at various positions *x*. When the load speed is higher than the critical speed the displacements are still significant, even when the load is 30 m away from the mid position (*x*=0), as seen in Fig. 5-14(e)~(f). On the other hand, at low speed the displacements become very small at 10 m from the central line, as shown in Fig. 5-14(a)~(d). As a result, the effect of the boundaries at the sides becomes more important when the load speed is higher than the critical speed. The same phenomena can be also seen in Fig. 5-13. Although the boundary has less influence for the speeds lower than the critical speed, the wavefronts for load speed close to the critical speed are wider than those for higher speed. A 10 m wavefront is found for load speed at 25 m/s and they extend to 20 m for 40 m/s and 30 m for 50m/s, as shown in Fig. 5-14(a)~(c). As a result, it is still very important that the model has sufficient width for speeds close to the critical speed even though it is lower than the critical speed.

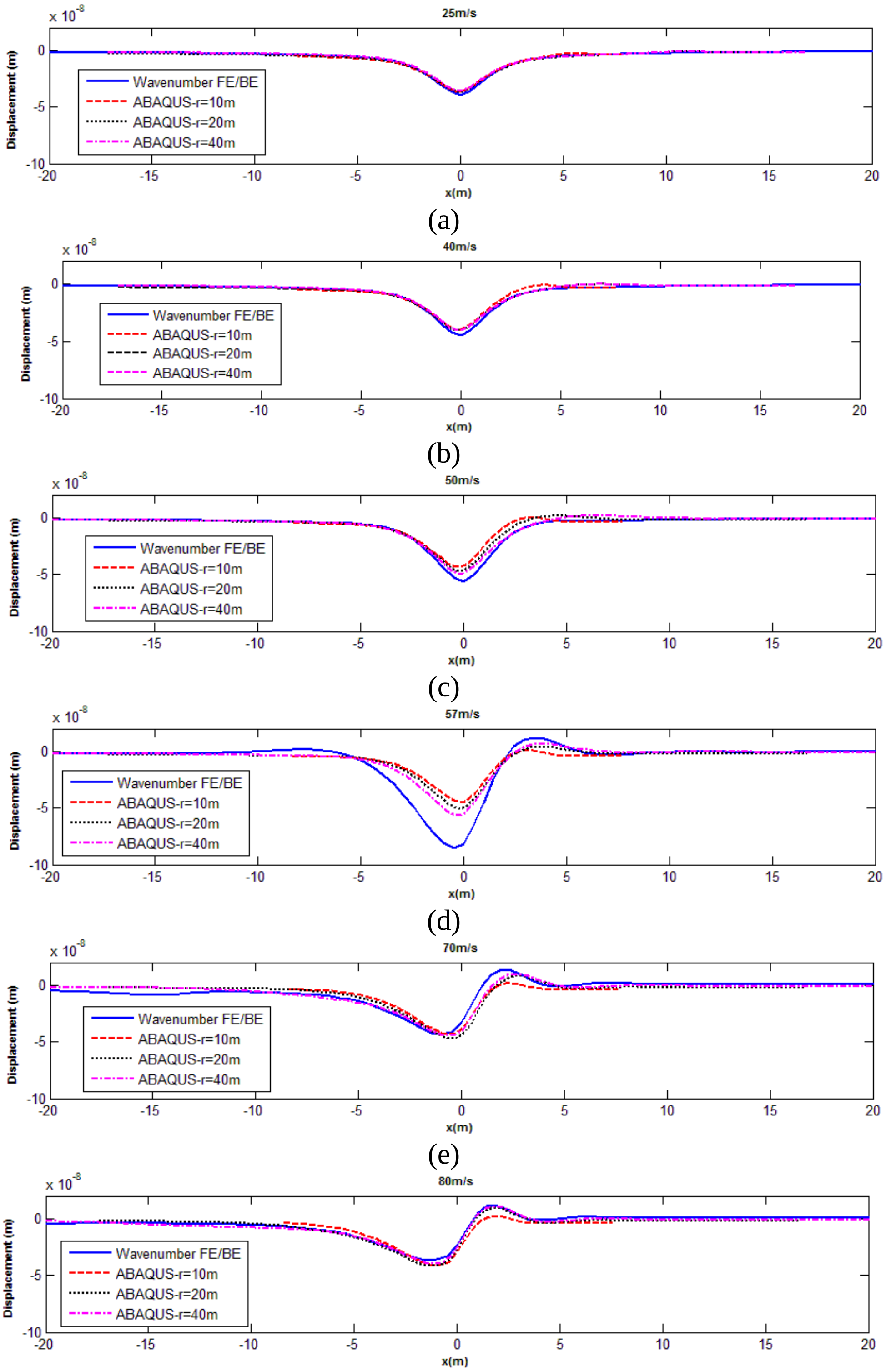

25m/s

(a)

40m/s

(b)

50m/s

(c)

57m/s

(d)

70m/s

(e)

80m/s

(f)

Figure 5-11 Displacement of the rail at the centre of the model plotted against load position for different load speeds; (a) *V*=25m/s; (b) *V*=40m/s; (c) *V*=50m/s; (d) *V*=57m/s; (e) *V*=70m/s; (f) *V*=80m/s

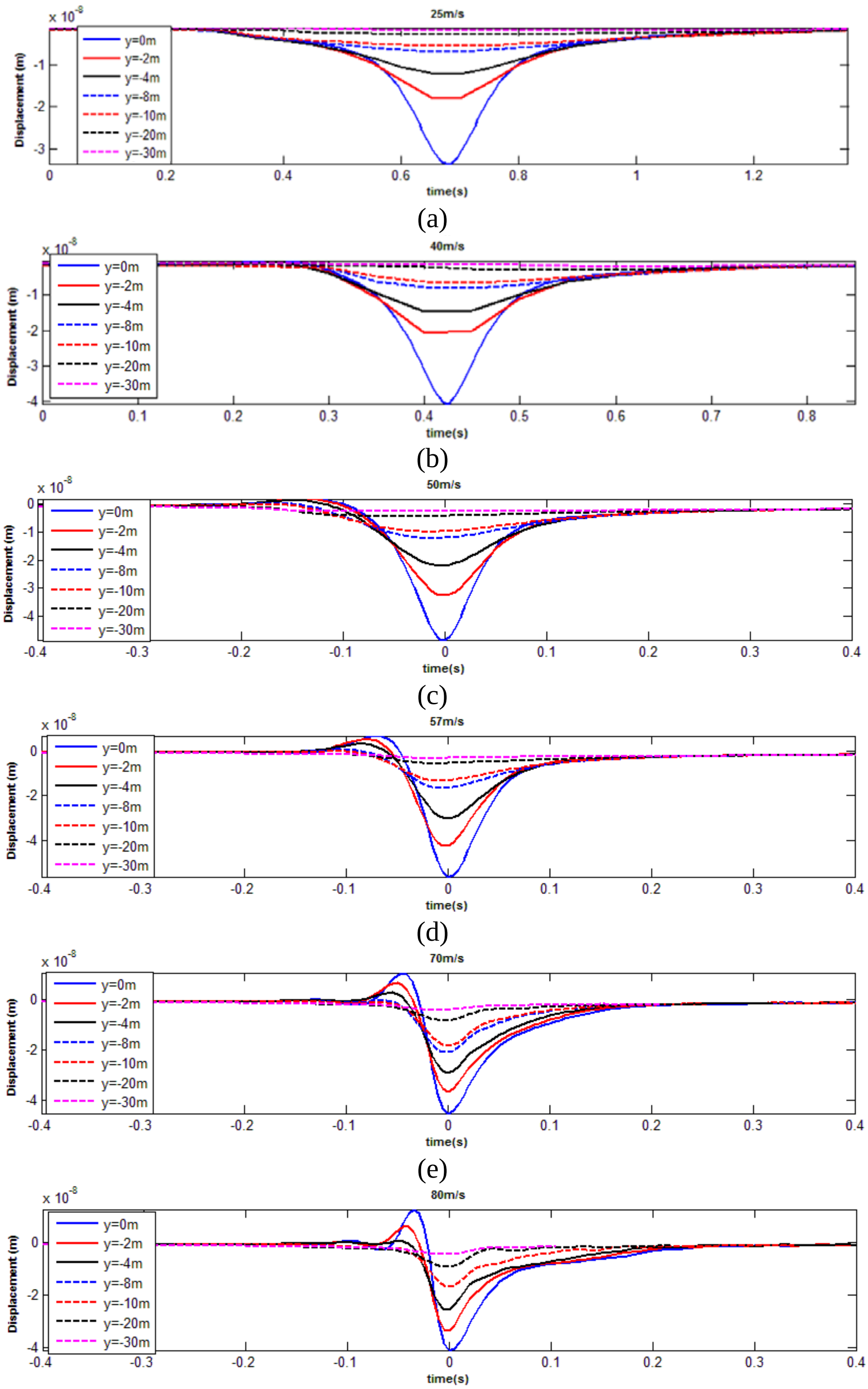

(a)

(b)

(c)

(d)

(e)

(f)

Figure 5-12 Displacement of the ground at the centre of the model plotted against load position at different depths; (a) *V*=25m/s; (b) *V*=40m/s; (c) *V*=50m/s; (d) *V*=57m/s; (e) *V*=70m/s; (f) *V*=80m/s

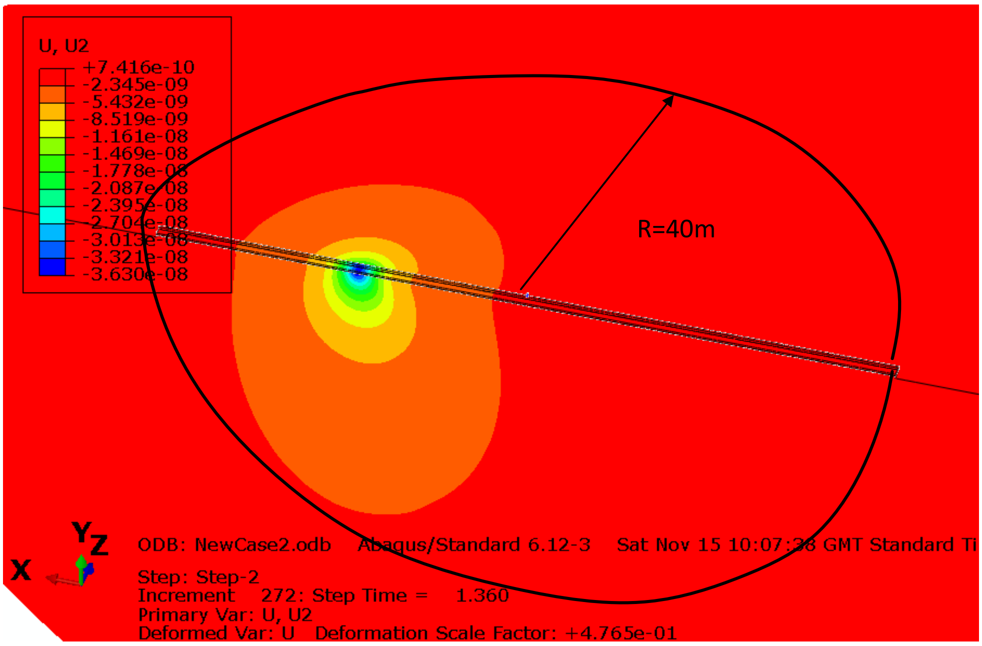

(a)

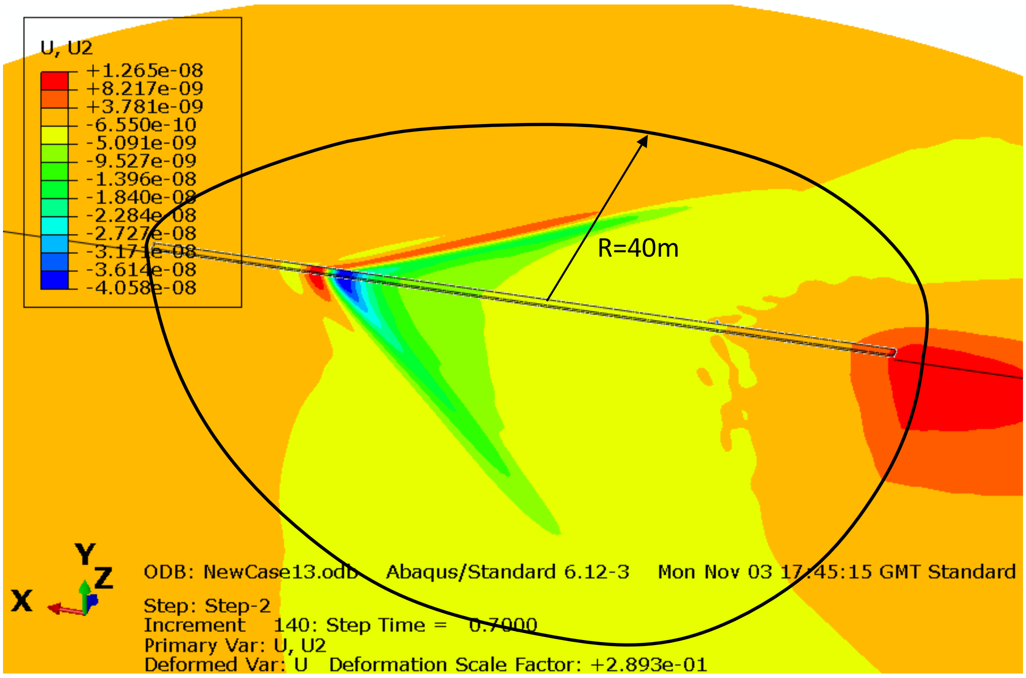

(b)

Figure 5-13 Displacement of the homogeneous half-space for two different load speeds; (a) load speed 25 m/s; (b) load speed 80m/s

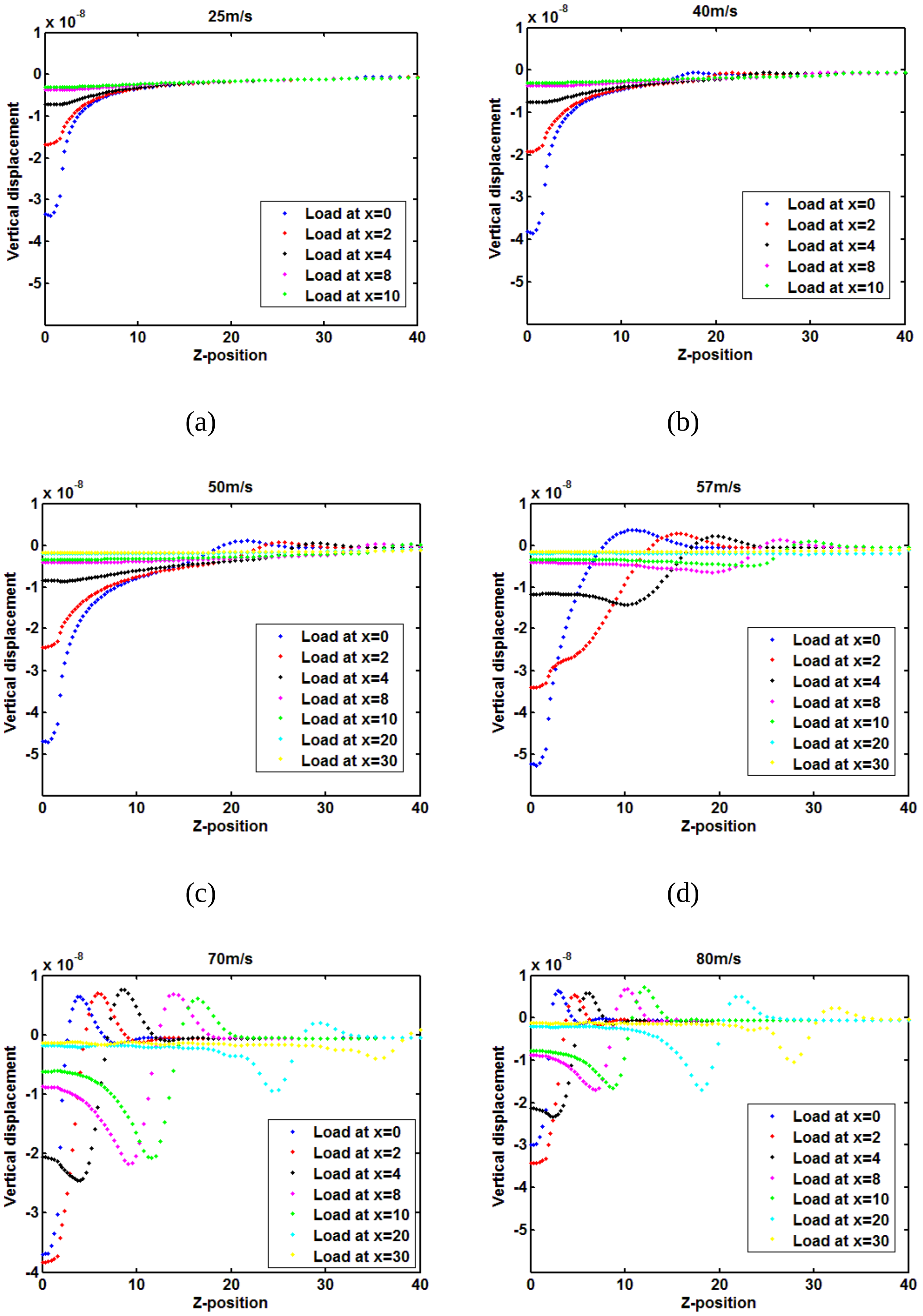

(a) (b)

(c) (d)

(e) (f)

Figure 5-14 Displacements of the ground at *x*=0 plotted against the transverse direction *z*, when the load is at different positions *x*; (a) *V*=10m/s; (b) *V*=25m/s; (c) *V*=50m/s; (d) *V*=57m/s; (e) *V*=70m/s; (f) *V*=80m/s

5.8 Assessment of critical speed for homogeneous half-space ground

Due to the initial transient discussed in Section 4.3.2, it will be necessary to allow the load to travel a sufficient distance to allow the waveform to reach steady state.

In order to give a more detailed assessment of the critical speed, Fig. 5-15 shows the maximum rail displacements at the midpoint for a 1 N load plotted against the load speed. The results from the ABAQUS models are shown for three different sizes of model. These are compared with the results from the wavenumber FE/BE method (Sheng et al., 2005) using the same parameters (apart from the damping).

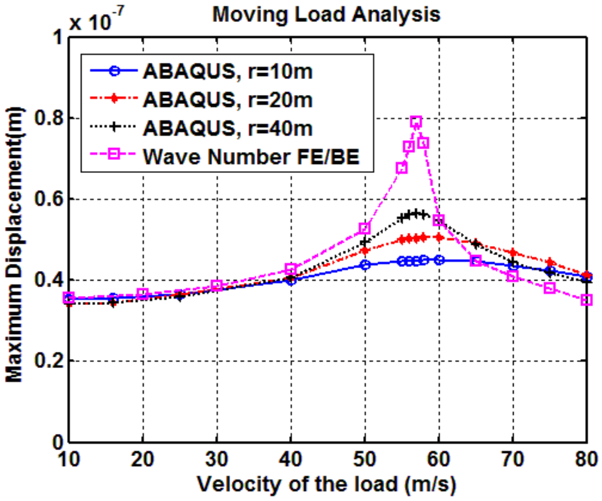

Figure 5-15 Maximum deflection for a moving load of amplitude 1 N for the homogeneous half-space ground

From these results it is clear that the critical speed of this homogeneous half-space ground/track model is 57 m/s. This corresponds to the Rayleigh wave speed in the ground. Small differences can be found between the FE model and wavenumber FE/BE models for the lower speeds. This is due to the limitation of using an element size of 0.25 m in the FE model, as discussed in Section 5.6, where the deflection was found to be 5% larger for a smaller element size. However, that model is too large for use in parametric study.

The results are almost the same when using the three different FE model sizes when the load speed is below 40 m/s. Therefore, a 10 m radius sphere model is good enough to achieve the correct results in this speed range. However significant differences are found between the models when the load speed is close to the critical speed. The difference between the FE and FE/BE results suggests that a much larger model is required for the speeds between 50 m/s and 60 m/s. On the other hand, reasonable agreement can be seen with the wavenumber FE/BE results when the speed is above 60 m/s, particularly for the 40 m radius model.

Fig. 5-16 shows the evolution of the deformation for a load speed 57 m/s. These results are obtained using a 40 m radius quarter sphere model with mesh size based on the strategy of mesh 1. The maximum element size is kept as 1 m. Results are shown at four different time steps. The results on the left show the top view and those on the right the side view; the load is moving from right to left. It can be seen that the amplitude of the displacement becomes larger with increasing time. Furthermore, the angle between the waveform and the mid plane changes continuously during the simulation. The development of the wavefronts depends on the geometrical spreading of the waves and the propagation velocities of the different waves (Fu & Zheng, 2014; Hall, 2003).

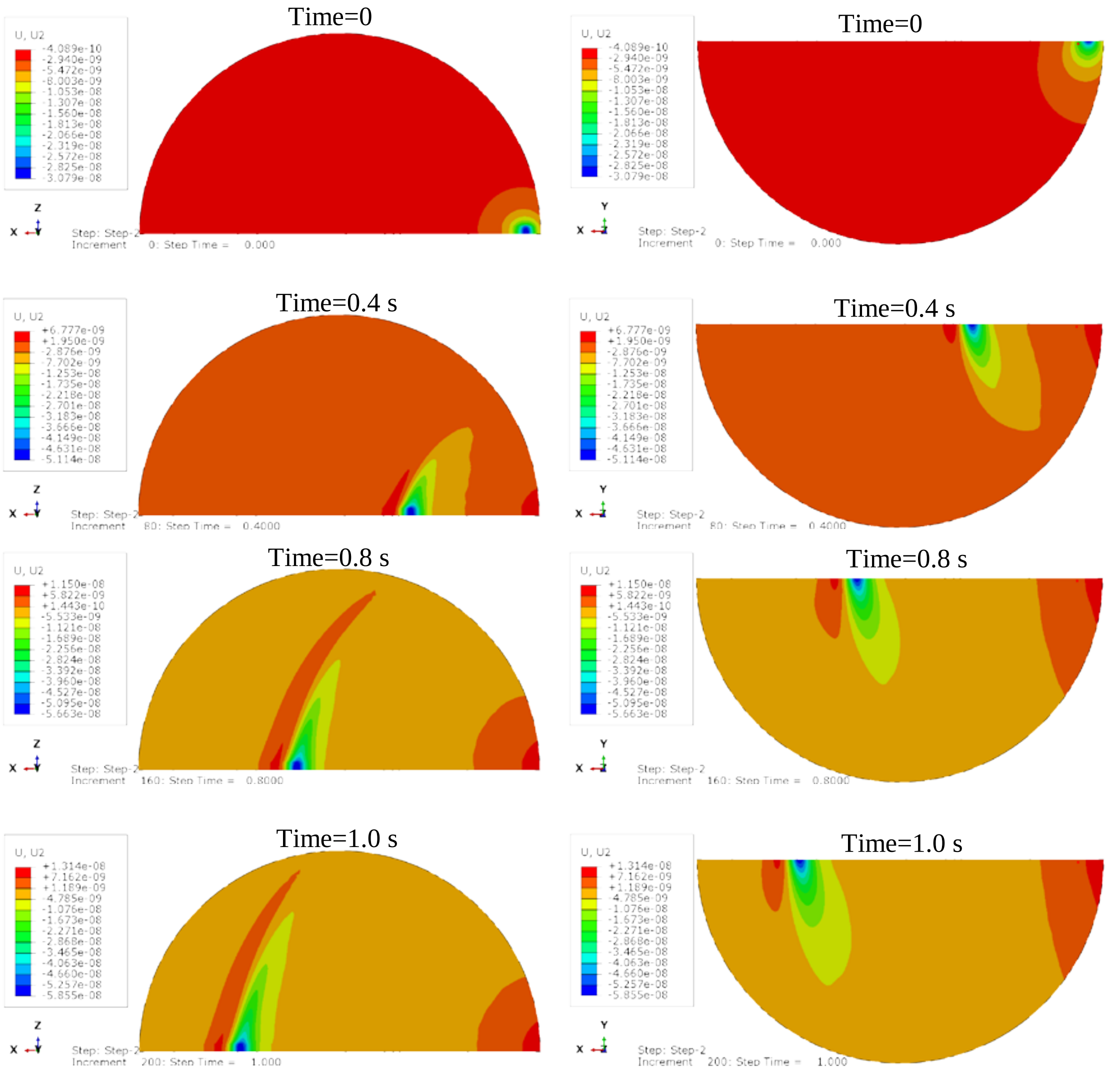

Figure 5-16 Evolution of the deformation under a moving load when load speed is 57 m/s (left: top view; right: side view)

5.9 Analysis of layered half-space ground model with a moving load

In this section a layered half-space ground is considered, as shown in Fig. 5-17. The same soft soil properties are used for the upper layer as in the homogeneous half-space model and a stiffer foundation is considered for the second layer, which uses double the wave speed of the first layer. The material properties are shown in Table 5-4.

Table 5-4 Layered half-space ground model properties

First-layer properties		second-layer properties
Young's Modulus, E	19.2 MN/m^2	76.8 MN/m^2
Poisson's ratio, v	0.33	0.33
Rayleigh damping	$\alpha = 0,\ \beta = 0.000159\,\text{s}$	$\alpha = 0,\ \beta = 0.000159\,\text{s}$
Mass density, ρ	2000 kg/m^3	2000 kg/m^3
P-wave speed, c_p	120 m/s	240 m/s
S-wave speed, c_s	60 m/s	120 m/s
Depth	2m	inf

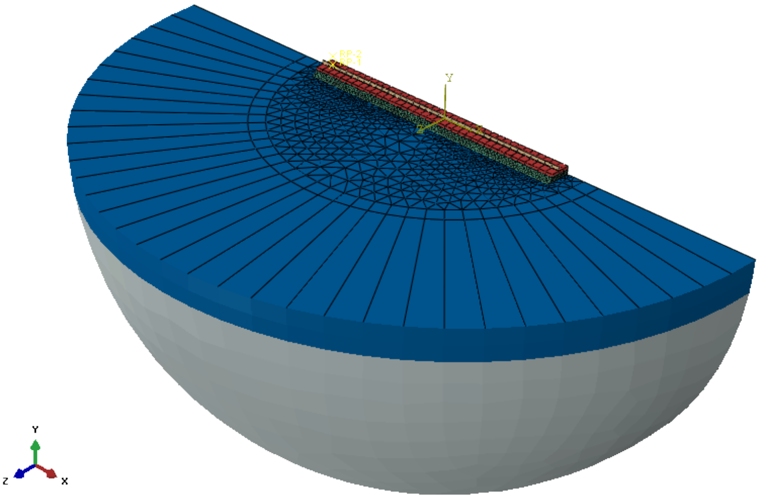

Figure 5-17 Layered half-space ground model

In order to investigate the required depth for the layered half-space, Fig. 5-18 shows the ground displacement in the spatial domain when the load speed is 80 m/s. For simplicity the ground model uses the same mesh type as that for the homogeneous half-space, as the element size is small enough for the stiffer ground property. Compared with Fig. 5-13(b), the displacement amplitude attenuates faster than for the homogeneous half-space. The displacement at a depth of 5 m is already around 10 times smaller than the results at the surface.

Thus, the amplitudes of the displacements at 30 m below the surface become negligible for different moving load speeds for either half-space or layered half-space and the displacements further than 30 m below the surface have minimal influence on the vibration at the surface for all moving speeds. This suggests that it is sufficient to extend the model to a depth of at most 30 m.

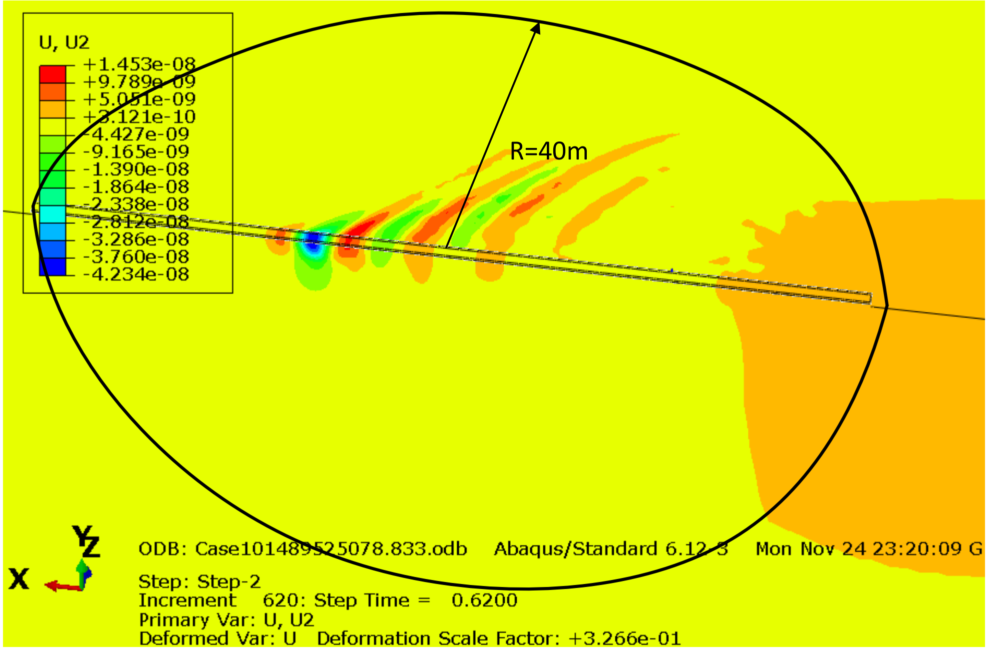

Figure 5-18 Displacement of the layered half-space for load speed 80 m/s

The maximum deflection of the track under a moving load is shown in Fig. 5-19 for the layered half-space. The results in this case are independent of the size of model below 60 m/s. However, close to the critical speed the size of the model is again very important; for a 40 m radius model the critical speed is predicted to occur at 85-90 m/s which is higher than the results from the homogeneous half-space. Relatively good agreement can be seen compared with the results from the wavenumber FE/BE model. However, small differences still can be found.

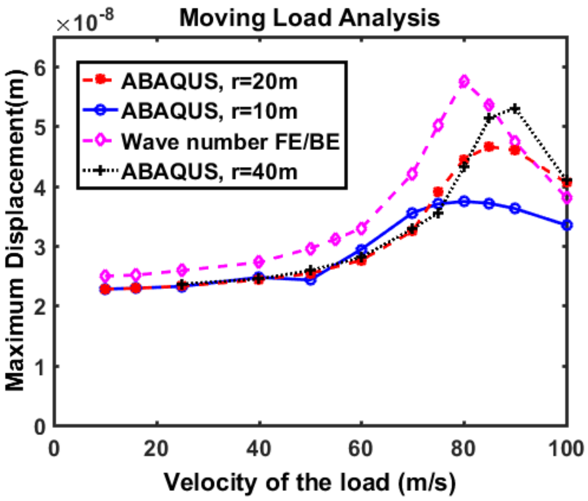

Figure 5-19 Maximum deflection for a moving load of amplitude 1 N for the layered half-space ground

5.10 Summary

A method of modelling the track/ground system in ABAQUS when a moving load is applied has been introduced by using finite and infinite elements. Fictitious displacements of the whole model are found due to the fact that it is unconstrained as a result of the infinite elements on the boundary. However, the use of a larger model can reduce this incorrect phenomenon; furthermore, it can be neglected when the load speed becomes higher. The meshing strategy and model size have been investigated and good agreement has been found compared with the results from a wavenumber FE/BE model. The critical speed for a homogeneous half-space ground is the same as that found from the wavenumber FE/BE model, but the amplitude is smaller, probably because the model is not large enough. However, small differences in critical speed are found for a layered half-space ground.

It is shown that the displacements are negligible at depths greater than 30 m below the surface for all moving speeds. However, different width requirements can be found for different load speeds. A wider model is shown to be necessary especially when the moving load is close to or higher than the critical speed. These effects will be discussed further in Chapter 6 using a cuboid mesh.

Chapter 6: Three-dimensional ground/track model based on cuboid mesh

6.1 Introduction

The numerical results obtained for a track on a homogeneous half-space suggest that much longer models are required when the load speed approaches the critical speed, in order to allow convergence to the steady state result. However, a depth of 30 m has been found to be sufficient in all cases considered. Therefore, a hemispherical model becomes inefficient when the length of the model has to be increased. In this chapter, three-dimensional cuboid models of the ground are introduced, with or without infinite elements, and used to investigate the required length of the model. The modelling strategy is introduced in Section 6.2. The influence of the boundaries at different load speeds is discussed and the use of appropriate Rayleigh damping is introduced to reduce the effect of reflections from the boundaries. The distances required to reach steady state for different load speeds are investigated for a homogeneous half-space and a layered half-space and the results are compared with those from the wavenumber FE/BE method. The response to a harmonic load is also compared between hemispherical and cuboid models and the influence of discrete sleepers is discussed.

6.2 Modelling of track and ground by using cuboid mesh

Two FE models of a homogeneous ground are shown in Fig. 6-1. Similarly to the hemispherical ground/track model, these cuboid models make use of symmetry in the *x*-*y* plane. However, instead of using infinite elements surrounding the finite domain, fixed boundaries are used in the first model, shown in Fig. 6-1(a). As discussed in Section 5.7, the reflections from the bottom of the model are expected to be negligible if the depth is greater than 30 m. However, when the load speeds exceed the critical speed, the waves attenuate slowly in the transverse direction. Therefore in the second model infinite elements are added to the side boundary, as shown in Fig. 6-1(b). The other boundary conditions remain fixed.

20-node quadratic brick elements (C3D20), as shown in Fig. 6-2, are used for the rail, railpad and sleeper due to hourglassing and shear locking problems, as discussed in Chapter 3. The same elements are used for the ground for models with and without infinite element. Additionally 12-node infinite elements (CIN3D12R) are used for the second model with infinite elements along the lateral boundary, shown in Fig. 6-1(b).

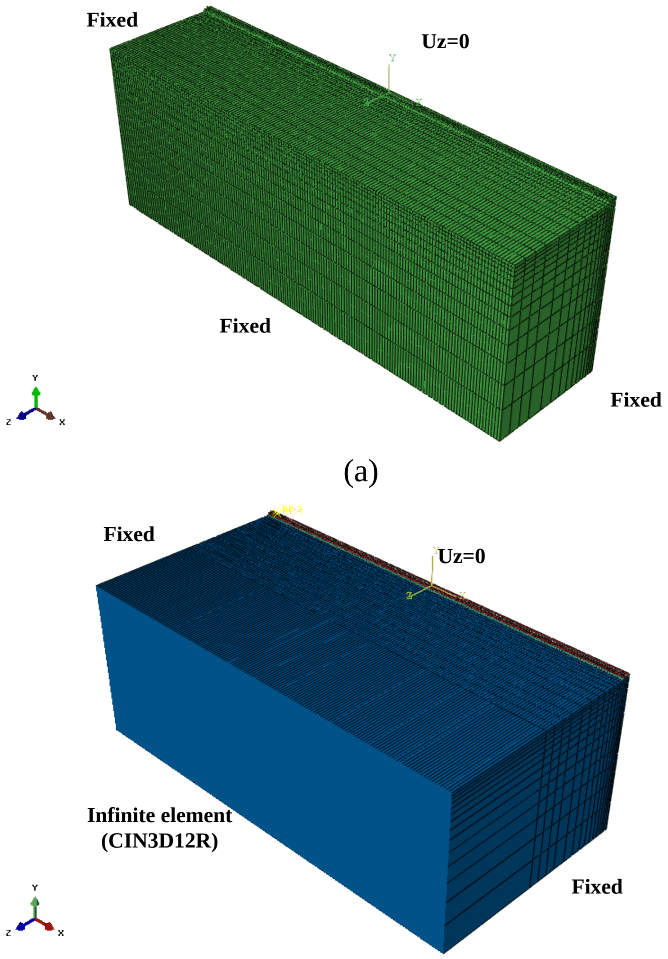

(a)

(b)

Figure 6-1 Cuboid model; (a) fixed boundary; (b) fixed boundary with infinite elements

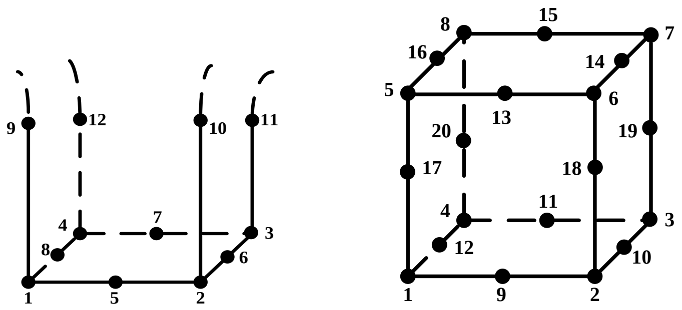

(a) (b)

Figure 6-2 Element types; (a) 12-node infinite element (CIN3D12R); (b) 20-node brick element (C3D20) (ABAQUS, 2013b)

The 12-node infinite element is used here, instead of the linear infinite element used in Chapter 5, for better compatibility with the quadratic elements in the finite domain. This also avoids the need for tie constraints. As in Chapter 5, a Python code has been used to generate the geometry of the track and ground, the definition of material properties, the mesh for the whole model, the combination of finite and infinite elements for the ground, boundary and constraint conditions and the moving load with specific contact model.

The ground properties used are the same as in Section 5.3 (see Table 5-1~5-4) including the damping model. For the track (rail, railpad, sleepers and ballast), the elements are 0.5 m long in the axial direction. Similarly to the mesh approach used in Section 5.6, the ground directly under the ballast has a maximum element size of 0.5 m. The element size increases gradually, with a stretch factor of 1.2, in the vertical and horizontal directions, as shown in Fig. 6-1. A fine mesh is required in the axial direction to achieve adequate accuracy but the graded mesh in the vertical and horizontal directions not only reduces the cost of the simulation but can also improve the representation of the Rayleigh waves, as discussed in Section 5.6. An example of results obtained from a mesh with a stretch factor of 1.2, which is commonly used (Zerwer et al., 2002), and a finer mesh with a stretch factor of 1.1 is shown in Fig. 6-3. This shows the displacement of the mid-point of the track for different load positions at a speed of 50 m/s. From this it is clear that the results are almost identical in both cases. Therefore, the stretch factor of 1.2 is used for all further simulations.

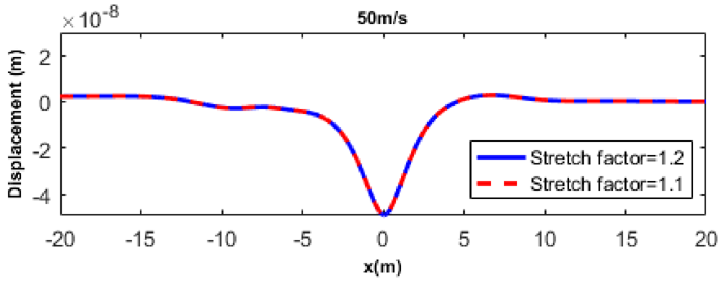

Figure 6-3 Midpoint displacement using different stretch factors for a load speed of 50 m/s

In order to have better contact conditions between the moving node and the rail surface, the load is started from a point 1 m away from the end of the model. Following the same moving load approach discussed in Section 3.2.1, an initial static analysis is applied first before introducing the load motion.

6.3 Cuboid model for homogeneous half-space with a moving load

6.3.1 Boundary effect for the fixed cuboid model

Results for a moving load are shown first using a 20x160x30 m cuboid model of the homogeneous ground. The rail displacements at the midpoint of the model are shown in Fig. 6-4 for different load speeds. The critical speed for this ground is around 57 m/s (see Section 5.8), which corresponds to the Rayleigh wave speed of the soil. Three coloured dotted lines are marked on Fig. 6-4. The black dotted line represents the time that the load arrives at the observer point. The blue dotted line represents the time of arrival of a Rayleigh wave starting from the left-hand end when the load starts moving. Finally, the red dotted line represents the time of arrival of a wave reflected from the side boundary, as explained below.

As seen in Fig. 6-4(a)~(b), no reflections from the boundary are found when the load speed is lower than the critical speed. However, a small wave can be seen before the load arrives at the observer point, which can be identified with the Rayleigh wave generated when the load starts moving.

On the other hand, a significant secondary feature is found when the load speed is higher than the critical speed, as seen in Fig. 6-4(d)~(f). This can be identified as the Mach cone that is reflected in the side boundary.

As discussed by (Andersen, Nielsen, & Krenk, 2007), a Mach cone occurs for surface waves when the load speed is higher than the wave speed in the ground in a similar way to sound in air. The angle of the cone is usually called the Mach angle. Three velocity regions are identified in Fig. 6-5. In the subsonic region, when the load speed is lower than the shear wave speed, the source remains within the wavefronts of the S-wave. When the load speed is between the S- and P-wave speeds this is referred to as the transonic region. Here, the source passes through the wavefront of the S-waves but remains within that of the P-waves. Finally, in the supersonic region, the load speed is higher than the P-wave speed, and the source passes through both wavefronts (Andersen et al., 2007).

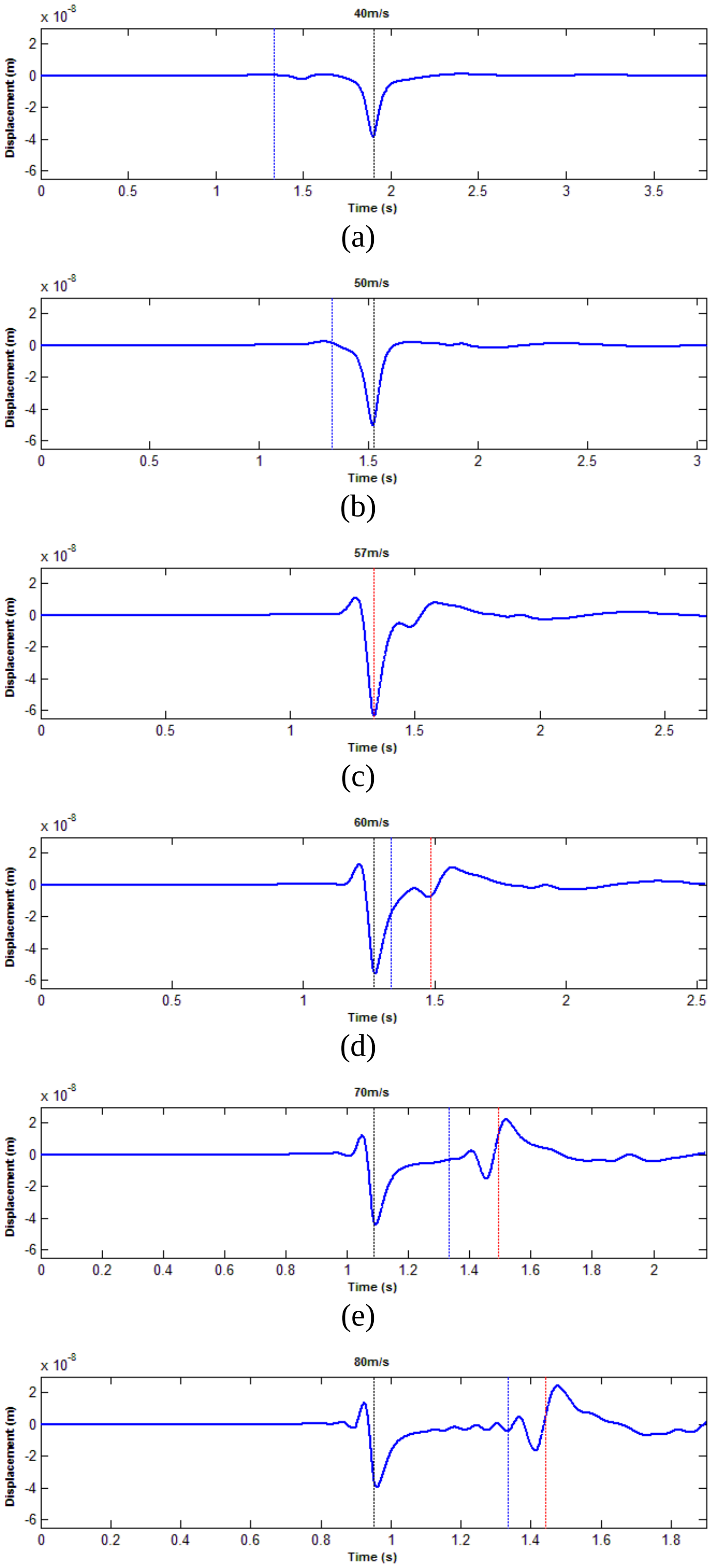

(a)

(b)

(c)

(d)

(e)

(f)

Figure 6-4 Rail midpoint displacement due to a moving load of 1 N for different load speeds; (a) *V*=40m/s; (b) *V*=50m/s; (c) *V*=57m/s; (d) *V*=60m/s; (e) *V*=70m/s; (f) *V*=80m/s;

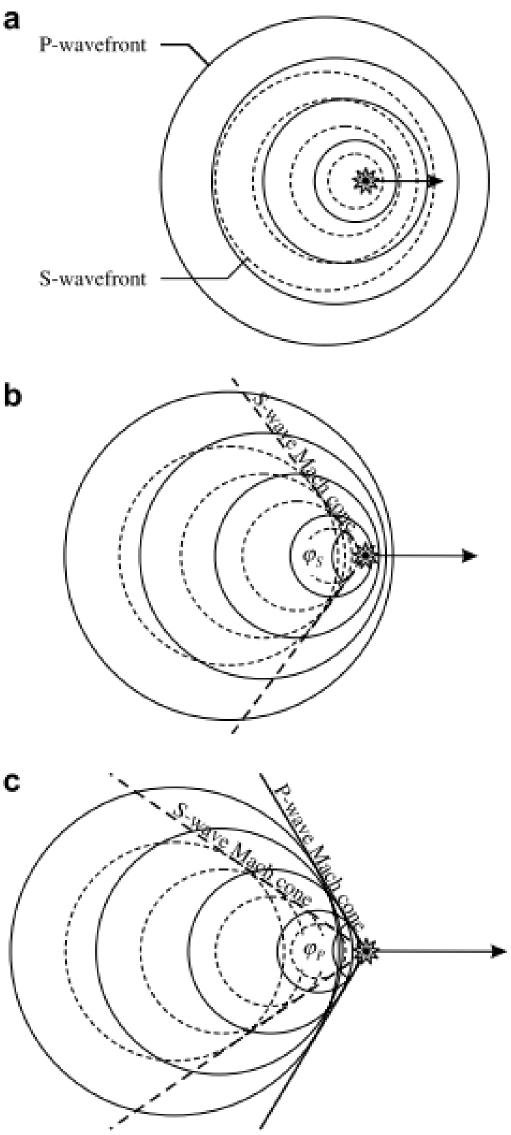

Figure 6-5 Propagation of P- and S-wavefronts from a moving point source for (a) subsonic, (b) transonic and (c) supersonic convection. (Andersen et al., 2007)

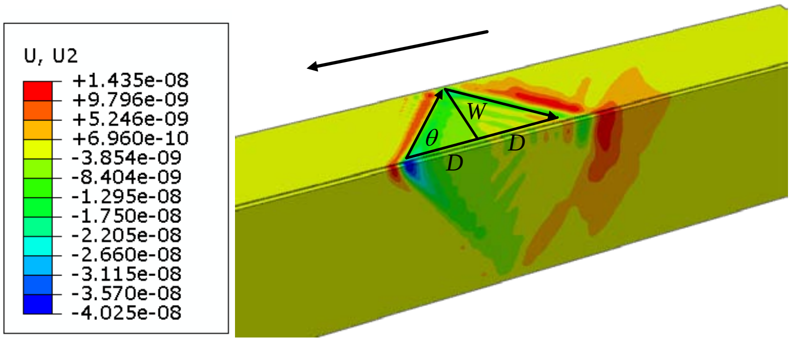

Figure 6-6 The route of the reflection propagating from the side boundary when load speed at 80 m/s

Due to this phenomenon, as seen in Fig 5-8, a wave propagates from the deflection under the load with an angle to the direction of travel that is given by

$$\sin\theta = \frac{c_R}{V} \qquad (6\text{-}1)$$

where V_R is the Rayleigh wave speed and V is the speed of the moving load. This is shown in Fig. 6-6, which also shows numerical results for a speed of 80 m/s. This wave propagates to the boundary, is reflected and then arrives back at the track after a time

$$t = \frac{x - x_1}{V} + \frac{2W}{V\tan\theta} \qquad (6\text{-}2)$$

where x_1 is the start point of the moving load, and x is the position of the observed point. W is the width of the model, which here is 20 m.

From these results (see also Fig. 5-8) it is clear that, for load speeds higher than the critical speed, the 20 m wide model with fixed boundaries is not wide enough to avoid the influence of the reflections. Therefore, the second cuboid model is considered consisting of infinite elements along the horizontal boundary to simulate the infinite domain. The results from this model are compared with those from the 20 m wide model with fixed boundaries in Fig. 6-7. The results of the two models are almost the same for speeds lower than the critical speed, as shown in Fig. 6-7(a)~(b). However, for speeds higher than the critical speed the reflection is reduced by the introduction of the infinite elements, as shown in Fig. 6-7(d)~(f). Nevertheless, a small reflection can still be seen. This can be attributed to the fact that the infinite elements only give perfect absorption when the direction of the incident wave is normal to boundary. However, as shown in Fig. 6-6 the incident wave from the moving load is not normal to the boundary.

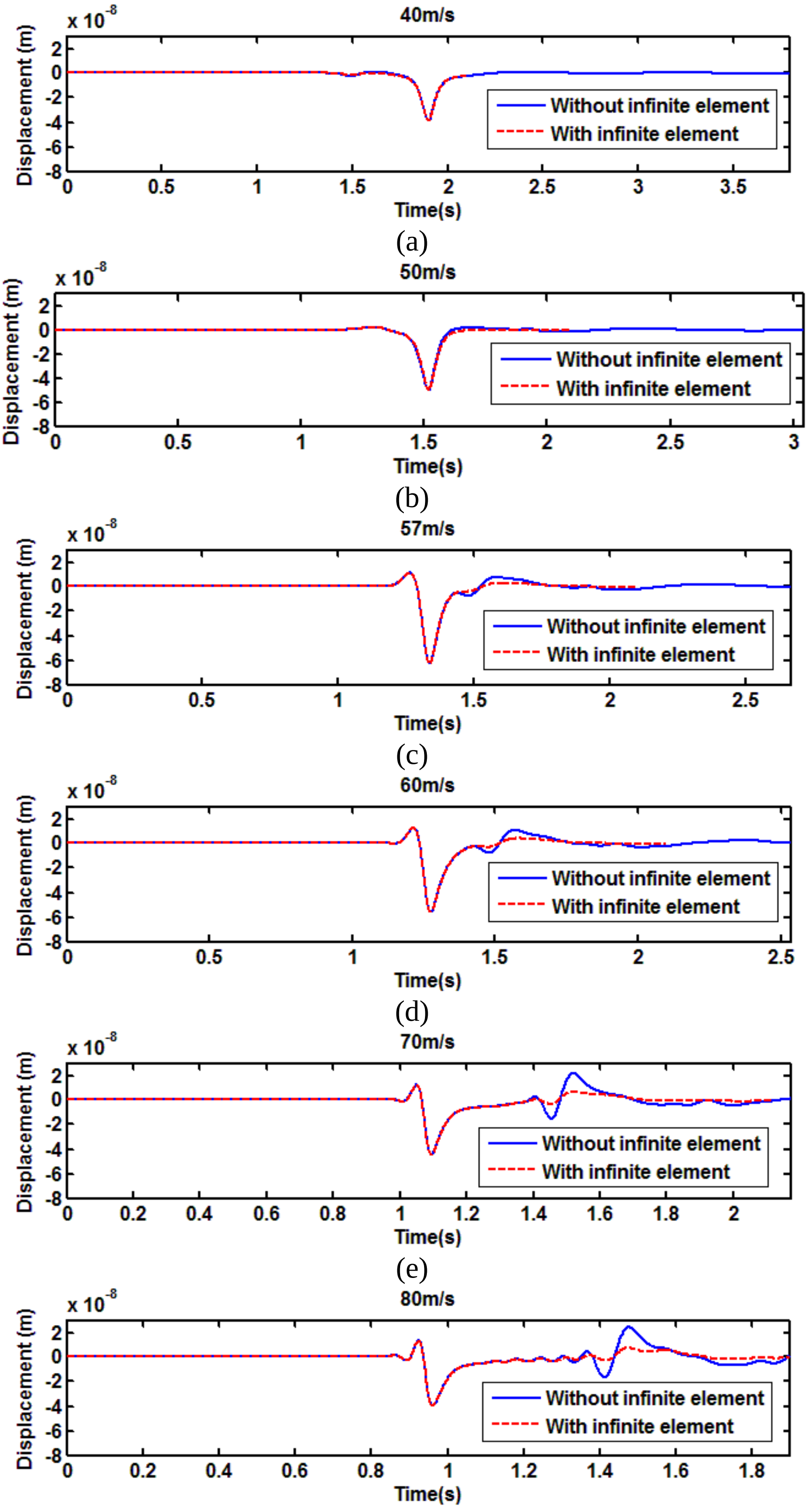

(a)

(b)

(c)

(d)

(e)

(f)

Figure 6-7 Comparison of midpoint displacement for a moving load of 1 N between the models with and without the infinite elements; (a) V=40m/s; (b) V=50m/s; (c) V=57m/s; (d) V=60m/s; (e) V=70m/s; (f) V=80m/s;

The maximum downward rail displacements at each position along the rail for different load speeds are plotted in Fig. 6-8. These are obtained from the model with fixed boundaries. The results for the load speeds higher than the critical speed, Fig. 6-8(d)~(f), show good convergence after an initial transient. As can be seen, the amplitude of the maximum displacements in the steady state is constant even in the presence of the reflection. This is because the reflection has a smaller downward displacement than the initial displacement under the load, as shown in Fig 6.4 so it does not affect the maximum displacement. The case close to the critical speed, shown in Fig. 6-8(c), has not yet achieved convergence and will be discussed further in Section 6.3.3 below.

However, in the results from the load speeds lower than the critical speed, Fig. 6-8(a)~(b), some oscillations can be seen. This is related to the width being insufficient suggesting that a wider model is still required for speeds close to but lower than the critical speed, as mentioned in Section 5.7. To demonstrate this, results from a 40 m wide model are compared with the results from the 20 m wide model in Fig. 6-9. The oscillations no longer occur when the wider model is used.

In summary, the reflection from the side boundary is evident when the load speed is higher than the critical speed. A small reflection still occurs even when the infinite elements are used, as the wave incident on the boundary is not perfectly absorbed. Moreover, for load speeds close to but lower than the critical speed the fixed boundaries affect the rail deflection. A wider model will be considered in Section 6.3.3. First, however, the influence of damping is discussed.

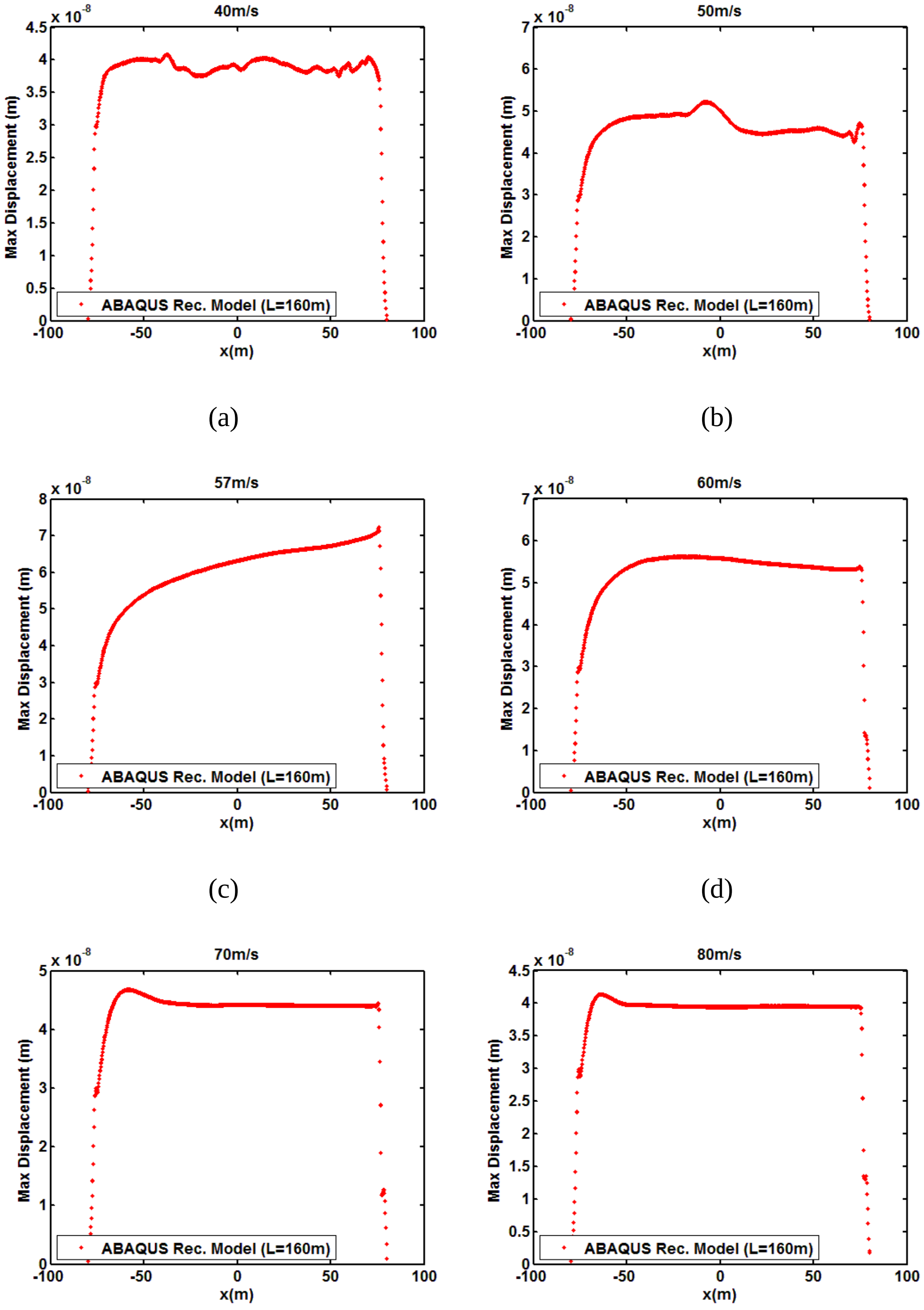

(a) (b)

(c) (d)

(e) (f)

Figure 6-8 The maximum displacements at each point along the rail found from a model with 20 m width and fixed boundaries; (a) *V*=40 m/s; (b) *V*=50 m/s; (c) *V*=57 m/s; (d) *V*=60 m/s; (e) *V*=70 m/s; (f) *V*=80 m/s

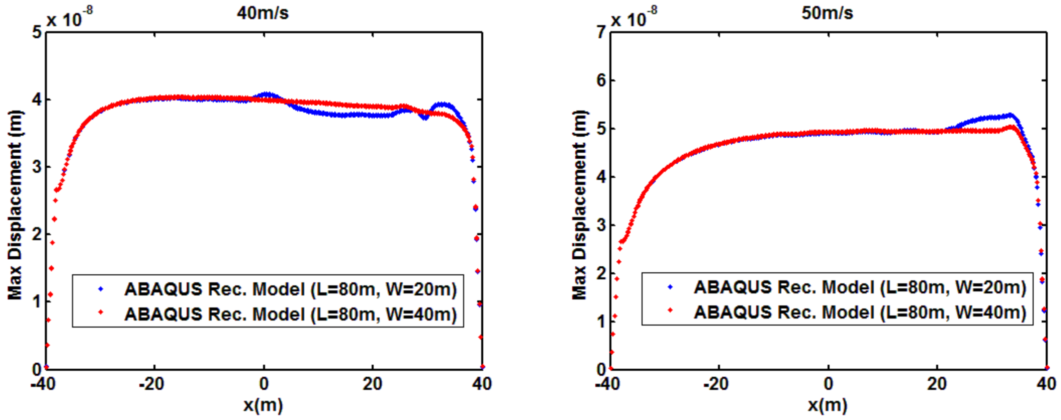

(a) (b)

Figure 6-9 The maximum displacement at each position along the rail found by using models with fixed boundaries and different widths; (a) *V*=40 m/s; (b) *V*=50 m/s

6.3.2 Influence of the Rayleigh damping parameters

Damping describes the energy dissipation. In an infinite medium, there are two main sources of attenuation of vibration, geometric attenuation and material damping. Geometric attenuation describes a reduction in wave amplitude as the wave propagates outward from the load. On the other hand, material damping causes attenuation by the transfer of the vibration energy to thermal energy.

As discussed in Chapter 4, Rayleigh damping is formed as a linear combination of the mass and stiffness matrices (see Eq. (4-5)). A given value of loss factor can be achieved at a single frequency (see Eq. (4-6)) for a model where either α or β are zero, or at two frequencies where both are non-zero. The influence of adopting different values for α and β on the reflections from the boundary is studied here. Four different sets of Rayleigh damping parameters are used, as listed in Table 6-1.

Table 6-1 List of Rayleigh damping parameters

α (s^{-1})	β (s)
0	0.000159
0	0.000636
3.925	0
0.98	0.000159

The equivalent loss factor according to Eq. (4-6), obtained by using these four different values of α and β , is plotted in Fig. 6-10. Also shown is a constant value of loss factor of 0.05 which may be seen as a target. Higher loss factors are found at low frequency when non-zero values of α are used. On the other hand, if α is zero the loss factor is proportional to frequency, tending to zero at zero frequency. Thus, β has a greater contribution at higher frequencies whereas α dominates the damping at the lower frequencies. However, the moving load problem has an undefined frequency range so it is difficult to determine a suitable value.

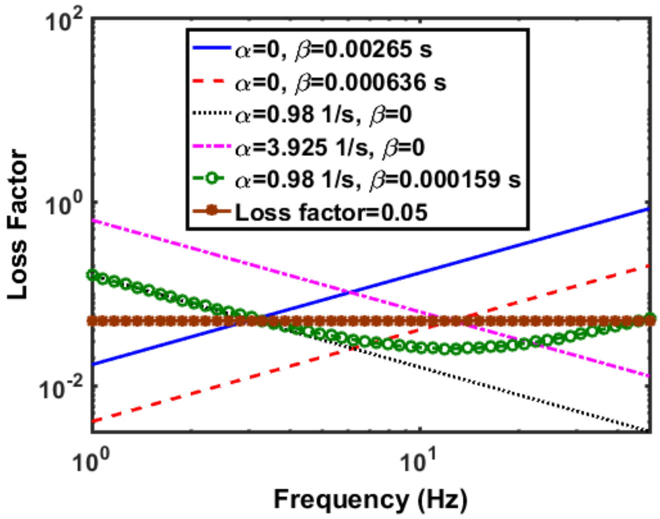

Figure 6-10 Equivalent loss factor

These various different damping models are investigated here in terms of the response to a moving load. A load speed of 60 m/s is used as an example. The displacement at the mid-point is shown in Fig. 6-11. The results in each case are compared with the original damping model (α = 0, β = 0.000159 s) as used in Chapter 5. The results in Fig. 6-11(a) show that even when β is increased by a factor of 4, only small differences are found compared with the result from the original model. The corresponding displacement field is shown in Fig. 6-12.

The reflection is reduced considerably when α is set to 3.925, as shown in Fig. 6-11(b) and Fig. 6-13. However, the amplitude of the maximum displacement becomes somewhat smaller than the results from the first model. Using a smaller value of α in combination with a non-zero value of β the maximum displacement agrees well with the results from the original model but a small reflection can be found, as shown in Fig. 6-11(c) and Fig. 6-14. β is assumed to be non-zero in order to control the reflection at higher frequency, which will be discussed in Section 6.5. Finally, a wider model with the same value of α as the previous model shows the best results, as shown in Fig. 6-11(d) and Fig. 6-15.

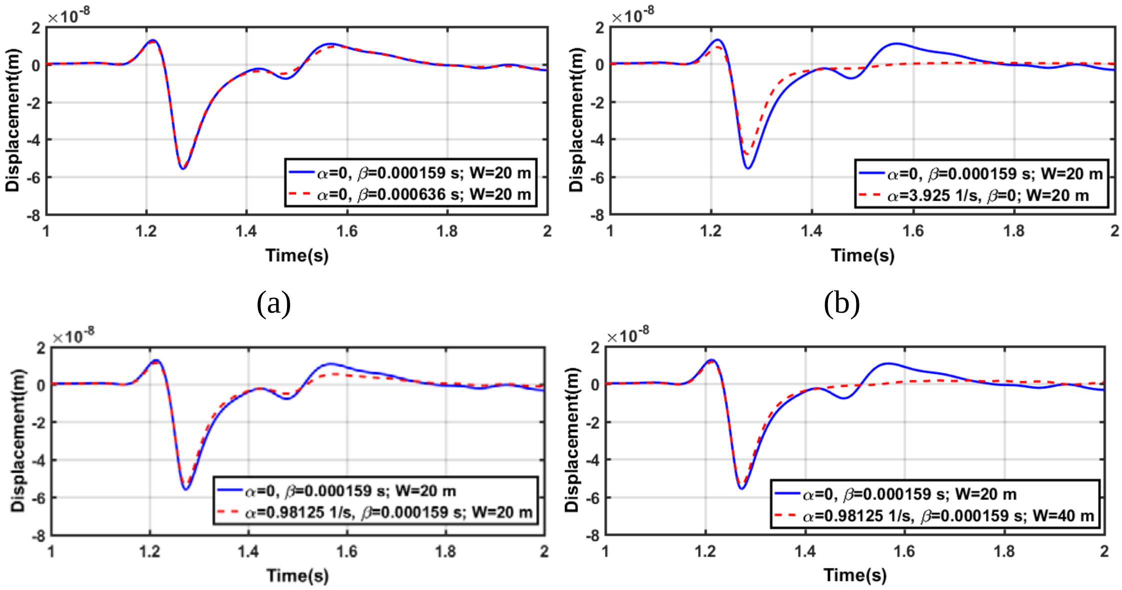

(a) (b)

(c) (d)

Figure 6-11 Comparison of four different model with the first model; (a) α=0, β=0.000636 s, W=20 m; (b) α=3.925 s^{-1}, β=0, W=20 m; (c) α=0.98 s^{-1}, β=0.000159 s, W=20 m; (d) α=0.98 s^{-1}, β=0.000159 s, W=40 m

To interpret these results it is useful to consider the decay with distance for a plane harmonic wave at circular frequency ω propagating in an elastic medium at a constant wave speed c

$$D=-20\log_{10}\left(\left|e^{i\bar{k}}\right|\right)=-8.69\,\mathrm{Im}(\bar{k})=8.69k\xi \tag{6-3}$$

where k is the wavenumber, which is given by $k=\omega/c$.The decay with distance for stiffness-proportional damping is proportional to the square of the frequency, $D=4.34\omega^2\beta/c$. So, for example, for $\beta=0.000636$ s (equivalent to $\eta=0.05$ at 12.5 Hz) the decay with distance is 0.002 dB/m at 1 Hz, rising to 4.8 dB/m at 50 Hz. Conversely for mass-proportional damping D is independent of frequency, $D=4.34\alpha/c$. Thus for $\alpha=3.25$ s^{-1}, D is 0.25 dB/m for all frequencies. As a result, it can be expected that mass-proportional damping will be equally effective at suppressing reflections from the domain boundaries at all frequencies, whereas stiffness-proportional damping will be ineffective at low frequencies.

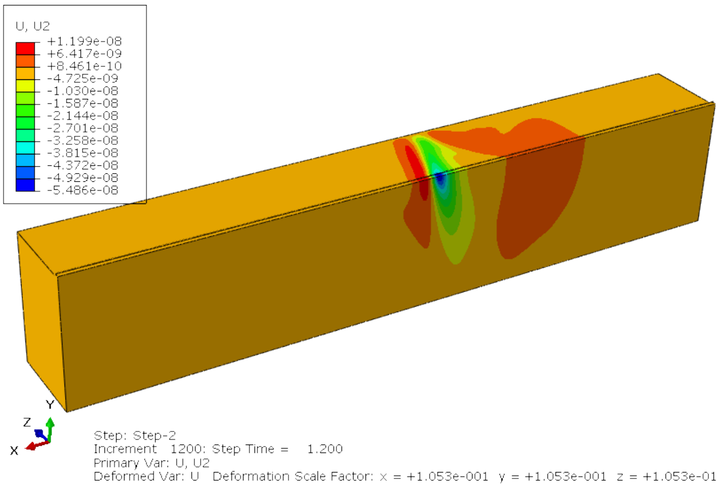

Figure 6-12 Displacements of the cuboid model when the load is at midpoint by stiffness damping β=0.000636 s (W=20 m)

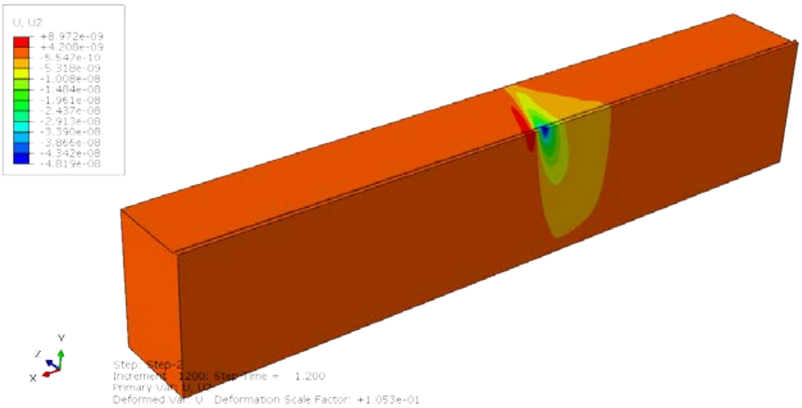

Figure 6-13 Displacements of the cuboid model when the load is at midpoint by mass damping α=3.925 s (W=20 m)

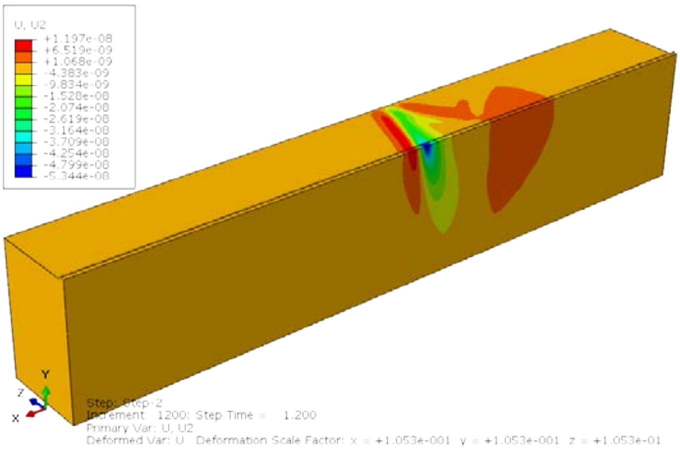

Figure 6-14 Displacements of the cuboid model when the load is at midpoint by Rayleigh damping α=0.98 s^{-1}, β=0.000159 s (W=20 m)

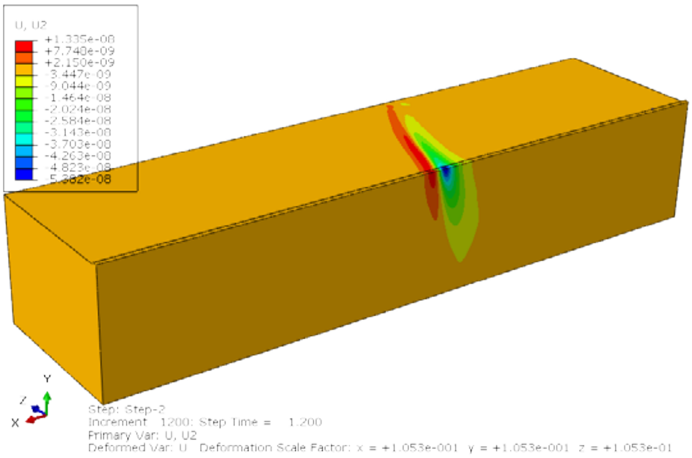

Figure 6-15 Displacements of the cuboid model when the load is at midpoint by mass damping α=0.98 s^{-1}, β=0.000159 s (W=40 m)

Finally, in Fig. 6-16 the results using α= 0.98 s^{-1} and β= 0.000159 s for the two different widths are compared with the results including infinite elements. A very clear reflection is found when the 20 m width model is used, which gives 1.5 dB reduction at 20 m based on mass-proportional damping. The results with the infinite elements have a smaller reflection but, as it is still present, this model should also be wider. On the other hand, almost no reflection is found when the 40 m wide model without infinite elements is used, which gives 3 dB of reduction at 40 m based on mass-proportional damping. As a result, a reduction of 3 dB is sufficient for the homogeneous half-space to avoid the effect from the reflection from the side.

Although a wider model with infinite elements could be used to have better results, the efficiency of a model including infinite element in ABAQUS is poor. A comparison between the calculation times required for the moving load problem when using three different ground models is given in Table 6-2. These simulations were run in parallel using 16 processors on a supercomputer, iridis 4, which has 2.6 GHz processors with 4 GB of memory per processor. The 40 m wide model without infinite elements is thus preferred to the model with infinite elements. As a result, a wider model without consideration of infinite element is used for further simulations.

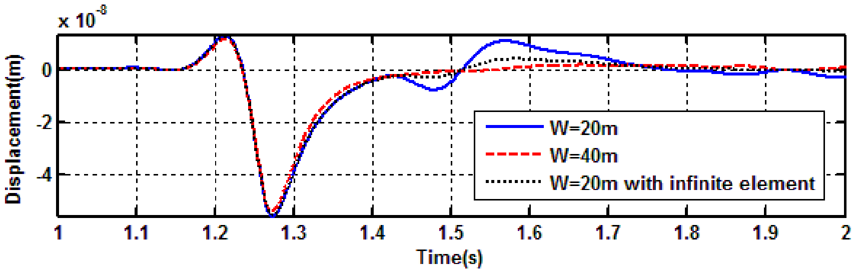

Figure 6-16 Rail displacement obtained by using different widths of model when load speed is 60 m/s

Table 6-2. Calculation times and model sizes required for various models in ABAQUS

V (m/s)	Cuboid 80x40x30 m Time (hr)	Cuboid 80x20x30 m with infinite elements Time (hr)	Hemisphere with infinite elements radius 40 m Time (hr)
40	11	27	18
57	7.8	19	12.5
80	5.5	13.5	9
dof	1,181,472	1,024,800	1,446,306

6.3.3 Investigation of the required length

As discussed in Sections 4.3.2 and 5.7, the results require sufficient time to reach steady state, especially close to the critical speed. The method introduced in Section 4.3 is used again here to determine the convergence point of the results. Examples are shown in Fig. 6-17.

Different model geometries are used for different load speeds to investigate the distances required for the result to reach steady state. In each case these are 40 m wide and 30 m deep and use the combined damping with α=0.98 and β=0.000159. A length of 80 m is found to be sufficient for most speeds but a longer model is required for load speeds close to the critical speed. As a result, a 40x320x30m model is used for speeds between 55 m/s and 60 m/s.

The maximum displacement is plotted against speed in Fig. 6-18 from which the critical speed can be seen. Results are also shown from the wavenumber FE/BE model (Sheng et al., 2005) for a constant value of loss factor of 0.05. Around 5% difference in displacement can be found between the various results from ABAQUS and the wavenumber FE/BE model at lower speeds (≤50 m/s) and higher speeds (≥60 m/s). This can be attributed to differences in mesh density as discussed in Section 5.4.3. However, the results from ABAQUS are around 25% lower than the results from the wavenumber FE/BE model for speeds close to the critical speed (57 m/s). This can be attributed to differences in the damping models used. The results from the wavenumber FE/BE method obtained by using different constant loss factors are shown in Fig. 6-19. These results show large differences when the load speeds are close to the critical speed, with larger amplitudes occurring for smaller loss factors. However, changes to the loss factor do not have much effect for the higher and lower speeds. As a result, it is clear that the damping has a significant influence for the region close to the critical speed.

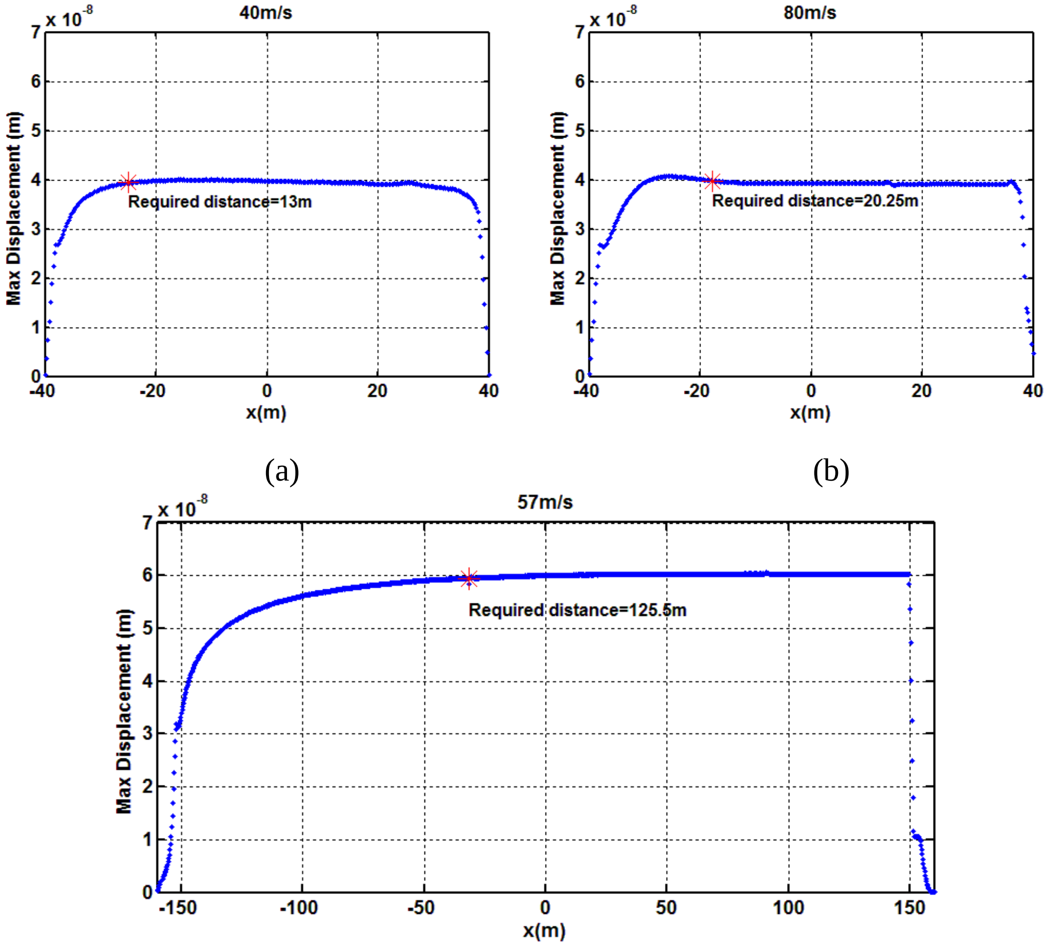

(a) (b)

(c)

Figure 6-17 The maximum displacements at each position along the rail from model with α=0.98 s^{-1}, β=0.000159 s and W=40 m; (a) V=40 m/s; (b) V=80 m/s; (c) V=57 m/s

It is difficult to make a direct comparison between the two models because of the different damping models used. A constant loss factor model is used in the wavenumber FE/BE software, which cannot easily be modified, whereas the FE model in ABAQUS uses viscous Rayleigh damping for the calculation in the time domain. The damping of the two models is equivalent at only one or two frequencies, as shown in Fig. 6-10. However, the moving load problem does not exhibit periodic phenomena so there is no resonance frequency that can be used to determine the frequency at which to set the models to be equal.

As discussed in Section 6.3.2, β does not have a significant influence on the results as it has more influence at higher frequency. In contrast, the results change a lot with different values of α. In the results in Fig. 6-18 three different values of α are used which are equivalent to η = 0.05 at 3 Hz, 1 Hz and 0.3 Hz whereas β is kept fixed as 0.000159 s. The dependence of the amplitude on speed is shown in Fig. 6-18 for the various damping levels. As can be seen, the damping only influences the results close to the critical speed where the amplitude increases with lower values of α. A better agreement with the wavenumber FE/BE model can be found when 0 is used for α. For comparison, the lengths required for convergence with these four different levels of damping are shown in Fig. 6-20. As shown, the required model size is the same for all speeds, except close to the critical speed where a longer model is required for smaller values of α.

In Fig. 6-21 the results are shown in the spatial domain for three different speeds, 40 m/s, 57 m/s, and 80 m/s, after they have reached steady state. Time domain results are extracted from ABAQUS at the converged point and transfered to the spatial domain. Results are shown for $\alpha = 0.1$ s^{-1} and 0 with $\beta = 0.000159$ s, as before. These are compared with the results from the wavenumber FE/BE model for a loss factor of 0.05. Good agreement can be seen for the lower and higher speeds but, as shown in Fig. 6-18, the maximum amplitude at the critical speed is lower for the FE model when $\alpha = 0.1$ s^{-1} is used. Although better agreement in terms of the maximum amplitude can be found when $\alpha = 0$ is used, significant reflections can be found. As a result, a non-zero value of alpha is still required to avoid the reflection.

In the end, the results from the cuboid model agree better with those of the wavenumber FE/BE model than the results from the hemispherical model due to the fact that a longer model can be used, which has been shown to be essential close to the critical speed.

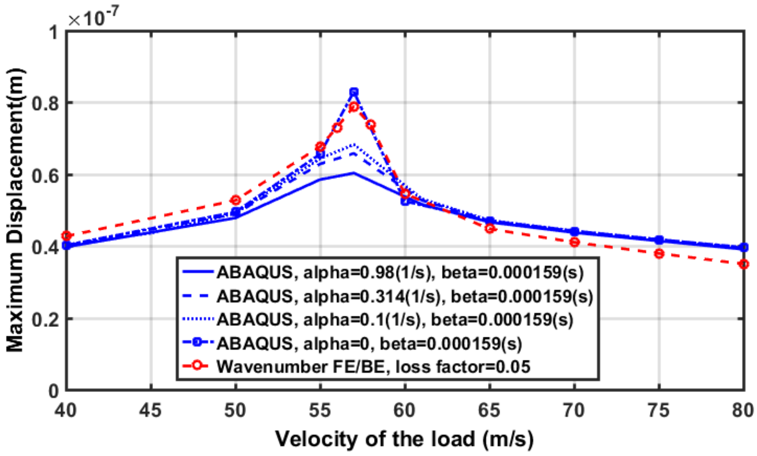

Figure 6-18 Maximum displacements plotted against load speed obtained by using different values of Rayleigh damping and compared with the wavenumber FE/BE model

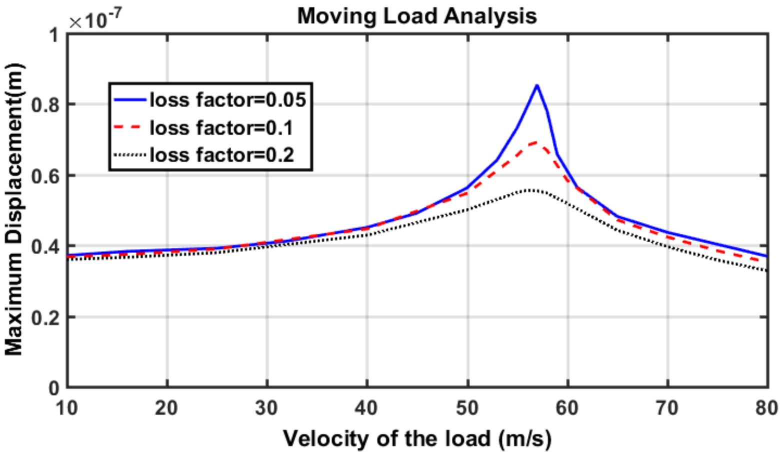

Figure 6-19 Maximum displacements plotted against load speed obtained by using wavenumber FE/BE method with different constant values of loss factor

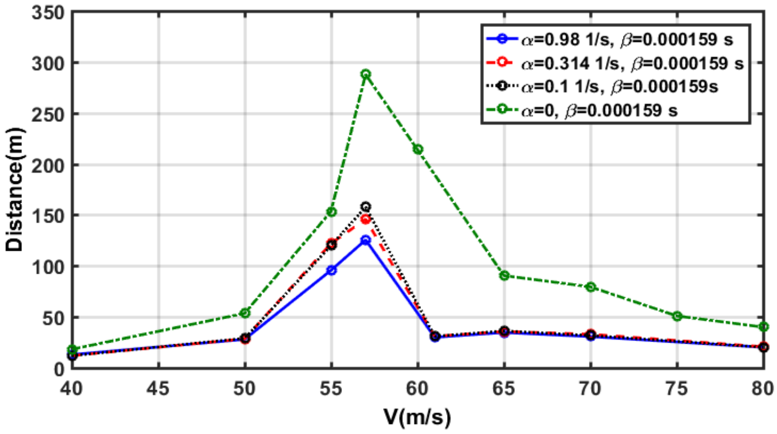

Figure 6-20 Required distances for different load speeds by using different Rayleigh damping

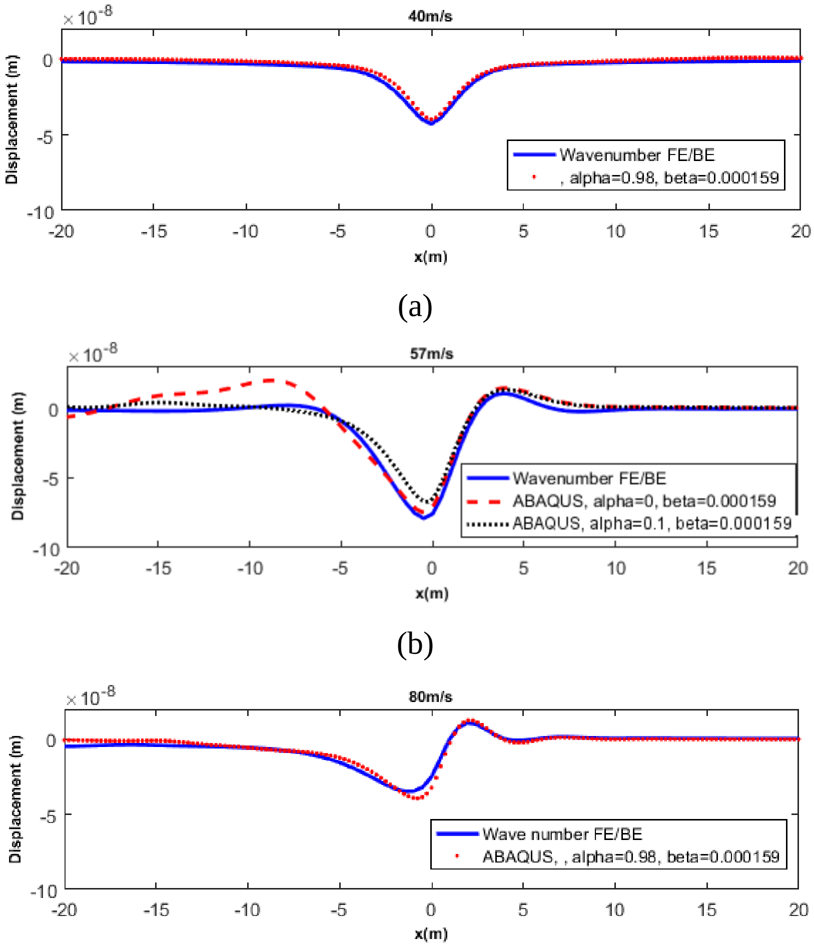

(a)

(b)

(c)

Figure 6-21 Displacement of the rail with different load speeds from ABAQUS and wavenumber FE/BE model (with loss factor 0.05); (a) *V*=40 m/s; (b) *V*=57 m/s; (c) *V*=80 m/s

6.4 Cuboid model for layered half-space with a moving load

Results are presented in this section for a moving load on the layered half-space ground, based on the parameters in Table 5-2. The same 80×40×30 m cuboid mesh with fixed boundaries as used for the homogeneous half-space is again used here with the same element sizes. It has been shown that a 40 m wide model can effectively reduce the reflection from the side boundary for the homogeneous half-space (see Fig. 6-11(d) and 6-15) using Rayleigh damping with $\alpha = 0.98$ s^{-1}, $\beta = 0.000159$ s. However, for a layered ground, when the travelling load speed is higher than the Rayleigh wave speed in the upper layer, an oscillation can be found behind the load (a more detailed discussion can be found in Chapter 7). As a result, the damping should be selected based on this oscillation frequency. For the case of the layered half-space considered here, this oscillation is found at about 10 Hz (see Fig. 6-27) and this is used as the dominant frequency at which to calculate the value for the equivalent loss factor for mass-proportional viscous damping value based on Eq. (4-6). The same stiffness-proportional damping value as used for the homogeneous ground is used in order to avoid the reflection at higher frequency. Thus, Rayleigh damping with $\alpha = 3$ s^{-1}, $\beta = 0.000159$ s is considered for the moving load simulations on the layered half-space.

In Fig. 6-22(a) the maximum displacement is plotted against load speed. Good agreement can be seen compared with the results from the wavenumber FE/BE model. The critical speed for the layered half-space ground can be identified as 85 m/s, which is higher than for the homogeneous half-space and higher than the Rayleigh wave speed in the soft soil layer. The length required to reach steady state for the layered ground is shown in Fig. 6-22(b). Compared with Fig. 6-20 it can be seen that the required model size is much smaller than for the homogeneous half-space, especially at the critical speed (85 m/s), and consequently the model length of 80 m used is sufficient.

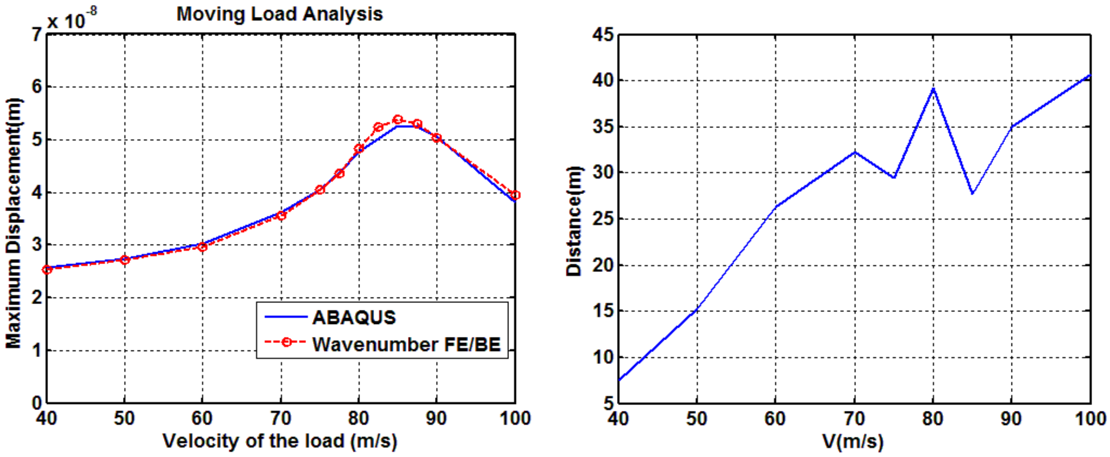

(a) (b)

Figure 6-22 Results for layered half-space ground. (a) Length of transient zone required for convergence to steady-state solution for different load speeds; (b) Maximum deflection of track during the passage of a unit load plotted as a function of speed

The rail displacements in the spatial domain at four different speeds are shown in Fig. 6-23; these results also agree well with the results from the wavenumber FE/BE model. A clearer oscillation behind the load can be seen for the two higher speeds, as shown in Fig. 6-23(c)~(d). Figure 6-24 shows the top view of the ground displacement at different load speeds and the same phenomenon can be also found. Even though this phenomenon cannot be found in the rail displacement at a load speed of 70 m/s, it is clear that an oscillation tail occurs when the load speed is higher than the Rayleigh wave speed of the upper layer, which is around 60 m/s here, as shown in Fig. 6-24(b)~(d).

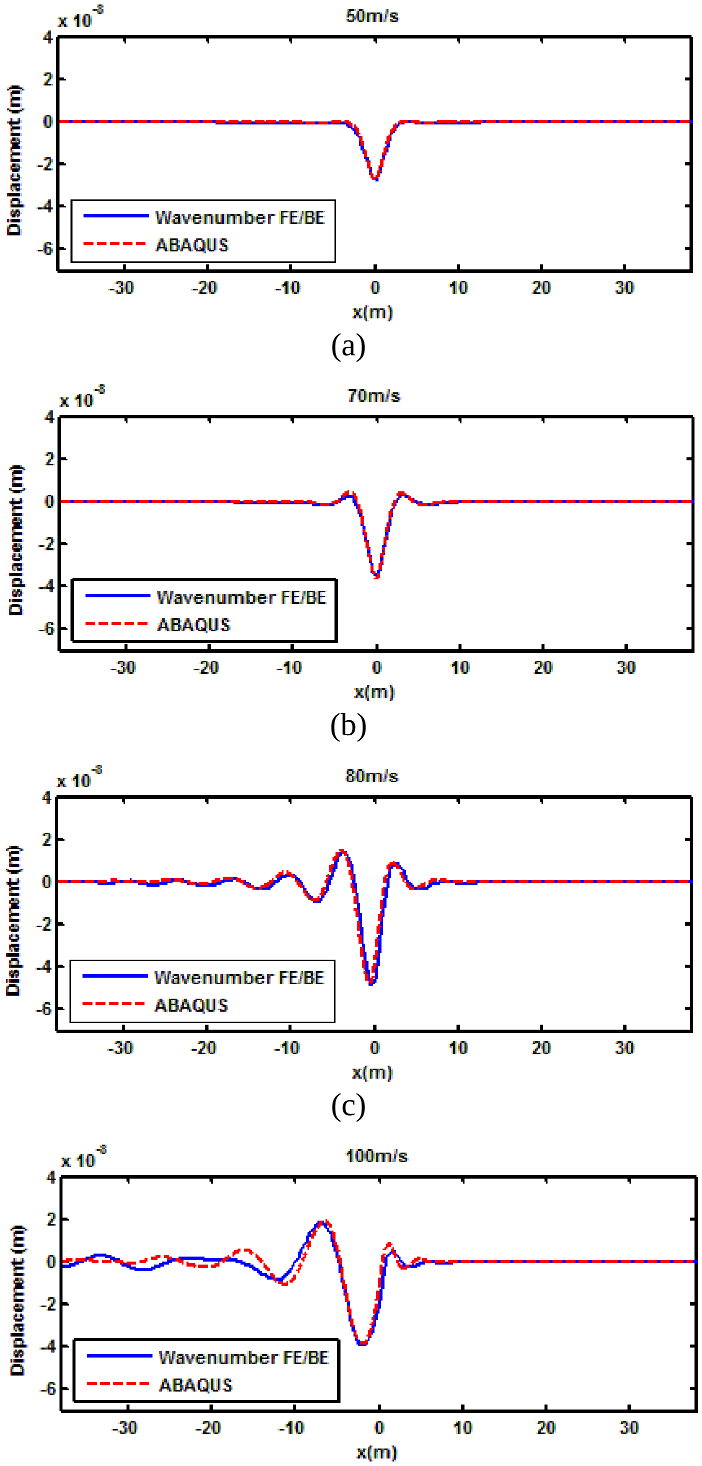

(a)

(b)

(c)

(d)

Figure 6-23. Comparison between the results from FE model and the results from wavenumber FE/BE for layered half-space; (a) V=50 m/s; (b) V=70 m/s; (c) V=80 m/s (d) V=100 m/s

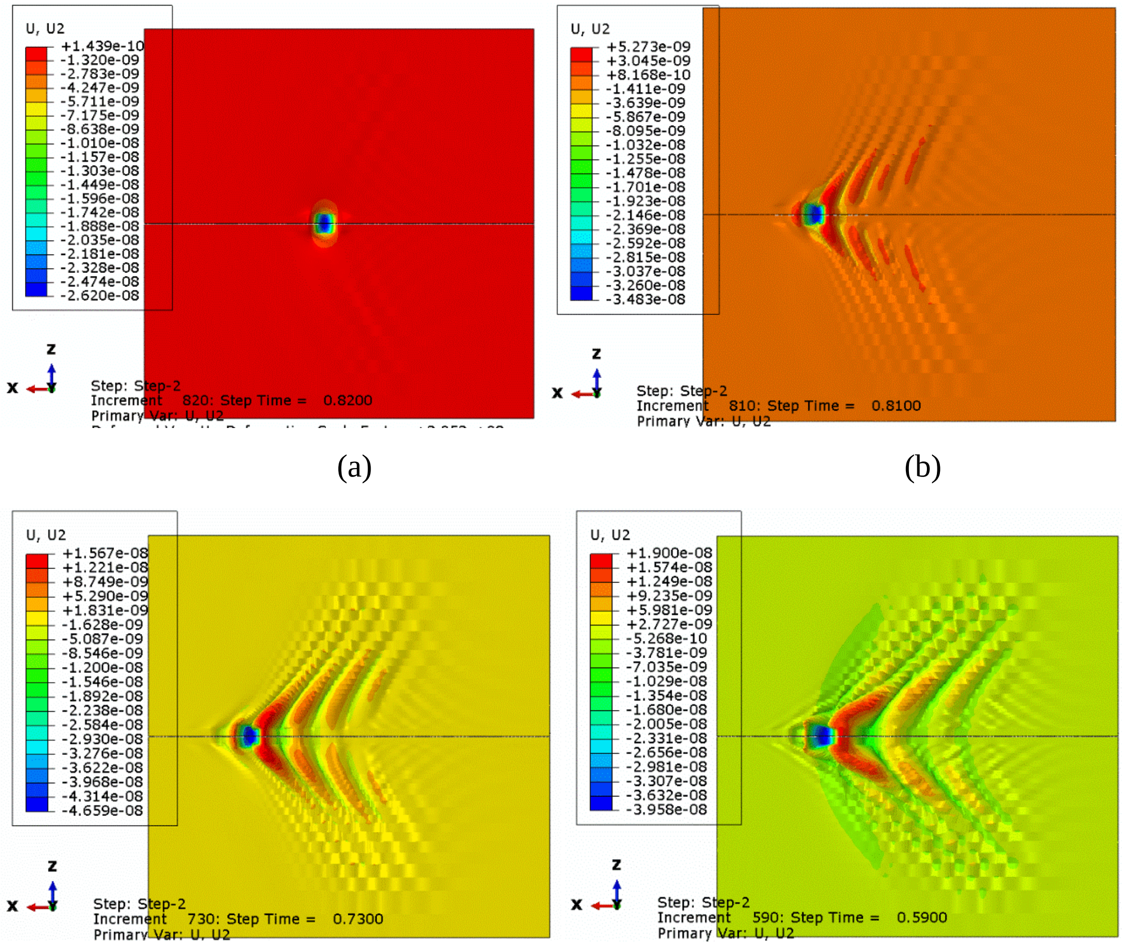

(a) (b)

(c) (d)

Figure 6-24**.** Displacement of the layered half-space in the space domain for different load speeds (top view); (a) *V*=50 m/s; (b) *V*=70 m/s; (c) *V*=80 m/s (d) *V*=100 m/s

6.5 Response of track/ground model to a harmonic load

The 40 m wide cuboid model with appropriate Rayleigh damping has been shown to be suitable for the moving load problem, even though a fixed boundary is used. In this section results are presented for a static harmonic load applied on the track for both hemispherical and cuboid models. A hemispherical model with 40 m radius is compared with a 80×40×30 m cuboid model without infinite elements and a 80×20×30 m cuboid model with infinite elements. The results for both the homogeneous half-space and the layered half-space are compared with the results from the wavenumber FE/BE model. The maximum element size at the track in these two models is 0.25 m, which gives 8 nodes per Rayleigh wavelength at 38 Hz (or 6 nodes per wavelength at 50 Hz).

Fig. 6-25 shows the point receptance of the track on the homogeneous half-space obtained from the hemispherical model. Here the damping model ($\alpha = 0.98$ s^{-1}, $\beta = 0.000159$ s) is chosen to fit to a loss factor of 0.05 at 3 Hz and 50 Hz. The receptance is flat at low frequencies, corresponding to a stiffness line, before dropping above 10 Hz. The results from the hemispherical model show very good agreement with those from the wavenumber FE/BE model provided that the radius is not too small and the response point is not too near the edge.

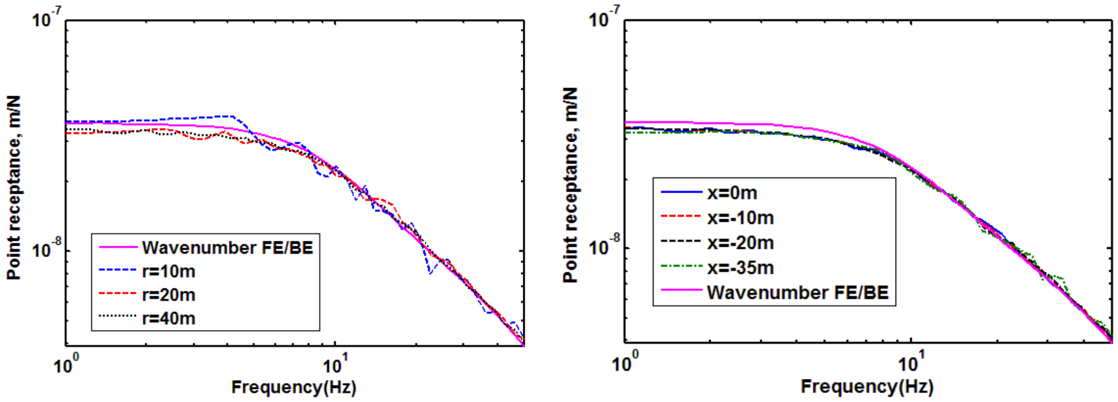

(a) (b)

Figure 6-25 Point receptance on the rail for homogeneous half-space ground ($\alpha = 0.98$ s^{-1}, $\beta = 0.000159$ s); (a) by using three different hemispherical models ; (b) when load applied at different locations for 40 m radius model

Results are shown in Fig. 6-26 for different damping models. Both hemispherical and cuboid models are compared. Here only small differences are found for the hemispherical model as the infinite elements control the reflections. In contrast, the results from the two cuboid models show significant variation depending on the value of damping used. Even though the results from the cuboid model with infinite elements show less fluctuation than those without the infinite elements, some small oscillations still can be found. The cuboid model with infinite elements will not be considered further as, although it gives improved results, it is much less efficient than the cuboid model without the infinite elements (see Table 6-2).

In Fig. 6-26(a)~(b) stiffness-proportional damping is used (α=0). Here, for the cuboid model without infinite elements, severe oscillations (±5 dB) are found at low frequencies due to reflections from the boundaries, as the equivalent loss factor is too small. Increasing β reduces this effect slightly, and the results become smoother at higher frequencies. Fig. 6-26(c)~(d) shows results for mass-proportional damping, in which β is taken to be zero. Here the oscillations at low frequency are much reduced and the results become similar at all frequencies.

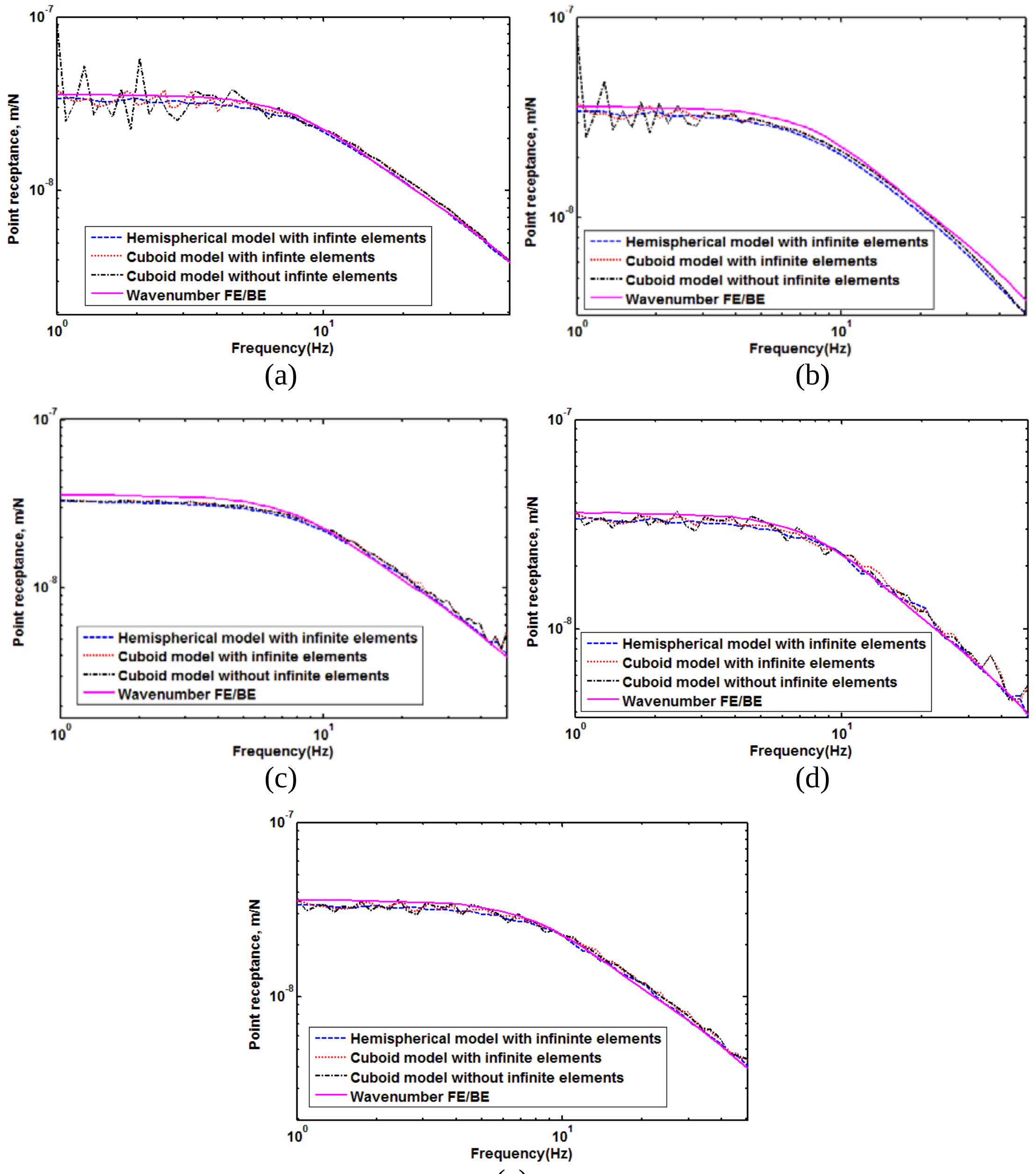

(a) (b)

(c) (d)

(e)

Figure 6-26 Point receptance on the rail for homogeneous half-space; (a) $\alpha = 0$, $\beta = 0.000636$ s; (b) $\alpha = 0$, $\beta = 0.00265$ s; (c) $\alpha = 3.925\ \mathrm{s}^{-1}$, $\beta = 0$; (d) $\alpha = 0.98\ \mathrm{s}^{-1}$, $\beta = 0$; (e) $\alpha = 0.98\ \mathrm{s}^{-1}$, $\beta = 0.000159$ s

Very good agreement can be seen in Fig. 6-26(c) whereas small oscillations (±1 dB) can still be found in Fig. 6-26(d). The value of damping used in Fig. 6-26(d) can be considered just sufficient, as a reduction of 6 dB is expected after 80 m (i.e. the distance to the boundary and back), see Eq. (6-3). In Fig. 6-26(e) the combined Rayleigh damping,

$\alpha = 0.98$ s^{-1} and $\beta = 0.000159$ s, gives good results across the whole frequency range with only a small oscillation (equivalent to less than 1 dB) at low frequency. The same values were found to give good performance for the moving load analysis, as presented in Section 6.3.2~3.

For the layered half-space, the receptance due to a harmonic load applied at the centre of the track is shown in Fig. 6-27. Unlike the homogeneous half-space ground, a clear peak can be seen at around 10 Hz which corresponds to the cut-on of waves in the upper soil layer (Thompson, 2009). The results based on the combined stiffness- and mass-proportional damping give the best agreement with the wavenumber FE/BE model for stationary harmonic load.

In the end the cuboid model with combined damping shows the best performance. Even though small oscillations can be found at low frequency, the differences are acceptable for the further simulations.

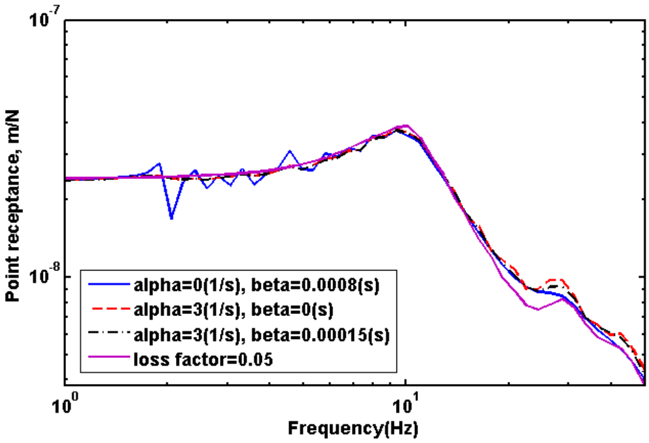

Figure 6-27 Receptance of layered half-space. Comparison of wavenumber FE/BE model (loss factor 0.05) with cuboid FE model with three different combinations of damping parameters

6.6 Influence of discrete sleepers

In the previous results in Chapters 5 and 6 an equivalent continuous track model has been used according to the parameters given in Section 5.3 (see also Table 4-8). In this section, a discrete sleeper model with sleeper spacing 0.6 m is introduced for comparison. The track model is identical to that studied previously in Fig. 4-35. The homogeneous half-space ground is not considered here due to the need for larger models leading to high simulation costs. A cuboid model with fixed boundaries and dimensions 80×40×30 m is used for the layered half-space ground. Properties can be found in Table 5-4. Results from orthotropic and isotropic railpad models are compared. The parameters used for the track, based on the same principles as discussed in Section 4.5.2, are listed in Table 6-3.

Table 6-3. Ballast track properties for discrete sleepers

Parameter	Value	Units
Rail mass density, ρ_r	7850	kg/m^3
Rail Young's modulus, E_r	2.1×10^{11}	N/m^2
Rail area, A_r	0.00763	m^2
Rail second moment of area, I	3.055×10^{5}	m^4
Railpad Young's modulus, E_p	1.2×10^{9}	N/m^2
Sleeper mass density, ρ_s	2500	kg/m^3
Sleeper Young's modulus E_s	3×10^{10}	N/m^2
Sleeper Poisson's ratio, v_s	0.15	
Sleeper height, h_s	0.2	m
Sleeper length (half), L_{sl}	1.3	m
Ballast Young's modulus, E_b'	5.2×10^{8}	N/m^2
Ballast mass density, ρ_b	2000	kg/m^3
Ballast Poisson's ratio, v_b	0.33	
Ballast top width (half), w_{b1}	1.3	m
Ballast bottom width (half), w_{b2}	1.6	m
Ballast height, h_b	0.3	m

Fig 6-28 shows the maximum displacement of the rail for the continuous and discretely supported models. Good agreement can be seen with the continuous model when orthotropic elements are used for the railpad. However, the critical speed observed from the model with discrete sleepers and isotropic railpads is around 25% higher than the results from continuous sleeper support. Furthermore, the results at lower speed are around 18% smaller than the results from the orthotropic railpad. This is due to the interaction between the track and the very soft ground. To help explain these results, Table 6-4 shows the maximum and minimum stress for the railpad in six directions from the results using isotropic and orthotropic railpad without consideration of ground, which can be treated as track on a very stiff ground, when a unit static load is applied in the middle. Although the results are quite different, the stress in the *y*-*y* direction (vertical) is almost identical. As a result, very small differences are found for the rail vertical receptance between models using the two elements, as shown in Section 4.5.3. However, significant differences can be found when soft ground is used, as shown in Table 6-5. The maximum stress in the *y-y* direction is 12 times higher when isotropic elements are used. Larger deflections occur when soft ground is considered that cause significant shear stresses in the *x-y* plane in the railpad, which constrains the rail deflection. In reality, the shear stress depends on the pad characteristic. However, the railpad model used here is not intended to be a reliable representation of the true shear stiffness, which is expected to be much lower than the vertical stiffness (Thompson and Verheij, 1997). This requires further investigation in the future.

Finally, the maximum and minimum stresses in the ballast layer at load speeds 40 m/s and 80 m/s obtained from the discrete sleeper model with orthotropic railpad are compared with the corresponding results from the continuous model in Tables 6-6~6-7.

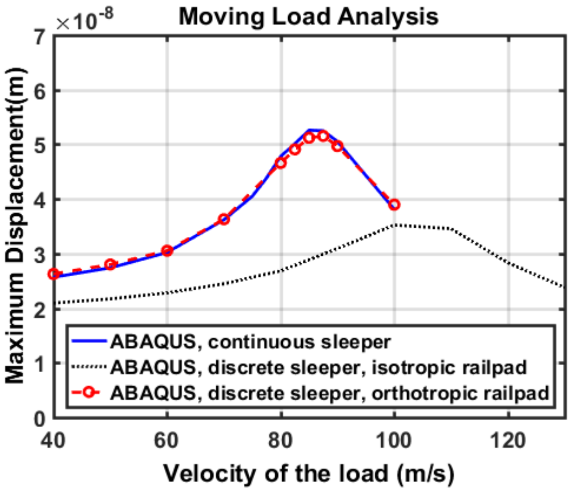

Figure 6-28 Maximum displacements plotted against load speed from track model using discrete sleepers and the continuous model for layered half-space

Table 6-4 Maximum and minimum stress for railpad from different railpad element (track model)

	σ_{xx}	σ_{yy}	σ_{zz}	σ_{xy}	σ_{yz}	σ_{xz}
Min stress						
Discrete (orthotropic railpad)	0	42.14	0	0	0	0
Discrete (isotropic railpad)	0.65	45.05	1.23	5.4	1.06	1.03
Max stress						
Discrete (orthotropic railpad)	0	1.743	0	0	0	0
Discrete (isotropic railpad)	2.48	2.067	0.2	5.4	1.06	1

Table 6-5 Maximum and minimum stress for railpad from different railpad element (track/ground model)

	σ_{xx}	σ_{yy}	σ_{zz}	σ_{xy}	σ_{yz}	σ_{xz}
Min stress						
Discrete (orthotropic railpad)	0	51.23	0	0	0	0
Discrete (isotropic railpad)	0.75	64.2	1.59	19.18	1.86	0.28
Max stress						
Discrete (orthotropic railpad)	0	0.91	0	0	0	0
Discrete (isotropic railpad)	2.59	12.7	0.23	24.62	1.96	0.35

Table 6-6 Maximum and minimum stress in ballast layer at load speed 40 m/s

	σ_{xx}	σ_{yy}	σ_{zz}	σ_{xy}	σ_{yz}	σ_{xz}
Min stress						
Continuous	2.78	2.08	1.6	0.27	0.2	0.23
Discrete (orthotropic railpad)	2.87	2.48	1.75	0.96	0.25	0.5
Max stress						
Continuous	1.77	0.14	1.38	0.27	0.83	0.23
Discrete (orthotropic railpad)	1.86	0.46	1.57	0.96	0.93	0.49

Table 6-7 Maximum and minimum stress in ballast layer at load speed 80 m/s

	σ_{xx}	σ_{yy}	σ_{zz}	σ_{xy}	σ_{yz}	σ_{xz}
Min stress						
Continuous	4.87	2.54	2.26	0.47	0.19	0.52
Discrete (orthotropic railpad)	5.6	4.01	2.92	0.63	0.29	0.88
Max stress						
Continuous	2.84	0.44	1.59	0.6	1.04	0.5
Discrete (orthotropic railpad)	2.94	0.96	2.12	1.1	1.36	0.72

In general, the amplitude of the stress in the ballast layer increases with increasing load speed. The stress levels from both models are very similar for the lower speed apart from the shear stress in *x*-*y* direction, which has a difference of around four times. However, less difference is found for the higher speed between the two models for the *x*-*y* direction (it is reduced to around 1.5 times) but the amplitude of the vertical stress from the discrete sleeper model is almost double that of the continuous sleeper model. Even though good agreement is found for the maximum rail deflection at different load speeds, as shown in Fig. 6-28, the discrete sleeper model will be used for the nonlinear model in Chapter 8 in order to capture the true stress behaviour.

6.7 Summary

A cuboid model of the ground has been developed for use with a moving load applied on the track/ground system. The most appropriate model geometry for different load speeds has been investigated. Reflection from the sides can be observed when the load speed is higher than the critical speed. Even though this reflection cannot be seen clearly for the lower speeds, a sufficiently wide model is still required for those speeds close to the critical speed due to their very wide wavefronts in the transverse direction. Infinite elements are considered along the side of the model but it is found that it is more efficient to increase the width of the model and use a suitable damping model.

It is shown that appropriate values for the Rayleigh damping can be used to avoid the reflection. A mass-proportional damping based on the width of the model is used in order to allow the wave attenuate efficiently along the horizontal direction. In the end a 40 m cuboid model with fixed boundary is used with α = 0.98 $s^{-1}$and β = 0.000159 s. This shows good results for a homogeneous half-space. Very good agreement is also found for assessment of critical speed in a layered half-space ground compared with the wavenumber FE/BE model.

Using this method, not only the problem of wave reflection has been solved, but also the efficiency of the simulation is much better than the model with infinite elements. The length required to reach steady state for different load speeds has been determined; this increases significantly near the critical speed of the homogeneous half-space. Assessment of the critical speed agrees well with the results from the wavenumber FE/BE method. Therefore, the cuboid model is used for the further simulation due to its good accuracy and efficiency. Furthermore, the problem of artificial displacements found with the hemispherical model with infinite elements has been overcome by using the cuboid model with fixed lower boundary.

The influence of discrete sleepers has been analysed and good agreement is found compared with the continuous sleeper model when orthotropic elements are used for the railpads in both models. However, the stress in the ballast layer, which is important for the nonlinear model, tends to be underestimated with the continuous model. As a result, the discrete sleeper model will be used for the nonlinear ground model in Chapter 8.

Chapter 7: Analysis of resonance effect for a track on a layered ground

7.1 Introduction

The influence of the damping model in suppressing unphysical reflections from the boundary of the model has been seen in Chapter 6. For a homogeneous half-space the Rayleigh damping coefficients can be chosen to match the desired loss factor over a particular frequency range, with the mass-proportional term ensuring that reflections from the boundary are sufficiently attenuated. However, as has been seen in Section 6.4, when the track is located on a layered ground, a resonance phenoemenon occurs in the track behind the load when it travels faster than the Rayleigh wave speed of the upper layer. As a result, a good understanding of this resonance phenomenon is important in establishing suitable damping models for the ground, especially for time domain modelling.

In this chapter, a parametric study is carried out to investigate this resonance frequency of a layered ground. For convenience, this analysis is carried out by using a three-dimensional semi-analytical method[2] (Sheng et al., 1999a, 1999b) instead of the time domain FE model used in the rest of this thesis, as this has a much better efficiency. This model is based on the formulation of Haskell and Thomson (Haskell, 1953; Thomson, 1950) and uses a two-dimensional Fourier transform over the axial and lateral coordinates to represent the layered ground in terms of the corresponding wavenumbers. The track is represented by a layered beam structure coupled to the ground over a finite strip. A static or moving load can be considered which may be either constant or harmonic.

Here three different methods are used to determine this resonance frequency for a track on a layered half-space. In the first method, the semi-analytical method is used to calculate the rail receptance induced by a stationary harmonic load applied on the rail (Sheng et al., 1999b). Second, a quasi-static load moving along the track is considered using the same model (Sheng et al., 1999a). The frequency spectra of the response in the non-moving frame to the moving load are obtained and used to identify the resonance frequency. Third, following the method of (Sheng et al., 1999a), dispersion curves from the layered half-space with and without the track are calculated and used to estimate the

---

[2] The model was programmed by Dr. Evangelos Ntotsios.

resonance frequency for different load speeds by finding the intersection points between the dispersion relationship and load speed line.

The layered half-space ground parameters used in Chapter 5 and 6 is used here as a reference. Six different sets of parameters based on different depth of the first layer and different P-, S-wave speed for the substratum are used and compared with results for a homogeneous half-space. Note here a softer layer is always considered for upper layer for all cases. The critical speed is determined first for each case from the semi-analytical model. Then the resonance frequency is assessed using the various methods and the results are compared. Finally, the results from the above methods are compared with the results from the formulae indicated by (Kacimi et al., 2013; Kouroussis et al., 2014; Mezher et al., 2015).

7.2 Parameters used in the study

A range of different cases are introduced here for ground with a single soft layer above a stiffer half-space. The parameters defining these cases are listed in Table 7-1. These are the P-, and S-wave speeds for the upper layer and the underlying half-space, as well as the depth of the first layer. The S-wave speed of the upper layer is kept fixed at 60 m/s and the other wave speeds are varied relative to this. The soil density is set to 2000 kg/m^3 throughout and the damping loss factor is 0.05 in each case.

Case 1 has the same properties as the layered ground considered in previous chapters and is used as the reference case for comparison with the others. In cases 2 and 3 the P-wave speeds of the two layers are varied whereas in cases 4 and 5 the S-wave speed of the underlying half-space is varied while keeping the P-wave speed equal to twice the value of the S-wave speed. In cases 6 and 7 the layer depth is varied while keeping the same wave speeds as case 1. The homogeneous half-space is an extreme case with an infinitely deep upper layer. The critical speeds will be discussed in Section 7.3.

The track properties used in each case are listed in Table 7-2. These are equivalent to the track model used in previous chapters. The wavenumbers are equally spaced both parallel and normal to the track. In each direction the maximum wavenumber is set to 10π rad/m. The number of wavenumber points in each direction is set to 2048.

Table 7-1 Parameters used to define the ground

Case No.	layer depth, H (m)	1st layer P-wave, c_{p1} (m/s)	1st layer S-wave, c_{s1} (m/s)	2nd layer P-wave, c_{p2} (m/s)	2nd layer S-wave, c_{s2} (m/s)	Critical speed, V_{cr} (m/s)
1	2	120	60	240	120	79
2	2	240	60	240	120	80
3	2	240	60	480	120	80
4	2	240	60	480	240	82
5	2	120	60	170	85	70
6	4	120	60	240	120	62
7	8	120	60	240	120	57
8	inf	120	60	-	-	57

Table 7-2 Track properties (for two rails)

Parameter	Value	Units
Rail mass	120	kg/m
Rail bending stiffness	1.28×10^7	Nm^2
Rail damping loss factor	0.01	
Railpad stiffness per unit length	10×10^8	N/m^2
Railpad damping loss factor	0.1	
Sleeper mass per unit length	541.8	kg/m
Ballast stiffness per unit length	4.64×10^9	N/m^2
Ballast mass per unit length	1740	kg/m
Ballast damping loss factor	0.04	
Ballast width at the bottom	3.2	m

7.3 Investigation of the critical speed

To determine the critical speed, the maximum displacement on the track induced by a moving point load is calcuated by using the three-dimensional semi-analytical track/ground model of (Sheng et al., 1999a). The results for the various parameter sets are shown in Fig 7-1.

As shown in Fig 7-1(a), compared with case 1, the maximum displacement is reduced at all speeds by around 18% when the P-wave speed of the first layer is doubled (case 2). Almost the same results are found when additionally the P-wave speed of the second layer is doubled (case 3). When both the P-wave speed and S-wave speed of the underlying layer are increased as well as the P-wave speed of the upper layer (case 4) the deflection reduces by about 30% compared with case 1. However, the critical speed found in these four cases remains almost the same, as shown in Table 7-1. The critical speed only increases slightly when the S-wave speed of the underlying half-space is increased.

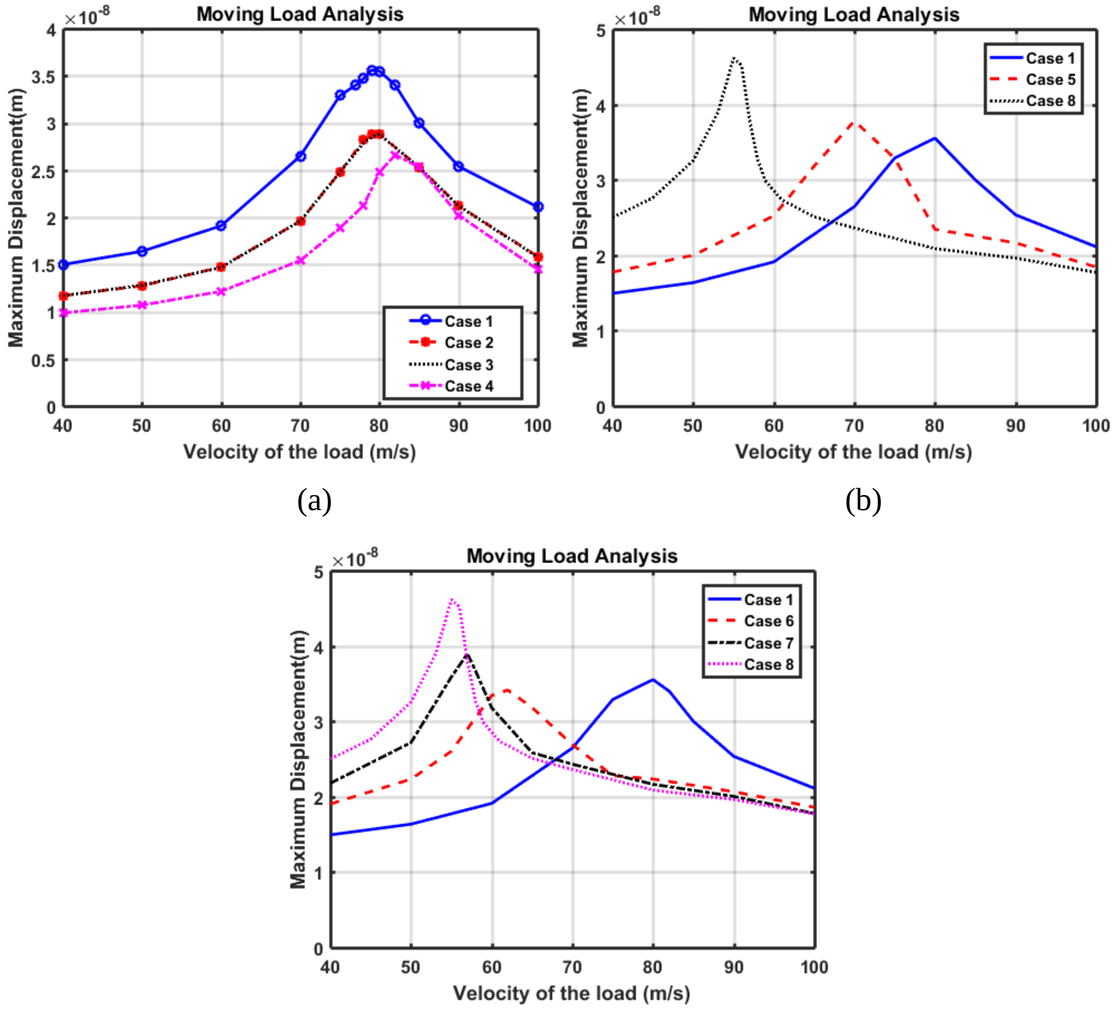

(a) (b)

(c)

Figure 7-1 Maximum displacement as a function of load speed for different cases; (a) variation of c_{p1}, c_{p2} and c_{s2}; (b) variation of c_{s2}; (c) variation of layer depth

Fig. 7-1(b) shows the influience of changing the S-wave speed of the underlying half-space. The critical speed changes from 79 m/s to 70 m/s when the S-wave speed of the second layer is reduced from 120 m/s to 85 m/s (case 5). Reducing it further to 60 m/s (the same properties as the upper layer) produces a homogeneous half-space, for which the critical speed is found to be 55 m/s. Thus, significant differences in critical speed are found when the shear wave speed of the lower layer is changed. Moreover, the displacement at the critical speed is increased as the soil becomes softer.

Fig. 7-1(c) shows the effect of varying the depth of the first layer. Here also the critical speed tends to decrease and the maximum deflection tends to increase as the layer depth is increased.

7.4 Investigation of the resonance frequency for layered half-space

7.4.1 Responses to a stationary harmonic load

The response due to a stationary harmonic load acting on the rail is shown in Fig. 7-2 in the form of the point receptance. As can be seen, the first resonance frequency occurs at around 10 Hz for cases 1 to 5, which have the same layer depth but different wave speeds for the ground. On the other hand, the resonance frequency decreases when the depth of the layer is increased, as seen for cases 6 and 7, and eventually no clear peak can be found for the homogeneous half-space (case 8). A second resonance frequency occurs at around 40 Hz in all cases. However, the receptance becomes much lower than at the first resonance frequency. As a result, the investigation focusses on the first resonance frequency.

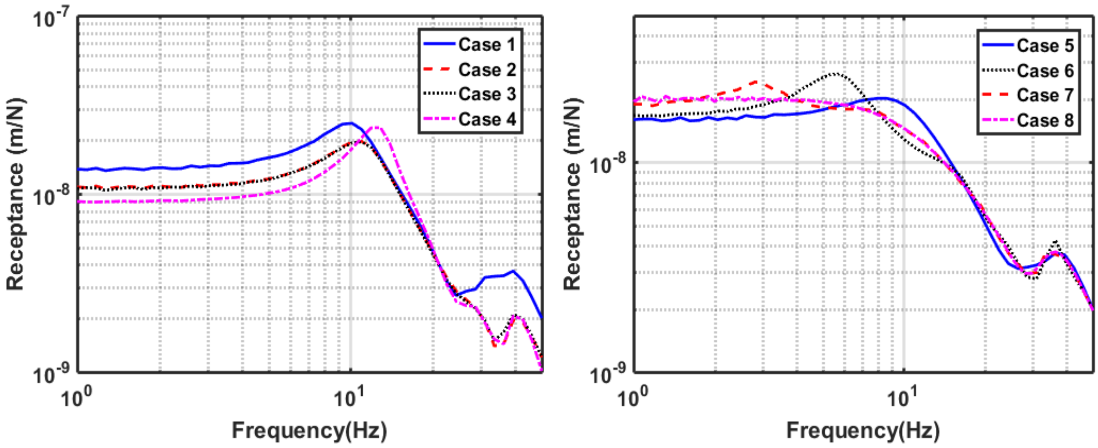

(a) (b)

Figure 7-2 Receptance of the rail from seven different models; (a) Cases 1~4; (b) cases 5~8

The resonance frequencies found in these seven cases are listed in Table 7-3. They will be compared with results from the other methods in Section 7.4.4 below.

Table 7-3 The resonance frequencies found in seven cases

	Resonance frequencies
Case 1	10 Hz
Case 2	11 Hz
Case 3	11 Hz
Case 4	13 Hz
Case 5	9 Hz
Case 6	6 Hz
Case 7	3 Hz

7.4.2 Responses from moving point load

In this section, the semi-analytical model of (Sheng et al., 1999a) is used to predict the response to a moving constant load. The results are calculated in the moving frame but they are transformed to the non-moving frame. Results are presented as time histories and frequency spectra of the response for a number of speeds in each case, both below and above the critical speed.

Fig. 7-3 presents the results for case 1. Significant peaks can be found at around 10 Hz for a load speed of 80 m/s and to a lesser extent 100 m/s, as shown in Fig. 7-3(a). This can also be seen as a clear oscillation in the displacement time history in Fig. 7-3(b). However, for 40 and 60 m/s there is no clear peak in the spectrum or oscillation in the time domain. The time-domain results are not shown for 40 m/s as they are visually similar to those for 60 m/s but the frequency content shifts to higher frequencies.

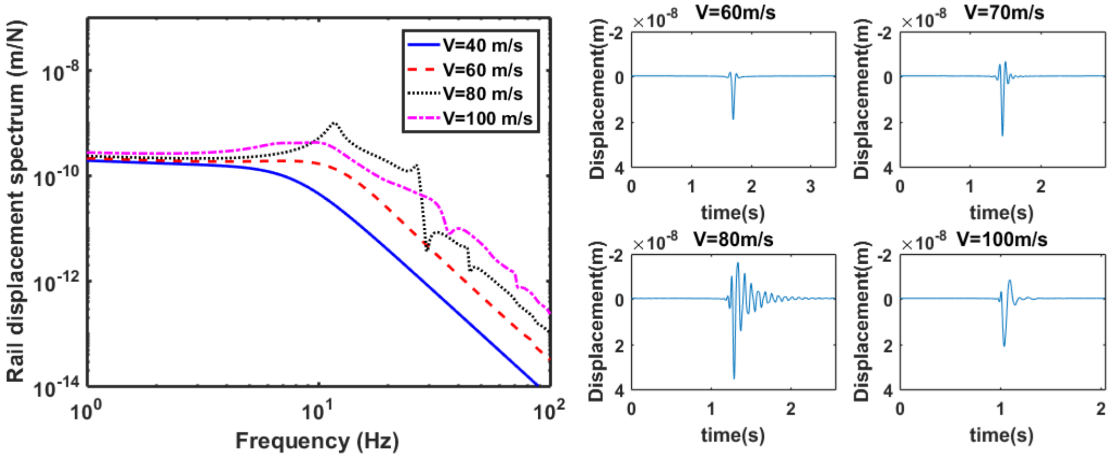

(a) (b)

Figure 7-3 Results from case 1 for different load speeds; (a) rail displacement spectrum; (b) rail displacement in the time domain

The results from cases 2~4 are shown in Figs 7-4 to 7-6. These show similar trends with a clear peak at around 10~15 Hz for speeds higher than 80 m/s, which tends to shift to a slightly lower frequency when the load speed increases further. Furthermore, with the stiffer substratum of case 4, shown in Fig. 7-6, the oscillation tends to become longer and the peak in the spectrum clearer at a load speed of 100 m/s.

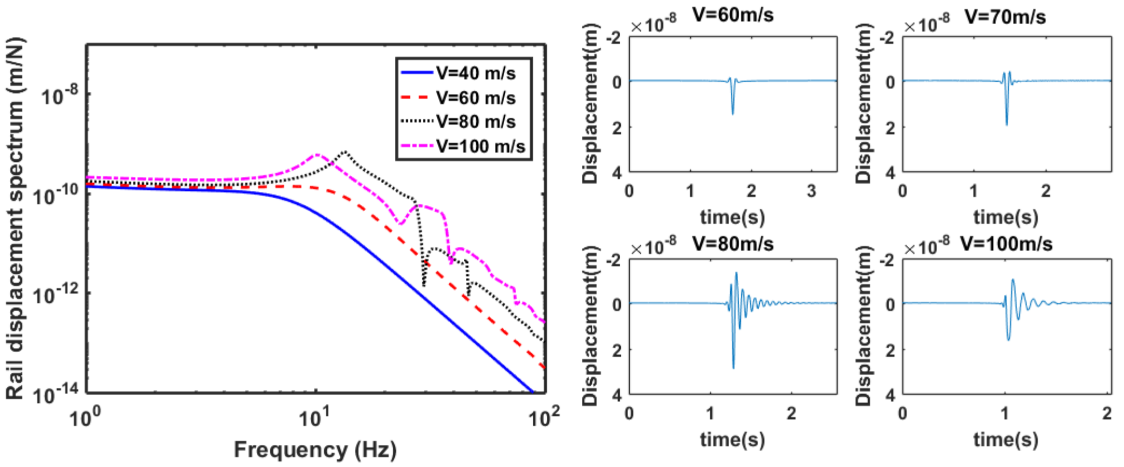

(a) (b)

Figure 7-4 Results from case 2 for different load speeds; (a) rail displacement spectrum; (b) rail displacement in the time domain

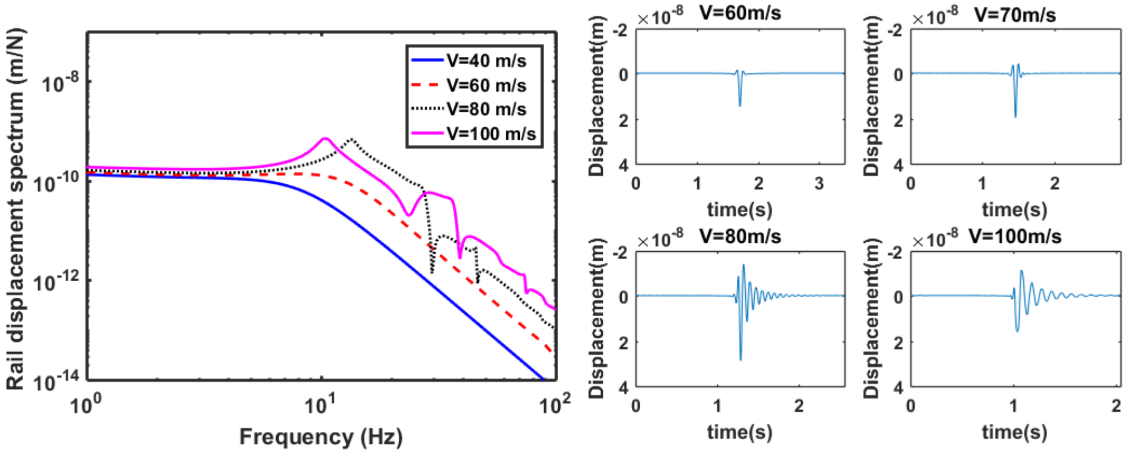

(a) (b)

Figure 7-5 Results from case 3 for different load speeds; (a) rail displacement spectrum; (b) rail displacement in the time domain

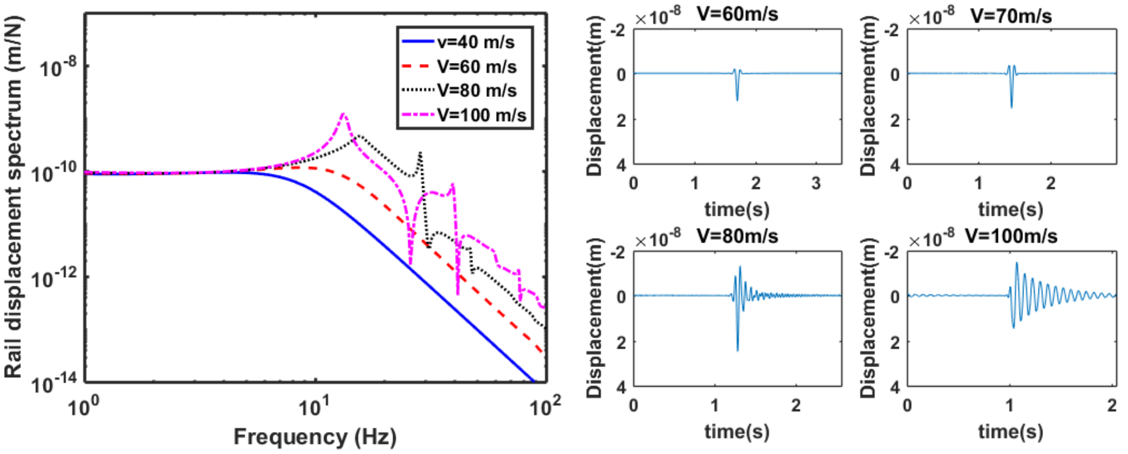

(a) (b)

Figure 7-6 Results from case 4 for different load speeds; (a) rail displacement spectrum; (b) rail displacement in the time domain

Fig. 7-7 shows the results for case 5, which has a lower S-wave speed of the underlying soil than case 1. In this case there is only a clear peak in the spectrum for a speed of 70 m/s, which corresponds to the critical speed. Similarly, in the time domain response there is only a clear oscillation at the critical load speed of 70 m/s.

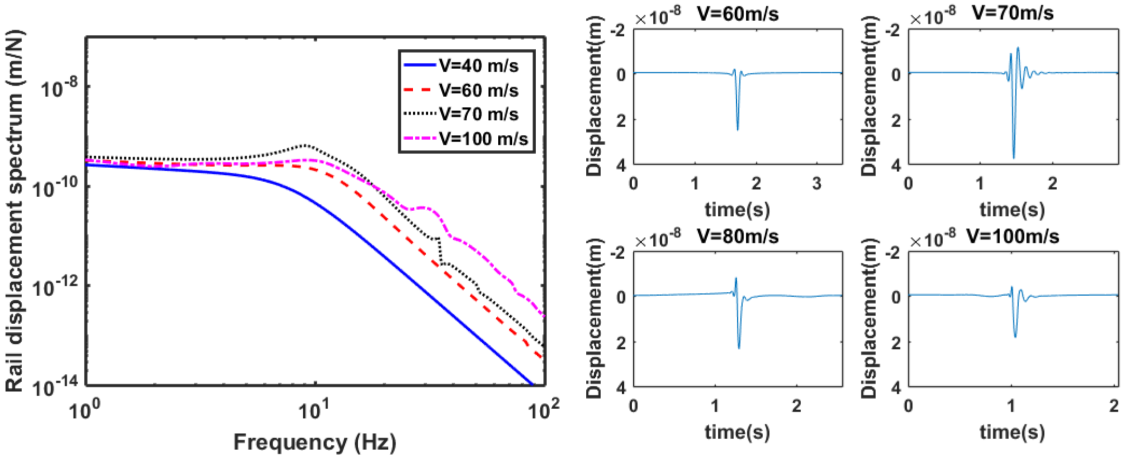

(a) (b)

Figure 7-7 Results from case 5 for different load speeds; (a) rail displacement spectrum; (b) rail displacement in the time domain

The results for cases 6 and 7, with the deeper surface layer, are shown in Fig. 7-8 and Fig. 7-9. The resonance frequency, which occurs here for load speeds higher than 60 m/s, decreases when the depth of the first layer increases. It occurs around 5-7 Hz for case 6 and 2.5-4 Hz for case 7. Furthermore, the peak at the first resonance frequency becomes less clear with increasing depth of the first layer. Furthermore, in the time histories a clear oscillation can be found at a load speed of 70 m/s for both cases.

The corresponding results from the homogeneous half-space are shown in Fig. 7-10. The resonance phenomenon cannot be identified in either the receptance or the time domain results.

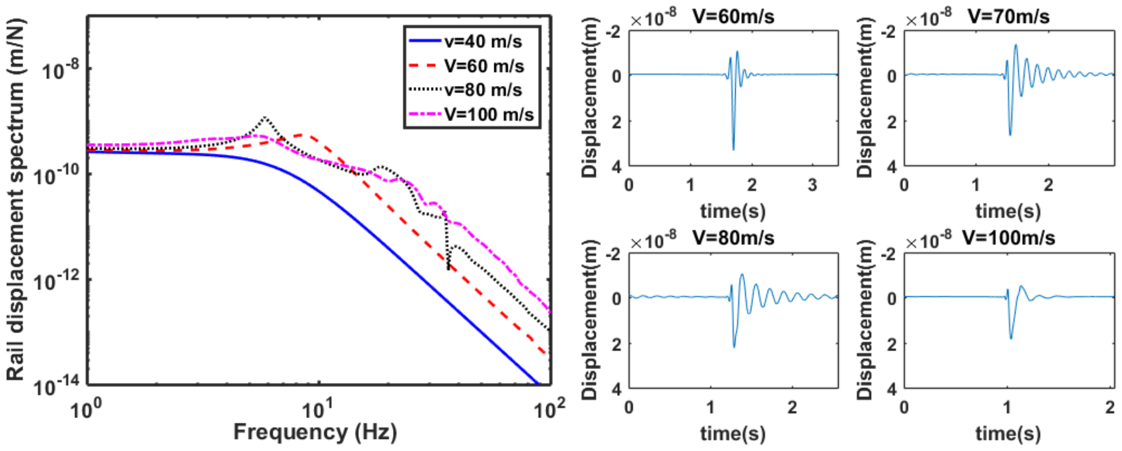

(a) (b)

Figure 7-8 Results from case 6 for different load speeds; (a) rail displacement spectrum; (b) rail displacement in the time domain

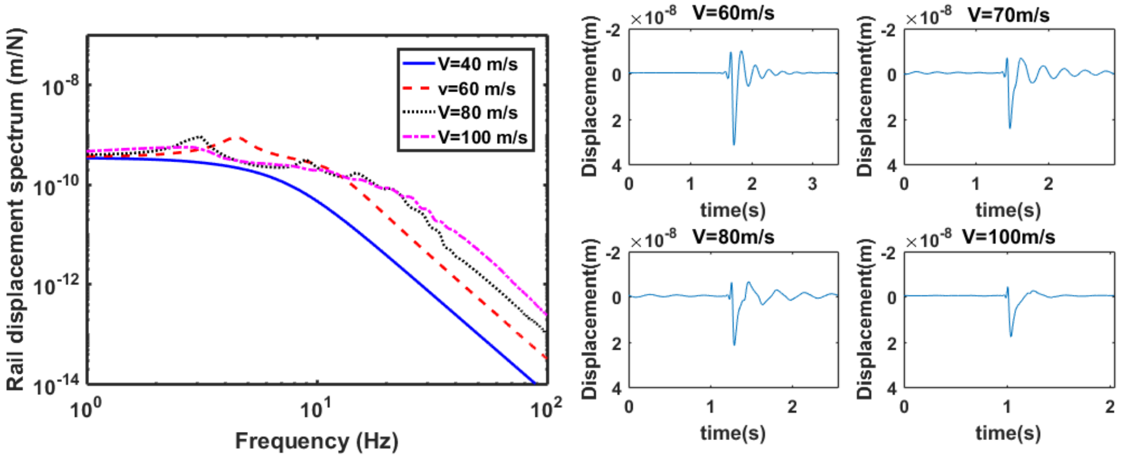

(a) (b)

Figure 7-9 Results from case 7 for different load speeds; (a) rail displacement spectrum; (b) rail displacement in the time domain

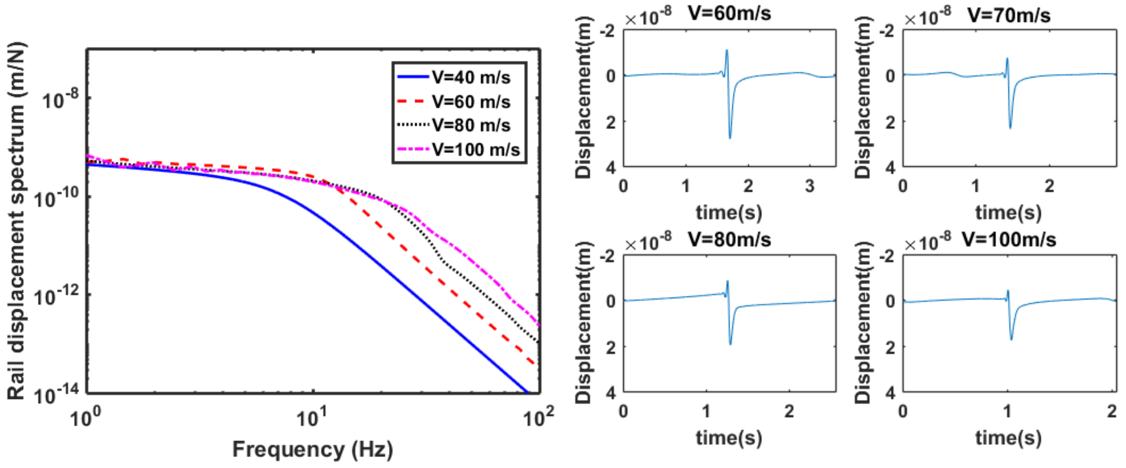

(a) (b)

Figure 7-10 Results from case 8 for different load speeds; (a) rail displacement spectrum; (b) rail displacement in the time domain

7.4.3 Dispersion curves

In this section, using the method introduced by Sheng et al., 1999a, the ground dispersion curves are used to identify the dominant frequency of the response. This method was also recently used by (Costa et al., 2015). Fig. 7-11 shows the results for case 1. The left-hand graph shows the dispersion diagram for the layered ground without track which can be obtained from the analytical model. This shows the coupled compressional and vertically-polarised shear waves. The propagating wave modes in the ground without track are represented by the solid lines and two dashed lines represent the Rayleigh wave speed of the top layer (upper line) and the shear wave speed of the underlying half-space (lower line). The line corresponding to the critical speed (79 m/s) is also shown. To account for the influence of the track, the right-hand graph shows a colour contour plot of the vibration amplitude excited by an oscillating vertical force on the track as a function of wavenumber in the ground at each frequency. The results shown in the figure are based on the response at the ground surface, directly underneath the track, the wavenumber being in the direction of the track. For improved clarity of the results these are plotted on a logarithmic scale. The range between red and blue is around eight orders of magnitude. The first propagating mode from the free field without consideration of the track is re-plotted on the dispersion plot obtained with the track.

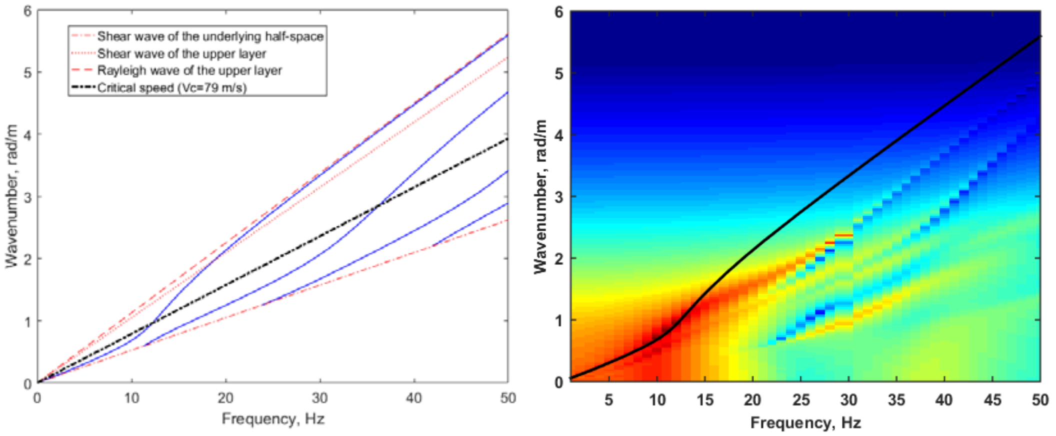

(a) (b)

Figure 7-11. Dispersion diagrams obtained from analytical model for case 1; (a) without track; (b) with track

As shown in Fig. 7-11(b), at higher frequency the wavenumber results obtained without the track are higher than the results including the track. This is due to the fact that the track is stiffer than the ground. However, below about 15 Hz the two results are very similar. Similar conclusion was indicated by Costa et al., 2015 who compared the dispersion curve from three different track models with the results without the track. According to (Sheng et al. 1999a) the resonance frequency induced by a moving point load can be found from the intersection point between the load speed line and the propagating mode dispersion curves. As the dispersion results are similar with or without the track in this frequency region, the intersection with the result without the track can be used. The corresponding intersection point occurs in this case at around 12 Hz. As the load speed increases the intersection point will shift to a slightly lower frequency.

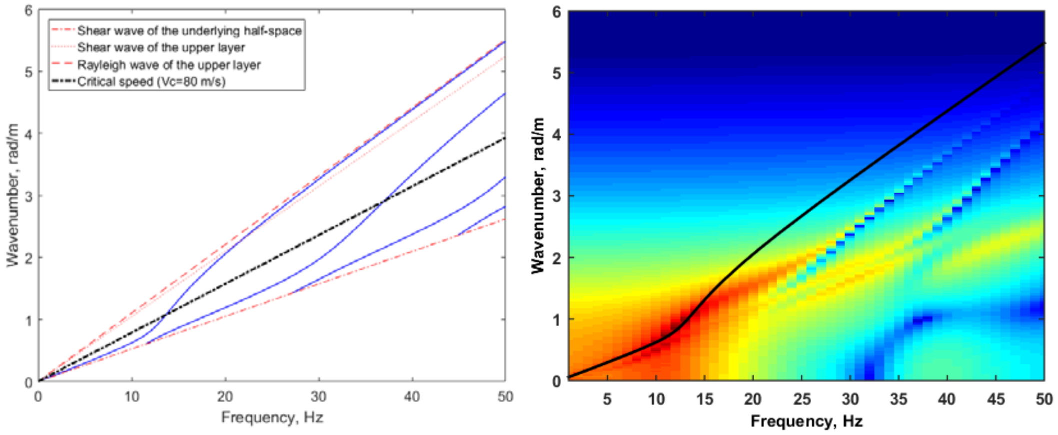

(a) (b)

Figure 7-12. Dispersion diagrams obtained with analytical results for case 2; (a) without track; (b) with track

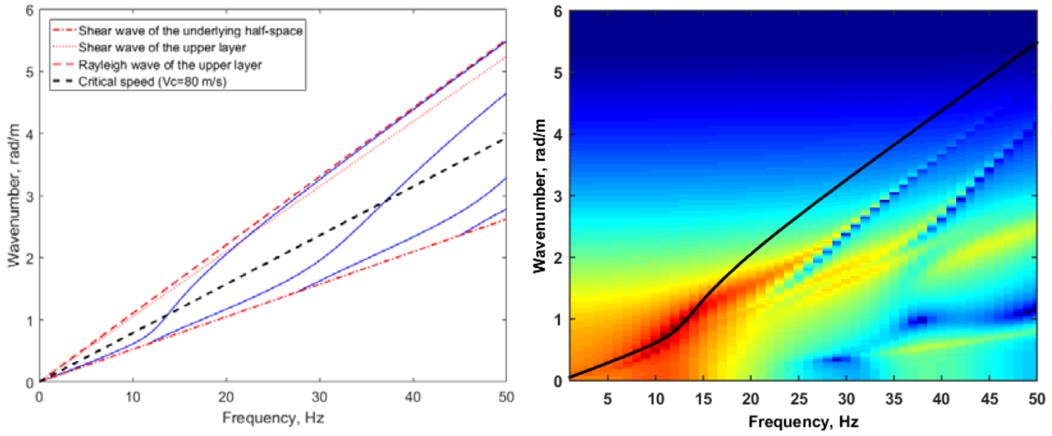

(a) (b)

Figure 7-13. Dispersion diagrams obtained with analytical results for case 3; (a) without track; (b) with track

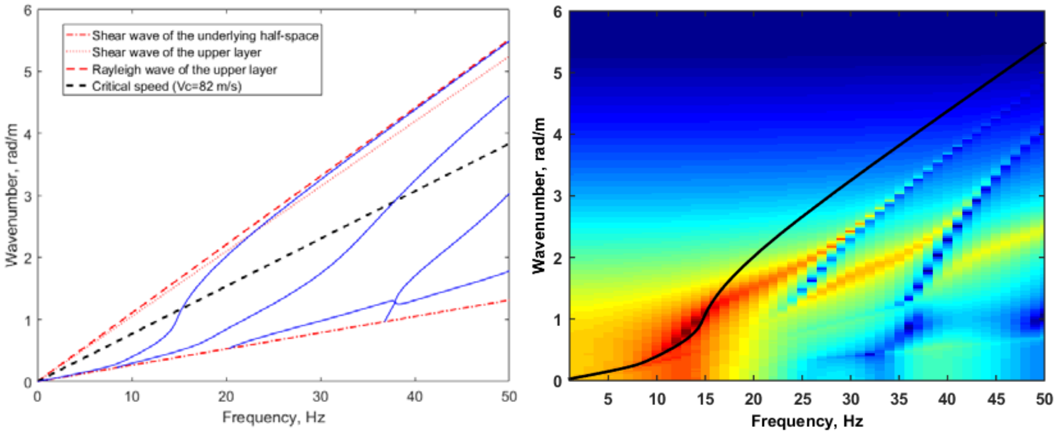

(a) (b)

Figure 7-14. Dispersion diagrams obtained with analytical results for case 4; (a) without track; (b) with track

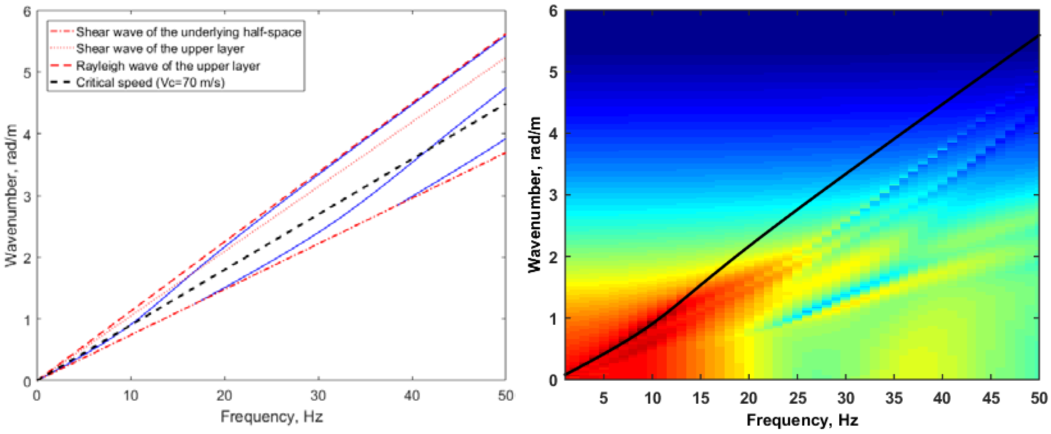

(a) (b)

Figure 7-15. Dispersion diagrams obtained with analytical results for case 5; (a) without track; (b) with track

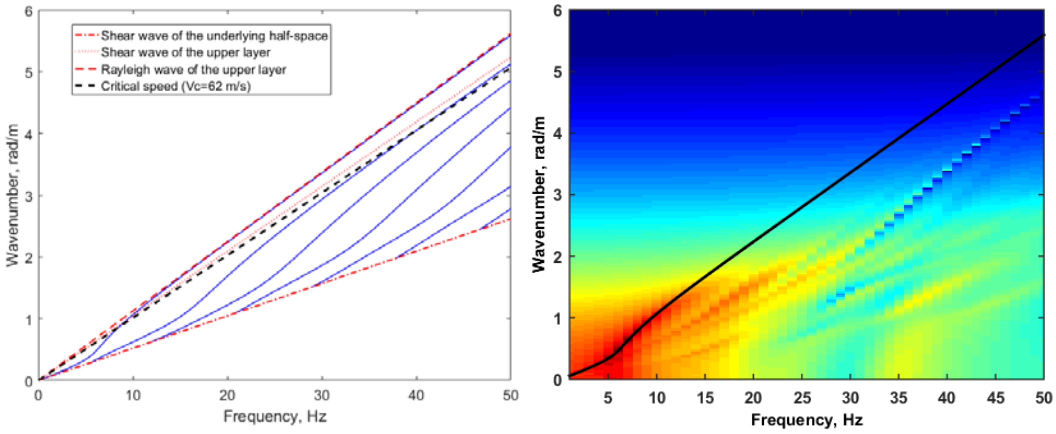

(a) (b)

Figure 7-16. Dispersion diagrams obtained with analytical results for case 6; (a) without track; (b) with track

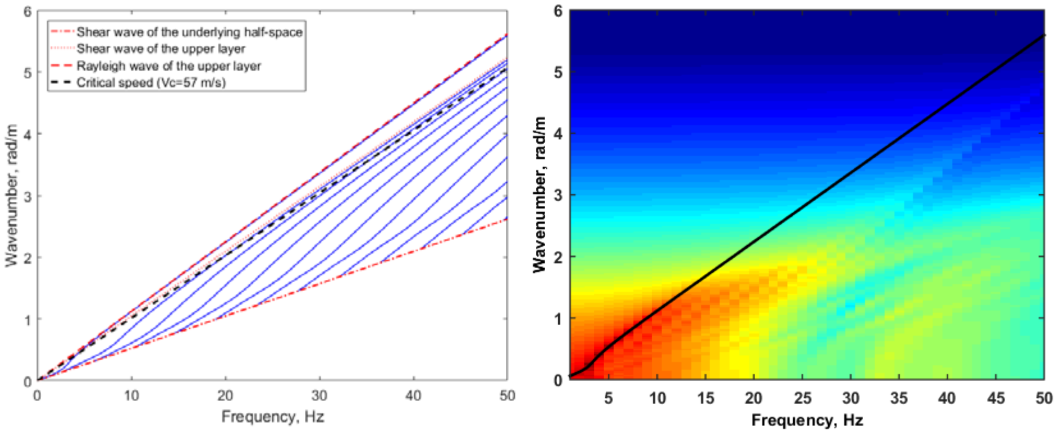

(a) (b)

Figure 7-17. Dispersion diagrams obtained with analytical results for case 7; (a) without track; (b) with track

Very similar results are found for cases 2~4 in Figs 7-12 to 7-14. The wavenumbers of the propagating waves lie between the Rayleigh wavenumber of the upper layer material and the shear wavenumber of the lower layer material. They rise from the wavenumber of the lower layer to that of the upper layer at around the cut-on frequency (see Section 2.2) of the upper layer. As a result, only very small differences are found in the dispersion curves when the P-wave speeds of the first or second layer are varied, as shown in Fig. 7-12 and 7-13. Larger differences are found when the S-wave speed is changed, as shown in Fig. 7-15.

Figs 7-16 and 7-17 show the corresponding results for cases 6 and 7 in which the depth of the first layer is increased. Here the wavenumber increases towards the Rayleigh wavenumber of the upper layer at a lower frequency leading to intersection with the load speed line at a lower frequency.

7.4.4 Discussion

In the previous sections, the resonance frequency has been estimated by three different methods. The results from these methods are compared in Fig. 7-18. The result obtained from the stationary harmonic load is independent of load speed whereas the other two results vary with load speed. However, the results obtained from the dispersion curves have generally good agreement with the results obtained from the spectrum of the response to a moving load and both results are similar to that obtained from the stationary harmonic load. For those results obtained for a moving load at load speeds lower than the critical speed, it is difficult to identify the resonance peak. As a result, no resonance frequency is shown in Fig. 7-18 for lower speeds.

The resonance frequency calculated from the dispersion curve can be identified at lower speeds than that from the spectrum of the moving load response. In most cases the result from the dispersion curve can be identified for speeds higher than the Rayleigh wave speed of the first layer. Furthermore, quite poor agreement is found between these two methods for speeds lower than the critical speed for cases 2-5. For case 5 the method based on the dispersion curves does not give a result above 70 m/s. This is due to the fact that the two layers have quite similar properties and the soil tends to become nearly non-dispersive.

Even though the resonance frequency changes significantly, up to a factor of 2, with different load speeds, a clear resonance phenomenon only occurs when the load speed is higher than the critical speed. For speeds higher than the critical speed, the differences are much smaller and the results agree relatively well with the results obtained from the stationary harmonic load, which does not consider the speed effects. Three empirical equations are introduced and compared with the results from the stationary harmonic load and the results from the moving load at the critical load speed.

According to (El Kacimi et al., 2013; Kouroussis et al., 2014), the resonance frequency can be calculated by

$$f_{reosance} = \frac{c_{p1}}{4H} \qquad (7\text{-}1)$$

where, V_{p1} is the P-wave speed of the first layer and H is the layer depth. The resonance frequency calculated from this formula is listed in Table 7-4. Differences of up to almost a factor of three can be found compared with the results from the present studies. (Mezher et al., 2015) give a modified formula

$$f_{reosance} = \frac{c_{s1}}{H} \qquad (7\text{-}2)$$

where, V_{s1} is the S-wave speed of the first layer. Estimates from this are all too large, by a factor of around 2~3 times, compared with the resonance frequency calculated from the stationary harmonic load, as shown in Table 7-4. A modified formula is suggested here to estimate the resonance frequency of a layered half-space:

$$f_{reosance} = \frac{c_{s1}}{2H} \tag{7-3}$$

A comparison of the resonance frequency calculated based on Eq. (7-1)~Eq. (7-3) with the results from the stationary harmonic load and the results at critical speed from the spectrum of quasi-static responses are shown in Table 7-5 and 7-6. The results from the quasi-static responses at the critical speed are used due to the fact that a clear oscillation tail can be found in the time domain. The results from the stationary harmonic load are used due to the fact that it is the only method without speed dependence that can be easily calculated and it is more efficient than the other methods. Furthermore, as seen it agrees well with the results from the quasi-static response at higher load speeds.

Significant differences can be found based on Eq. (7-2) compared to the two different methods. Better results are found based on Eq. (7-1); however, significant differences are found for cases 2~4, which include higher P- and S-wave speeds for the substratum. Differences of less than 50% based on Eq. (7-3) can be found compared with the results from stationary harmonic load, apart from case 5 for which a difference of around 67% is found compared with the results from the stationary harmonic load. This is due to the fact that the properties for the two layers are very similar, making this situation similar to a homogeneous half-space which is non-dispersive and does not have this resonance phenomenon (see Fig. 7-10). On the other hand, better agreement, less than 25% difference, can be found when comparing with the results of quasi-static response at the critical speed, as shown in Table 7-6. Note here that none of the formulae mentioned above consider any speed dependence. Therefore, they are inevitably approximations. However, Eq. (7-3) tends to give relatively good agreement compared with the results from stationary harmonic load and quasi-static loads.

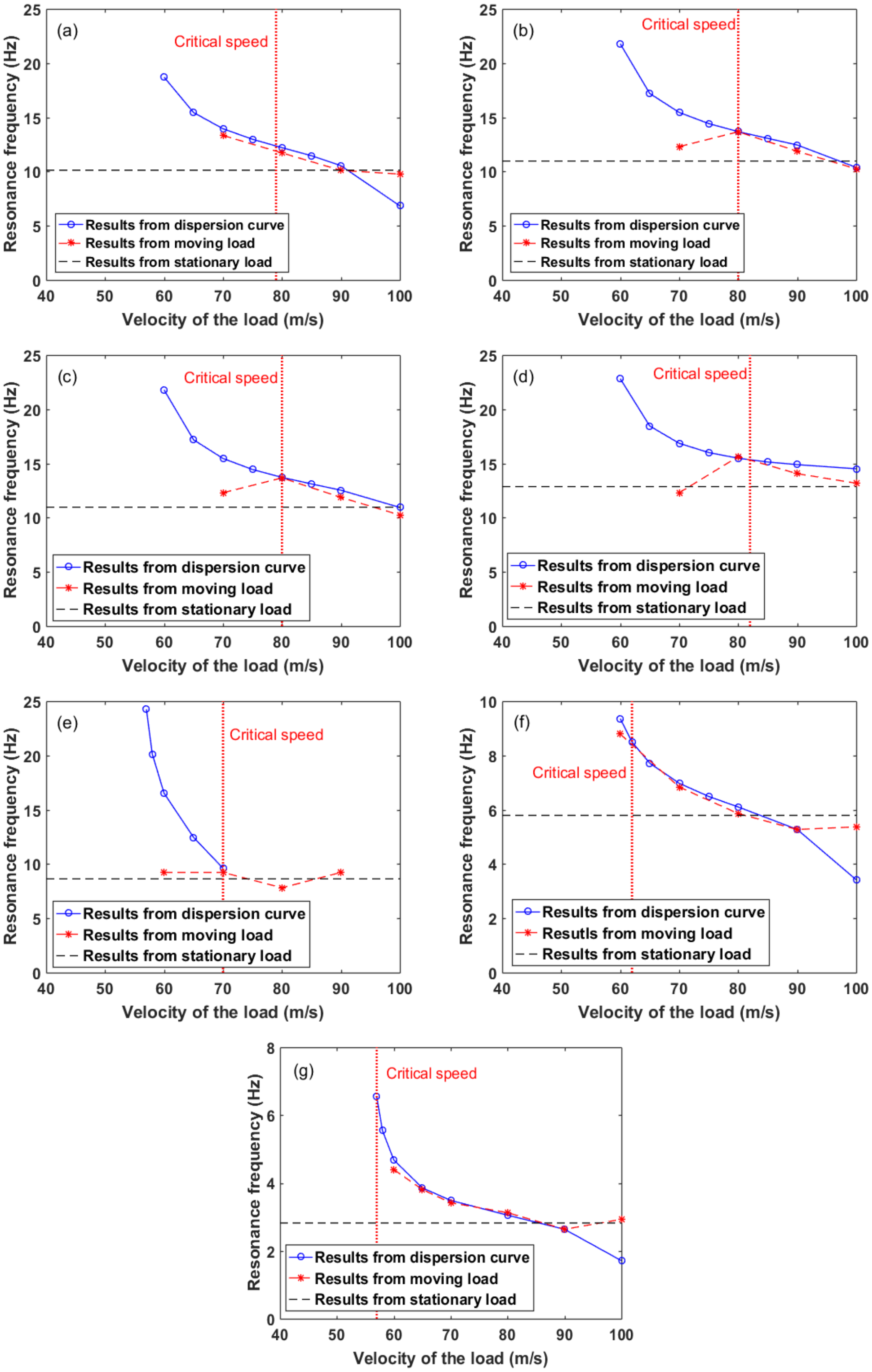

Figure 7-18. Resonance frequency at different load speeds obtained by using three different methods; (a) Case 1; (b) Case 2; (c) Case 3; (d) Case 4; (e) Case 5; (f) Case 6; (g) Case 7

Table 7-4 Comparison of resonance frequency based on three different equations with the results from stationary harmonic load

	Results from stationary harmonic load	Results at V_{cr} from the spectrum of quasi-static response	Based on Eq. (7-1)	Based on Eq. (7-2)	Based on Eq. (7-3)
Case 1	10 Hz	12 Hz	15 Hz	30 Hz	15 Hz
Case 2	11 Hz	14 Hz	30 Hz	30 Hz	15 Hz
Case 3	11 Hz	14 Hz	30 Hz	30 Hz	15 Hz
Case 4	13 Hz	15 Hz	30 Hz	30 Hz	15 Hz
Case 5	9 Hz	9 Hz	15 Hz	30 Hz	15 Hz
Case 6	6 Hz	8.5 Hz	7.5 Hz	15 Hz	7.5 Hz
Case 7	3 Hz	-	3.75 Hz	7.5 Hz	3.75 Hz

Table 7-5 Difference between the results based on Eqs (7-1) to (7-3) and the results for a stationary harmonic load

	Based on Eq. (7-1)	Based on Eq. (7-2)	Based on Eq. (7-3)
Case 1	50%	200%	50%
Case 2	173%	173%	36%
Case 3	173%	173%	36%
Case 4	131%	131%	15%
Case 5	67%	233%	67%
Case 6	25%	150%	25%
Case 7	25%	150%	25%

Table 7-6 Difference between the results based on Eqs (7-1) to (7-3) and the results at V_{cr} from the spectrum of quasi-static response

	Based on Eq. (7-1)	Based on Eq. (7-2)	Based on Eq. (7-3)
Case 1	25%	150%	25%
Case 2	114%	114%	7%
Case 3	114%	114%	7%
Case 4	100%	100%	0%
Case 5	67%	233%	67%
Case 6	-12%	76%	-12%
Case 7	25%	150%	25%

7.5 Summary

A parametric study of the resonant characteristic of a layered half-space is carried out. Simulations are performed using a range of ground properties to show the dependence of the critical speed and the resonance frequency of track/ground system on the wave speeds of the upper layer and underlying half-space and the layer depth.

The critical speed is shown to be independent of the P-wave speeds of either layer. On the other hand, it decreases when the S-wave speed of the second layer is reduced. When the layer depth is increased, the critical speed also decreases. It reduces by around 25% when the layer depth is increased from 2 m to 4 m. However, much small differences are found when it is increased further.

The resonance frequency of the layered ground is studied using three methods. From results due to a moving load it is found to be influenced by the speed of the moving point load and tends to decrease when the load speed increases. Changes to the P-wave speed for upper and half-space layer and S-wave speed for half-space have minimal effect on the resonance frequency. Larger differences are found when the depth of the first layer is changed. A much clearer oscillation behind the load can be found with a stiffer top layer and shallow layer depth, especially when the load speed is close to the critical speed. Furthermore, a longer oscillation in the time domain is found when the difference between the S-wave speed of the two layers becomes significant.

The dispersion curve is almost the same at low frequency whether the track model is included or not. Therefore, for calculating the resonance frequency, the track can be neglected. It is expected that the oscillation behind the load occurs when the load speed is higher than the Rayleigh wave speed of the first layer, due to the fact that the waves start to propagate in this layer. However, for some cases, no oscillation is found behind the load in the time domain even though the load speed is higher than the surface wave speed.

The resonance frequency obtained from the moving point load and the dispersion curve are similar. The resonance frequency estimated from the results for a stationary harmonic load applied on the track/ground model give a good approximation even though the results are influenced in practice by the speed of the moving point load.

Based on the present study, the resonance frequency of a layered ground appears to be related to the first layer S-wave speed and the depth of the first layer, not the P-wave speed. Consequently, an approximate formula is proposed, which gives results within 50% of the results from a stationary harmonic load.

Chapter 8: Soil nonlinearity

8.1 Introduction

In previous chapters a finite element time domain model has been developed for the track and ground and the response to moving loads has been determined. The requirements have been established for the ground model geometry, grid size and damping model, and effective ways of dealing with the boundaries have been demonstrated. However, the motivation for developing time domain models has been to be able to study the effect of soil nonlinearity. Especially for soft ground, the linear elastic material, used in the previous chapters, may cause underestimation of the vibration amplitude and incorrect assessment of critical speed. Thus, in this chapter soil nonlinearity is taken into account in the model.

Of particular interest in this regard is the soft soil site at Ledsgård, south of Gothenburg in Sweden, where field tests were carried out in the late 1990s with trains running at or near the critical speed (Kaynia et al., 2000; Madshus et al., 2000). Extensive soil investigations were also carried out (Costa et al., 2010; Hall, 2003). This is used as a case study to investigate the effect of introducing nonlinearity in the model.

The nonlinear model used is introduced in Section 8.2. It is based on the shear modulus reduction curve that can be obtained from laboratory tests and is implemented in a user-defined subroutine UMAT within the software ABAQUS. At each time step the soil stiffness in each element is determined based on the instantaneous octahedral shear strain. Plastic behaviour is not considered here as it can be considered to be small compared with the transient dynamic deflections and the objective is not to study long-term track settlement. The results are compared with site measurements from Ledsgård (Costa et al., 2010). The influence of the soil nonlinearity on the critical speed and stress-strain behaviour of the embankment and ground are investigated in Sections 8.3~8.4. Furthermore, in the light of the nonlinear analysis, the use of an equivalent linear analysis for the moving load problem is discussed in Section 8.5. Finally, a moving vehicle model excited by rail unevenness is introduced into the model and the results from the soil nonlinear model are discussed and compared with measurements from Ledsgård (Sheng et al., 2003) in Section 8.6.

8.2 Soil nonlinear model

As mentioned in Section 2.7, one of the most important parameters for soil stiffness variation is the shear strain level. The dependence on this can be defined from a number of cyclic triaxial tests. During cyclic loading, the stress-strain behaviour of the soil typically follows a nonlinear hysteresis loop, as shown schematically in Fig. 8-1. The slope of the stress-strain curve can be identified as the soil stiffness or modulus. The dissipated energy, which is related to the damping ratio, can be determined from the area of the loop. The secant shear modulus G_{sec} is defined from the maximum values of stress and strain as indicated in Fig. 8-1. As the amplitude of the loading increases, it can be seen that this modulus reduces in the example shown, with the maximum shear modulus G_{max} occurring for very small amplitudes. As discussed in Section 2.7, the ratio of the secant shear modulus at a given strain level to the maximum shear modulus can be identified as the shear modulus reduction (Iwasaki, et al., 1978; Kramer, 1996 Kokusho, 1980, Vucetic and Dobry, 1991, Seed et al., 1970). Fig. 8-2(a) shows shear modulus reduction curves obtained from cyclic triaxial tests at different amplitudes, for material samples obtained at Ledsgård (Costa et al., 2010). In contrast to the stiffness, the damping ratio tends to increase when the strain level increases, as shown in Fig. 8-2(b).

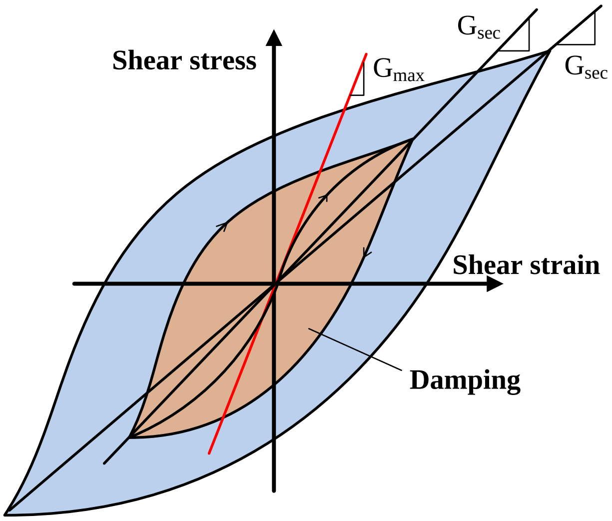

Figure 8-1 Shear-strain path during cyclic loading

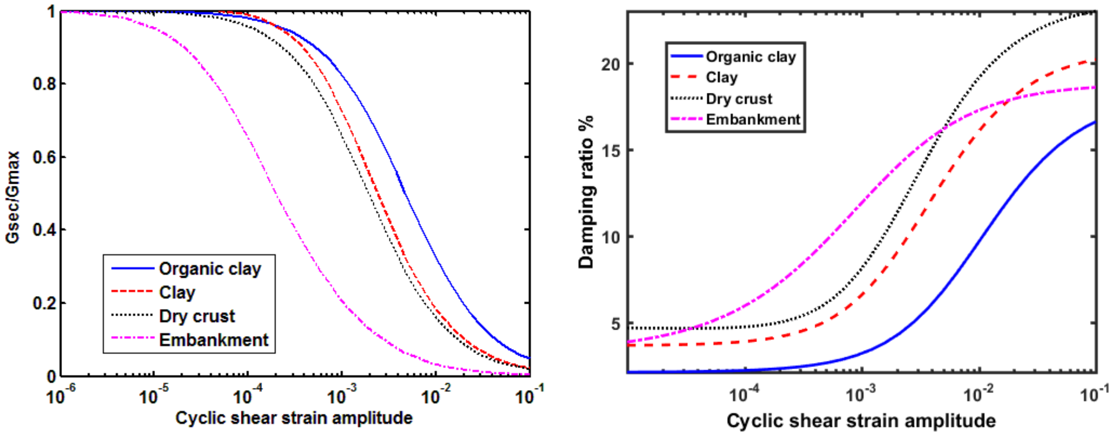

Figure 8-2 Nonlinear soil characteristics obtained for different soil layers at Ledsgård (Costa et al., 2010) (a) shear modulus reduction curves; (b) damping ratio

Shear modulus reduction curves such as these have been defined by fitting empirical formulae (Ishibashi et al., 1993) (details are given in Appendix C) to experimental data. These functions have then been implemented through a user-defined material subroutine UMAT in the commercial finite element program, ABAQUS, to give a nonlinear constitutive material model, which is updated element by element. For each integration point within a finite element, the subroutine receives variables such as the incremental strain vector and the previous stress vector, and returns the current stress vector and updated Jacobian matrix (i.e. the current tangent modulus matrix). The new shear modulus is obtained from the modulus reduction curve, which is expressed in terms of the shear strain value. However, due to the fact that in general the deflection involves multiple strain components, the octahedral shear strain is used as the strain index to evaluate the value of modulus reduction for each time step. This is given by

$$\gamma_{oct} = \frac{1}{3}\sqrt{\left(\varepsilon_{xx}-\varepsilon_{yy}\right)^2+\left(\varepsilon_{yy}-\varepsilon_{zz}\right)^2+\left(\varepsilon_{xx}-\varepsilon_{zz}\right)^2+6\left(\gamma_{xy}^2+\gamma_{yz}^2+\gamma_{xz}^2\right)} \quad (8\text{-}1)$$

where ε_{xx}, ε_{yy} and ε_{zz} are the strains in the three coordinate directions and γ_{xy}, γ_{yz} and γ_{zx} are the shear strains. From the new shear modulus, determined from the modulus reduction curve, the new constitutive matrix

$$[D]=\begin{bmatrix}\lambda+2\mu & \lambda & \lambda & 0 & 0 & 0\\ \lambda & \lambda+2\mu & 0 & 0 & 0 & 0\\ \lambda & 0 & \lambda+2\mu & 0 & 0 & 0\\ 0 & 0 & 0 & \mu & 0 & 0\\ 0 & 0 & 0 & 0 & \mu & 0\\ 0 & 0 & 0 & 0 & 0 & \mu\end{bmatrix} \tag{8-2}$$

is obtained, in which λ and μ are the Lamé constants given by

$$\lambda=\frac{2Gv}{(1-2v)};\ \mu=G \tag{8-3}$$

with G the shear modulus and v the Poisson's ratio. Here the Poisson's ratio is assumed to be constant. The stress matrix is then updated for the next time step i+1 based on this new tangent constitutive matrix

$$\{\sigma\}_{i+1}=[D]_i\{\varepsilon\}_i \tag{8-4}$$

and the strain which is updated by the strain increment $d\varepsilon$

$$\{\varepsilon\}_i=\{\varepsilon\}_{i-1}+\{d\varepsilon\}_i \tag{8-5}$$

The stress vector is given by

$$\{\sigma\}=\{\sigma_{xx}\quad \sigma_{yy}\quad \sigma_{zz}\quad \tau_{xy}\quad \tau_{yz}\quad \tau_{xz}\}^T \tag{8-6}$$

where σ_{xx}, σ_{yy} and σ_{zz} are the stresses in the three coordinate directions and τ_{xy}, τ_{yz} and τ_{zx} are the shear stresses. Similarly the strain vector is given by

$$\{\varepsilon\}=\{\varepsilon_{xx}\quad \varepsilon_{yy}\quad \varepsilon_{zz}\quad \gamma_{xy}\quad \gamma_{yz}\quad \gamma_{xz}\}^T \tag{8-7}$$

Rayleigh damping is used in which the damping matrix is proportional to the mass and stiffness matrices with the factors α and β as discussed in Section 4.3 (see also Eq. 4-5). The values of α and β are chosen to match the target damping ratio to a certain value ξ at two representative frequencies, ω_1 and ω_2, discussed in Section 4.4 (see also Eq. 4-8).

For a constant value of α, the mass-proportional component of damping can be incorporated directly using the ABAQUS FE code for built-in constitutive models. However, for a user-defined material, the stiffness-proportional damping must be incorporated within the user-defined material subroutine. This can be achieved by adding the corresponding stress term:

$$\left\{\sigma_d\right\}_{i+1} = \beta\left[D\right]_i \left\{\dot{\varepsilon}\right\}_i \tag{8-8}$$

where $\dot{\varepsilon}$ is the strain rate. This term is added to the stress resulting from the elastic responses at each integration point. As a result, the total stress is given by

$$\left\{\sigma_{\mathrm{T}}\right\}_{i+1} = \left\{\sigma\right\}_{i+1} + \left\{\sigma_d\right\}_{i+1} \tag{8-9}$$

In the present work only constant values of α and β are used. For a constant value of β, the stiffness-proportional term will reduce as the stiffness degrades. However, for a constant value of α, the mass-proportional term corresponds to an increasing value of damping ratio as the stiffness degrades. This can be seen for a single degree of freedom system with natural frequency ω_0, mass m and stiffness k_i at time step i; the damping ratio is given by

$$\xi_i = \frac{\alpha m \omega_0}{2k_i} \tag{8-10}$$

Consequently, when the stiffness degrades, the damping ratio will increase. Although β has a greater influence at higher frequencies, α dominates the damping ratio for the lower frequencies which are more relevant in the present calculations. As a result, the damping ratio in the model will increase according to the inverse of the shear modulus reduction.

8.2.1 Traxial test modelling

To verify the implementation of the constitutive model, a finite element model of a simple triaxial test has been implemented. A confining pressure is applied around the surface of the cylinder and a geostatic step is used to derive stable initial conditions before applying successive vertical displacements. From the resulting reaction forces the shear modulus reduction can be determined as a function of strain.

A three-dimensional quarter model of the triaxial test is used as shown in Fig. 8-3. ABAQUS calculates the stress (total stress) which is in equilibrium with the initial loading and boundary conditions and gives the converged stresses distribution. Nonlinear soil models are introduced for four different soil materials, representing the embankment, crust, organic clay, and clay (see Fig. 8-2), which will be used for modelling site in Ledsgård. The shear modulus reduction is evaluated by determining the ratio of deviator stress to strain and dividing this by the initial shear modulus. The results are compared with the data from (Costa et al., 2010) in Fig. 8-4. Good agreement can be seen in each case, confirming the correct implementation of the nonlinear models.

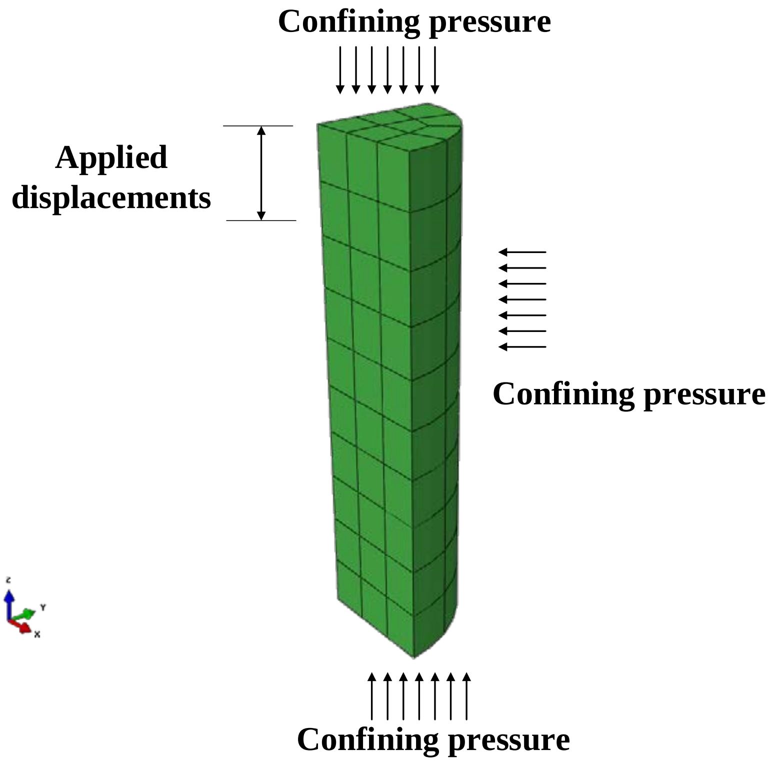

Figure 8-3 ABAQUS three-dimensional quarter model for cyclic triaxial test

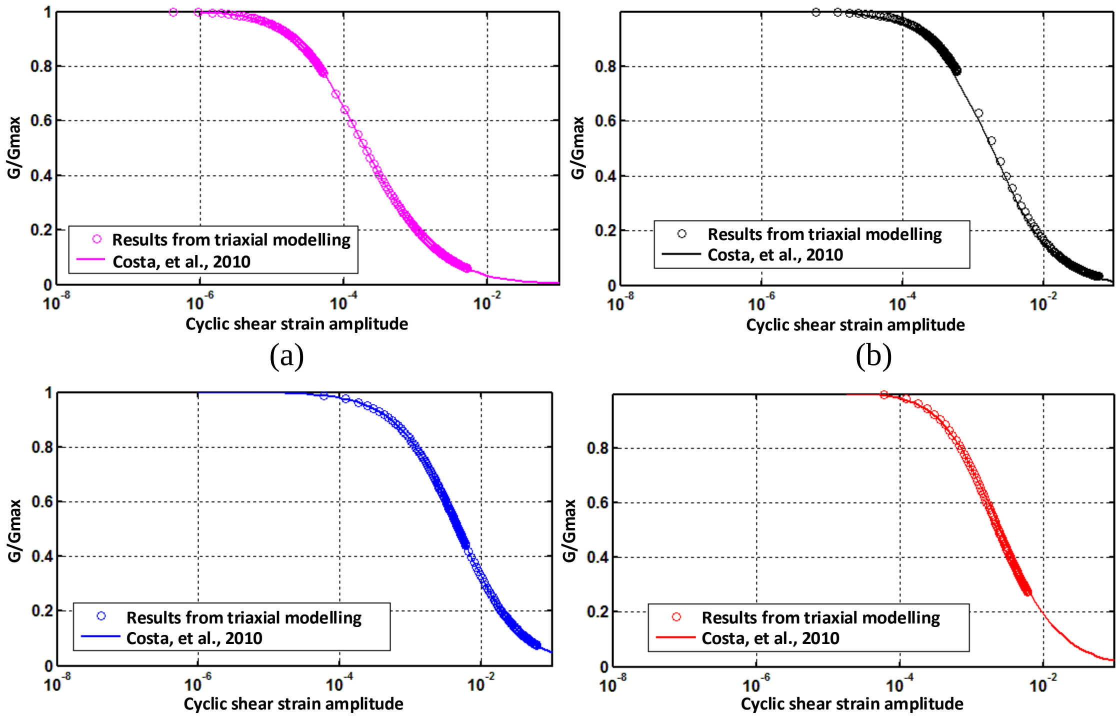

(a) (b)

(c) (d)

Figure 8-4 Shear modulus reduction curve for four different soil properties obtained from FE model of triaxial test; (a) embankment; (b) crust; (c) organic clay; (d) clay

8.3 Numerical model for Ledsgård site in Sweden

A three-dimensional FE model has been constructed of the track and ground at the site at Ledsgård. Small-strain soil properties are available from various in-situ tests, including cross-hole tests, Spectral Analysis of Surface Waves (SASW) and Seismic Cone Penetration Testing (SCPT) (Costa et al., 2010; Hall, 2003). In addition to the embankment, three main soil layers were identified, referred to as dry crust, organic clay, and clay. Measured shear wave speeds as a function of depth are shown in Fig. 8-5(b) along with the values assumed here. The cross-section of the model is shown in Fig. 8-5(a). The lower clay layer is assigned a shear wave speed that varies with depth. The material properties used for the various layers are listed in Table 8-1.

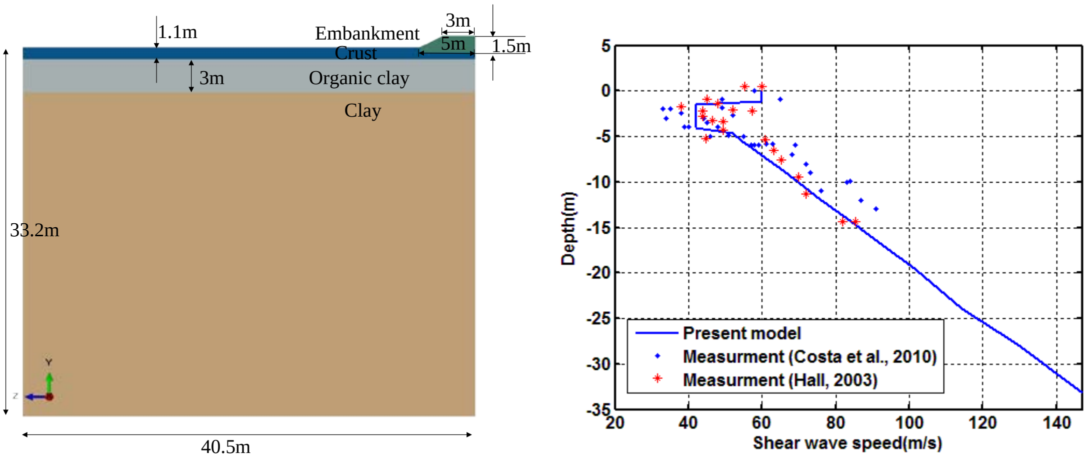

(a) (b)

Figure 8-5 Soil and railway embankment geometry and shear wave speeds at Ledsgård based on soil investigations; (a) cross-section; (b) shear wave speed

The FE mesh used is shown in Fig. 8-6. Use is made of symmetry about the track centreline. A cuboid model is used, with fixed boundaries, a width of 40.5 m and a depth of 33.2 m, see Fig. 8-5(a). The length of the model required to achieve convergence to steady state depends on the load speed (see Section 4.3 and 6.3.3) with longer models required if the load speed approaches or exceeds the critical speed. Here, the model is 80 m long, which is found to be sufficient for convergence. It has been found previously (see Section 6.3.2) that, provided that the model is wide enough, there is little benefit in using absorbing elements at the boundaries. This relies on using a damping model with a sufficiently large mass-proportional term, allowing the energy to be dissipated sufficiently to avoid the reflections interfering with the results. The target damping ratios based on average soil investigation for the four different materials are listed in Table 8-1. Rayleigh damping coefficients are shown in Table 8-2; these are obtained from Eq. (8-9) using target frequencies of 3 and 20 Hz. The nonlinear model includes the shear modulus reduction curves shown in Fig. 8-2.

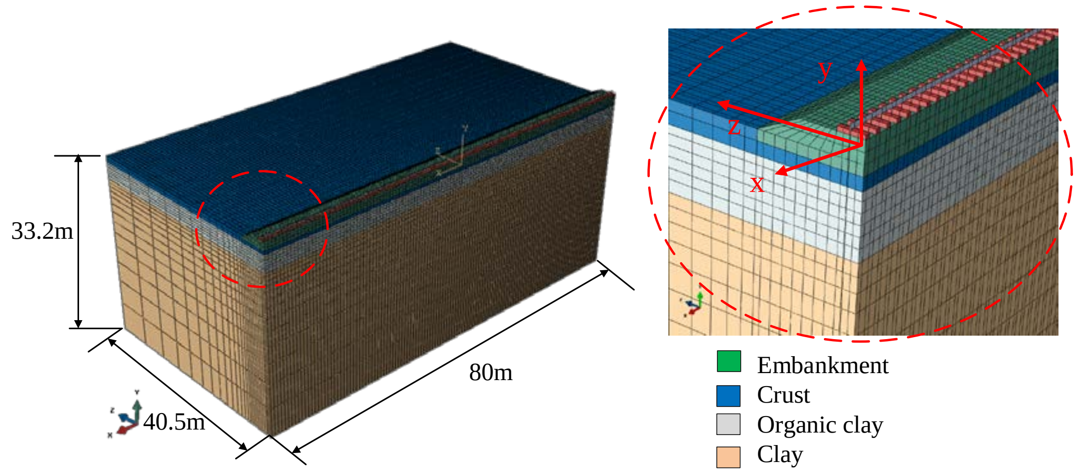

Figure 8-6 Three-dimensional track/ground model

Table 8-1. Embankment and ground properties

	Thickness (m)	P-wave speed (m/s)	S-wave speed (m/s)	Shear modulus (MPa)	Poisson's ratio	Density (kg/m^3)
Embankment	1.5	470	250	112.5	0.3	1800
Crust	1.1*	500	60	5.4	0.5	1500
Organic clay	3.0	500	42	2.2	0.5	1250
Clay	29.1	1500	50~122.9	3.7~22	0.5	1470

*: 0.5 m under embankment

Table 8-2 Embankment and ground Rayleigh damping coefficients

	alpha	beta	Target damping ratio
Embankment	4.5	0.0015	12%
Crust	2.64	0.001	7%
Organic clay	1.553	0.000599	4%
Clay	2.64	0.001	7%

Fully-integrated quadratic cuboid finite elements are used for the whole ground model. To represent the railpads, solid elements are used to represent linear springs with vertical stiffness 4.7x10^8 N/m to connect the rail to each sleeper (for calculation of the equivalent stiffness see Section 4.5). Discrete concrete sleepers with a spacing of 0.67 m are included. The sleepers have a half-length of 1.3 m, a height of 0.2 m, mass density 2500 kg/m^3, Young's modulus 3×10^{10} N/m^2 and Poisson's ratio 0.15. The ballast is included as part of the embankment layer and this in turn is embedded to a depth of 0.4 m into the upper ground layer. The largest node spacing is set to be 0.25 m in the vicinity of the track, which is sufficient for accurate modelling of local deflections up to around 50 Hz.

However, similar to Chapter 6, the element size is gradually increased with a stretch factor of 1.2 in the horizontal direction outside the width of the track region, and in the vertical direction for the clay layer, as shown in Fig. 8-6. This prevents the model from becoming too large and has been found to be acceptable provided that far-field wave propagation is not of interest (see Section 5.4.3). The total number of degrees of freedom in the model is 1.76 million.

Results are presented for a set of moving axle loads; surface roughness excitation is neglected at this stage. Details of the train, X2000, are available from the literature (Costa et al., 2010); a summary is given in Table 8-3. For linear analysis it is sufficient to model a single moving load and to use superposition to determine the response to the whole train but for nonlinear analysis this is no longer possible. Multiple loads are therefore applied on the rail at the locations of the various axles and these are moved along the track according to the train speed. In the experiments (Costa et al., 2010) the train ran in both directions. To represent the northbound train, with the locomotive leading, only two vehicles (eight axles) are considered, because the maximum deflections occurred for the front vehicle. However, the full train set, consisting of a driving trailer vehicle, three passenger carriages and a locomotive, is considered for analysis of the southbound direction.

Table 8-3. Details of X2000 high speed train used in field tests (Costa et al., 2010)

	Length		Axle load
Locomotive	16.5 m	1st bogie axle loads	181 kN
		2nd bogie axle loads	180 kN
3 × passenger carriages	24.7 m	3rd ~ 8th bogie axle loads	122 kN
Driving trailer	21.5 m	9th bogie axle loads	117 kN
		10th bogie axle loads	160 kN

8.4 Results for nonlinear models

In this section results are presented from two nonlinear models as well as a linear model based on the small-strain parameters given in Table 8-1. These results are compared with measurements from Ledsgård (Costa et al., 2010).

8.4.1 Parameters for nonlinear models

The parameters for the organic clay are the most important for the behaviour of the whole system, as this is the softest layer, see Table 8-1. Measurement data for this material, obtained from triaxial tests (Costa et al., 2010), is shown in Fig. 8-7 in the form of the shear modulus reduction and damping ratio. Significant scatter can be observed in these experimental results. Two lines are given, based on an empirical equation proposed by Ishibashi et al. (Ishibashi et al., 1993) (see Appendix C). These are fitted approximately to the data by choosing appropriate values of mean effective confining pressure and plasticity index. The mean effective confining pressure is set to 300 kPa and the plasticity index is set to 100 for nonlinear model 1 and 140 for nonlinear model 2. These functions are used in the material constitutive model described in Section 8.2 to represent the soil nonlinearity. The damping ratios shown in Fig. 8-7 are calculated based on the shear modulus reduction factor according to Eq. (8-10). It can be observed that the second nonlinear model fits the damping ratio data better than the first, although both give a reasonable fit to the modulus reduction data.

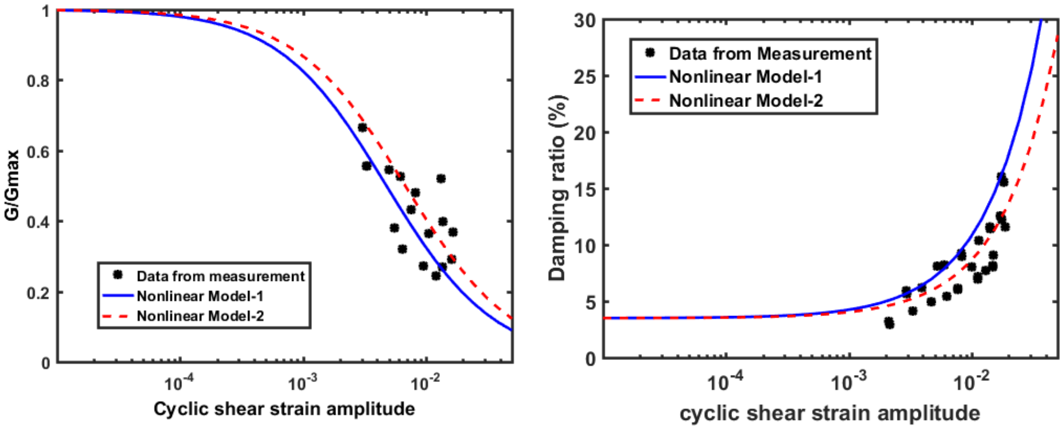

Figure 8-7 Shear modulus reduction curve and damping ratio for organic clay layer; (a) shear modulus reduction; (b) damping ratio

8.4.2 Track displacements from nonlinear models

The results from these two nonlinear models, as well as the linear model, are compared with the measurements in Fig. 8-8 for a train speed of 50 m/s. Good agreement with the measurements is found by using the second nonlinear model, which is slightly stiffer than the first one. The peak deflection from the first nonlinear model is almost double that from the second one. On the other hand, the results from the linear model tend to be too small compared with the measurement. A large spike can be found close to the location of the first axle passing in the measurement. This is assumed to be a measurement error due to the fact that the same phenomenon can also be found for the results in the southbound direction, as seen in Fig. 8-10.

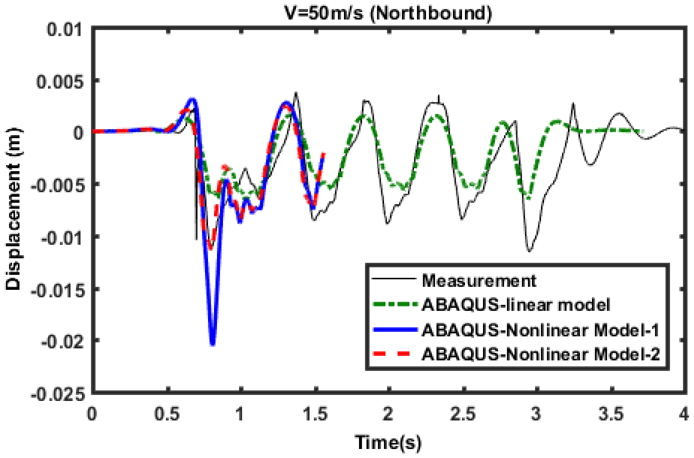

Figure 8-8 Northbound displacement, comparison between linear, nonlinear models and measurement for load speed 50 m/s

Fig. 8-9 shows the results from the two nonlinear models for the northbound direction for three different load speeds, 19 m/s, 45 m/s and 50 m/s. As can be seen, at the lower speed the two nonlinear models give very similar results. On the other hand, significant differences can be found between them for the load speeds of 45 m/s and 50 m/s at the position of the first bogie, whereas the differences are much smaller at other positions.

The results from the lower speed (see Fig. 8-9(a)) correspond approximately to the results obtained from a static analysis. The deflection under each axle can be discerned, with a nearly symmetric pattern of deflection under each bogie. Although the first four axles, which are on the locomotive, have equally high loads, the maximum deflection occurs at the position of the fourth axle due to the influence of the adjacent axles in the second and third bogies. On the other hand, at higher speeds (see Fig. 8-9(b)~(c)) the maximum deflection occurs at the leading axle and the deflection pattern becomes non-symmetric.

When the first load is suddenly applied, large strains occur in the surface layers immediately beneath the load, leading to stiffness degradation and particularly high track deflections for the softer nonlinear model 1. The region of influence is limited by the low wave speed in the soil. Subsequently, this deflection spreads into adjacent areas of the soil so that the region of influence increases and the local strains are lower for the later axle loads, leading to smaller stiffness degradation.

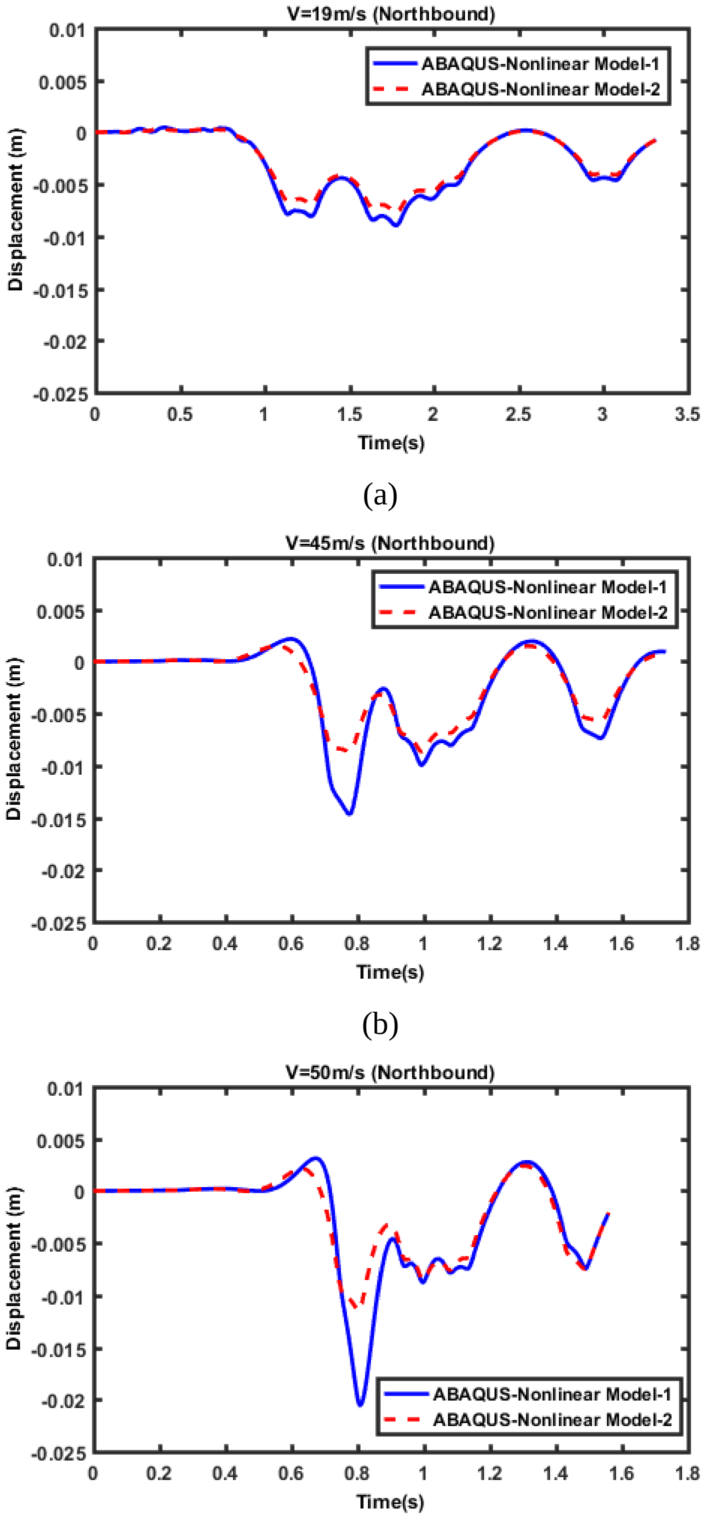

(a)

(b)

(c)

Figure 8-9 Northbound displacement comparison between two nonlinear models for different load speeds; (a) *V*=19 m/s; (b) *V*=45 m/s; (c) *V*=50 m/s

Fig. 8-10 shows the results for the southbound direction for two different load speeds. Fig. 8-10(a) compares the track deflections under the train with measurements for 19 m/s, showing good agreement even for the linear model. The results from the nonlinear models (not shown) are similar. In contrast, as shown in Fig. 8-10(b), for a train speed of 56.7 m/s the results from the linear model are around 40% smaller than the measurements, whereas the second nonlinear model gives good agreement.

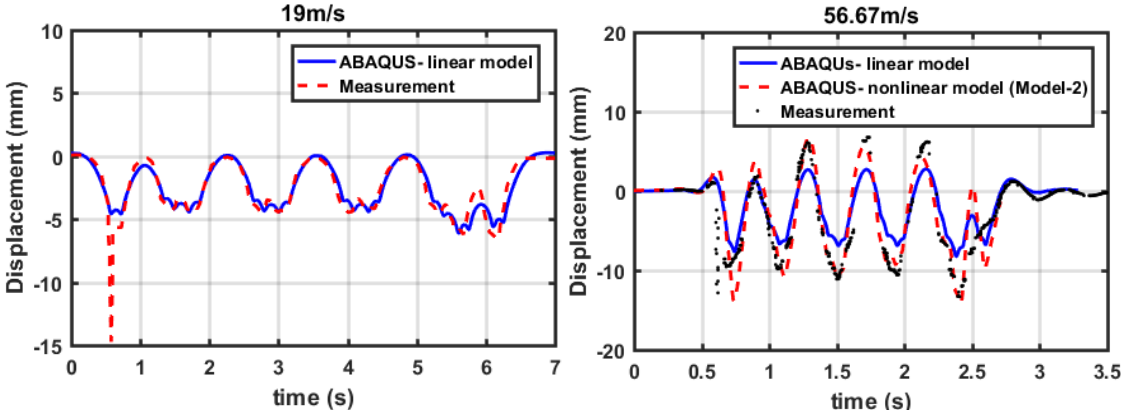

(a) (b)

Figure 8-10 Southbound displacement from linear model for two different speeds; (a) V=19 m/s; (b) V=56.7 m/s

8.4.3 Assessment of octahedral shear strain

The maximum strain level occurs at the position of the first axle load of the locomotive; for the first nonlinear model in Fig. 8-8 it is around double that found from the second nonlinear model. This can also be seen in Fig. 8-11, which shows the octahedral shear strain on the top surface of the organic clay layer for the two different nonlinear models. The results are shown in the spatial domain at a specific time step (when the results have achieved steady state) so the *x* coordinates are arbitrary. The strain distribution behind the region of maximum strain is very similar in the results from the two nonlinear models, with strain values around 0.18% from the first nonlinear model and 0.15% from the second one. This is due to the fact that the differences between the two shear modulus reduction curves are smaller for lower strain levels, as shown in Fig. 8-7. For example, for a strain level of 0.1% the modulus reduction is 0.83 for the first nonlinear model and 0.88 for the second nonlinear model. However, when strain level increases to 0.5%, the modulus reduction for the first nonlinear model drops to 0.48 but it is 0.6 for the second one. As a result, larger differences can be found when the strain level exceeds 0.1%.

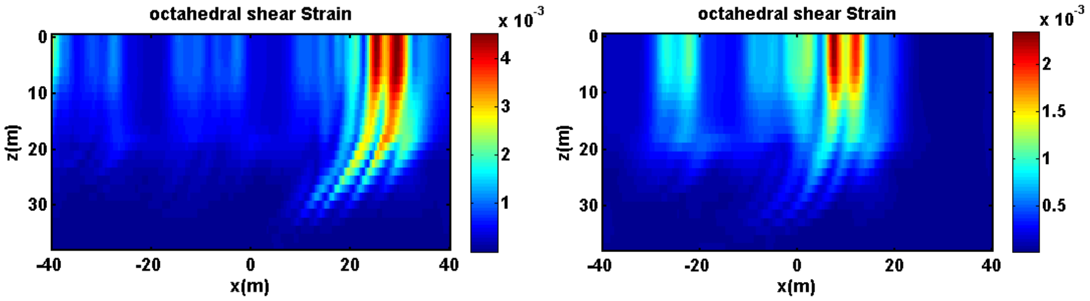

(a) (b)

Figure 8-11 Octahedral shear strain on the top surface of organic clay layer when train speed is 50 m/s for two different nonlinear models (northbound); (a) nonlinear model 1; nonlinear model 2

The strains below the rail at the top of the organic clay layer are shown in Fig 8-12. This shows more clearly the difference between the two nonlinear models. Here, the *x*-coordinate of the results from nonlinear model 2 have been aligned with those from nonlinear model 1. The strain increases further when the soil becomes softer. Consequently, the maximum strain level from the first nonlinear model is around double that from the second one, as also found for the displacement in Fig. 8-10. In the remainder of the results only nonlinear model 2 is considered.

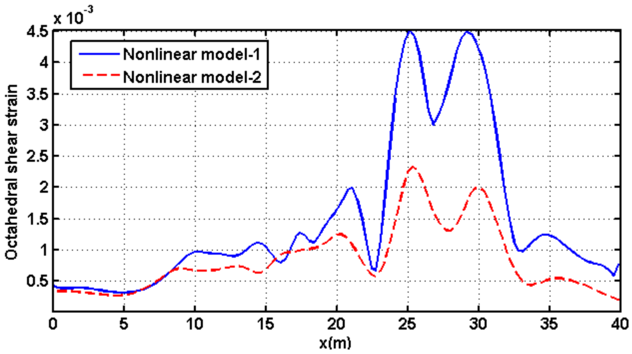

Figure 8-12 Octahedral shear strain variation below the rail on the top surface of the organic clay layer from two different nonlinear models

To compare the results from linear and nonlinear models, the octahedral shear strain at the top surface of the organic clay layer is shown in Fig. 8-13 for a load speed at 56.7 m/s. The strain level from the nonlinear model is not only larger than that from the linear model but the shape of the deflection is different. A clear wave-shaped pattern occurs for the nonlinear model. This is because the load speed is higher than the wave speed in the ground in this case, whereas for the linear model it is still below the critical speed (see Section 8.4.2 below). It is clear that this effect is larger for the nonlinear model at 56.7 m/s than at a speed of 50 m/s in Fig. 8-11(b). Furthermore, even though the strain levels decrease further away from the track, octahedral shear strains of around 10^{-3} can still be found at 30 m away from the track for the nonlinear model, as shown in Fig. 8-13(b), while even for the linear model high strains are found out to 20 m.

In order to have better understanding of the stress distribution in the soil when the train is passing and to identify the region that behaves nonlinearly, the octahedral shear strain in the *y-z* plane (front view) below the first and fourth axle loads is shown in Fig. 8-14. These results are for load speeds of 19 m/s and 56.7 m/s from the northbound runs. At a load speed of 19 m/s the strains are similar below the two axles, but the maximum strain occurs below the fourth axle location. For the higher load speed, a larger region of high strain occurs at the first axle location and the maximum strain occurs at this position. Based on the shear modulus reduction curve (Fig. 8-7), the shear modulus starts to degrade significantly when the strain level exceeds 0.1% for the organic clay.

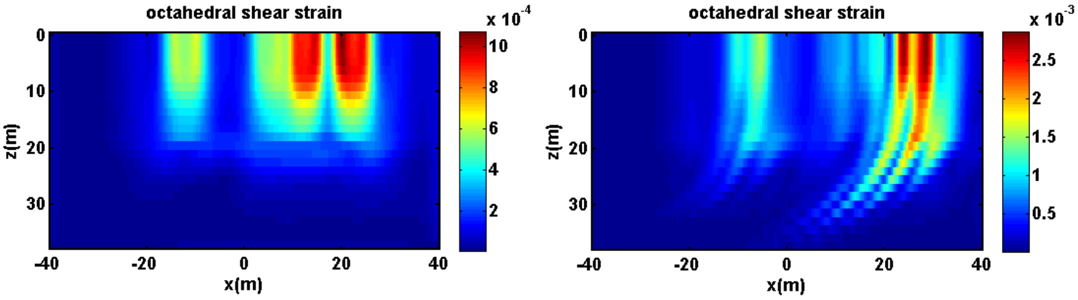

(a) (b)

Figure 8-13 Octahedral shear strain at the top surface of the organic clay layer from linear and nonlinear model at load speed 56.7 m/s (northbound); (a) linear model; (b) nonlinear model 2

As can be seen from Fig. 8-14, the maximum octahedral shear strain occurs in the organic clay layer, between 1.1 m and 4.1 m below the surface, which is the softest layer of the whole system. For the lower speed, only a small region is found with strain levels higher than 0.001, which is at the top of the organic clay layer for the first axle and at the bottom of the organic clay for the 4th axle load. For the higher load speed, the region of high strain under the leading axle becomes deeper. Furthermore, a wider region is found with strain level higher than 0.001 for the 4th axle load

The maximum octahedral shear strains are shown in Fig. 8-15 as a function of the depth for two different train speeds. Results are shown for linear and nonlinear models. As can be seen, the strain levels are typically 10^{-3}, which is too large to allow the use of the small strain approximation (see Fig. 8-7). Nevertheless, for the load speed of 19 m/s, the results of the linear and nonlinear models are very similar, except at the embankment, whereas for a load speed of 56.7 m/s Fig. 8-15(b) shows that the strain level in the organic clay and crust layer for the nonlinear model is around 57% and 70% higher than for the linear model. As a result, consideration of soil nonlinearity is particularly important for the organic clay and crust layers, which have shear wave speeds of 42 m/s (Young's modulus 6.6 MPa) and 60 m/s (Young's modulus 16 MPa).

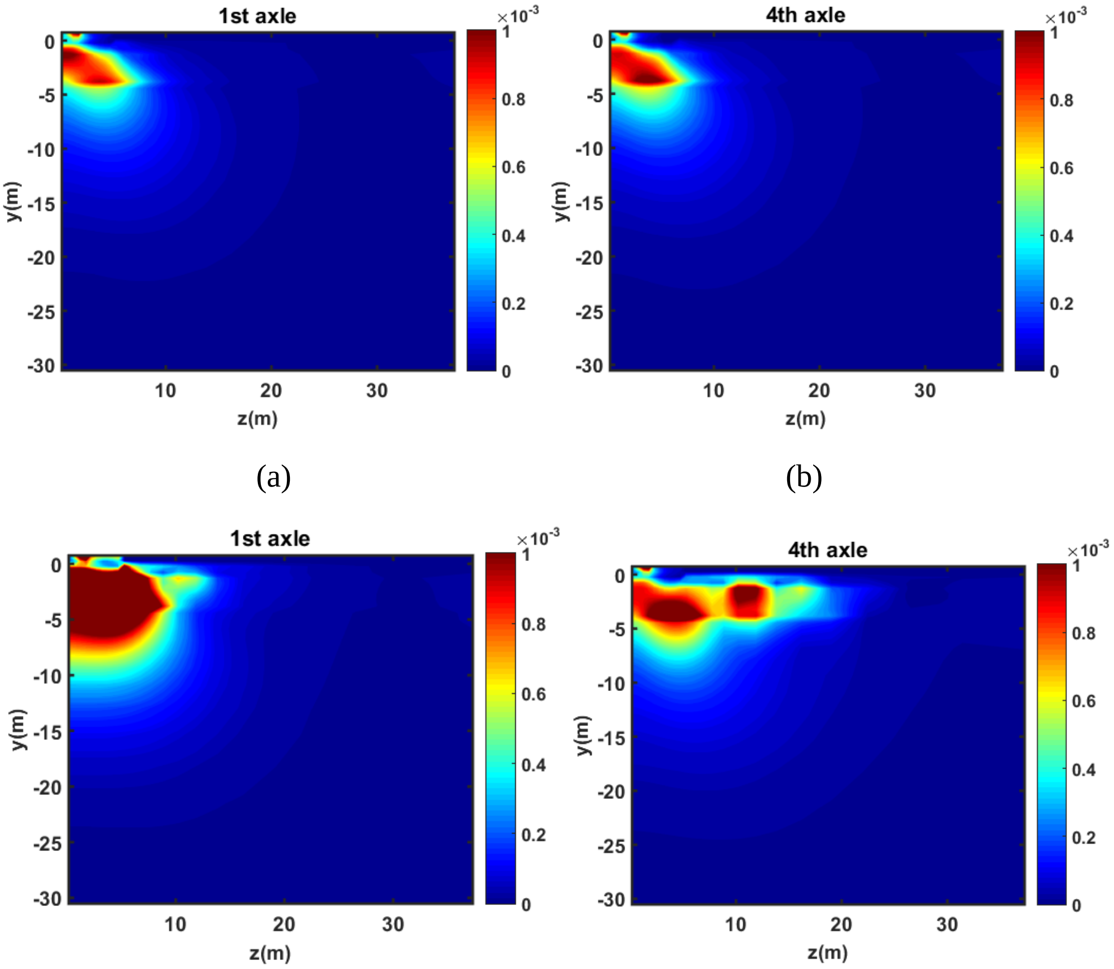

(a)

(b)

(c)

(d)

Figure 8-14 Octahedral shear strain in the *y*-*z* plane below the first and fourth axles for different load speeds (northbound); (a) *V*=19 m/s, 1st axle; (b) *V*=19 m/s, 4th axle; (c) *V*=56.7 m/s, 1st axle; (d) *V*=56.7 m/s, 4th axle

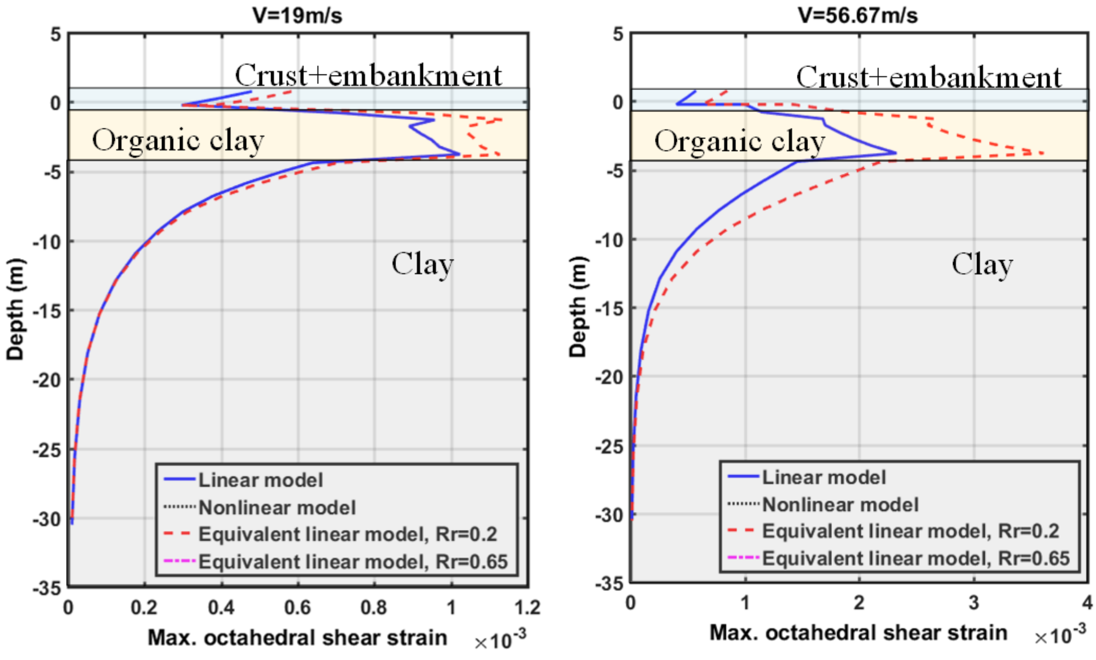

(a) (b)

Figure 8-15 The maximum octahedral shear strain along the depth from northbound analysis for two different load speed; (a) *V*=19 m/s; (b) *V*=56.7 m/s

8.4.4 Assessment of critical speed

The maximum upward and downward displacements obtained for different train speeds are shown in Fig. 8-16. Results are shown from the site measurements (Costa et al., 2010), the linear model and the second nonlinear model. The critical speed, identified as the speed at which the maximum deflection occurs, is found at around 55~60 m/s. A similar value is also identified in the literature (Costa et al., 2010; Kaynia et al., 2000; Madshus et al., 2000; Woodward et al., 2015). Good agreement is found between the measurements and the nonlinear model. The maximum downward displacement at the critical speed, at around 15 mm, is roughly double the result obtained due to the static load. On the other hand, the linear model predicts a critical speed of around 70 m/s, which is ~20% higher than the result from the nonlinear model. Furthermore, the maximum deflections close to the critical speed are much smaller for the linear model than for the nonlinear one. It is clear that soil nonlinearity should be considered for this site at the higher train speeds, although the results from the linear model agree reasonably well with the measurements for speeds lower than 40 m/s.

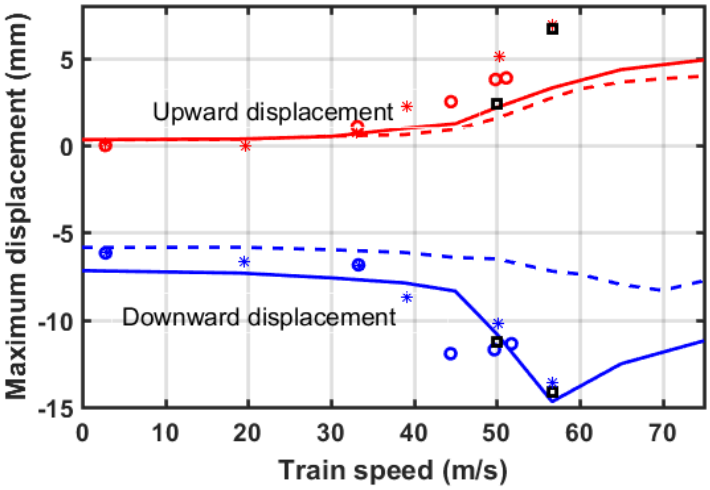

Figure 8-16. Maximum upward and downward sleeper displacements for different train speeds; -: northbound nonlinear model; □: southbound nonlinear model; --: linear model; o: northbound measurement data; *: southbound measurement data

Fig. 8-17 shows the maximum octahedral shear strains at different depths within the organic clay layer obtained from the nonlinear model for different train speeds. In each case the maximum strain at a given depth is shown. The strain level increases significantly when the load speeds are higher than around 45 m/s and reaches a level at higher speeds that is around three times larger than the results at low speed. Comparing these values with the modulus reduction curves in Fig. 8-7 it can be seen that the modulus will be reduced to between 90% and 70% of the small strain stiffness (according to nonlinear model 2).

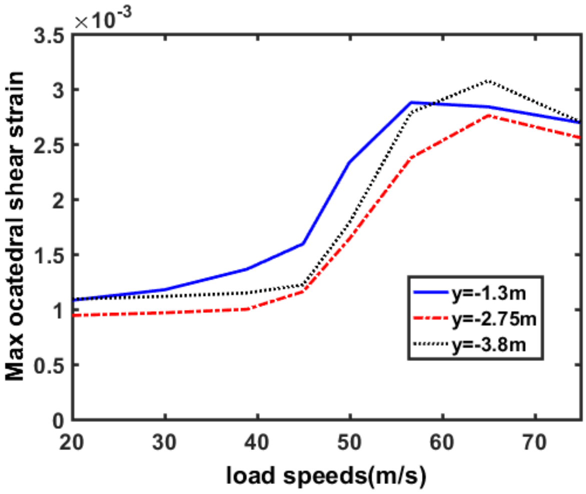

Figure 8-17. Maximum octahedral strain level at various depths in the organic clay layer at different load speeds

It is clear from the results presented in this section that incorrect behaviour can be found if the soil nonlinearity is neglected in the model. The linear model underestimates the displacements while it slightly overestimates the critical speed. Furthermore, the strain levels from the linear model are much smaller than those from the nonlinear model when the load speed approaches the critical speed. Nevertheless, the linear model gives acceptable results for lower speeds where the strains are less than about 10^{-3}.

8.5 Equivalent linear model

8.5.1 Procedure

Even though better agreement is found by using a nonlinear model, such a model tends to be much more computationally expensive than a linear model, in the present cases by about a factor of 20~70 for different cases. Therefore, an equivalent linear model, as used by previous authors (Costa et al., 2010; Hall, 2003; Kaynia et al., 2000; Madshus et al., 2000) is considered here as an alternative.

The equivalent linear model is an approximate approach that can account for soil nonlinearity to some extent. An iterative procedure based on the effective shear strain is required in order to achieve convergence. Convergence can be assumed if the difference between the shear modulus and damping ratio obtained in successive iterations is less than about 5~10% (Kramer, 1996). An effective shear strain is required to characterise the strain level from a transient record. This is often defined as

$$\gamma_{eff} = R_r \gamma_{\max} \tag{8-11}$$

where R_r is an empirical factor usually between 0.2 and 1 (Katayama et al., 1992; Yoshida et al., 2002) and $\gamma_{\max}$ is the maximum shear strain level for a specific layer (Kramer, 1996). As a result, a medium that is inhomogeneous with depth is obtained. This methodology has been used previously for calculations of the track/ground deflections induced by moving trains (Kaynia et al., 2000; Madshus et al., 2000). In a variation of this approach, instead of defining the same material modulus for an entire layer, Costa et al. allowed the material to be inhomogeneous in the width direction as well by identifying the maximum shear strain level element by element (Costa et al., 2010).

An approximate shear modulus reduction is used in references (Hall, 2003; Kaynia et al., 2000; Madshus et al., 2000) without any iteration. The procedure introduced by Costa et al. (Costa et al., 2010) requires more iterations to get to convergence because the criterion is applied to each element instead of an entire layer.

Here a simpler equivalent linear analysis based on the procedure given in (Kramer, 1996) is considered owing to the practical difficulties of updating every element at each iteration in the commercial software. Even though the strain distribution is different in the present case from the 1D wave propagation considered in (Kramer, 1996), the interest of the present paper is focussed on the region close to the track where it can be expected that relatively good predictions can be obtained. Again γ_{oct} is used here instead of the shear strain to determine the maximum strain, due to the complex three-dimensional strains occurring during train passage, as mentioned in Section 8.2. This was also used in (Costa et al., 2010; Halabian & Naggar, 2002).

Curves of the shear modulus reduction and damping ratio for the embankment, crust, organic clay and clay are used, as shown in Fig. 8-2 (Costa et al., 2010). Based on the conclusions from Section 8.4, the shear modulus reduction curve and damping ratio from the second nonlinear model (Fig. 8.7) are used here for investigating the factor to calculate the appropriate effective shear strain.

8.5.2 Investigation of the value R_r for the equivalent linear model based on nonlinear results

The influence of using different values of R_r is discussed here. For convenience, to avoid extensive iterations, the maximum strain level at each layer from the nonlinear model is used as the first calculation for the equivalent linear analysis. These are converted to effective strain by multiplying by the chosen value of R_r according to Eq. (8-11). From the effective strain, reduced shear modulus values are determined and used in a linear analysis as the first iteration. New shear modulus and damping ratio for each layer are then calculated based on the effective strain from the first iteration and these are used for the second iteration. The results from this second iteration are compared with those from the first step, as shown in Fig. 8-18 and 8-19, for values of R_r of 0.65 and 0.2.

This shows the shear modulus reduction and damping ratio that are input to the model for the next step. Note that the values of shear modulus plotted at the first iteration are not those used in the nonlinear model; they are the values of reduced shear modulus obtained from the maximum strains coming from the nonlinear model. They are different in Fig. 8-18 and 8-19 due to the use of different factors R_r.

If convergence has been achieved, the difference in shear modulus reduction and damping ratio between successive iterations should be less than 5~10% (Kramer, 1996). From Fig. 8-18, the results obtained using R_r = 0.65 at 56.7 m/s show differences of around 25% between the first and second iteration, whereas the results for R_r = 0.2 in Fig. 8-19 show much smaller differences indicating convergence has been achieved.

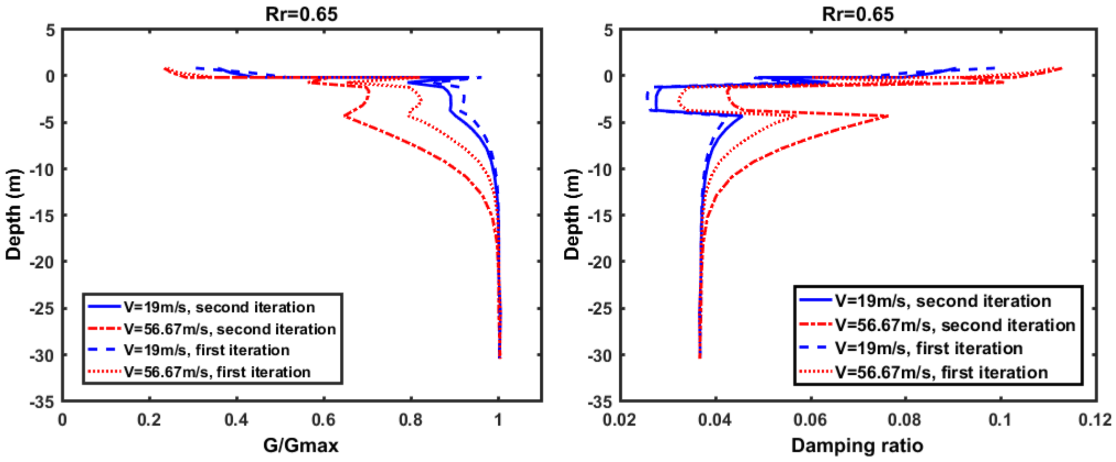

(a) (b)

Figure 8-18 Variation of shear modulus reduction and damping ratio with depth obtained using R_r=0.65 for two different load speeds, showing initial results and results after two iterations ; (a) shear modulus reduction; (b) damping ratio

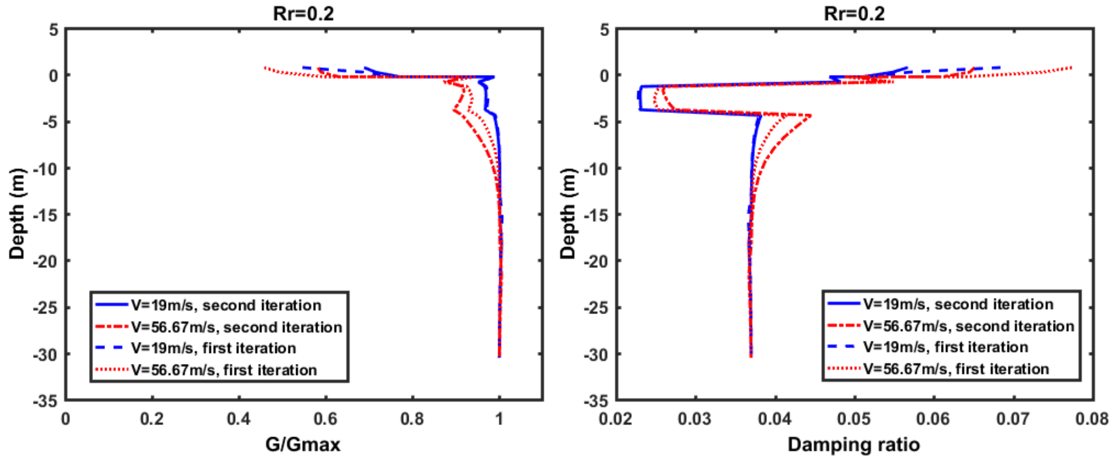

(a) (b)

Figure 8-19 Variation of shear modulus reduction and damping ratio with depth obtained using R_r =0.2 for two different load speeds, showing initial results and results after two iterations; (a) shear modulus reduction; (b) damping ratio

Looking at this a different way, the distributions of shear strain over the transient record can be considered. In order to able to choose an appropriate equivalent value that can capture the correct dynamic behaviour during the nonlinear analysis, the cumulative distribution function is used here. Fig. 8-20 shows the cumulative distribution functions of the normalized octahedral shear strain level obtained from the nonlinear model at the top surface of the organic clay. Results are shown for four different locations, from 0.7 m to 5.3 m away from the track centreline. In each case the value is normalized by the maximum strain at that position. From these results it can be seen that the median value (cumulative distribution function value of 0.5) occurs at around a normalised strain of 0.2 for the locations close to the track.

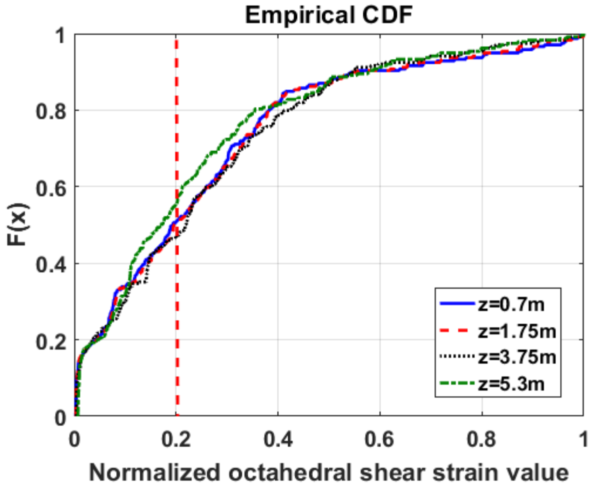

Figure 8-20 Cumulative distribution function of octahedral shear strain at load speed 56.7 m/s for the top surface of organic clay layer

In Fig. 8-21 the maximum octahedral shear strains as a function of the depth obtained in the converged results from the equivalent linear analysis with different values of R_r are compared with the results from linear and nonlinear models for two different train speeds. As can be seen, the strain levels are typically 10^{-3}, which is too large to allow the use of the small strain approximation (see Fig. 8-7). Nevertheless, for the load speed of 19 m/s, small differences are found between the four different models, confirming that it is unnecessary to take soil nonlinearity into account in this case, whereas Fig. 8-21(b) shows that for a load speed of 56.7 m/s the maximum strain level in the organic clay layer is around 57% higher for the nonlinear model than for the linear model. Furthermore, the strain level with R_r=0.2 is very similar to the results from the nonlinear model whereas the strain level is overestimated by around a factor of 2 when R_r=0.65 is used.

Fig. 8-22 shows the time histories of track displacement for the southbound train. These agree well with the measurements when R_r=0.2 is used for the equivalent linear analysis, whereas they are overestimated when using the factor of R_r=0.65.

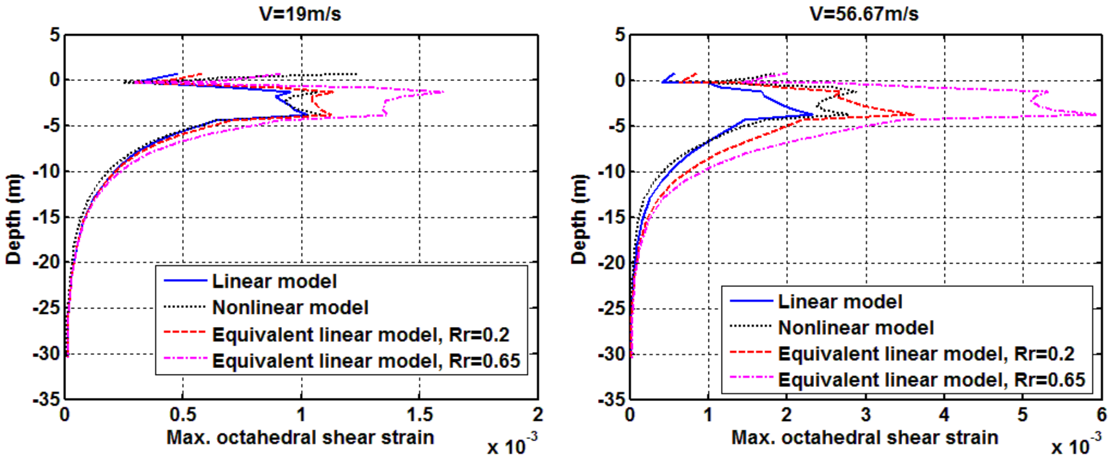

(a) (b)

Figure 8-21 Variation of maximum octahedral shear strain from two different speeds; (a) V=19 m/s; (b) V=56.7 m/s

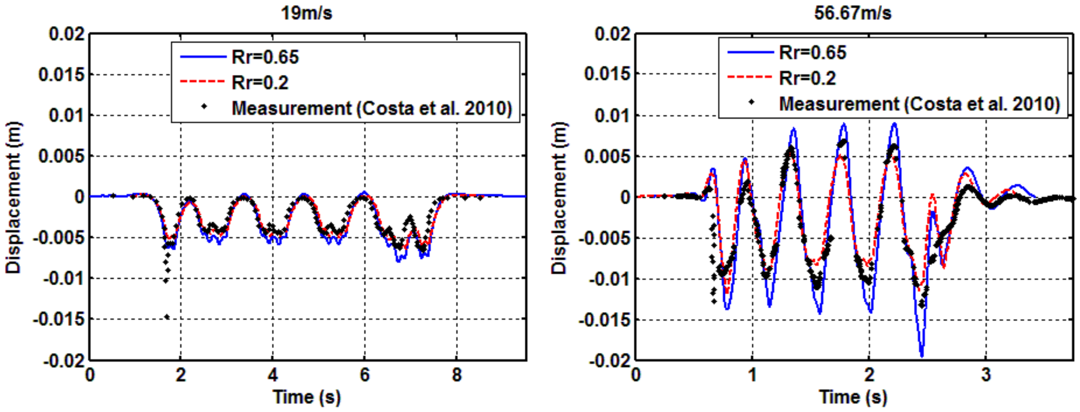

(a) (b)

Figure 8-22 Southbound displacement from equivalent linear model; (a) V=19 m/s; (b) V=56.7 m/s

Finally, the calculation times required for linear, equivalent linear and nonlinear analysis are compared in Table 8-4. As it is shown, the nonlinear analysis is much more expensive than the others and the equivalent linear analysis is much more efficient than the nonlinear analysis.

Table 8-4. Comparison of calculation times for train speed of 56.7 m/s in the southbound direction

	Calculation time (hr)	Iterations
Linear analysis	6	-
Equivalent linear analysis, R_r=0.65	18	3
Equivalent linear analysis, R_r=0.2	12	2
Nonlinear analysis	420	-

8.6 Moving vehicle analysis

In this section a moving vehicle model is introduced, with dynamic excitation due to track roughness as well as the quasi-static response to the moving loads calculated in the previous section. The model of the track/ground system is based on the equivalent linear method introduced in Section 8.5. The modelling procedure introduced in Section 3.2.1 is used for the vehicle, in which the vehicle is simulated using standard finite elements without the need for coupling with an external subroutine. The node-to-surface contact feature is used to simulate the sliding motion on a frictionless surface and the default contact property ‘hard contact’ is used without contact damping. A constant moving speed is implemented by defining the displacement of the moving vehicle along the direction of travel at each time step.

A random roughness profile with frequency content between 1.25 and 40 Hz is introduced into the rail geometry. The roughness profile is generated from a one-third octave spectrum as a sum of 17 harmonic components with random phases in each one-third octave band. Fig. 8-23 shows the target spectrum and the actual spectrum generated by this process. The roughness profile is plotted against distance in Fig. 8-24. A nominal roughness spectrum is used for the target as the actual roughness at the site is unknown. The node spacing along the rail varies between 0.12 and 0.21 m (due to discrete supports). Taking the larger of these values, this suggests that the model can be used up to 48 Hz, based on 6 nodes per shear wavelength. Therefore, the node spacing is sufficient to capture the minimum wavelength of the roughness 0.21 m for V=19 m/s and 0.6 m for V=56.7 m/s based on Nyquist criterion.

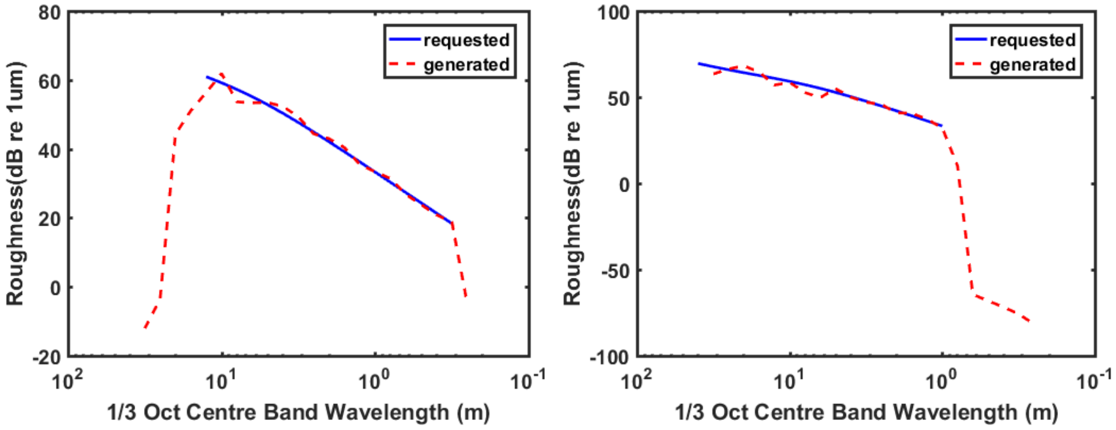

Figure 8-23 Roughness spectrum for different load speeds; (a) *V*=19 m/s; (b) *V*=56.7 m/s

A five degree of freedom vehicle model is used to represent one quarter of the X2000 train carriage, as shown in Fig. 8-25. Lumped mass elements are used for the vehicle car body and wheels and a rigid beam element is used for the bogie. Multiple vehicle models are used for each bogie with different parameters for the locomotive and passenger coaches to represent the whole train set. (Parameters were provided in confidence and so are not reproduced here). Instead of running the whole train set, however, simulations for a single vehicle of each type are used here for better efficiency. As the model is linear, the total dynamic responses can be calculated by superposition of the results from the two types of vehicle taking account of the location of the axle loads. A number of contact iterations are required in order to achieve the convergence if both vehicle axle loads and rail irregularity are considered. As a result, simulations of moving quasi-static loads and moving dynamic loads are calculated separated in order to improve the efficiency. The moving load analysis does not include the rail irregularity and the moving dynamic load results do not include the effect of the axle load allowing the two effects to be considered separately.

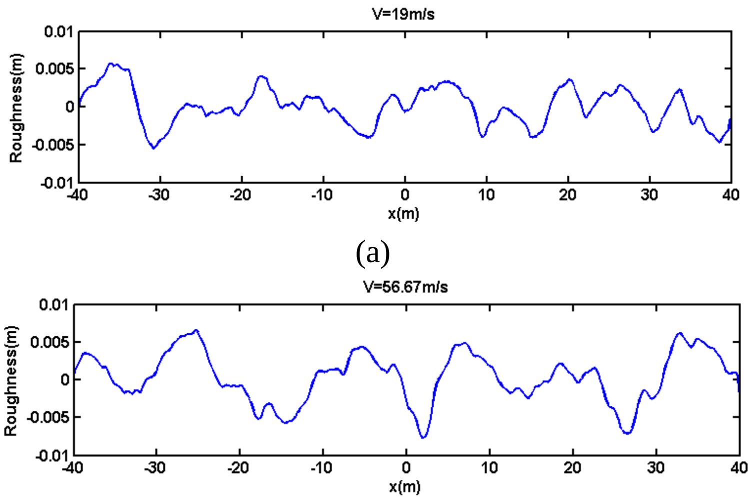

(a)

(b)

Figure 8-24 Rail roughness profile used for two different speeds; (a) *V*=19 m/s; (b) *V*=56.7 m/s

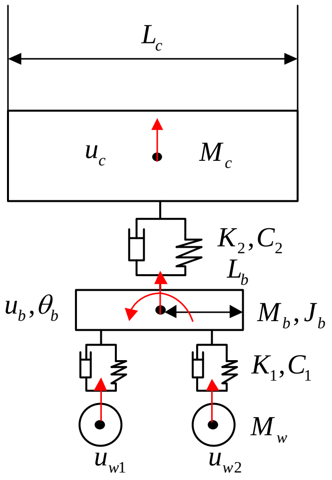

Figure 8-25 Five degree of freedom vehicle model

8.6.1 Data analysis

Before showing results from the moving vehicle analysis, quasi-static results are shown first. The displacement at the midpoint of the model in the time domain and results in the spatial domain at a specific time step are compared and discussed.

Fig. 8-26 shows the ground displacement as a function of time at 0.7 m and 7.5 m away from the central line when load speed is 70 km/h. These results are at the midpoint of the model. Even though a static step was applied to avoid transients occurring when the force is first applied, transients can still be seen in the early part of the response to the moving point load, (see also Fig. 6-3). This transient response is small compared with the response to the moving load occurring at the track, as shown in Fig. 8-26(a). However, further from the track the quasi-static vibration decays rapidly with distance and the amplitude of the transient displacement is sometimes even larger than the displacement induced by the moving load, as shown in Fig. 8-26(b). To help rectify this, a Hamming window is applied in order to attenuate this transient response. The results with and without the window are shown in Fig. 8-26. Although better results are obtained, the transient response is still clearly visible for the results further from the track, as shown in Fig. 8-26(b).

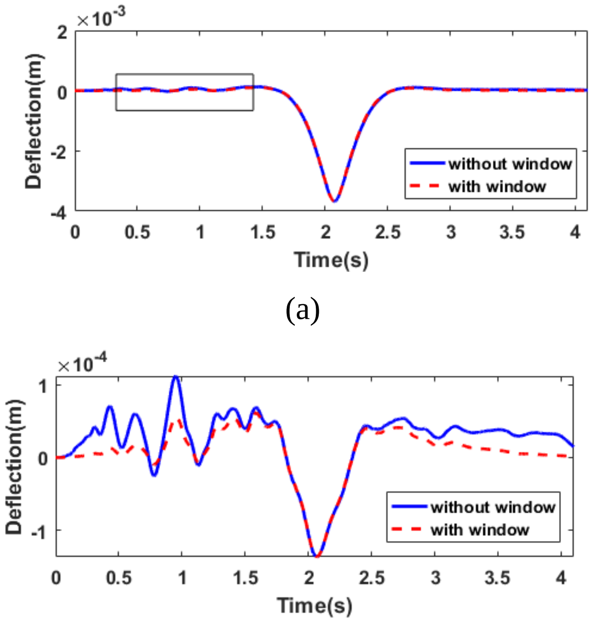

(a)

(b)

Figure 8-26 Midpoint results with/without window from moving point load for load speed 19 m/s in the time domain; (a) z=0.7 m; (b) z=7.5 m

On the other hand, Fig. 8-27 shows the corresponding results in the spatial domain at a time step that is sufficient for the transient to be avoided. This does not show the same oscillations. However, a Hamming window is still applied in order to attenuate the result from close to the boundary. Subsequently, instead of using time domain results to determine the response to the moving loads, these results in the spatial domain at a specific time step are used to avoid this transient issue.

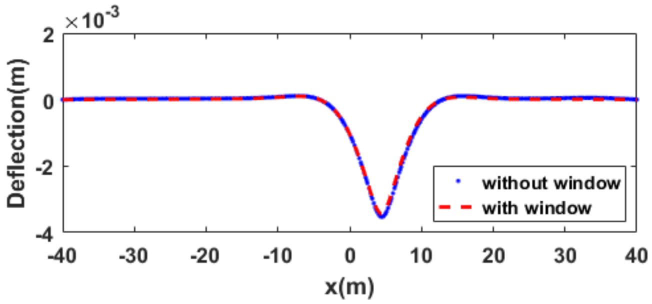

(a)

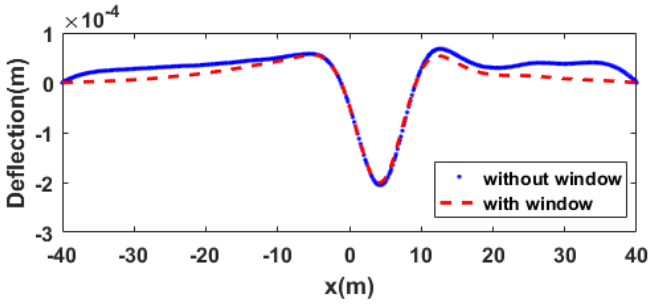

(b)

Figure 8-27 Results from moving point load with/without window for load speed 19 m/s in the space domain when load is applied at x = 4 m away from the centre; (a) z=0.7 m; (b) z=7.5 m

As described in Section 8.3, the FE mesh used for the ground model in the transverse direction is continuously increasing with a stretch factor of 1.2. The node spacing increases from 0.17 m beneath the track to 0.52 m at 7.5 m. For moving dynamic loads, the propagation wavelength in the transverse direction can no longer be considered large compared with the elements, as was the case for the results from the moving load. As a result, the grid size in the transverse direction should ideally be refined to be equal to the size in the running direction for better prediction. However, very low frequencies are of most interest for the vibration at this site. The results at 7.5 m from the track can be considered reliable up to around 20 Hz based on 6 elements per wavelength. A better grid refinement is required to study further distances and higher frequencies.

For clarity, the results obtained in the time domain are post-processed into the frequency domain by using the fast Fourier transform and then converting the spectra into one-third octave bands. The vertical velocity in one-third octave bands due to the moving quasi-static load (i.e. still with no roughness) at z=0.7 m (under the rail) and 7.5 m from the track centreline is shown in Fig. 8-28. It can be seen that the result for 56.7 m/s is 20 dB higher than that at 19 m/s at the location under the rail and 40 dB higher at the location

7.5 m for frequencies up to 5 Hz. This agrees with results shown by (Sheng et al., 2003). However, the results for both speeds do not continue to fall at high frequency, as would be expected (Ju, Liao, & Ye, 2010; Sheng et al., 2003, 2004a). To help rectify this, a window is applied in the space domain, as mentioned above, before superposition. More reasonable predictions can be found for both speeds.

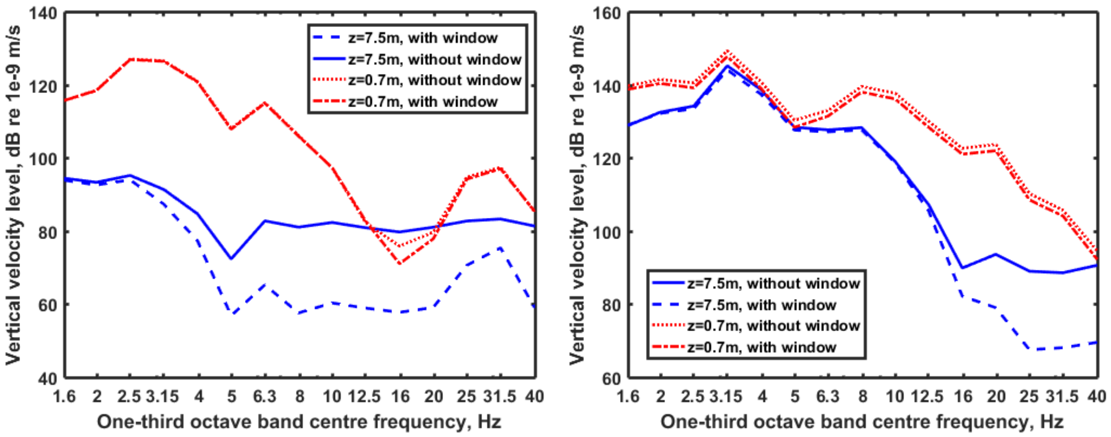

(a) (b)

Figure 8-28 Results due to moving loads calculated by superposition in the space domain for two different load speeds; (a) 19 m/s; (b) 56.7 m/s

8.6.2 Validation of model including vehicle

The ground vibration at 7.5 m from track is compared with the results from measurement (Sheng et al., 2003). Fig. 8-30 shows the vertical velocity in one-third octave bands obtained from ABAQUS compared with the measurements at two different load speeds, 19 m/s and 56.7 m/s. The results from moving axle loads and moving dynamic loads are presented separately. Relatively good agreements are found between the results from ABAQUS and the measurement at the two different speeds, apart from the higher speed results at higher frequency. The dynamic responses become the dominant component above a certain frequency, around 2.5 Hz for 19 m/s and 10 Hz for 56.7 m/s, whereas the response to the moving load is dominant below these frequencies. Poor agreement, with a difference of around 13 dB, is found at 12.5 Hz. This could be due to incorrect rail irregularity input or insufficient element size for this frequency. A better prediction can be obtained with finer mesh.

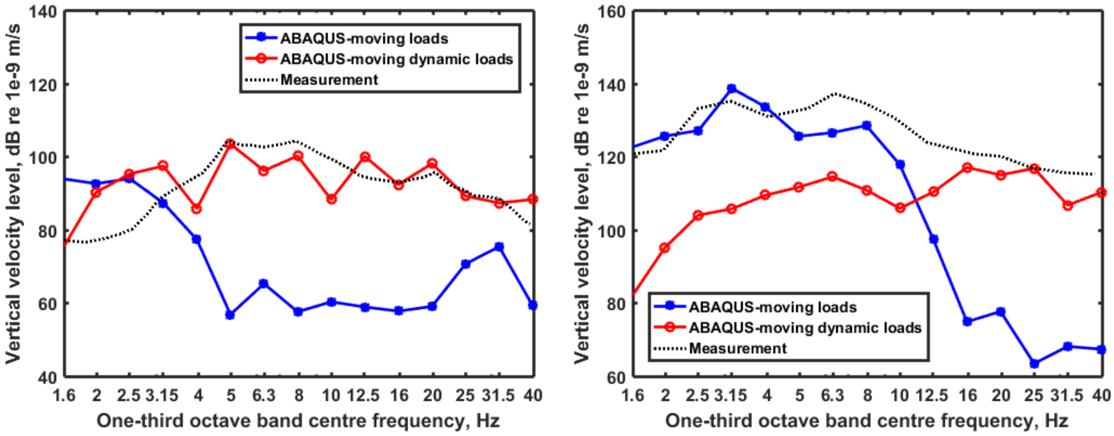

(a) (b)

Figure 8-29 Results from ABAQUS at 7.5m from the track compared to the measurement (Sheng et al., 2003).; (a) load speed 19 m/s ; (b) load speed 56.7 m/s

8.7 Summary

In this chapter, nonlinear models of the ground have been introduced into a three-dimensional track/ground finite element model that operates in the time domain. Soil nonlinearity has been implemented within the FE model in terms of shear modulus degradation curves based on laboratory results. Good agreement has been found compared with site measurements at the soft soil site at Ledsgård, Sweden. The effect of soil nonlinearity becomes significant at this site when the load speeds approach or exceed around 70% of the critical speed. The maximum track displacements for load speeds close to the critical speed are around twice those found at lower speeds. The maximum strain levels in the subgrade increase by around a factor of three.

Consideration of soil nonlinearity is significantly important for the crust and organic layer, the shear wave speed of which are 60 m/s and 42 m/s.

A linear model based on the small-strain stiffnesses measured in situ gives good results for low speeds. However, the critical speed obtained from this linear model is ~20% higher than that obtained from the nonlinear model and the displacements from the linear model are underestimated for speeds approaching the critical speed.

Two different shear modulus reduction curves have been considered in the nonlinear model, both of which are broadly consistent with soil data obtained in triaxial tests. The results are found to be very sensitive to the choice of this curve. The damping is based on constant Rayleigh coefficients but it is found that the damping ratio increases due to the stiffness degradation and this fits the data from triaxial test quite well.

The maximum strain levels are found in the organic clay layer, which is the softest layer. High strain levels can be found for the higher load speed in the region under the leading axle. On the other hand, a wider region is found that has strain level larger than 0.001 at the following axle. Octahedral shear strains of around 10^{-3} can still be found at 30 m away from the track for the nonlinear model.

Results from an equivalent linear approach have been compared with the results from the nonlinear model. From this it is shown that consistent results are found if the equivalent strain is taken as 20% of the maximum strain value. This shows better agreement with the nonlinear analysis and the measurements than the conventional factor of 65% used in earthquake analysis. Nevertheless, further investigation is required in order to reach a more general conclusion that can be applied to other sites and to displacements further from the track.

Finally a vehicle model is coupled to the track including roughness excitation. Space domain results with window is suggested for data analysis in order to avoid the transient issue from the beginning. Good agreement is found for sleeper displacement spectrum compared to site measurement. Relatively good agreement is found from this model compared with measurements apart from the results for higher speed at higher frequency.

Chapter 9: Conclusions and Recommendations for future work

9.1 Conclusions

In this work a modelling approach for vehicle/track/ground interaction in the time domain has been developed and validated. The main conclusions from the work are summarised in this section. Section 9.1.1 presents conclusions relating to the modelling procedure for vehicle/track/ground interaction and guidelines for modelling are given in Section 9.1.2. The effects of critical speed and resonance frequency are summarised in Section 9.1.3. Finally, the influence of soil nonlinearity is discussed in Section 9.1.4.

9.1.1 Development of vehicle/track/ground interaction model that can account for soil nonlinearity

A modelling approach for vehicle/track/ground interaction in the time domain has been developed using the FE commercial software, ABAQUS. A python code has been developed to construct the model geometry (including spherical and cuboid meshes) and other required parameters. A user-defined material subroutine UMAT has been implemented in order to account for soil nonlinearity.

Two different approaches have been investigated for modelling the coupling between the vehicle and the track, based on a sliding contact model and a user-defined subroutine. These are compared using simulations of a moving axle load and a sprung-mass system on a simply supported beam. It is shown that using the in-built contact model is much more efficient, around 2~3 times faster, than using a user-defined subroutine.

To introduce the ground, it is important to avoid reflections from the artificial model boundaries. Two meshing approaches, a hemispherical model with infinite elements and a cuboid model without/without infinite element, are compared. Even though good absorption is shown at the boundary for the hemispherical model, artificial displacements are found to occur due to the unconstrained boundary when a moving load is applied. Furthermore, if larger models are required, the simulation cost tends to be very expensive due to the need to expand the model in three directions. In the end, a cuboid mesh without infinite elements has been shown to be the optimum meshing approach in terms of prediction accuracy and efficiency. The base was fixed to prevent rigid-body motions and, rather than use infinite elements at the sides, these were also fixed. Provided that a suitable damping model is used, the spurious reflections from the sides of the model can be suppressed with a sufficient width of model. On the other hand, if infinite elements are used the model does not need to be so wide but the calculations are found to be considerably more costly.

9.1.2 Numerical modelling guidelines for vehicle/track/ground interaction model in the time domain

Based on a number of simulations, guidelines for modelling vehicle/track/ground interaction are given in terms of the element types, track model, model length and width.

Several different models for the track vibration are introduced and compared, based on beams, plane stress and three-dimensional solid elements. To compare these models, equivalent parameters are derived, including those for the rail, railpad, sleeper and ballast. The different models have been compared in terms of the response to a stationary harmonic load, a moving quasi-static load and moving dynamic loads. It is suggested that an Euler-Bernoulli beam is more appropriate than a Timoshenko beam for modelling the response of the rail to a moving point load, in order to avoid unrealistic rail deflection under the load, which causes unrealistic high frequency components in the non-moving frame.

The inclusion of ballast density is shown to affect the track frequency response in the range 80~400 Hz. The first and second cut-on frequencies of waves in the rail decrease when the ballast density is included in the model. Good agreement has been found in terms of the rail receptance between continuous and discretely supported models for frequencies up to 1000 Hz. However, the type of elements used for the railpads cause significant effects when the track is coupled to a soft ground. Better agreement between continuous and discretely supported models is found for excitation by a moving load when orthotropic elements are used for the railpad due to the influence of the shear stress in the railpad if isotropic elements are used.

For a moving load, it has been shown that the distance required to reach a steady-state solution becomes very large when the load speed is close to the critical speed, particularly for a homogeneous half-space. For an example of a layered half-space, an 80 m long model is found to be sufficient to reach the steady sate. An appropriate Rayleigh damping is adopted in order to avoid the reflections from the side boundary based on the decay rate with distance. A reduction of at least 3 dB at 40 m is required in order effectively to reduce the reflection from the side. For a layered ground the damping model should be based on the resonance frequency when the load speed is higher than the wave speed of the upper layer.

Comparisons are also made with a wavenumber FE/BE model in the frequency domain, and good agreement is found provided that suitable parameters are used for the damping model. Different models of soil damping have been considered using a combination of mass- and stiffness-proportional damping in order to approximate a constant loss factor, often found in field measurements of soil damping. In the case of a layered ground this damping model can be equated to a particular loss factor at the resonance frequency of the ground layer but with a homogeneous half-space there is no obvious dominant frequency at which to match the two damping models.

9.1.3 Critical speed and resonance frequency of different grounds

For a layered half-space the dependence of the critical speed on the wavespeeds of the upper layer and the underlying half-space and the layer depth is studied. It is found to correspond to the Rayleigh wave speed for a homogeneous half-space but for a layered ground it can be considerably higher. The critical speed decreases with increasing depth of the first layer and S-wave speed, whereas the amplitude of the maximum displacement tends to increase.

Oscillations are found in the track response to a moving load for a layered ground. The frequency of these oscillations has been investigated and compared with estimates from the dispersion curve and the resonance frequency obtained from a stationary harmonic load. Although the oscillation frequencies are influenced by the speed of the moving point load, relatively good agreement is found with the results from the other methods. A formula is suggested to estimate the resonance frequency for a layered ground in terms of the depth of the upper soft layer and its S-wave speed.

9.1.4 Better understanding the influence of soil nonlinearity

A simple soil nonlinear model has been introduced which only requires an appropriate shear modulus reduction curve. This has been tested against the published measurement data for a site at Ledsgård in Sweden. By choosing an appropriate stiffness degradation curve, the dependence of the damping ratio is also correctly predicted by using constant

Rayleigh damping parameters. Better agreement compared to measurements is found for speeds close to the critical speed when the nonlinear model is used.

When a linear model is used for the soil, not only the maximum rail deflection but also the strain level are underestimated. From simulations for the site at Ledsgård, these results are found to be around 50% lower than the results from the nonlinear model at the critical speed. Moreover, the critical speed is predicted to be around 15% higher than the measurement. As a result, if a linear analysis is used for design, this may underestimate the risk of critical speed effects occurring. Nevertheless, good agreement still can be found for lower speeds using the linear model; for Ledsgård this can be used up to around 70% of the critical speed.

Consideration of soil nonlinearity becomes important when the octahedral strain level is higher than 0.001. Measured data on soil samples contains considerable variation so that two different shear modulus reduction curves have been identified that are both consistent with the measured data. Significant differences are found from nonlinear models based on these two shear modulus reduction curves. Better results are obtained from a reduction curve that fits the measured damping ratio as well as the shear modulus reduction. Finally, the results from equivalent linear analysis are compared with those from the nonlinear model. It is found that these are sensitive to the value used for the effective shear strain. If the conventional value of 0.65 of the maximum shear strain is used, the results are overestimated, with values around double that from the nonlinear model. A factor of 0.2 is suggested to be more appropriate for the case of a train pass-by for the example considered.

9.2 Recommendations for future work

Some suggestions for future work are proposed in this section in terms of improvements to the model and other applications.

9.2.1 Investigation of the nonlinear shear modulus degradation curve

The shear modulus degradation obtained from laboratory measurements (Costa et al., 2010) has been approximated by an empirical model. However, there are many other models, which include the confining pressure, plasticity index, excitation frequency, etc., based on a various triaxial tests, that can predict the shear modulus degradation curve. These should be investigated to give, better understanding, e.g. of the influence of the confining pressure and plasticity index on the nonlinear soil response for vehicle/track/ground interaction dynamics.

9.2.2 Long-term behaviour for ballast and soil

Ballast and subgrade settlement is an important issue for many railways. However, these have not been considered in the current work as the models do not include the plastic deformation required to take into account the permanent strain (settlement). Ballast and subgrade settlement can be obtained if an elastoplastic model is considered. Furthermore, there are a number of empirical models for predicting the ballast and subgrade settlement. A better understanding of the use of these empirical models can be obtained by comparing their results with those from an elastoplastic FE model.

9.2.3 Investigation of the railpad properties

As shown in the results, the critical speed is influenced by the shear stiffness of the railpad. Better estimates of the actual stiffness of the railpad and clips in different directions and the influence of this on the critical speed need to be taken into account. Furthermore, the nonlinear properties of railpads should also be considered.

9.2.4 Investigation of the soil damping

Soil damping is a complex parameter. Two different damping models have been used and compared. In the time domain simulations viscous damping based on the Rayleigh damping model has been used whereas in frequency domain models structural damping with a constant loss factor has been used. These have been compared in terms of the rail deflections. Good agreement has been found for a layered half-space based on the appropriate equivalent loss factor calculated in terms of a single resonance frequency. However, far field results have not been compared. A better understanding of the soil damping is required as neither model may be completely representative of the damping occurring in reality. Comparisons with measurement data are required.

9.2.5 Further investigation of the factor of effective strain for equivalent linear analysis

Even though good agreement is found when factor of 0.2 is used to calculate the effective strain level in equivalent linear analysis, it can be expected that this value may vary with different ground properties and excitation force. More examples with different geotechnical profiles is required in order to reach a more general conclusion.

9.2.6 Further investigation of the need to consider soil nonlinearity

A case study has been analysed in the present work in order to investigate the importance of soil nonlinearity. Consideration of soil nonlinearity is found to be extremely necessary especially for speeds close to the critical speed for very soft ground properties. Other cases should be considered to reach a better understanding of the situations in which consideration of soil nonlinearity is required.

9.2.7 Mesh strategies

A graded mesh has been used in the present work and good agreement has been found compared to the measurement. However, the graded mesh is only appropriate for near-field predictions. As a result, other meshing strategies should be considered in order to investigate the responses in the far field.

Appendices

Appendix A. Track modelling

A.1 Analytical model of ballasted track with harmonic load

Dynamic analysis of railway track is commonly based on a two-dimensional system consisting of a beam on a single or double layer support. The Simplest model is the Winkler foundation, in which the rail is represented by an infinite Euler-Bernoulli beam supported by a single continuous elastic layer. The rail displacement due to a static load or a harmonic force can be determined using this model. However, it is a simple model which neglects many features of the real system; furthermore, it only considers the vertical displacement of the rail. In order to include other aspects of the track a two-layer support model can be introduced. The two-layer support model of the track is also an infinite model but involves more track components in the system, including the rail, sleeper, pad and ballast. The pad and ballast are assumed to be linear elastic elements defined by their stiffness per unit length and the sleeper is represented by a layer of mass. The rail and sleeper displacements can be found from the calculation. In both models damping can also be included in the elastic layers.

A harmonic force acting on the single-layer support track system at *x*=0, is shown in Fig. A-1. EI is the rail bending stiffness and ρA is the rail mass per unit length; furthermore, s is the foundation stiffness per unit length and *x* is the distance along the rail. The displacement amplitude, u, and the mobility, Y, at frequency ω can be found by solving the wave propagation problem (Thompson, 2009).

The harmonic displacement amplitude at *x*=0 is given by,

$$u\left(0\right)=\frac{-iF}{4EIk_p^3}\left(1-i\right) \qquad \textit{(A-1)}$$

and the point mobility,

$$Y\left(\omega\right)=\frac{\left(1-i\right)\omega}{4EIk_p^3} \qquad \textit{(A-2)}$$

where k_p is the wavenumber in the supported beam which can be calculated by (Thompson, 2009)

$$s_p=s_B\left(1+i\eta_r\right)^{-1/4}\left(1-\frac{s\left(1+i\eta\right)}{\rho A\omega^2}\right)^{1/4}\approx s_B\left(1-\frac{i\eta_r}{4}\right)\left(1-\frac{\left(1+i\eta\right)}{\left(\omega/\omega_0\right)^2}\right)^{1/4} \qquad \textit{(A-3)}$$

where η_r and η are the damping loss factors of the rail and the foundation, respectively. In addition, the natural frequency ω_0 and the free wavenumber in the undamped rail k_B , are introduced which are given by the following equations,

$$\omega_0 = \sqrt{\frac{s}{\rho A}} \tag{A-4}$$

$$k_B = \left(\frac{\rho A \omega^2}{EI} \right)^{1/4} \tag{A-5}$$

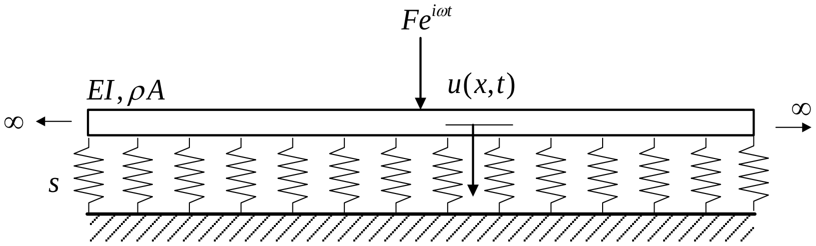

Figure A-1 Single-layer support track model

The double-layer support track model is shown in Fig. A-2. A harmonic force again acts at x=0. Most of the track parameters are the same, but the pad stiffness, mass per unit length of the sleeper and ballast stiffness are also considered in this model.

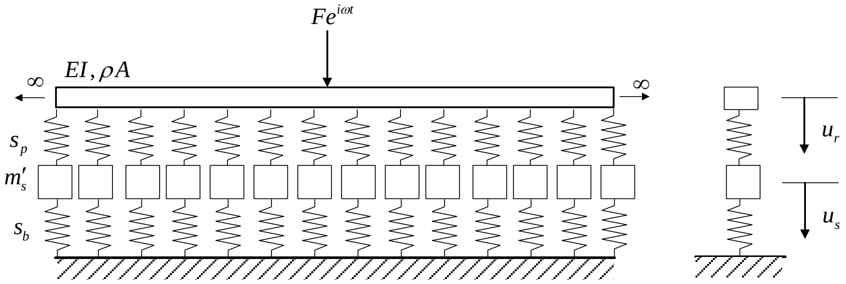

Figure A-2 Double-layer support track model

The formulations for the displacement and point mobility at frequency ω at x = 0 are the same as for the single-layer support, Eq. (A-1)~(A-2), except that, the foundation stiffness, s, is replaced by the frequency-dependent support stiffness, $s(\omega)$, given by

$$s(\omega) = \frac{s_p\left(1+i\eta_p\right)\left(s_b\left(1+i\eta_b\right)-\omega^2 m_s'\right)}{\left(s_p\left(1+i\eta_p\right)+s_b\left(1+i\eta_b\right)-\omega^2 m_s'\right)} \tag{A-6}$$

where s_p is the pad stiffness, m_s' is the sleeper mass, s_b is the ballast stiffness and η_p and η_b are the damping loss factor of the railpad and the ballast, respectively. Hence, the wavenumber of the two-layer support can be determined by Eq. (A-3), and the displacement and mobility of the rail can be calculated by Eq. (A-1), (A-2).

The displacement of the sleeper, u_s, can be determined by

$$u_s = u_r \frac{s_p}{(s_p + s_b - \omega^2 m_s')} \tag{A-7}$$

A.2 Analytical model of moving load applied on a single-layer track system

In this section existing analytical models (Fryba, 1999) of a rail on a Winkler foundation with a moving load are introduced as shown in Fig. A-3. The parameters are the same as in Section A.1.

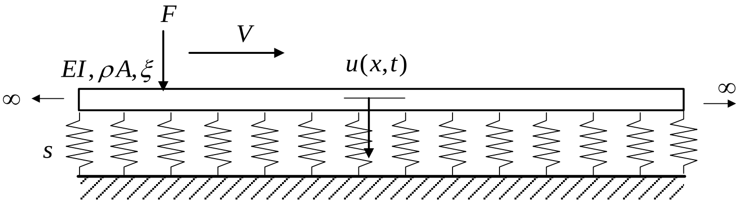

Figure A-3 Winkler foundation with a moving load

The rail support layer is assumed to be linear and elastic and given by its stiffness per unit length, s. EI is the rail bending stiffness, ρA is the rail mass per unit length, and ξ is the damping ratio of the beam. The load F is moving at speed V.

A new coordinate is introduced, moving with the load,

$$z = \lambda\left(x - Vt\right) \tag{A-8}$$

where x is the distance along the rail, t is time and

$$\lambda = \left(\frac{s}{4EI}\right)^{\frac{1}{4}} \tag{A-9}$$

The displacement amplitude at any position x

$$u(x,t) = u_0 u\left(z\right) \tag{A-10}$$

where u_0 is given by

$$u_0 = \frac{F\lambda}{2s} \tag{A-11}$$

and $u(z)$ is the dimensionless deflection of the beam given by (Fryba, 1999)

$$u(z) = \frac{2}{a_1(D_1^2 - D_2^2)} e^{-bs}\left(D_1 \cos a_1 s + D_2 \sin a_1 s\right), \quad \text{for } s > 0 \tag{A-12}$$

$$u(z) = \frac{2}{a_2(D_3^2 - D_4^2)} e^{bs}\left(D_3 \cos a_2 s + D_3 \sin a_2 s\right), \quad \text{for } s < 0 \tag{A-13}$$

where

$$D_1 = a_1 b, \quad D_2 = b^2 - \frac{1}{4}\left(a_1^2 - a_2^2\right),$$

$$D_3 = a_2 b, \quad D_4 = b^2 + \frac{1}{4}\left(a_1^2 - a_2^2\right) \tag{A-14}$$

and for $c < 1, \quad d \ll 1$, *b, a₁, a₂* can be approximated as

$$b \approx \left(1 - c^2\right)^{1/2}, a_{1,2} \approx \left[1 + c^2 \pm \frac{2cd}{\left(1 - c^2\right)^{1/2}}\right]^{1/2} \tag{A-15}$$

where

$$c = \frac{V}{V_{cr}}, \; d = \zeta \tag{A-16}$$

and V_{cr} is the critical speed given by

$$V_{cr} = \sqrt[4]{\frac{4sEI}{(\rho A)^2}} \tag{A-17}$$

The approximation in equation (A-19) gives good results except when the load speed approaches the critical speed where the error increases. The results can be obtained by solving the equations

$$\begin{cases} a_1^2 = 2c^2 + b^2 + 2cd/b \\ a_2^2 = 2c^2 + b^2 - 2cd/b \\ b^6 + 2c^2 b^4 + \left(c^4 - 1\right) b^2 - c^2 d^2 = 0 \end{cases} \tag{A-18}$$

by a numerical method.

Appendix B. Wavenumber FE/BE method for track/ground interaction with a moving load

The wavenumber FE/BE method is a so-called 2.5D approach which is based on the assumption that the geometry in the longitudinal direction is invariant (Sheng et al., 2005). This has been implemented in software known as WANDS (Nilsson et al., 2007). This has been used here to obtain solutions for the steady-state response to a moving load and to a static harmonic load for comparison with the FE models developed here. The cross-section of the track/ground model used is shown in Fig. B-1. The rail is modelled as an Euler-Bernoulli beam, whereas solid finite elements are used to model the railpads, sleepers and ballast and boundary elements are used to model the unbounded homogeneous soil. The results are obtained in the wavenumber domain by solving for the displacement at each frequency ω and wavenumber β. The results in the spatial domain can be recovered by using an inverse discrete Fourier transform with respect to the wavenumber

$$\hat{u}(x,y,z,\omega)=\frac{1}{2\pi}\sum_{-\beta_{\max}}^{\beta_{\max}}\tilde{u}(\beta,y,z,\omega)e^{i\beta x}\Delta\beta \qquad \textit{(B-1)}$$

where $\hat{u}$ and $\tilde{u}$ are the displacement functions in space and wavenumber domain, respectively. $\Delta\beta$ is the wavenumber spacing (or resolution), β_{max} is the maximum wavenumber. These two parameters need to be chosen carefully to obtain reliable results. The resolution depends on the chosen wavenumber, which has to be fine enough to capture the peaks in the integrand. However, the maximum wavenumber should be large enough to cover all the relevant waves at the frequencies of interest. Here β_{max} is set to 6.42 rad/m and $\Delta\beta$ is chosen to give 1024 wavenumbers over the range from $-\beta_{max}$ to β_{max} (Jin & Thompson, 2014).

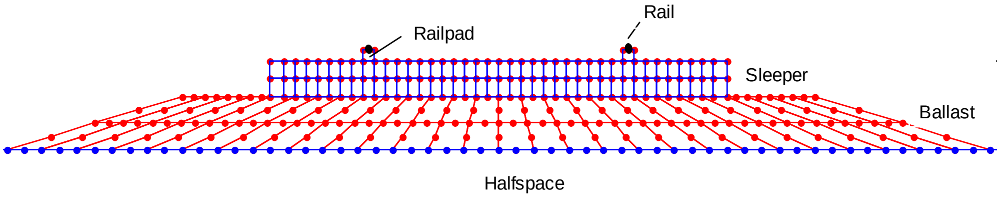

Figure B-1. Cross-section of track and ground model in wavenumber FE/BE method

Appendix C. Shear modulus reduction curve

The shear modulus reduction curve is based on the following functions proposed by Ishibashi et al. (Ishibashi et al., 1993) in terms of cyclic shear strain amplitude, mean effective confining pressure and the soil's plasticity index. The shear modulus reduction is written as

$$\frac{G}{G_{\max}} = K\left(\gamma, I_p\right)\bar{\sigma}_0^{m\left(\gamma, I_p\right)-m_0} \tag{C-1}$$

where $\bar{\sigma}_0$, γ , I_p are the mean effective confining pressure, cyclic shear strain amplitude and plasticity index. When the shear strain is smaller than 10^{-6}

$$K\left(\gamma, I_p\right) = 1 \tag{C-2}$$

$$m\left(\gamma, I_p\right) - m_0 = 0 \tag{C-3}$$

For shear strains larger than 10^{-6}

$$K\left(\gamma, I_p\right) = 0.5\left\{1 + \tanh\left[\ln\left(\frac{0.000102 + n\left(I_p\right)}{\gamma}\right)^{0.492}\right]\right\} \tag{C-4}$$

$$m\left(\gamma, I_p\right) - m_0 = 0.272\left\{1 - \tanh\left[\ln\left(\frac{0.000556}{\gamma}\right)^{0.4}\right]\right\} e^{-0.0145 I_p^{1.3}} \tag{C-5}$$

where

$$n\left(I_p\right) = \begin{cases} 0.0 & \text{for} \quad I_p = 0 \\ 3.37\times10^{-6} I_p^{1.404} & \text{for} \quad 0 \le I_p \le 15 \\ 7.0\times10^{-7} I_p^{1.976} & \text{for} \quad 15 \le I_p \le 70 \\ 2.7\times10^{-5} I_p^{1.115} & \text{for} \quad I_p > 70 \end{cases} \tag{C-6}$$

List of References

Abadi, T., Le Pen, L., Zervos, A., & Powrie, W. (2016). A Review and Evaluation of Ballast Settlement Models using Results from the Southampton Railway Testing Facility (SRTF). *Procedia Engineering*, *143*, 999–1006.

ABAQUS. (2012). Getting Started with Abaqus: Keywords Edition 6.12.

ABAQUS. (2013a). Abaqus 6.13-Analysis User's Guide: Volume IV: Elements.

ABAQUS. (2013b). Abaqus Theory Manual v6.12.

Andersen, L., Nielsen, S. R. K., & Krenk, S. (2007). Numerical methods for analysis of structure and ground vibration from moving loads. *Computers & Structures*, *85*(1–2), 43–58.

Anderson, W. F., & Fair, P. (2008). Behavior of Railroad Ballast under Monotonic and Cyclic Loading. *Journal of Geotechnical and Geoenvironmental Engineering*, *134*, 316–327.

Aubry, D., Hujeux, J. C., Lassoudiere, F., & Meimon, Y. (1982). A double memory model with multiple mechanisms for cyclic soil behaviour. In *Geomech., Int. Symp. Num. Mod.* (pp. 3–13). Balkema.

Auersch, L. (2005). The excitation of ground vibration by rail traffic: theory of vehicle–track–soil interaction and measurements on high-speed lines. *Journal of Sound and Vibration*, *284*(1–2), 103–132.

Aursudkij, B., McDowell, G. R., & Collop, A. C. (2009). Cyclic loading of railway ballast under triaxial conditions and in a railway test facility. *Granular Matter*, *11*(6), 391–401.

Beresnev, I. A., & Wen, K. (1996). Nonlinear Soil Response A Reality ? *Bulletin of the Seismological Society of America*, *86*(6), 1964–1978.

Bettess, P. (1977). Infinite elements. *International Journal for Numerical Method in Engineering*, *11*(January 1976), 53–64.

Biggs, J. M. (1964). *Introduction to Structural Dynamics*. Mcgraw-Hill, Inc.: USA.

Boyce, H. R. (1980). A non-linear model for the elastic behaviour of granular materials under repeated loading. In *Proc., Int. Symp. on Soils under Cyclic and Transient Loading* (pp. 285–294).

Brown, S. F., Brodrick, B. V., Thom, N. H., & McDowell, G. R. (2007). The Nottingham railway test facility, UK. *Proceedings of the ICE - Transport*, *160*(2), 59–65.

Cheng, Y. P., Nakata, Y., & Bolton, M. D. (2003). Discrete element simulation of crushable soil. *Géotechnique*, *53*(7), 633–641.

Chopra, A. K. (2007). *Dynamic of Structures-Theory and Applications to Earthquake*

Engineering (Third Edit).

Connolly, D., Giannopoulos, A., & Forde, M. C. (2013). Numerical modelling of ground borne vibrations from high speed rail lines on embankments. *Soil Dynamics and Earthquake Engineering*, *46*, 13–19.

Costa, P. A., Calçada, R., & Cardoso, A. S. (2012). Track–ground vibrations induced by railway traffic: In-situ measurements and validation of a 2.5D FEM-BEM model. *Soil Dynamics and Earthquake Engineering*, *32*(1), 111–128.

Costa, P. A., Calçada, R., Cardoso, A. S., & Bodare, A. (2010). Influence of soil non-linearity on the dynamic response of high-speed railway tracks. *Soil Dynamics and Earthquake Engineering*, *30*(4), 221–235.

Costa, P. A., Colaço, A., Calçada, R., & Cardoso, A. S. (2015). Critical speed of railway tracks. Detailed and simplified approaches. *Transportation Geotechnics*, *2*, 30–46.

Cundall, P. A., & Strack, O. D. L. (1979). A discrete numerical model for granular assemblies. *Géotechnique*, *29*(1), 47–65.

Dieterman, H. A., & Metrikine, A. (1996). The equivalent stiffness of a half-space interacting with a beam. critical velocities of a moving load along the beam. *European Journal of Mechanics A/Solids*, *15*, 67–90.

Dieterman, H. A., & Metrikine, V. A. (1997). Steady state displacements of a beam on an elastic half space due to a uniformly moving load. *European Journal of Mechanics - A/Solids*, *16*(2), 295–306.

Dominguez, J. (1993). *Boundary Elements in Dynamics*. London: Elsevier Applied Science.

Dunkin, J. W. (1965). Computation of modal solutions in layered, elastic media at high frequencies. *Bulletin of the Seismological Society of America*, *55*(2), 335–358.

Eason, G. (1965). The stresses produced in a semi-infinite soild by a moving surface force. *International Journal of Engineering Science*, *2*, 581–609.

El Kacimi, A., Woodward, P. K., Laghrouche, O., & Medero, G. (2013). Time domain 3D finite element modelling of train-induced vibration at high speed. *Computers & Structures*, *118*, 66–73.

Esveld, C. (2001). *Modern Railway Track*. Delft University of Technology.

Fenander, A. (1997). Frequency dependent stiffness and damping of railpads. *Proceedings of the Institution of Mechanical Engineers, Part F: Journal of Rail and Rapid Transit*, *211*, 51–62.

Fernandes, V. A. (2014). *Numerical analyis of nonlinear soil behavior and heterogeneity effects on railway track response*. PhD thesis at École Centrale Paris.

François, S., Schevenels, M., Galvín, P., Lombaert, G., & Degrande, G. (2010). A 2.5D coupled FE–BE methodology for the dynamic interaction between longitudinally invariant structures and a layered halfspace. *Computer Methods in Applied Mechanics and Engineering*, *199*(23–24), 1536–1548.

Fryba, L. (1999). *Vibration of Solids and Structures Under Moving Loads* (Third edit). London: Thomas Telford.

Fu, Q., & Zheng, C. (2014). Three-dimensional dynamic analyses of track-embankment-ground system subjected to high speed train loads. *The Scientific World Journal*, *2014*, 1–19.

Galvín, P., François, S., Schevenels, M., Bongini, E., Degrande, G., & Lombaert, G. (2010). A 2.5D coupled FE-BE model for the prediction of railway induced vibrations. *Soil Dynamics and Earthquake Engineering*, *30*(12), 1500–1512.

Galvín, P., Romero, A., & Domínguez, J. (2010). Fully three-dimensional analysis of high-speed train–track–soil-structure dynamic interaction. *Journal of Sound and Vibration*, *329*(24), 5147–5163.

Gomes Correia, A., & Cunha, J. (2014). Analysis of nonlinear soil modelling in the subgrade and rail track responses under HST. *Transportation Geotechnics*, *1*(4), 147–156.

Gomez-Revuelto, I., Garcia-Castillo, L. E., & Demkowicz, L. F. (2012). A comparison Between PML, Infinite Elements and an iterative bem as mesh trucation methods for HP self-adaptive procedures in electromagnetics. *Progress In Electromagnetics Research*, *126*(February), 499–519.

Gu, Y., Liu, J., & Du, Y. (2007). 3D consistent viscous-spring artificial boundary and viscous-spring boundary element. In *Engineering Mechanics* (Vol. 24, pp. 31–37).

Halabian, A. M., & Naggar, M. H. El. (2002). Effect of non-linear soil – structure interaction on seismic response of tall slender structures. *Soil Dynamics and Earthquake Engineering*, *22*, 639–658.

Hall, L. (2003). Simulations and analyses of train-induced ground vibrations in finite element models. *Soil Dynamics and Earthquake Engineering*, *23*(5), 403–413.

Hardin, B. O., & Drnevich, V. P. (1972). Shear Modulus and Damping in Soils: Measurement and Parameter Effects. *Journal of the Soil Mechanics and Foundations Division*, *98*(6), 603–624.

Harkness, J. (2009). Potential particles for the modelling of interlocking media in three dimensions. *International Journal for Numerical Method in Engineering*, *80*, 1573–1594.

Harkness, J., Zervos, A., Le Pen, L., Aingaran, S., & Powrie, W. (2016). Discrete element simulation of railway ballast: modelling cell pressure effects in triaxial tests. *Granular Matter*, (65), 1–13.

Haskell, N. A. (1953). The dispersion of surface waves on multilayered media. *Bulletin of the Seismological Society of America*, *43*, 17–34.

Hickes, R. G. (1970). *Factors influencing the resilient properties of granular materials*.

Hornych, P., Kazai, A., & Piau, J. M. (1998). Study of the resilient behaviour of unbound granular materials. In *5th International Conference on the Bearing Capacity of Roads and Airfields* (pp. 1277–1287).

Hunt, G. A. (1994). *Analysis of requirements for railway construction on soft ground. Technical Report LR TM 031, British Rail Research, London, England*.

Indraratna, B., & Christie, D. (2005). Effect of confining pressure on the degradation of ballast under cyclic loading. *Geotechnique, 55*(4), 325–328.

Indraratna, B., Ionescu, D., & Christie, H. D. (1998). Shear Behaviour of Railway Ballast based on Large Scale Triaxial Testing. *Journal of Geotechnical Engineering*, *124*(5), 439–449.

Indraratna, B., Kumar, P., & Jayan, S. (2010). Experimental and Numerical Study of Railway Ballast Behavior under Cyclic Loading. *International Journal of Geomechanics*, *10*, 136–144.

Indraratna, B., & Salim, W. (2002). Modelling of particle breakage of coarse aggregates incorporating strength and dilatancy. *Geotechnical Engineering, 155*(4), 243–252.

Indraratna, B., & Salim, W. (2005). *Mechanics of Ballasted Rail Tracks: A Geotechnical Perspective*. Taylor & Francis Group.

Indraratna, B., Salim, W., & Rujikiatkamjorn, C. (2007). Development and application of constitutive model for railway ballast. In *International Workshop on Consitutive Modelling* (pp. 685–696). Hong Kong.

Indraratna, B., Salim, W., & Rujikiatkamjorn, C. (2011). *Advanced Rail Geotechnology - Ballasted Track*. CRC Press.

Indraratna, B., Thakur, P., Vinod, J., & Salim, W. (2012). Semiempirical Cyclic Densification Model for Ballast Incorporating Particle Breakage. *International Journal of Geomechanics*, *12*(3), 260–271.

Ishibashi, I., & Zhang, X. (1993). Unified dynamic shear moduli and damping ratio of sand and clay. *Soils and Foundations, 33*(1), 182–191.

Ishihara, K., Sodekawa, M., & Tanaka, Y. (1978). Effects of over consolidation on liquefaction characteristics of sands containing finew. *Dynamic Geotechnical Testing, ASTM*, *654*, 246–264.

Iwan, W. D. (1967). On a class of models for the yielding behavior of continuous and composite systems. *Journal of Applied Mechanics*, *34*(3), 612–617.

Iwasaki, T., Tatsuoka, F., & Takagi, Y. (1978). Shear moduli of sand under cyclic torsional shear loading. *Soils and Foundations, 18*(1), 39–56.

Jin, Q., & Thompson, D. (2014). Prediction of Ground Vibration From Trains Using a Multi-Body Vehicle Model Coupled To a 2.5D FE/BE Model of the Track and

Ground. *The 21st International Congress on Sound and Vibration*, (July).

Ju, S. H., Liao, J. R., & Ye, Y. L. (2010). Behavior of ground vibrations induced by trains moving on embankments with rail roughness. *Soil Dynamics and Earthquake Engineering*, *30*(11), 1237–1249.

Karlström, A., & Boström, A. (2006). An analytical model for train-induced ground vibrations from railways. *Journal of Sound and Vibration*, *292*(1–2), 221–241.

Katayama, I., Ozeki, K., Yamaya, A., & Seshimo, Y. (1992). Non-linear free-field soil response analysis of a vertical array data. *Technical Report NCEER*, 735–761.

Kausel, E., & Roësset, J. M. (1981). Stiffness matrices for layered soils. *Bulletin of the Seismological Society of America*, *71*(6), 1743–1761.

Kausel, E., & Tassoulas, J. L. (1981). Transmitting boundaries: A closed-form comparison. *Bulletin of the Seismological Society of America*, *71*(1), 143–159.

Kaynia, A. M., Madshus, C., & Zackrisson, P. (2000). Ground vibration from high-speed trains: prediction and countermeasure. *Journal of Geotechnical and Geoenvironmental Engineering*, *126*(6), 531–537.

Kennedy, J. H., Woodward, P. K., Banimahd, M., & Medero, G. M. (2012). Railway track performance study using a new testing facility. *Proceedings of the ICE - Geotechnical Engineering*, *165*(5), 309–319.

Kenney, J. T. (1954). Steady-state vibrations of beam on elastic foundation for moving load. *Journal of Applied Mechanics*, *76*, 359–364.

Knothe, K. ., & Grassie, S. . (1993). Modelling of railway track and vehicle/track interaction at high frequencies. *Vehicle System Dynamics*, *22*(3–4), 209–262.

Knothe, K., & Wu, Y. (1998). Receptance behaviour of railway track and subgrade. *Archive of Applied Mechanics*, *68*(7–8), 457–470.

Kokusho, T. (1980). Cyclic triaxial test of dynamic soil properties for wide strain range. *Soils and Foundations*, *20*(2), 45–60.

Kouroussis, G., Connolly, D. P., & Verlinden, O. (2014). Railway-induced ground vibrations – a review of vehicle effects. *International Journal of Rail Transportation*, *2*(May 2016), 69–110.

Kouroussis, G., Verlinden, O., & Conti, C. (2009). Ground propagation of vibrations from railway vehicles using a finite/infinite-element model of the soil. *Proceedings of the Institution of Mechanical Engineers, Part F: Journal of Rail and Rapid Transit*, *223*(4), 405–413.

Kouroussis, G., Verlinden, O., & Conti, C. (2011a). Finite-dynamic model for infinite media: corrected solution of viscous boundary efficiency. *Journal of Engineering Mechanics*, *137*(7), 509–511.

Kouroussis, G., Verlinden, O., & Conti, C. (2011b). Free field vibrations caused by high-speed lines: Measurement and time domain simulation. *Soil Dynamics and Earthquake Engineering*, *31*(4), 692–707.

Kramer, S. L. (1996). *Geotechnical Earthquake Engineering*. Prentice-Hall, Inc.

Krylov, V. V. (1995). Generation of ground vibrations by superfast trains. *Applied Acoustics*, *44*(2), 149–164.

Krylov, V. V. (1996). Vibrational impact of high-speed trains . I . Effect of track dynamics. *J. Acoust. Soc. Am.*, *100*(5), 3121–3134.

Krylov, V. V. (1998). Effects of track properties on ground vibrations generated by high-speed train, *84*, 78–90.

Krylov, V. V, & Ferguson, C. (1994). Calculation of low-frequency ground vibrations from railway trains. *Applied Acoustics*, *42*(3), 199–213.

Kuhlemeyer, R. L. ., & Lysmer, J. (1973). Finite element method accuracy for wave propagation problems. *Journal of the Soil Mechanics and Foundations Division*, *99*(5), 421–427.

Kumar, S. S., Krishna, A. M., & Dey, A. (2013). Parameters influencing dynamic soil properties : a review treatise. In *National Conference on Recent Advances in Civil Engineering* (pp. 1–10).

Lackenby, J., Indraratna, B., McDowell, G., & Christie, D. (2007). Effect of confining pressure on ballast degradation and deformation under cyclic triaxial loading. *Géotechnique*, *57*(6), 527–536.

Lai, C. G., Calleril, A., Faccioli, E., & Martino, A. (2000). Mathematical modelling of railway-induced ground vibrations. *Proceedings of the International Workshop Wave 2000, Bochum, Germany*, 99–110.

Lane, H. (2007). *Computational Railway Dynamics - Integrated Train - Track - Subgrade Modeling and Simulations*. Chalmers University of Technology.

Lane, H., Kettil, P., & Wiberg, N.-E. (2008). Moving finite elements and dynamic vehicle interaction. *European Journal of Mechanics - A/Solids*, *27*(4), 515–531.

Le Pen, L. M., & Powrie, W. (2011). Contribution of base, crib, and shoulder ballast to the lateral sliding resistance of railway track: a geotechnical perspective. *Proceedings of the Institution of Mechanical Engineers, Part F: Journal of Rail and Rapid Transit*, *225*(2), 113–128.

Leshchinsky, B., & Ling, H. (2013). Effects of Geocell Confinement on Strength and Deformation Behavior of Gravel. *Journal of Geotechnical and Geoenvironmental Engineering*, *139*(2), 340–352.

Lieb, M., & Sudret, B. (1998). A fast algorithm for soil dynamics calculations by wavelet decomposition. *Archive of Applied Mechanics*, *68*(3), 147–157.

Lim, W. L., & McDowell, G. R. (2005). Discrete element modelling of railway ballast.

Granular Matter, *7*(1), 19–29.

Lin, M., & Huang, T. (1996). The effects of frequency on damping properties of sand. *Soil Dynamics and Earthquake Engineering*, *15*, 269–278.

Liu, J., Du, Y., Du, X., Wang, Z., & Wu, J. (2006). 3D viscous-spring artificial boundary in time domain. *Earthquake Engineering and Engineering Vibration*, *5*(1), 93–102.

Lombaert, G., & Degrande, G. (2009). Ground-borne vibration due to static and dynamic axle loads of InterCity and high-speed trains. *Journal of Sound and Vibration*, *319*(3–5), 1036–1066.

Lombaert, G., Degrande, G., Kogut, J., & François, S. (2006). The experimental validation of a numerical model for the prediction of railway induced vibrations. *Journal of Sound and Vibration*, *297*(3–5), 512–535.

Lopez-Caballero, F., & Modaressi Farahmand-Razavi, A. (2008). Numerical simulation of liquefaction effects on seismic SSI. *Soil Dynamics and Earthquake Engineering*, *28*(2), 85–98.

Lu, M., & McDowell, G. R. (2006). The importance of modelling ballast particle shape in the discrete element method. *Granular Matter*, *9*(1–2), 69–80.

Lu, M., & McDowell, G. R. (2010). Discrete element modelling of railway ballast under monotonic and cyclic triaxial loading. *Géotechnique*, *60*(6), 459–467.

Lysmer, J., & Kuhlemeyer, R. L. (1969). Finite dynamic model for infinite media. *Journal of Engineering Mechanics*, *95*(EM4), 859–877.

Lysmer, J., Ukaka, T., Tsai, C., & Seed, H. B. (1975). *FLUSH: A computer program for approximate 3-D analysis of soil-structure interaction problems*. Berkeley, California.

Madshus, C., & Kaynia, A. M. (2000). High-speed railway lines on soft ground: dynamic behaviour at critical train speed. *Journal of Sound and Vibration*, *231*(3), 689–701.

Mezher, S. B., Connolly, D. P., Woodward, P. K., Laghrouche, O., Pombo, J., & Costa, P. A. (2015). Railway critical velocity - Analytical prediction and analysis. *Transportation Geotechnics*, *6*, 84–96.

Miura, K., Kobayashi, S., & Yoshida, N. (2000). Equivalent linear analysis considering large strain and frequency dependent charactersitics. In *12th World Conf. on Earthq. Eng* (pp. 1832–1839). Auckland, New Zealand.

Nguyen, V.-H., & Duhamel, D. (2008). Finite element procedures for nonlinear structures in moving coordinates. Part II: Infinite beam under moving harmonic loads. *Computers & Structures*, *86*(21–22), 2056–2063.

Nguyen, V.-H., Duhamel, D., & Nedjar, B. (2003). A continuum model for granular materials taking into account the no-tension effect. *Mechanics of Materials*, *35*(10), 955–967.

Nilsson, C.-M., & Jones, C. J. C. (2007). *Theory Manual for WANDS 2.1: Wave-Number-Domain FE-BE Software For Structures And Fluids*.

Qiang, X., Jianyun, C., Jing, L., & Shuli, F. (2012). New artificial boundary condition for saturated soil foundations. *Earthquake Engineering and Engineering Vibration, 11*(1), 139–147.

Sadeghi, J. (1997). *Investigation of characteristics and modelling of railway track system*. PhD thesis at University of Wollongong.

Saleeb, A. F., & Kumar, A. (2011). Automated Finite Element Analysis of Complex Dynamics of Primary System Traversed by Oscillatory Subsystem. *International Journal for Computational Methods in Engineering Science and Mechanics*, *12*(4), 184–202.

Salim, W., & Indraratna, B. (2004). A new elastoplastic constitutive model for coarse granular aggregates incorporating particle breakage. *Canadian Geotechnical Journal*, *41*(4), 657–671.

Seed, H. B., & Idriss, I. M. (1970). *Soil moduli and daming factors for dynamic response analysis*. Berkeley, California.

Selig, E. T., & Waters, J. M. (1994). *Track Geotechnology and Substructure Management*. London: Thomas Telfoed Ltd.

Sheng, X., Jones, C. J. C., & Petyt, M. (1999a). Ground vibration generated by a load moving along a railway track. *Journal of Sound and Vibration*, *228*(1), 129–156.

Sheng, X., Jones, C. J. C., & Petyt, M. (1999b). Ground vibration generated by harmonic load acting on a railway track. *Journal of Sound and Vibration*, *225*(1), 3–28.

Sheng, X., Jones, C. J. C., & Thompson, D. J. (2003). A comparison of a theoretical model for quasi-statically and dynamically induced environmental vibration from trains with measurements. *Journal of Sound and Vibration*, *267*(3), 621–635.

Sheng, X., Jones, C. J. C., & Thompson, D. J. (2004a). A theoretical model for ground vibration from trains generated by vertical track irregularities. *Journal of Sound and Vibration*, *272*(3–5), 937–965.

Sheng, X., Jones, C. J. C., & Thompson, D. J. (2004b). A theoretical study on the influence of the track on train-induced ground vibration. *Journal of Sound and Vibration*, *272*(3–5), 909–936.

Sheng, X., Jones, C. J. C., & Thompson, D. J. (2005). Modelling ground vibration from railways using wavenumber finite- and boundary-element methods. *Proceedings of the Royal Society A: Mathematical, Physical and Engineering Sciences*, *461*(2059), 2043–2070.

Sheng, X., Jones, C. J. C., & Thompson, D. J. (2006). Prediction of ground vibration from trains using the wavenumber finite and boundary element methods. *Journal of Sound and Vibration*, *293*(3–5), 575–586.

Shenton, M. J. (1975). Deformation of railway ballast under repeated load-ing conditions. In Elsevier Inc. (Ed.), *Railroad Track Mechanics and Technology* (pp. 405–425).

Shih, J.-Y., Thompson, D. J., & Zervos, A. (2016). The effect of boundary conditions, model size and damping models in the finite element modeling of moving load on a track/ground system. *Soil Dynamics and Earthquake Engineering, 89*, 12–27.

Shih, J.-Y., Thompson, D., & Zervos, A. (2014). Assessment of track-ground coupled vibration induced by high-speed trains. In *The 21st International Congress on Sound and Vibration*.

Song, C., & Wolf, J. P. (1997). The scaled boundary finite-element method-alias consistent. *Computer Methods in Applied Mechanics and Engineering, 147*, 329–355.

Suiker, A. S. J., & Borst, R. de. (2003). A numerical model for the cyclic deterioration of railway tracks. *International Journal for Numerical Methods in Engineering, 57*(4), 441–470.

Suiker, A. S. J., Selig, E. T., & Frenkel, R. (2005). Static and Cyclic Triaxial Testing of Ballast and Subballast. *Journal of Geotechnical and Geoenvironmental Engineering*, (June), 771–782.

Thach, P.-N., Liu, H.-L., & Kong, G.-Q. (2013). Vibration analysis of pile-supported embankments under high-speed train passage. *Soil Dynamics and Earthquake Engineering*, *55*, 92–99.

Thompson, D. J. (2009). *Railway Noise and Vibration, Mechanisms, Modelling and Means of Control*. Oxford: Oxford Elsevier Ltd.

Thompson, D. J., Jones, C. J. C., Wu, T. X., & de France, A. (1999). The influence of the non-linear stiffness behaviour of rail pads on the track component of rolling noise. *Proceedings of the Institution of Mechanical Engineers, Part F: Journal of Rail and Rapid Transit*, *213*(4), 233–241.

Thompson, D. J., Vliet, van W. J., & Verheij, J. W. (1998). Developments of the indirect method for measuring the high frequency dynamic stiffness of resilient elements. *Journal of Sound and Vibration*, *213*(1), 169–188.

Thompson, D., & Verheij, J. (1997). The dynamic behaviour of rail fasteners at high frequencies. *Applied Acoustics*, *52*(1), 1–17.

Thomson, W. T. (1950). Transmission of elastic waves through a stratified solid medium. *Journal of Applied Physics*, *21*(2), 89.

Timoshenko, S. (1926). Methods of analysis of statical and dynamical stresses in rail. In *Proceedings of the Second International Congress on Applied Mechanics* (pp. 407–418).

Timoshenko, S., & Goodier, J. N. (1951). *Theory of Elasticity*. New Yourk: Mcgraw-Hill, Inc.: USA.

Triepaischajonsak, N., & Thompson, D. J. (2015). A hybrid modelling approach for predicting ground vibration from trains. *Journal of Sound and Vibration*, *335*, 147–173.

Uzan, J. (1985). Characterization of granular materials. *Transportation Research Record, 1022*, 52–59.

Varandas, J. N. (2013). *Long-Term Behaviour of Railway Transitions Under Dynamic Loading*. PhD thesis at Universidade Nova De Lisboa.

Verruijt, A. (2009). *Soil dynamics*. Delft.

Vincent, N., Bouvet, P., Thompson, D. J., & Gautier, P. E. (1996). Theoretical optimization of track components to reduce rolling noise. *Journal of Sound and Vibration*, *193*(1), 161–171.

Vostroukhov, A. V, & Metrikine, A. V. (2003). Periodically supported beam on a visco-elastic layer as a model for dynamic analysis of a high-speed railway track. *International Journal of Solids and Structures*, *40*(21), 5723–5752.

Vucetic, M., & Dobry, R. (1991). Effect of soil plasticity on cyclic response. *Journal of Geotechnical Engineering, 117*(1), 89–107.

Waas, G. (1972). *Linear two-dimensional analysis of soil dynamic problems in semi-infinite layer media*. PhD thesis at University of California.

Wolf, J. P., & Song, C. (1996). Finite-element modelling of unbounded media. In *Eleventh World Conference on Earthquake Engineering*. Ele.

Woodward, P. K., Laghrouche, O., Mezher, S. B., & Connolly, D. P. (2015). Application of coupled train-track modelling of critical speeds for high-speed trains using three-dimensional non-linear finite elements. *International Journal of Railway Technology*, *4*(3), 1–35.

Wu, T. X., & Thompson, D. J. (1999). The effects of local preload on the foundation stiffness and vertical vibration of railway track. *Journal of Sound and Vibration*, *219*(5), 881–904.

Xia, H., Cao, Y. M., & De Roeck, G. (2010). Theoretical modeling and characteristic analysis of moving-train induced ground vibrations. *Journal of Sound and Vibration*, *329*(7), 819–832.

Xu, Q., Chen, J., Li, J., & Wang, M. (2012). Study of an artificial boundary condition based on the damping-solvent extraction method. *Frontiers of Structural and Civil Engineering, 6*(3), 281–287.

Yang, Y. B., & Hung, H. H. (2001). A 2.5D finite/infinite element approach for modelling visco-elastic bodies subjected to moving loads. *International Journal for Numerical Methods in Engineering, 51*(11), 1317–1336.

Yang, Y. B., Hung, H. H., & Chang, D. W. (2003). Train-induced wave propagation in layered soils using finite/infinite element simulation. *Soil Dynamics and Earthquake*

Engineering, *23*(4), 263–278.

Yang, Y. B., & Yau, J. D. (1997). Vehicle-bridge interaction element for dynamic analysis. *Journal of Sound and Vibration*, *123*, 1512–1518.

Yoshida, N., & Iai, S. (1998). Nonlinear site response and its evaluation and prediction. In *Proc. 2nd International Symposium on the Effect of Surface Geology on Seismic Motion* (pp. 71–90). Yokosuka, Japan.

Yoshida, N., Kobayashi, S., Suetomi, I., & Miura, K. (2002). Equivalent linear method considering frequency dependent characteristics of stiffness and damping. *Soil Dynamics and Earthquake Engineering*, *22*, 205–222.

Zdravkovic, L., & Kontoe, S. (2008). Some issues in modeling boundary conditions in dynamic geotechnical analysis. In *The 12th Interactional Conference of International Association for Computer Methods and Advances in Geomechanics* (pp. 1–6). Goa, India.

Zerwer, A., Cascante, G., & Hutchinson, J. (2002). Parameter Estimation in Finite Element Simulations of Rayleigh Waves. *Journal of Geotechnical and Geoenvironmental Engineering*, *128*, 250–261.

Zhai, W. M., Wang, K. Y., & Lin, J. H. (2004). Modelling and experiment of railway ballast vibrations. *Journal of Sound and Vibration*, *270*(4–5), 673–683.

Zhai, W., & Sun, X. (1994). A detailed model for investigating vertical interaction between railway vehicle and track. *Vehicle System Dynamics*, *23*(sup1), 603–615.

Zhang, J., Andrus, R. D., & Juang, C. H. (2005). Normalized Shear Modulus and Material Damping Ratio Relationships. *Journal of Geotechnical and Geoenvironmental Engineering*, *131*(4), 453–464.